Investigating Electronic And Structural Properties Of Hybrid Materials

Thesis submitted for the degree of

Doctor of Philosophy (Science)

in
Physics (Theoretical)

by

Debayan Mondal

Registration number: 05146/Ph.D.(Sc.)Proceed/2020
Date of Registration : 3rd December, 2020

Under the Guidance of

Prof. Priya Mahadevan

Department of Physics

University of Calcutta

Kolkata-700 073, India

2023

Dedicated to,

My beloved family, without whose endless love and support, I could not achieve this...

Acknowledgements

In this memorable moment of submitting my Ph.D thesis, I would like to take this opportunity to express my hearty gratitude to those generous people who have guided me, motivated me and have been still with me all through a period of five and a half years of my academic journey in the S. N. Bose National Centre For Basic Sciences, where this journey has touched the summit at last. First and foremost, I wish to express my profound gratitude to Prof. Priya Mahadevan for being the unwavering pillar of support and guidance throughout my research journey and the completion of my Ph.D. thesis. Without her sincere assistance, this academic endeavour would have remained in the shadows, never seeing the light of day. Prof. Mahadevan's invaluable advice has not only shaped my academic trajectory but has also been a guiding light, casting illumination on the path of my future career and life. I consider myself incredibly fortunate to have had the opportunity to collaborate with such a kind and supportive mentor. I find it marked not only by academic growth but by an emotional connection. Her guidance has been a beacon of light during moments of uncertainty, and her belief in my capabilities has been the driving force behind my academic and personal development. I would also like to offer thanks to Dr. Manoranjan Kumar and Dr. Thirupathaiah Setti of the S. N. Bose National Centre For Basic Sciences and Dr. Sameer Sapra from IIT-Delhi for their valuable suggestions and comments. I must extend my heartfelt thanks to the entire S. N. Bose Centre, a sanctuary that has cradled my academic journey with not just good research facilities but also a serene, comforting, and peaceful environment. Each corner of this institution has been a silent witness to the moments of discovery and contemplation, shaping not just my research but also my experience as a scholar. Equally deserving of my sincere appreciation is the C.S.I.R (India), whose consistent support through scholarships has been a steady anchor throughout my entire Ph.D. program. The support and resources provided by PARAM Shivay (IIT-Bhu) and PARAM Yukti (JNCASR) Facility under the National Supercomputing Mission, Government of India. are gratefully acknowledged. I am deeply grateful to Prof. DD Sarma (IISc, Bangalore) and Prof. Narayan Pradhan(IACS, Kolkata) for their unwavering support and invaluable guidance during my research. Their insightful approach to understanding experimental nuances and commitment to interpreting microscopic phenomena have greatly enriched my work. The fruitful discussions and thoughtful comments from both Prof. DD Sharma and Narayan Pradhan have been instrumental in enhancing my comprehension and interpretation of experimental findings. . I am also glad to have so many energetic and enthusiastic collaborators during my journey: Prof. DD Sarma (IISc, Bangalore), Prof. Narayan Pradhan (IACS, Kolkata), Prof. Sayan Bhattacharyya (IISER

Kolkata), Prof. Renguo Xie (Jilin University, China), Dr. Atindra Nath Pal (SNBNCBS, Kolkata) and Dr. Aparna Deshpande (IISER Pune) With sincere appreciation, I extend my thanks to the members of the PMG Group who have significantly shaped my academic path. A special acknowledgement goes to my seniors— Sagar Da, Poonam Di and Sumanti Di. Their mentorship has been invaluable, providing me with rich insights and guidance that go beyond this academia. Turning the spotlight to my juniors—Krishnendu, Shrinjini, Sanuja, Shivam(M), Shivam(J) and Madhurita —I am grateful for their suggestions and collaborative efforts that have been a source of inspiration, creating a vibrant and supportive atmosphere within the group. Now, I want to express my sincere gratitude to those people whose inspiration helped me to reach here in the S. N. Bose centre for my higher studies; firstly, all of my teachers, Mr. Sujit Chakraborty, Mr. Meghnath Saha, Mrs. Tapasi Roy during my school days; Prof. Subhasish Roy Prof. Manas Maity, Prof. Arani Chakravarti, Prof. Sudipta Das, of the Visva Bharati (Department of Physics) during my graduate days they are all my path-makers and helped me to dream. As I stand at the culmination of this academic chapter, my heart overflows with gratitude and love for the ones who stood by me through it all. Premasis, Tanmoy, Prasun, Rafiqul, Shubhrasis, Susmita, Biswajit Panda, Nur, Didhiti, Anwesha, Anupam and Swarnali – Their presence has been the anchor in the storm, the lighthouse in uncharted waters, and the home where my heart finds solace. In this very moment I, do, remember my beloved juniors like Ananya, Rajdeep, Samir, Sumit, Soham, Ardhendu, Aishwaryo, Achinta, Shubhajit, Harmit and Sayan for their help, well wishes and warm company. I must name our SNB dance group members Ria, Amrita, Sreya, Anwesha, Subhajit, Athira, Shaili Di, Sucheta Di, Tania, Snehamoyee, Swarnali, Anupam, Anish, Priyanka Di, Dhiraj Da and Indrani for the memorable moments of colorful cultural activities in this Centre. I express my heartful thanks to Subhamita for this group and for introducing the rhythm of dance again in my life. I am thankful to my best buddies in S. N. Bose Centre, Deblina Di and Priyanka Di. They make my life more beautiful and helped me cheer up my mood even on the worst days. No thanks would be enough for their love, support, tolerance, and forgiveness. They help me to figure out my confusion, and shared various glorious as well as miserable moments over the last three years. They supported me at every work as well as personal annoyance. These people are family to me. I shall never forget about Pabi, for being more than a friend; he has been always there for support and as a valuable research collaborator. His unwavering encouragement and collaborative efforts have made a significant impact on my academic journey. The threads of friendship with Anibrata, Anupam and Manisha have been woven with the purest hues of joy, laughter, and shared

dreams. Anibrata, my confidant and kindred spirit, in his presence, challenges have become shared adventures, and triumphs have become celebrations. Anupam is more than a friend; he was a gentle melody in my everyday life, creating moments that still linger in my soul. Manisha, a cherished one, her warmth and understanding have been the balm to my soul. her presence has turned ordinary moments into extraordinary memories, the comfort of knowing there's someone always by my side. In these quiet corridors of memory, there's a bittersweet symphony of emotions tied to Shubhadip Da, who is more than a brother to me and who knows me in ways words can never convey. The tears we've shared, the laughter that echoed in the quietest corners of this institute— they are the bond that defies definition. Last but not the least extend my heartfelt gratitude to my parents, whose constant support, encouragement, and sacrifices have been the bedrock of my academic career. Their boundless love, guidance, and belief in my abilities have been the driving force behind my pursuit of knowledge. Their sacrifices, both seen and unseen, have prepared the road for my scholarly endeavors. I am eternally grateful to them for instilling ideals in me. Thank you for being such pillars of strength and inspiration during this journey, Mom and Dad. And to my brother Debasish, a steadfast companion in every twist and turn of this challenging road. Their silent sacrifices and unspoken understanding have been the bedrock on which my dreams have stood.

Debayan Mondal
S. N. Bose National Centre for Basic Sciences
Kolkata - 700106, India
December, 2023

Abstract

This thesis highlights the crucial role of the structure in determining the electronic properties of hybrid (organic-inorganic) materials, especially focusing on hybrid perovskites and single molecular junctions. Integration of organic molecules into the inorganic framework imparts unique characteristics to these materials.

Considering the inorganic perovskites, an empirical quantity, the tolerance factor which is defined in terms of the ionic radius is found to describe trends in the distortions. The recent shift to hybrid perovskites with organic molecules adds complexity to understanding structural distortions. Early studies highlight the role of hydrogen bonding, focusing on the molecule's shape, diverging from the conventional tolerance factor ideas. This thesis extends the exploration to symmetric molecules, examining if their presence eliminates octahedral tilts, potentially yielding a cubic perovskite structure. In contrast to inorganic perovskites, where structural changes align with the tolerance factor, hybrid perovskites demand a nuanced examination, considering the molecule's shape and orientation as crucial factors influencing hydrogen bonding and octahedral tilts. After examining the factors that determine the distortions in hybrid perovskites, we went on to examine if the shapes of the nanocrystals could be controlled. Due to variations in precursors, ligands, temperature, and reaction medium, nanocrystals predominantly acquire diverse shapes. By tuning the growth conditions and therefore the formation energy, the study shows that multifaceted nanocrystals can be stabilized. Optical property analysis of nanocrystal facets, especially in the presence of Mn doping, adds complexity to the exploration.

The journey embarked upon in this thesis seamlessly bridges concepts from 3D hybrid perovskites to 2D perovskites, where molecular interactions, lattice distortions, and quantum confinement effects intricately shape the electronic band structure. The choice of spacer cation in 2D perovskites influences edge states and overall electronic structure, unveiling unique properties at the edges compared to the bulk. Cation exchange processes manipulate edge state emissions, proposing theoretical frameworks elucidating the weak interaction at the surface compared to the bulk, allowing for dual emission phenomena.

Beyond the understanding of material properties, this thesis probes the behaviour of individual molecules in electronic circuits, with a specific focus on the "jump to molecular contact" phenomenon in single molecular junctions. This thesis unveils unique aspects of charge transport through molecules on gold electrodes, offering insights into directional bonding and contact formation. The focus on the response of metal/molecule/metal

junctions to external stimuli aligns with broader exploration. Examining temperature-dependent conductance changes, especially with organometallic molecule ferrocene, reveals distinctive traces. The proposed theoretical framework emphasizes the role of intramolecular rotation in dynamic junction formation, deepening our understanding of the complex interplay between temperature, molecular dynamics, and electronic behaviour.
In summary, this thesis provides a thorough investigation into the varied structural and electronic properties of 2D/3D perovskites and single molecular junctions. The discoveries not only enhance our fundamental understanding but also establish the groundwork for potential applications in catalysis, optoelectronics, and molecular electronics.

Publications

[1] Lucheng Peng, Sumit Kumar Dutta, **Debayan Mondal**, Biswajit Hudait, Sanjib Shyamal, Renguo Xie, Priya Mahadevan, and Narayan Pradhan. Arm growth and facet modulation in perovskite nanocrystals. *Journal of the American Chemical Society*, 141(40):16160–16168, 2019. doi: 10.1021/jacs.9b09157. URL https://doi.org/10.1021/jacs.9b09157. PMID: 31510737.

[2] Feng Liu, Tongjin Zhang, **Debayan Mondal**, Shiyong Teng, Ying Zhang, Keke Huang, Dayang Wang, Wensheng Yang, Priya Mahadevan, Yong Sheng Zhao, Renguo Xie, and Narayan Pradhan. Light-emitting metal–organic halide 1d and 2d structures: Near-unity quantum efficiency, low-loss optical waveguide and highly polarized emission. *Angewandte Chemie International Edition*, 60(24):13548–13553, 2021. doi: https://doi.org/10.1002/anie.202017274. URL https://onlinelibrary.wiley.com/doi/abs/10.1002/anie.202017274.

[3] **Debayan Mondal** and Priya Mahadevan. Shape control of emissive properties of mn-doped cspbbr3 nanocrystals. *The Journal of Physical Chemistry C*, 125(21):11462–11467, 2021. doi: 10.1021/acs.jpcc.1c02368. URL https://doi.org/10.1021/acs.jpcc.1c02368.

[4] Biswajit Pabi, **Debayan Mondal**, Priya Mahadevan, and Atindra Nath Pal. Probing metal-molecule contact at the atomic scale via conductance jumps. *Phys. Rev. B*, 104: L121407, Sep 2021. doi: 10.1103/PhysRevB.104.L121407. URL https://link.aps.org/doi/10.1103/PhysRevB.104.L121407.

[5] Suman Bera, Biswajit Hudait, **Debayan Mondal**, Sanjib Shyamal, Priya Mahadevan, and Narayan Pradhan. Transformation of metal halides to facet-modulated lead halide perovskite platelet nanostructures on a-site cs-sublattice platform. *Nano Letters*, 22

(4):1633–1640, 2022. doi: 10.1021/acs.nanolett.1c04624. URL https://doi.org/10.1021/acs.nanolett.1c04624. PMID: 35157475.

[6] Arnab Mandal, Sanuja Kumar Khuntia, **Debayan Mondal**, Priya Mahadevan, and Sayan Bhattacharyya. Spin texture sensitive photodetection by dion–jacobson tin halide perovskites. *Journal of the American Chemical Society*, 145(45):24990–25002, 2023. doi: 10.1021/jacs.3c10195. URL https://doi.org/10.1021/jacs.3c10195. PMID: 37906676.

[7] Rejaul Sk, **Debayan Mondal**, Imrankhan Mulani, Priya Mahadevan, and Aparna Deshpande. Emergent negative differential resistance with an undisturbed topological surface state. *The Journal of Physical Chemistry C*, 126(39):16744–16750, 2022. doi: 10.1021/acs.jpcc.2c05185. URL https://doi.org/10.1021/acs.jpcc.2c05185.

[8] Feng Liu, **Debayan Mondal**, Kai Zhang, Ying Zhang, Keke Huang, Dayang Wang, Wensheng Yang, Priya Mahadevan, and Renguo Xie. Zero-dimensional plate-shaped copper halide crystals with green-yellow emissions. *Mater. Adv.*, 2:3744–3751, 2021. doi: 10.1039/D1MA00061F. URL http://dx.doi.org/10.1039/D1MA00061F.

Contents

List of Figures

List of Tables

Chapter 1

Introduction

1 General Introduction

The investigation of hybrid (organic-inorganic) materials, particularly hybrid perovskites, holds significant importance due to their extensive applications in solar cells and optoelectronic devices[6, 7, 19, 20, 22, 32, 35, 36]. With an organic molecule integrated into the inorganic structure, these hybrid materials exhibit distinct characteristics that profoundly impact their performance. This research aims to unravel the intricate structural and electronic behavior of hybrid perovskites, providing key insights for optimizing technologies and advancing applications in renewable energy and electronic devices.

Traditionally, the exploration of perovskite structures has been guided by empirical considerations, such as the tolerance factor[15], influenced by ionic radii. The recent shift towards hybrid perovskites, featuring organic molecules, introduces new challenges in comprehending structural distortions. Pioneering studies[30, 51] have demonstrated the influence of hydrogen bonding on structural distortions, emphasizing the role of the molecule's shape, a departure from the conventional focus on the tolerance factor.

This thesis extends the exploration to symmetric molecules, questioning whether their presence would eliminate octahedral tilts, resulting in a cubic perovskite structure. Unlike inorganic perovskites, where structural changes are often described by the tolerance

factor, hybrid perovskites require a more detailed examination considering the shape and orientation of the molecule as a pivotal parameter influencing hydrogen bonding and, consequently, octahedral tilts.

Beyond the established understanding of hydrogen bonding, this thesis also delves into the realm of nanocrystal shapes. Due to the variations in precursors, ligands, temperature, and reaction medium, nanocrystals predominantly obtained a different shape[7, 8, 13, 23]. By exploring growth conditions and formation energy, the study stabilizes multifaceted nanocrystals, challenging conventional limitations. Optical property analysis of nanocrystal facets, particularly in the presence of Mn doping, adds another layer to the multifaceted exploration.

The journey bridges concepts from 3D hybrid perovskites to 2D perovskites, where molecular interactions, lattice distortions, and quantum confinement effects play intricate roles in shaping the electronic band structure. The choice of spacer cation in 2D perovskites influences edge states and overall electronic structure, revealing unique properties at the edges compared to the bulk. Cation exchange processes manipulate edge state emissions, proposing theoretical frameworks that elucidate the weak interaction at the surface compared to the bulk, allowing for dual emission phenomena.

Exploring beyond material properties, the thesis investigates individual molecules in electronic circuits, specifically focusing on the "jump to molecular contact" phenomenon in single molecular junctions. Unusual features emerge in charge transport through molecules attached to gold electrodes, revealing directional bonding mechanisms and providing insights into contact formation. Recent emphasis on investigating the response of metal/-molecule/metal junctions to external stimuli aligns with the broader exploration. Temperature-dependent conductance changes in single-molecule junctions, particularly with organometallic molecule ferrocene, reveal distinct traces, with a theoretical framework highlighting the impact of intra-molecular rotation on dynamic junction formation.

In summary, this interdisciplinary thesis contributes to the evolving landscape of hybrid materials, offering a comprehensive exploration of their diverse structural and electronic

properties. The findings not only advance fundamental understanding but also pave the way for potential applications in catalysis, optoelectronics, and molecular electronics. The interdisciplinary nature of this research opens avenues for continued exploration and collaboration in the dynamic field of materials science.

2 Exploring the Perovskite Structure and Its Tolerance Factor: A Delicate Balance

The perovskites given by the chemical formula ABX_3, where A and B are cations, typically of different sizes, and X is an anion[34, 47, 58], represent a class of extensively studied materials. The unique properties of perovskites make them vital for various applications, from solar cells to catalysis, and their formation hinges on a delicate parameter known as the tolerance factor. The perovskite structure is characterized by a three-dimensional arrangement of corner-sharing octahedral units (BX_6), forming a three-dimensional network. The A cations occupy the cuboctahedral sites located between the octahedra[17]. This arrangement leads to a highly symmetrical and stable structure, which, in the absence of external factors, would result in a perfect cubic lattice. However, real-world materials often deviate from this idealized structure due to the diverse sizes of A and B cations, and this is where the concept of the tolerance factor comes into play. The tolerance factor[15], denoted by "t," is a dimensionless parameter used to determine whether a compound is likely to adopt the perovskite structure or deviate from it. It is calculated using the radii of the cations involved in the formula, A, B, and X. The tolerance factor is defined as:

$$t = \frac{(r_A + r_X)}{\sqrt{2}(r_B + r_X)} \tag{1.1}$$

where r_A, r_B, and r_X represent the ionic radii of A, B, and X ions, respectively.

The tolerance factor is critical because it helps predict the structural stability and the likelihood of structural distortions in perovskite compounds. If the calculated tolerance

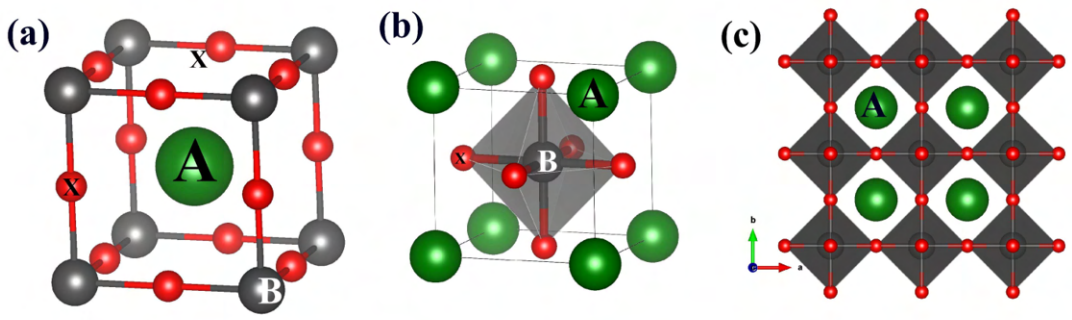

FIGURE 1.1: a) The structural unit of a perfect cubic perovskite comprises B cations located at the corners of the cube, anions positioned at the center of the cube's edges, and A cations situated at the body center of the cube. (b) The B cation exhibits octahedral coordination, surrounded by six anions. (c) Visualizing the perovskite structure involves depicting it as a network of corner-shared BX_6 octahedra, with the A cation occupying the voids within the octahedra.

factor falls within a certain range, it suggests that the compound is more likely to adopt the ideal perovskite structure. However, if the tolerance factor deviates significantly from this range, structural distortions and tilting of the octahedral units become more pronounced. In the range of 't' values between 0.9 and 1.0, cubic perovskite structures are typically observed, while 't' values falling between 0.80 and 0.89, often due to the presence of a smaller A cation or a larger B cation, tend to result in distorted perovskite structures characterized by octahedral tilting[14, 21, 43]. This behaviour can be qualitatively explained by considering fundamental electrostatic interactions. For instance, when the A cation is smaller in size, it leads to a reduction in the unit cell volume. Consequently, the distances between the B and X ions become shorter, resulting in an increased Coulomb repulsion between the electrons associated with B and X ions. To counteract this enhanced repulsion, the structure undergoes octahedral tilting, which prevents further reduction in the B-X bond lengths and leads to deviations from the ideal 180° B-X-B angles. As a consequence, the B-X distances also become longer.

For example, considering the effective ionic radii according to the Shannon model[78] for Sr^{2+} (1.44 Å), Ti^{4+} (0.60 Å), and O^{2-} (1.42 Å), an ideal cubic structure, as in the case of $SrTiO_3$, yields a value of t = 1.0. However, in the case of $CaTiO_3$, where the effective ionic

radius of Ca^{2+} is 1.12 Å, t is calculated to be 0.88. This t value indicates the occurrence of octahedral tilting, resulting in an orthorhombic unit cell structure. However, whether a reduction in the unit cell volume would primarily manifest as B-X bond compression or octahedral tilting depends on the relative compressibilities of the BX_6 and AX_{12} units within the perovskite structure. An in-depth investigation involving both experimental and theoretical analysis, as documented in a combined study[105] on the well-known perovskite $CaSnO_3$, has revealed that when the SnO_6 and CaO_{12} units exhibit similar compressibilities, changes in the Ca-O and Sn-O bond lengths occur uniformly under pressure, without introducing angular distortions. Conversely, a scenario where the SnO_6 and CaO_{12} units are nearly rigid results in dominant angular distortions. However, experimental observations have indicated that an approach solely based on the concept of "rigid units" is not appropriate. Instead, the experimental data suggests that the CaO_{12} unit exhibits greater compressibility compared to the SnO_6 unit. This difference in compressibility causes the Sn-O-Sn bond angle to undergo a significant change under pressure from the outset, in contrast to the Sn-O bond length.

On the other hand, when the value of t exceeds 1, typically due to the presence of a larger A cation or a smaller B cation, a low-dimensional hexagonal variant of the perovskite structure emerges. An oversized A cation can generate excessive internal pressure, capable of disrupting the corner-shared octahedral network. This disruption leads to anion vacancies in some of the octahedra. To maintain ionic coordination, octahedra with fewer anions bend and become face-shared with others. This results in parallel chains of face-shared octahedra separated by the A cation. This particular structure is known as a 2H perovskite structure. For instance, it is predicted that $BaMnO_3$ adopts a 2H perovskite structure[81], with t measured at 1.06 Å.

2.1 Tolerance Factor in Hybrid Perovskites

Recently, in contrast to traditional perovskites, which are based on inorganic atoms, there has been a lot of focus on hybrid perovskites as a consequence of their successful use in

solar cells as well as their remarkable optoelectronic properties. These hybrid perovskites are a distinct subclass of perovskite materials, characterized by the incorporation of organic cations, such as Methylammonium (MA) and Formamidinium (FA), into the A-site position. These organic cations have larger ionic radii and a complex structure compared to traditional inorganic cations, requiring us to rethink our previous knowledge of inorganic perovskites in order to understand the structural deviations we observe. This was not solely linked to establishing ionic radii for a non-spherical entity such as a molecule; rather, it necessitated the exploration of novel concepts to grasp the essence of the deformations. The work by Jang et. al[30] demonstrated that the hydrogen atoms within the molecule established hydrogen bonds with the anions within the inorganic framework. Their findings led them to the conclusion that this interaction was responsible for the observed structural distortions. Sagar and Mahadevan[51] built on this idea, showing that when an asymmetric molecule is in place, the hydrogens at one end of the molecule interact more with the inorganic cage, pushing the molecule toward one end. This also leads to the structure having a dipole moment, and it causes the anions to move closer to the hydrogens, resulting in the tilting of octahedra. In this thesis, we expand on these concepts by exploring a broader range of possibilities involving molecules at the A-site, resulting in three-dimensional perovskite structures. We have observed some common characteristics.

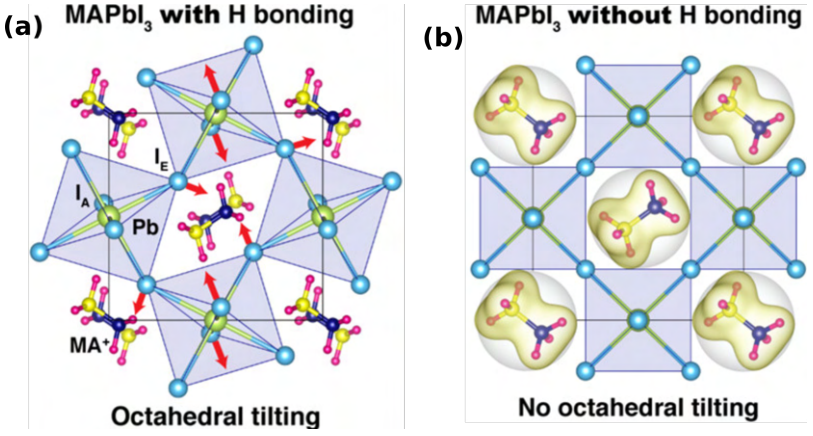

FIGURE 1.2: Hybrid perovskite structure ($MAPbI_3$) when (a) Interaction between hydrogen associated with the molecule and the inorganic network is active shows octahedral tilting (b) Interaction between hydrogen associate with the molecule and the inorganic network is inactive does not shows any distortions.[30])

Initially, we examined a molecule with identical functional groups at both ends and considered whether the presence of a symmetric molecule would lead to the absence of octahedral tilts, consequently resulting in a cubic perovskite structure. This raised the question of whether the molecule's symmetry could be an additional factor influencing the presence or absence of structural distortions. Notably, in the case of $FAPbCl_3$, the Pb-Cl-Pb bond angles are close to 180° in the plane parallel to the molecule's C_2 symmetry axis. However, the orientation of the molecule within the perovskite cage is also influenced by other factors, particularly the number of bonds the hydrogen atoms can form with the anions. Consequently, even with two symmetric molecules, very different orientations may be favored.

In contrast to inorganic perovskites, where structural changes in a series (with variations only at the A-site) could be adequately explained by the tolerance factor, this straightforward relationship no longer holds for three-dimensional hybrid perovskites. Various additional factors come into play, making it a more complex scenario. To explore this aspect, we have examined two distinct scenarios, one involving a symmetric molecule (formamidinium) and the other two asymmetric molecules (methylammonium and ethylammonium). We have scrutinized the structural distortions that occur in each case. It becomes evident that the shape of the molecule has a significant influence on the extent of hydrogen bonding with the anions, thereby dictating the octahedral tilts.

In the case of the asymmetric molecule, methylammonium (MA), which features different groups at its two ends, experiences dissimilar bonding with the inorganic cage. This results in both the molecule being off-center and the anions within the inorganic network moving closer to the hydrogen atoms. Consequently, the Pb-X-Pb bond angles deviate significantly from the ideal value of 180°. On the other hand, for ethylammonium (EA), which is larger and even more asymmetric than MA due to its larger alkyl group, the Pb-X-Pb bond angles in the bc plane (parallel to the molecular C-N bond) remain mostly unchanged. However, the bond angles in the ac plane (perpendicular to the molecular C-N bond) increase when transitioning from MA to EA, while keeping the anion constant.

In contrast, the results for the symmetric molecule formamidinium (FA), which possesses the same functional group on both sides of a central carbon atom, with a size intermediate to MA and EA, show distinct outcomes. For the chloride-based compound, the center of the molecule aligns with the center of the ac plane. The Pb-X-Pb angles parallel to the molecule's symmetry plane remain largely undistorted, while the angles in the plane perpendicular to the symmetry plane exhibit significant deviations. In the case of the bromide-based compound, the molecule does not shift towards any particular anion in the plane of the molecule. Nevertheless, the Pb-Br-Pb angles deviate significantly from the ideal values due to steric repulsion between the electrons on the bromine atom and the hydrogen atoms. These findings underscore that, in hybrid perovskites, the shape of the A-site cation, in addition to its size, plays a pivotal role in driving structural distortions. The off-centering of the methylammonium molecule occurs at the expense of reducing the number of hydrogen bonds formed with the anions. Without this off-centering, six bonds would form between the hydrogens and the anions. However, the more localized chloride atoms prevent the hydrogens from approaching too closely due to steric effects, leading to two shorter bonds between H and the chloride atoms in the ac plane and a slightly longer bond with the chloride atom towards which the molecule moves (ab plane). In the case of the more delocalized bromide anions, a shorter hydrogen bond is formed with the bromine atom towards which the molecule moves (bc plane), while the bromide atoms in the ac plane form longer hydrogen bonds. These results provide insights into the strength of the hydrogen-anion network bonds, which are crucial for understanding the molecule's dynamics.

3 Exploring Perovskites Nanocrystals: Small Wonders with Big Potential

3.1 What Are Nanocrystals?

Nanocrystals are crystalline structures at the nanoscale, typically composed of inorganic materials. They exhibit highly regular, ordered arrangements of atoms, which distinguish them from amorphous nanoparticles. These minute structures can be engineered to possess specific sizes, shapes, and compositions, offering a high degree of control over their properties.

3.2 Unique Properties of Nanocrystals

Nanocrystals possess a range of unique properties that set them apart from their bulk counterparts. These properties include:

1. Size-Dependent Optical Properties: The size of nanocrystals directly impacts their optical properties. Quantum dots, a type of nanocrystal, exhibit tunable colors based on their size, making them invaluable in applications like quantum dot displays and biological imaging.

2. High Surface Area: Due to their small size, nanocrystals have an extremely high surface area relative to their volume. This property is exploited in catalysts, where a larger surface area leads to enhanced reactivity.

3. Quantum Confinement: In semiconductor nanocrystals, electrons are confined within the nanocrystal, leading to quantum confinement effects. This property is crucial for applications like LEDs and solar cells.

4. Enhanced Magnetic Properties: Magnetic nanocrystals can exhibit enhanced magnetic properties, useful in data storage and medical applications.

5. Improved Mechanical and Thermal Properties: Nanocrystals can have exceptional mechanical and thermal properties, making them valuable in reinforcing materials like polymers and composites.

3.3 Perovskite Nanocrystals

To introduce lead halide perovskite nanocrystals, we can place them in the context of research involving colloidal semiconductor nanocrystals. This field of investigation has a rich history spanning several decades and remains dynamic today. Traditional colloidal semiconductor nanocrystals are primarily composed of binary compounds, known for their relatively simple crystal structures. These structures encompass tetrahedrally bonded compounds, such as zinc-blende (comprising chalcogenides like ZnS, ZnSe, CdS, CdSe, HgTe, and pnictides like InP, InAs) or wurtzite (including ZnS, ZnSe, CdS, CdSe). Additionally, compounds like PbS and PbSe with face-centered rock-salt-type structures fall into this category[3]. Semiconductor nanocrystals that are spherical or cubic and smaller than 20 nm, displaying quantum confinement in all three dimensions, are often referred to as quantum dots (QDs). In these conventional semiconductor nanocrystals, the anions and cations within the crystal structures occupy identical crystallographic positions or sublattices. In contrast, a new generation of perovskite nanocrystals, based on $CsPbX_3$ (with X representing Cl, Br, or I), has recently emerged as highly efficient optical materials for various optoelectronic applications. Considerable research endeavors have been devoted to comprehending the fundamental principles governing their formation and achieving stable nanocrystals with exceptional optical properties[6, 28, 37].

3.4 The Significance of Facet Modulation in the context of semiconductor nanocrystals

Nanoscale materials exhibit unique physical and chemical properties that are profoundly influenced by their size and structure. This phenomenon has prompted extensive research efforts aimed at advancing the controlled synthesis of nanomaterials[11, 25, 30, 32, 35].

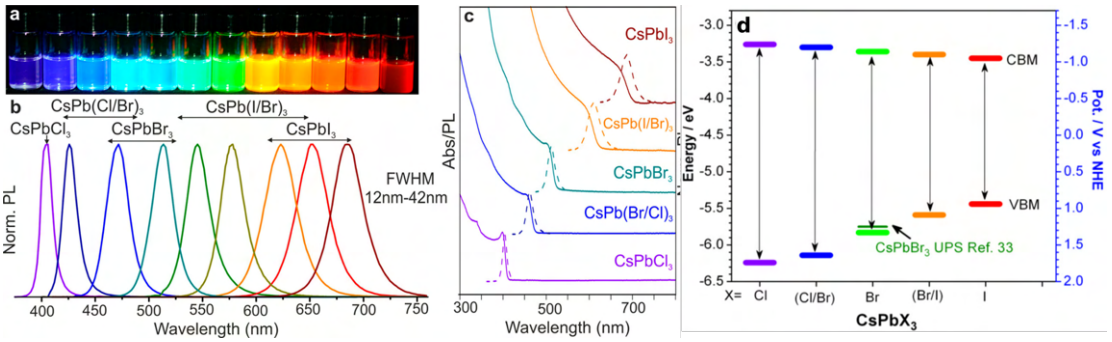

FIGURE 1.3: Colloidal $CsPbX_3$ nanocrystals (NCs), where X represents Cl, Br, or I, demonstrate adjustable bandgap energies across the entire visible spectrum. The tuning is achieved by manipulating the size and composition of the nanocrystals, resulting in vivid and precisely defined emissions. This is evident in (a) toluene colloidal solutions illuminated with a UV lamp ($\lambda = 365$ nm); (b) characteristic photoluminescence spectra ($\lambda_{exc} = 400$ nm for all except $CsPbCl_3$ samples, which have $\lambda_{exc} = 350$ nm); and (c) typical optical absorption and photoluminescence spectra. does not shows any distortions.[112] (d) Band edge energies of $CsPbX_3$ NCs[113]

The ultimate goal is to intentionally create nanostructured materials with customizable architectures and predictable characteristics through strategic design. This, in turn, enables the development of specific functionalities.

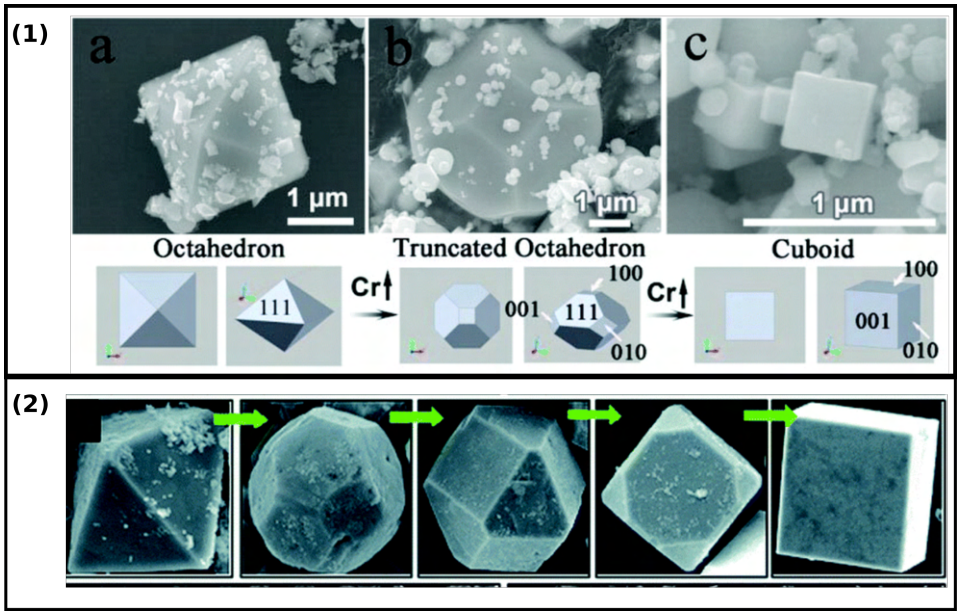

FIGURE 1.4: (1) Dopant induced shape evolution of WO_3 nanocrystals at (a) 0% Cr, (b) 2.5% Cr and (c) 10.0 % Cr.[115] (2)shape evolution of $NaNbO_3$ crystals from octahedra to cubes using NaOH ligand.[116]

In general, the growth of colloidal crystals with controlled shapes is considered a kinetic process. During this process, low-energy facets persist, while high-energy facets disappear,

resulting in a specific final shape enclosed by these low-energy surfaces. While initially, controlling the geometric shape of nanocrystals may seem like a scientific curiosity, its significance extends far beyond aesthetics. The shape not only influences the physical and chemical properties of nanocrystals but also dictates their suitability and value in various applications, spanning from catalysis to electronics, photonics, information storage, and energy conversion/storage.

For example, let's consider Cu_2O nanocrystals, which display highly facet-dependent photocatalytic activity and electrical conductivity. Octahedral nanocrystals that expose 111 facets are both photocatalytically active and electrically conductive, whereas nanocubes with 100 facets are inactive and non-conductive[38]. Consequently, researchers are actively exploring different methods to engineer the shapes of these nanocrystals. For instance, Sun et al. discovered that polyvinylpyrrolidone (PVP) can selectively stabilize the [100] facets of silver nanocrystals, thereby promoting the formation of silver nanocubes[30]. Huang et al. reported the use of facet-specific peptide sequences as regulatory agents for the predictable synthesis of platinum nanocrystals with selectively exposed crystal surfaces [11].

3.5 Facet Modulation for perovskite nanocrystals

In a comprehensive study on halide perovskite materials, the synthetic approach developed by Kovalenko and his colleagues played a central role [ref]. Typically, high-temperature reactions for these nanocrystals result in structures with six stable facets, often taking the form of cubes or platelets. While isotropic nanocrystals with cube shapes were formed for all three halides and exhibited intense emissions[1, 27, 29], the challenge remained to create stable facets with different shapes and observe their unique properties.

Considerable efforts have been invested in diversifying the ligands and precursors used in the synthesis [7, 13, 23], adjusting reaction temperatures[7], finding alternative solutions to prevent rapid cooling[8], and incorporating various additives to enhance the phase and optical stability of these nanocrystals[20, 23, 29, 31]. However, the question

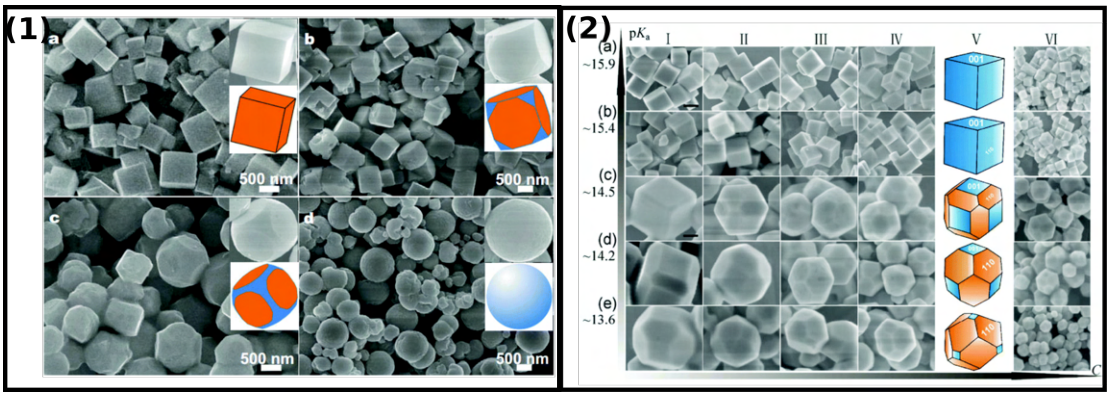

FIGURE 1.5: (1) shape evolution of $NaNbO_3$ crystals at different volume ratios of ethylene glycol (EG) to water: (a) 1/13, (b) 3/11, (c) 5/9, and (d) 11/3 [110] (2) Shape evolution of $SrTiO_3$ at different pK_a values and concentrations. High pK_a values lead to the exposure of more 001 facets, while low pK_a values lead to 110 facets in $SrTiO_3$ crystal growth processes[109]

of stabilizing facets beyond the six sides of the cube or directing the growth of specific facets in perovskite nanocrystals remained open. Despite some size adjustments in certain cases [source], the predominant shape for nanocrystals produced in high-temperature reaction setups continued to be the cube. In a departure from previous findings, Peng and colleagues[24] presented a novel approach to modulate the shape of isotropic perovskite nanocrystals through controlled arm growth. Their investigations revealed that these arm-like structures originated from intermediate 26-faceted rhombic cuboctahedron nanocrystals with $CsPbBr_3$ structures, which formed under conditions characterized by a shortage of halides (as referenced). Following treatment with OLA-H-Br, these multi-faceted intermediate structures with polyhedral shapes transformed into six-faceted armed nanostructures (Figure 1.6).

This thesis delves into the shape modulation in isotropic $CsPbBr_3$ structures through controlled arm growth. Building on experimental observations, the study systematically investigates the impact of diverse experimental conditions on growth, emphasizing the role of surface facets in nanocrystal formation. Surface energies are calculated considering variations in chemical potentials for Cs, Pb, Br, and H under different conditions. Notably, the findings align with experimental evidence, shedding light on the thermodynamic stability of facets and providing valuable insights into the formation of hexapod structures

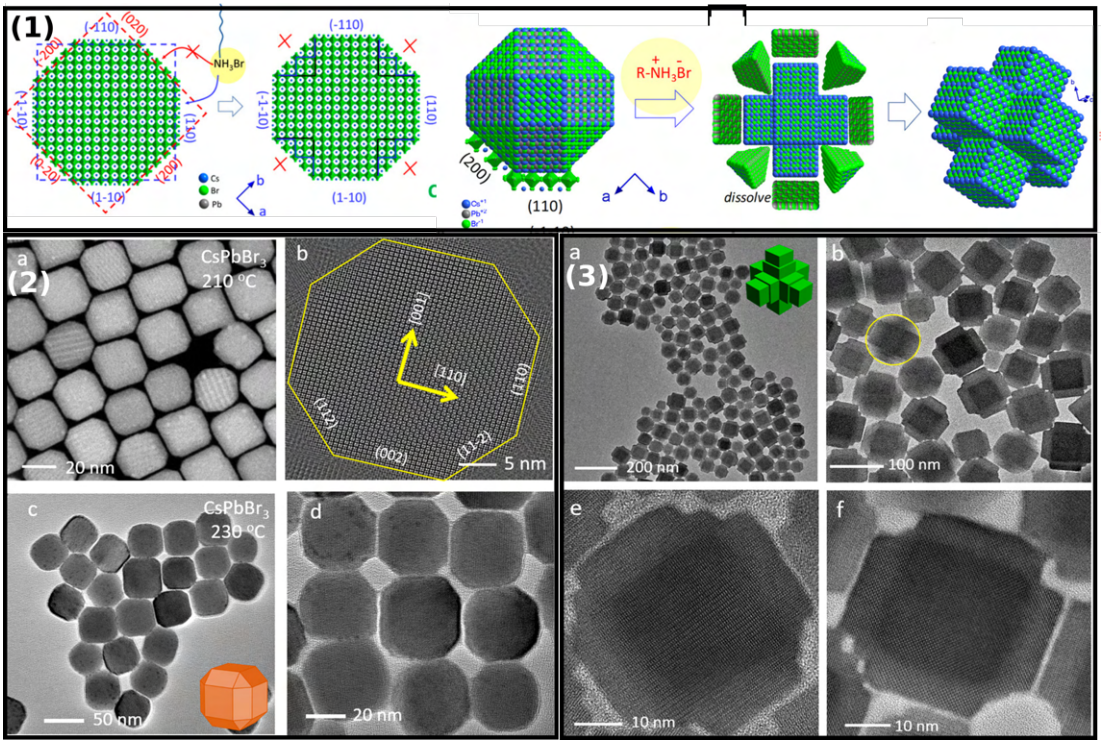

FIGURE 1.6: (1) Schematic presentation of the transformation of a $CsPbBr_3$ polyhedron to armed nanostructures with a treatment of alkylammonium bromide solution. (2) HAADF-STEM image of $CsPbBr_3$ polyhedron shaped nanostructures obtained before the injection of OLA–HBr (3) (a-d) TEM images of two-step arm growth of $CsPbBr_3$ hexapods.[24]

in $CsPbBr_3$ nanostructures.

4 The Vital Role of Doping in Perovskite Nanocrystals: A Path to Enhanced Performance

In many instances, the enhancement of nanocrystals' functionalities has traditionally involved a process known as doping. Doping is the deliberate introduction of specific atoms or ions (dopants) into the crystal structure of a material. In the context of perovskite nanocrystals, doping is a powerful tool for fine-tuning their properties and achieving superior performance. Here are some key reasons why doping is crucial:

1. Enhanced Optical Properties: Doping allows researchers to modify the bandgap of perovskite nanocrystals. By introducing dopants, they can shift the absorption and

emission spectra to match the requirements of specific applications. This capability is pivotal for the development of efficient light-emitting devices and photovoltaics.

2. Improved Stability: Perovskite nanocrystals can be sensitive to environmental factors like moisture and oxygen. Doping with appropriate elements or molecules can enhance their stability, making them more resilient to degradation and extending their operational lifetime.

3. Enhanced Charge Transport: Doping can improve charge carrier mobility and reduce recombination losses, which are critical factors in the performance of solar cells. This can lead to higher power conversion efficiencies in photovoltaic devices.

4. Tailored Applications: Doping allows for the customization of perovskite nanocrystals for specific applications. Whether it's optimizing their properties for efficient LEDs, efficient sensors, or high-performance lasers, doping provides versatility in tailoring these nanocrystals.

5. Advanced Materials Discovery Through doping, researchers can explore entirely new functionalities and properties. For example, magnetic doping can introduce magnetic properties into perovskite nanocrystals, expanding their utility in fields like data storage and sensing.

At times, dopants are strategically placed within the bandgap of the host material. This positioning potentially enables the transformation of wide bandgap semiconductors into intermediate bandgap semiconductors. While these aspects of dopant functionality have been extensively researched and are reasonably well understood, a perplexing aspect arises when the same dopant atom, within the same material, exhibits varying behavior due to different structural arrangements. This phenomenon challenges our current understanding and requires further exploration to unravel the underlying mechanisms.

4.1 Tuning Emissivity with Mn Doping in different facet of Perovskite Nanocrystals

Emissivity refers to a material's ability to emit light when excited. In the context of perovskite nanocrystals, high emissivity is a crucial property for efficient light emission in optoelectronic devices. This property is central to their performance in applications like LEDs and lasers. Mn doping, the deliberate incorporation of manganese ions into the perovskite nanocrystal lattice, represents a promising strategy to enhance their emissivity. This thesis delves into a fascinating aspect of nanocrystal behavior, where nanocrystals assume different shapes and explore the underlying reasons behind why Mn doping may result in light emission in some cases while remaining non-emissive in others. The study of Pb-based halide perovskites has garnered significant attention due to their exceptional solar cell efficiency and improved optoelectronic properties. Various approaches, including the introduction of dopant atoms and the utilization of different synthesis techniques, have been employed to investigate these materials. When examining nanocrystals of inorganic Pb-based halide perovskites using transmission electron microscopy (TEM), they often exhibit cubic facets[44]. Recent research, however, has shown that modifying the growth conditions can lead to variations in the nanocrystals' shapes. Under halide-deficient conditions, it was observed that more facets, beyond those expected for a typical cubic nanocrystal, were stabilized. This resulted in the formation of a polyhedron with 26 facets. Further adjustments to the growth conditions allowed for additional modifications of the nanocrystal's shape. The introduction of more halide salts caused the non-cubic facets to disappear, leaving behind a structure with only cubic facets. However, unlike the regular cubic-shaped nanocrystal initially formed, this modified structure featured protruding arms, resulting in a larger surface area[24].

Given that the nanocrystal structures realized under different experimental conditions possessed well-defined facets, they provided an ideal system for investigating why Mn doping was emissive in some cases but not in others. In this thesis, we investigated inorganic halide perovskite $CsPbBr_3$ nanocrystals. Our theoretical approach involved varying the

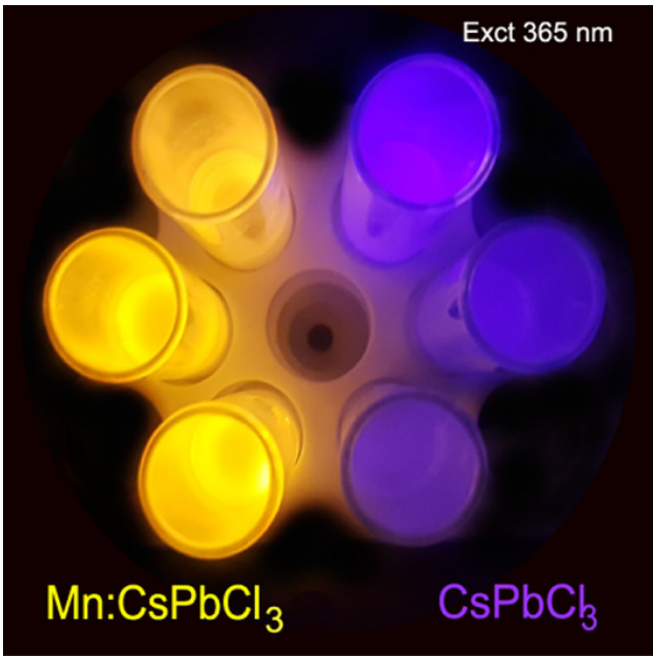

FIGURE 1.7: Digital images of $CsPbCl_3$ and Mn:$CsPbCl_3$ nanocrystals in illuminated reaction flask.[111]

halide content to influence the nanocrystal shape. To elucidate the mechanisms governing shape modulation, we considered the thermodynamic stabilization of distinct facets under different experimental conditions and computed their relative energies. Halide-deficient conditions favored the stabilization of facets associated with a polyhedral structure with 26 faces, while halide-rich conditions minimized the energy associated with the cubic facets. Subsequently, we explored the effects of Mn doping on these facets and observed that Mn doping in the cubic facets resulted in emissive behavior, whereas non-cubic facets remained non-emissive. Recent experimental investigations into Mn doping in $CsPbCl_3$ nanocrystals with shape variations have shown that doping was feasible in structures with arm-like extensions formed under halide-rich conditions, but not within the polyhedron formed under halide-poor conditions[53]. Although the initial assessment of dopant concentration relied on Mn emissivity, we present evidence that Mn doping can occur without resulting in emission. This discovery may account for the variations in emissivity observed in different shapes and underscores the potential of nanocrystal shape manipulation for tailoring materials with optimized optoelectronic properties. These findings hold promise for

fine-tuning the emissivity of perovskite nanocrystals in a variety of optoelectronic applications, offering a deeper understanding of the relationship between nanocrystal shape, doping, and light emission.

5 Unveiling the Unique facts of 2D Perovskites: Contrasting with their 3D Counterparts

The dimensionality of a material strongly affects its optical and electronic properties. As we transition from a three-dimensional (3D) to a two-dimensional (2D) perovskite, the compound's properties undergo significant alterations. While bulk 3D perovskites have garnered global attention for their notable enhancements in power conversion efficiency, their susceptibility to environmental factors such as moisture, temperature, and ion migration hinders their seamless commercialization[4, 26, 27, 30, 38]. In this compound space, 2D perovskite materials emerge as a transformative intermediary, bringing in structural-chemical stability. These organic–inorganic 2D perovskite materials exhibit a layered structure wherein a substantial organic cation layer serves as a spacer sandwiched between two inorganic metal halide octahedral layers[5]. The use of hydrophobic spacer cations serves the dual purpose of isolating the inorganic octahedral layers from water molecules and safeguarding the authentic structure from degradation. The layered structures manifest in two distinct phases—the Ruddlesden–Popper phase and Dion–Jacobson phase—depending on the types of spacer cations employed. The alternation of inorganic and organic layers naturally forms multiple quantum wells, coupled with spin–orbit-coupling leading to Rashba splitting[102]. This distinctive arrangement imparts intriguing chemical and physical properties to 2D perovskite materials, including exciton dynamics, charge carrier transport, and electron–phonon coupling, courtesy of the quantum confinement effect. Despite commendable stability, the limited charge transport and a relatively large bandgap pose challenges to the widespread application of 2D perovskite materials in solar cells. A promising solution lies in the concept of 2D/3D multidimensional hybrid perovskites, combining the

long-term stability of 2D perovskites with the high performance of 3D perovskites simultaneously. In this chapter, we provide a succinct overview of the structural versatility, synthesis techniques, unique photophysical properties, potential device fabrication, and recent advancements in 2D perovskite structures aimed at resisting degradation.

5.0.1 Crystal structure of 2D perovskite materials

A 2D perovskite can be envisioned as a thin layer exfoliated from the conventional 3D perovskite material along a specific crystallographic direction[32]. This 2D structure is formed through the corner-sharing of metal halide octahedral frameworks (BX_6). 2D perovskites are expressed by the general formula $A'_mA_{n-1}B_nX_{3n+1}$, where A', depending on its valency, functions as a monolayer or a bilayer connecting the inorganic 2D sheets ($A_{n-1}B_nX_{3n+1}$). The A'site typically incorporates long-chain organic cations, A site consists of regular monovalent cations, B site features divalent metal cations, and X site contains halide anions. The integer n signifies the total number of BX_6 octahedral layers trapped between two A' cation layers[79]. This arrangement leads to the formation of multiple quantum well structures, where the sandwiched octahedral layers act as the depth of the well, and the organic cation layers act as the barrier of the well.

By appropriately altering the value of n, the properties of 2D perovskite can be modified through both quantum and dielectric confinement effects. When $n = 1$, the structure represents purely 2D perovskites, while n values between 2 and 4 yield quasi-2D perovskites. Similarly, when $n = \infty$, the structure tends towards 3D perovskites. Depending on the crystallographic direction (e.g., (100), (110), and (111))[56] along which the bulk 3D perovskite is cut and considering aromatic or aliphatic alkylammonium cation L substitution. The (100) oriented 2D perovskites, characterized by the structural formula $(L)_2A_{n-1}B_nX_{3n+1}$, are referred to as (100)-2D perovskites and are categorized into three main groups based on the spacer cation L: Ruddlesden–Popper (RP) perovskites, Dion–Jacobson (DJ) perovskites, and alternating cations in the interlayer space (ACI) perovskites (see Figure 8). Among these, (100)-2D perovskites have been extensively explored and currently dominate

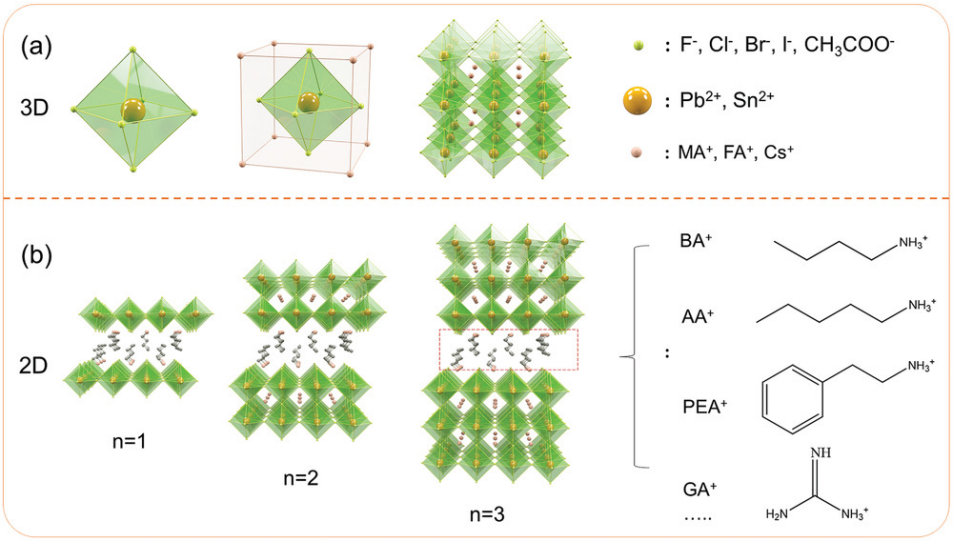

FIGURE 1.8: a) The schematic illustration of the crystal structures for 3D perovskite, in which A is the cation of methylammonium (MA^+), formamidinium (FA^+), or caesium (Cs^+); B is the cation of lead (Pb^{2+}) or tin (Sn^{2+}), and X is the anion of chlorine (Cl^-), bromine (Br^-), iodine (I^-), or acetate ($CH3COO^-$). b) The 2D hybrid perovskite with larger-size ammonium (butylamine: BA^+; phenylethylamine: PEA^+; amylamine: AA+; etc. as spacer cations.[114]

the perovskite domain[47, 71]. The RP phase of (100)-2D perovskites adopts a layered structure with the general formula $(L)_2A_{n-1}B_nX_{3n+1}$, where L represents a long-chained monoamine organic cation spacer layer. These atomic layers are typically stacked together by van der Waals forces, with the organic cation layers adhering to the inorganic octahedral cation layer. The incorporation of hydrophobic atoms in the organic spacer cation layer enhances stability by protecting the inorganic octahedral BX_6 layer from water and air contamination. An inorganic layer offset in the same plane with one octahedral unit displacement is a characteristic feature. Layered RP perovskite materials have demonstrated a noteworthy power conversion efficiency (PCE) of 12.52 in solar cell applications. DJ perovskite, on the other hand, is derived by replacing the monoammonium cation of RP perovskite with diammonium cations. DJ perovskites follow the general formula $(L)A_{n-1}B_nX_{3n+1}$, where L is the diammonium spacer cation with a valency of +2[49]. The presence of a diamino organic cation contributes to the relative stability of DJ perovskite compared to the RP perovskite structure. In DJ perovskites, the inorganic layers are stacked directly on top of each other without any dimensional offset, contrasting with

the RP perovskites. ACI-type perovskites share compositional equivalence with 3D perovskites, having the formula $R(MA)_nM_nX_{3n+1}$, where R represents a large cation. ACI phases exhibit higher symmetry than RP phases.

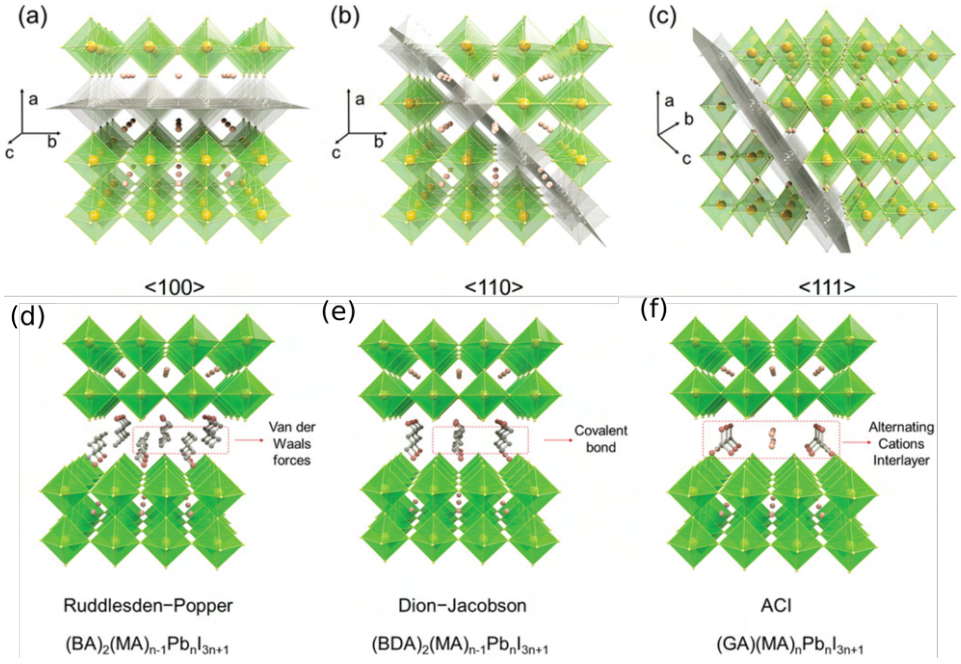

FIGURE 1.9: (a–c) The diagrammatic sketch for common three types of the derivation of 2D perovskite with inserting spacer cation along (100), (110), and (111) plane of 3D perovskite. The structure comparison of (d) Ruddlesden–Popper (RP) phase, (e) Dion–Jacobson (DJ) phase, and (f) alternating cations in the interlayer (ACI) phase 2D perovskites, which are derived from (100)-oriented[114]

5.0.2 Structural, electronic and optical properties of 2D perovskites

2D perovskites offer a diverse range of optoelectronic properties compared to conventional 3D perovskites. Noteworthy characteristics such as larger exciton binding energy and enhanced photoluminescence (PL) make them favorable for applications in light-emitting diodes (LEDs). Materials intended for use in the photovoltaic industry must exhibit excellent light-harvesting and emission qualities[32]. The structural layering of 2D perovskites provides the advantage of tailoring bandgaps, stability, and other electronic properties by manipulating the thickness and composition of the layers. As previously mentioned, the customized bandgap significantly influences the material's light absorption and emission quality, enhancing functionality and efficiency. The transition from 3D to 2D introduces

the quantum confinement effect, creating a wider bandgap by separating energy levels. This dimensional confinement not only influences the bandgap but also adds value to optoelectronic properties. Optical, electronic, and energetic properties will be discussed in this section. By reducing the dimension from 3D to 2D, energy levels become separated, resulting in a wider bandgap. The quantum confinement effect establishes different physical properties compared to the 3D counterpart[57]. The bandgap of a 2D perovskite material can be conveniently tuned by adjusting the thickness of the inorganic layer or changing the number of octahedral layers 'n'. The transition from semiconductor to metal occurs as the 'n' value changes from 1 to ∞, enhancing electronic properties. Examples such as $(BA)_2(MA)_{n-1}Pb_nI_{3n+1}$ and $(PEA))_2(MA)_{n-1}Pb_nI_{3n+1}$ demonstrate a decrease in bandgap from 2.24 eV to 1.52 eV and 2.41 eV to 1.68 eV, respectively, by increasing 'n' from 1 to ∞[99]. This trend indicates that the bandgap increases with decreasing dimensionality, and the decrease in bandgap is solely related to the dimension of the material. 2D perovskite materials act as natural quantum wells, with organic cation layers acting as raised 'barriers' and inorganic layers as deep 'wells'[40]. The excitons formed inside 2D perovskite materials become trapped within these natural quantum wells, making them suitable for light-emitting devices. The exciton confinement property of 2D perovskite materials ensures stability at room temperature. In addition to these properties, 2D perovskites exhibit a distinct dielectric constant offset compared to their 3D counterparts. This offset, with a high dielectric constant for inorganic layers and a low dielectric constant for organic layers in a 2D hybrid perovskite, is responsible for the dielectric confinement effect, beneficial for forming bound electrons. The dielectric constant decreases with a decrease in layer thickness[46]. This change in the dielectric constant affects the exciton binding energy. For example, the exciton binding energy of $(BA)_2(MA)_{n-1}Pb_nI_{3n+1}$ decreases from 380 meV to 270 meV to 220 meV by increasing the number of layers from $n = 1$ to $n = 2$ to $n > 2$.

In conclusion, 2D hybrid perovskites exhibit fascinating properties such as a low dielectric coefficient and a strong exciton binding energy, making them promising candidates for various optoelectronic applications.

5.1 Understanding Edge States in Two-Dimensional Ruddlesden-Popper Perovskites: Insights from Photophysics

The photophysics of 2D RP perovskites is influenced by low-energy edge states, enhancing the optoelectronic properties of these materials[2, 33, 37]. The photogenerated excitons dissociate into long-lived free carriers at the crystal edge when they diffuse from the bulk to the edge region (Blancon et al., 2017; Feng et al., 2018; Zhao et al., 2020). Further, with increasing the number of inorganic layers in each unit from n=1 to n=5, the exciton binding energies have been seen to vary from 450 meV to 100 meV[1, 8–10], indicating it's tunability. One viewpoint that exists is that the formation of edge states above a critical thickness has been associated with the strain relaxations of the surface with respect to the bulk. These structural relaxations lead to states which are located in the band gap, as has been seen in various semiconductors. However, some of the experimental results do not support this picture. There are instances of n = 1 perovskites showing anomalous conductivity at the edges, which is attributed to edge states[33]. In the case of perfect crystals, their crystal structures exhibit a continuous, uniform pattern with no discernible boundaries. In practice, though, the crystal structure typically includes inherent boundaries. These boundaries give rise to differences in the chemical compositions of the atoms located at the crystal's edges compared to those found in the interior. Consequently, the material's edge region displays distinct properties when contrasted with its bulk. For example, the different edge configurations have been confirmed to significantly impact the optoelectronic properties of the typical 2D material, graphene [25, 34]. As for 2D RP perovskites, their edge regions have been reported to exhibit many unique properties different from the bulk region. The most characteristic property of the edge states is the low energy PL emission. The edge state was first observed in $(BA)_2(MA)_{n-1}Pb_nI_{3n+1}$ with n > 2[2]. Through photoluminescence (PL) mapping using various spectral bands, the study exclusively detected lower energy emissions (at 1.68 eV) at the crystal's edge in an exfoliated crystal of $(BA)_2(MA)_{n-1}Pb_nI_{3n+1}$ (where n = 3). This was in addition to the conventional emission band at 2.01 eV, which emanated from all regions of the crystal[2, 37]. Zhao et al.[37] discovered that the emission from the edge states in $(BA)_2(MA)_{n-1}Pb_nI_{3n+1}$ can

be manipulated through a cation exchange process involving MA^+ and BA^+ ions. They observed that emission could be eliminated by rinsing the material with a BAI solution and generated by rinsing with an MAI solution. Importantly, this cation exchange process was found to be repeatable.

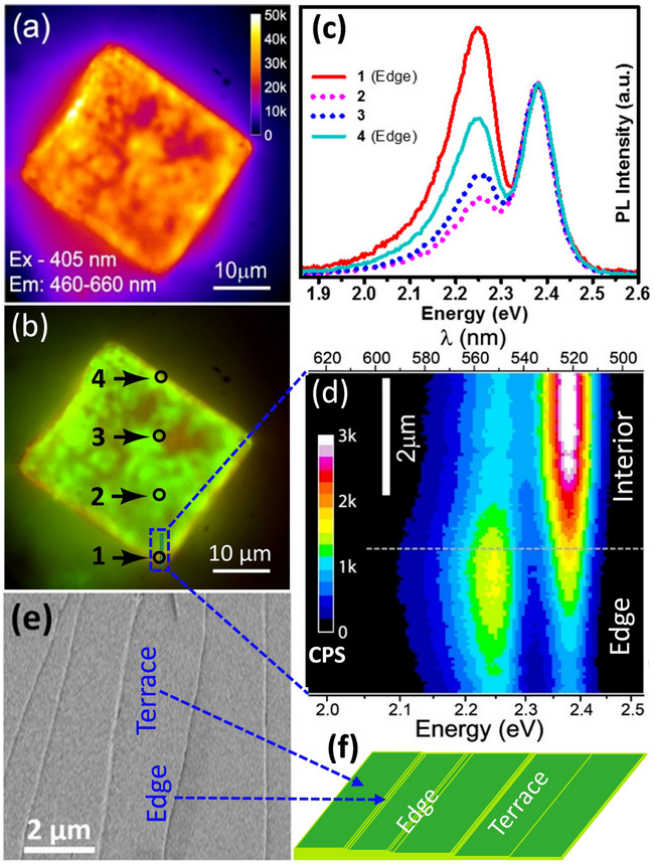

FIGURE 1.10: (a) Fluorescence intensity (false color) image of a $(BA)_2PbI)4$ single crystal, (b) pseudo-coloured PL intensity image generated by the superposition of PL images collected at two energies. The intensities are adjusted to reproduce nearly a true color of the crystal as visualized through the microscope. (c)Spatially resolved PL emission spectra from the edges (1,4) and the interior regions (2,3), locations marked in(b)). (d)Spectrally resolved PL image of a rectangular strip at the bottom of the crystal (marked with a dotted rectangular in(b)). Intensity calibration is in counts per seconds (cps). (e)A representative SEM image of the top surface of $(BA)_2PbI)4$ single crystal. (f) Schematic representation showing the edges present on the surface of a layered crystal.[93]

Shortly thereafter, Zhang et al.[39] conducted a theoretical exploration into the origin of edge states and proposed that these states arose due to distinct chemical properties exhibited by iodine (I) and lead (Pb) atoms. The principal factor driving charge separation in the edge states was identified as the presence of unsaturated iodine bonds at the

periphery. In two-dimensional perovskites, the valence band maxima (VBM) were predominantly constituted by I atomic orbitals, while the conduction band minima (CBM) were formed by Pb atom orbitals. Although the unsaturated iodine and lead bonds at the edge region didn't introduce trap states within the original bandgap, they did influence orbital localization. Metallic Pb atoms were capable of rectifying unsaturated chemical bonds and repairing defects through changes in their oxidation states, thereby promoting electron delocalization. On the other hand, the unsaturated covalent bonds of iodide exerted a strong force that localized holes. This disparity in confinement between electrons and holes resulted in charge separation, giving rise to the edge states. Furthermore, the prolonged existence of carriers in these edge states could be explained by the limited overlap of wave functions between electrons and holes and the brief quantum coherence between excited and ground electronic states.

In this thesis through Density Functional Theory (DFT) simulations, we intend to elucidate the roles of organic-inorganic interactions, lattice distortions, and quantum confinement effects in shaping the electronic band structure of these materials. We hypothesize that the interplay between organic cations and inorganic frameworks plays a pivotal role in generating the edge state as well as the dual-band gap phenomenon. The interaction is found to be weaker at the surface, compared to what is found in the bulk. This allows for the easy removal of the molecular units from the surface and the edges compared to the bulk. The consequent reconstructions that take place to accommodate the removal of a molecular unit lead to the modified electronic structure of regions of the surface/edges compared to the bulk. This leads to the dual emission and also provides us with a route to quench it. The primary defect being formed is neutral, involving a molecule in addition to an apical anion. It is therefore surprising to see that the energy to form the second similar defect, especially at the edges is lower than what is required for the first. This suggests that depending on the synthesis conditions, one can have large regions with these defects forming. We have also found that the formation energy of some defects is negative and can be changed to become positive so that the defects don't form under certain experimental conditions. Zhao et al[37]. also found by their TEM-SAED experiments that the edge

state dual emission of 2D RP perovskites can be generated or eliminated by MA+ or BA+ solution treatment, respectively.

6 Beyond Perovskites: Unraveling Molecular Mysteries in Single Molecular Junctions

While earlier studies concentrated on the influence of molecules within inorganic networks on electronic and structural properties indirectly, we went on to examine individual molecules directly integrated into electronic circuits. One fundamental question that has captivated researchers is the modulation of resistance in a molecule covalently attached to two electrodes. In the realm of perovskites, the influence of molecules within the inorganic network has provided valuable insights into modifying system properties. However, the exploration of single molecular junctions opens up a new avenue, allowing us to probe the intricate electronic behavior of individual molecules within an electronic circuit. As we delve into this, our research aims to uncover the underlying mechanisms that govern the resistance tuning of covalently attached molecules. By placing different molecules within these circuits, We start putting together the crucial components of molecular electronics. This shift in focus holds promise for not only advancing our fundamental understanding of molecular electronics but also for paving the way towards innovative applications in the field of nanotechnology.

6.1 Exploring Single Molecules for Better Electronics

In the world of nanotechnology, scientists have achieved a groundbreaking feat: the ability to connect organic molecules, as minuscule as 1 nm, between two metallic leads and delve into their electronic transport characteristics. This burgeoning field of study, known as single molecular junctions[4], has witnessed remarkable progress despite facing formidable experimental challenges.

Recent advancements in experimental techniques have allowed researchers to wire organic molecules within the nanometer range, providing a unique window into the behavior of individual molecules in electronic circuits. What's even more fascinating is the introduction of a third metal lead, positioned in proximity to act as a gate electrode. This innovation enables scientists to dynamically adjust the conductance of the molecule electrostatically, ushering in a new era of precision and control[10, 12, 20, 45].

The ability to control basic properties of molecular junctions prompts a critical evaluation of our understanding of electron transport at the nanoscale. Faithful modeling demands a meticulous consideration of the atomic and molecular arrangements constituting the junction. However, the lack of atomistic information from experiments poses a significant challenge, as these junctions form spontaneously under the influence of atomic and molecular interactions—a form of self-assembly that eludes direct imaging.

Theoretical approaches, including tight-binding methods, density functional theory (DFT), and the nonequilibrium Green's function (NEGF) method, have been indispensable in unraveling the complexities of single molecular junctions. DFT, a widely used guide for interpreting experiments, faces scrutiny regarding its reliability and sensitivity to methodological choices and assumptions. The NEGF method, particularly effective in the far-from-equilibrium regime at high voltage bias, contributes valuable insights.

Despite the myriad challenges, the agreement between experimental results and computational models is surprisingly robust, prompting intriguing questions about the completeness of our current understanding. The uncertainties arise not only from computational methods but also from assumptions about experimental conditions that are challenging to validate directly.

Several factors add complexity to the evaluation of specific molecular junctions, including the variability in binding sites, fluctuating geometries of longer molecules, uncertainties in surface chemistry and level alignments, and the nanoscale details of electrode size and shape. Yet, the field persists in its quest to comprehend the physics of these systems fully.

As researchers continue to unlock the mysteries of single molecular junctions, the journey into the nanoscale promises not only a deeper understanding of electron transport but also the potential discovery of novel physics. The review of experimental and theoretical results serves as a guide, navigating the complexities of this intricate realm and shedding light on the exciting possibilities that lie ahead in the exploration of single molecular transport.

6.1.1 Mechanically Controllable Break Junctions

Due to the typical size of molecules being around 1 nm, conventional top-down microfabrication methods lack the precision needed for the controlled arrangement of molecules. As a result, the approaches utilized depend on a combination of finely adjusting the nanometer-scale gap between contact electrodes through electromechanical means and allowing molecules to self-assemble within this gap. The three commonly utilized techniques include the mechanically controlled break-junction (MCBJ) method[28], the electromigration break junction technique, and methodologies employing scanning tunneling microscopy (STMs)[5, 19, 53, 57].

Among the three most prevalent techniques employed, the mechanically controlled break-junction (MCBJ) method stands out as a powerful tool for studying atomic and molecular junctions. There are two main fabrication methods within the MCBJ technique: the notched-wire MCBJ and the lithographically fabricated MCBJ.

The notched-wire MCBJ is a simpler approach, adaptable to various metal electrodes. It involves creating a weak spot in a macroscopic metal wire by cutting a notch. The wire is mounted on a flexible substrate, and by bending the substrate, strain is concentrated at the notch, ultimately breaking the wire. Fine control of the gap is achieved by a piezoelectric actuator, allowing the formation and breaking of atomic-size contacts[1].

The lithographically fabricated MCBJ, while sharing the same principles, replaces the prenotched metal wire with a suspended bridge in a thin metal film produced by electron-beam lithography. This modification reduces the mechanical displacement ratio, making

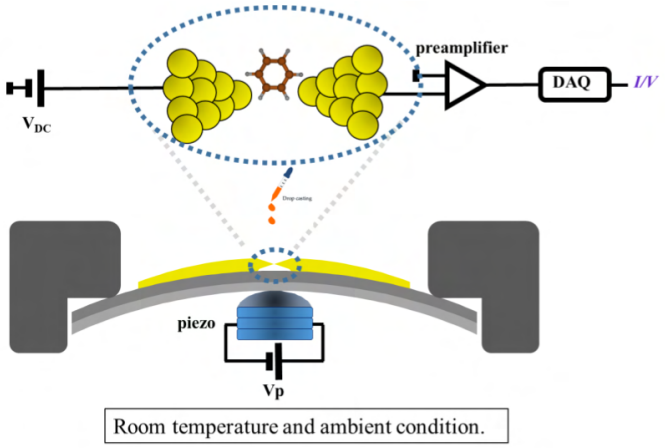

FIGURE 1.11: Schematic of a mechanically controllable break junction (MCBJ) set up,

the junctions less sensitive to external perturbations. Although it introduces clean-room preparation complexities, this method allows the production of multiple MCBJ samples on a single wafer. Both MCBJ methods, particularly effective when performed at cryogenic temperatures or under ultrahigh vacuum (UHV)[50], offer intrinsic cleanliness of the broken metal surfaces. Gold (Au) emerges as the preferred electrode material, preserving intrinsic quantum conductance properties even under ambient conditions due to its low reactivity. The choice of suitable anchor groups allows specific binding to target molecules, making Au a standout material for single-molecule transport experiments[97].

Intriguingly, working under UHV or cryogenic conditions opens avenues for exploring various metal electrodes and different forms of metal-molecule bonding. Hydrogen, for instance, binds to clean platinum electrodes without the need for anchor groups, demonstrating the versatility and potential of MCBJ in uncovering the intricacies of molecular interactions at the nanoscale.

6.1.2 Decoding the Impact of Structural Geometry in Single Molecular Junctions

In this thesis, we delve into the phenomenon known as the "jump to molecular contact" in the context of single molecular junctions, focusing on the charge transport through 4,4'-bipyridine (4,4'-BPY) and 2,2'-bipyridine (2,2'-BPY) molecules attached to gold electrodes[40].

The "jump in contact" phenomenon is an abrupt change in electrical conductivity or contact resistance at a microscopic level[15, 61]. This behavior, observed in both metallic and molecular systems, adds a layer of complexity to our understanding of electrical conductance at the nanoscale. The jump in conductivity is believed to be driven by changes in the atomic and electronic structure of the materials. Possible mechanisms include phase transitions, surface contamination, and alterations in the crystal lattice. Further analysis through microscopy and spectroscopy techniques is necessary to gain a more detailed understanding of these mechanisms as the occurrence of jump-in contact poses challenges for the reliability and performance of electronic devices. Sudden changes in resistance can lead to malfunctions, reduced efficiency, and potential long-term damage. This "jump to contact" phenomenon has been revealed in previous research on metallic contacts like Gold (Au), Platinum (Pt), Copper (Cu), and Silver (Ag), and our study captured these phenomena theoretically by an abrupt inflection in the energy with applied strain for these metals, suggesting a change in the local structure/charge density. This jump in energy correlates with a distinctive increase in conductance, providing a microscopic understanding of the "jump to contact" phenomenon. While Gold and Silver electrodes exhibited the "jump to contact", simulations for Tungsten showed no discernible signature, and Iridium displayed a small inflection, consistent with experimental reports[62]. In this thesis, our investigation focuses on single molecular junctions using 4,4'-BPY and 2,2'-BPY molecules attached to gold electrodes. Surprisingly, both molecules form molecular junctions during the breaking traces. However, 4,4'-BPY exhibits isotropic behavior, displaying conductance jumps in both breaking and making traces, a characteristic absent in 2,2'-BPY. Utilizing density functional theory (DFT) and molecular dynamics (MD) simulations, we uncover two pivotal mechanisms contributing to the "jump to molecular contact" phenomenon. Firstly, the unique behavior of 4,4'-BPY, with stable minima in both flat and vertical positions, is attributed to the remarkably stronger bond formed by nitrogen in this molecule compared to 2,2'-BPY. Secondly, an alternative mechanism suggests that the robust Au-N bond in 4,4'-BPY allows the molecule to break by pulling along a few gold atoms, contributing to the observed phenomenon. The findings contribute to the ongoing efforts to establish

a unified conceptual framework for understanding metal-molecule interactions in bond formation, advancing our knowledge in the dynamic field of molecular electronics.

6.1.3 Temperature's Influence: Exploring the temperature-dependent Conformational Changes in Single Molecular Junctions with Ferrocene

In the dynamic realm of molecular electronics, recent years have witnessed a heightened focus on understanding the electronic structure and transport properties of metal/molecule/metal junctions. These microscopic circuits respond intricately to external stimuli, including light, temperature, mechanical force, electric fields, and environmental conditions[4, 9, 37, 46, 59, 60]. Among the critical parameters shaping the behavior of these junctions, the conformation or geometry of the molecule within the junction stands out, exerting a profound influence on charge transfer and the evolution of the junction itself. Our investigation hones in on the conductance measurements of ferrocene, distinguished by its barrel-shaped structure comprising an iron atom sandwiched between two cyclopentadienyl (Cp) rings. Notably, ferrocene exhibits temperature-dependent rotational dynamics, particularly in the motion of the Cp rings[17, 31]. As the temperature decreases, the rotational motion slows down due to a finite activation energy barrier[3, 8, 16, 39, 56]. A recent experiment involving a single-molecule junction with an organometallic molecule, ferrocene, has unveiled intriguing temperature-dependent conductance changes. At low temperature (77K), two distinct conductance traces are observed, one at $10^{-1}G_0$ (high) and another at $10^{-2}G_0$ (low). Remarkably, at room temperature (300K), the low conductance trace is absent. Earlier studies have associated low conductance with the parallel configuration and high conductance with the perpendicular configuration. This thesis provides a theoretical understanding of the observed temperature-dependent conductance changes in ferrocene within the molecular junction. This behavior arises from temperature-induced alterations in the rotational dynamics of the Cp rings, disrupting the coupling between the metal and the molecule. Importantly, this effect is most pronounced when the Cp rings are in direct contact with the metallic electrodes, rendering the presence of a specific configuration exquisitely sensitive to temperature variations.

References

[1] Nicolás Agraıt, Alfredo Levy Yeyati, and Jan M Van Ruitenbeek. Quantum properties of atomic-sized conductors. *Physics Reports*, 377(2-3):81–279, 2003.

[2] Quinten A Akkerman, Valerio D'Innocenzo, Sara Accornero, Alice Scarpellini, Annamaria Petrozza, Mirko Prato, and Liberato Manna. Tuning the optical properties of cesium lead halide perovskite nanocrystals by anion exchange reactions. *Journal of the American Chemical Society*, 137(32):10276–10281, 2015.

[3] Quinten A Akkerman, Gabriele Rainò, Maksym V Kovalenko, and Liberato Manna. Genesis, challenges and opportunities for colloidal lead halide perovskite nanocrystals. *Nature materials*, 17(5):394–405, 2018.

[4] Markus Appel, Bernhard Frick, Tinka Luise Spehr, and Bernd Stühn. Molecular ring rotation in solid ferrocene revisited. *The Journal of Chemical Physics*, 142(11), 2015.

[5] Sriharsha V Aradhya and Latha Venkataraman. Single-molecule junctions beyond electronic transport. *Nature nanotechnology*, 8(6):399–410, 2013.

[6] Arieh Aviram and Mark A Ratner. Molecular rectifiers. *Chemical physics letters*, 29(2):277–283, 1974.

[7] Alexei Bagrets, Stefan Schmaus, Ali Jaafar, Detlef Kramczynski, Toyo Kazu Yamada, Mébarek Alouani, Wulf Wulfhekel, and Ferdinand Evers. Single molecule magnetoresistance with combined antiferromagnetic and ferromagnetic electrodes. *Nano Letters*, 12(10):5131–5136, 2012.

[8] J-C Blancon, Andreas V Stier, Hsinhan Tsai, Wanyi Nie, Costas C Stoumpos, Boubacar Traore, L Pedesseau, Mikael Kepenekian, Fumiya Katsutani, GT Noe,

et al. Scaling law for excitons in 2d perovskite quantum wells. *Nature communications*, 9(1):2254, 2018.

[9] J-C Blancon, Hsinhan Tsai, Wanyi Nie, Costas C Stoumpos, Laurent Pedesseau, Claudine Katan, Mikaël Kepenekian, Chan Myae Myae Soe, Kannatassen Appavoo, Matthew Y Sfeir, et al. Extremely efficient internal exciton dissociation through edge states in layered 2d perovskites. *Science*, 355(6331):1288–1292, 2017.

[10] Thomas M Brenner, David A Egger, Leeor Kronik, Gary Hodes, and David Cahen. Hybrid organic—inorganic perovskites: low-cost semiconductors with intriguing charge-transport properties. *Nature Reviews Materials*, 1(1):1–16, 2016.

[11] Michael Bühl and Sonja Grigoleit. Molecular dynamics of neutral and protonated ferrocene. *Organometallics*, 24(7):1516–1527, 2005.

[12] J Calabrese, NL Jones, RL Harlow, N Herron, DL Thorn, and Y Wang. Preparation and characterization of layered lead halide compounds. *Journal of the American Chemical Society*, 113(6):2328–2330, 1991.

[13] Brian Capozzi, Jianlong Xia, Olgun Adak, Emma J Dell, Zhen-Fei Liu, Jeffrey C Taylor, Jeffrey B Neaton, Luis M Campos, and Latha Venkataraman. Single-molecule diodes with high rectification ratios through environmental control. *Nature nanotechnology*, 10(6):522–527, 2015.

[14] Yunhua Chen, Sara R Smock, Anne H Flintgruber, Frédéric A Perras, Richard L Brutchey, and Aaron J Rossini. Surface termination of cspbbr3 perovskite quantum dots determined by solid-state nmr spectroscopy. *Journal of the American Chemical Society*, 142(13):6117–6127, 2020.

[15] Longji Cui, Sunghoon Hur, Zico Alaia Akbar, Jan C Klöckner, Wonho Jeong, Fabian Pauly, Sung-Yeon Jang, Pramod Reddy, and Edgar Meyhofer. Thermal conductance of single-molecule junctions. *Nature*, 572(7771):628–633, 2019.

[16] Nadim Darwish, Albert C Aragones, Tamim Darwish, Simone Ciampi, and Ismael Diez-Perez. Multi-responsive photo-and chemo-electrical single-molecule switches. *Nano letters*, 14(12):7064–7070, 2014.

[17] Stefaan De Wolf, Jakub Holovsky, Soo-Jin Moon, Philipp Loper, Bjoern Niesen, Martin Ledinsky, Franz-Josef Haug, Jun-Ho Yum, and Christophe Ballif. Organometallic halide perovskites: sharp optical absorption edge and its relation to photovoltaic performance. *The journal of physical chemistry letters*, 5(6):1035–1039, 2014.

[18] Yitong Dong, Tian Qiao, Doyun Kim, David Parobek, Daniel Rossi, and Dong Hee Son. Precise control of quantum confinement in cesium lead halide perovskite quantum dots via thermodynamic equilibrium. *Nano letters*, 18(6):3716–3722, 2018.

[19] Letian Dou, Yang Yang, Jingbi You, Ziruo Hong, Wei-Hsuan Chang, Gang Li, and Yang Yang. Solution-processed hybrid perovskite photodetectors with high detectivity. *Nature communications*, 5(1):5404, 2014.

[20] Anirban Dutta, Rakesh Kumar Behera, Sumit Kumar Dutta, Samrat Das Adhikari, and Narayan Pradhan. Annealing cspbx3 (x= cl and br) perovskite nanocrystals at high reaction temperatures: phase change and its prevention. *The journal of physical chemistry letters*, 9(22):6599–6604, 2018.

[21] Anirban Dutta, Sumit Kumar Dutta, Samrat Das Adhikari, and Narayan Pradhan. Tuning the size of cspbbr3 nanocrystals: all at one constant temperature. *ACS Energy Letters*, 3(2):329–334, 2018.

[22] Mateusz Dyksik, Herman Duim, Duncan K Maude, Michal Baranowski, Maria Antonietta Loi, and Paulina Plochocka. Brightening of dark excitons in 2d perovskites. *Science advances*, 7(46):eabk0904, 2021.

[23] Mateusz Dyksik, Shuli Wang, Watcharaphol Paritmongkol, Duncan K Maude, William A Tisdale, Michal Baranowski, and Paulina Plochocka. Tuning the excitonic properties of the 2d (pea) 2 (ma) n- 1pb n i3 n+ 1 perovskite family via

quantum confinement. *The Journal of Physical Chemistry Letters*, 12(6):1638–1643, 2021.

[24] María C Gélvez-Rueda, Eline M Hutter, Duyen H Cao, Nicolas Renaud, Constantinos C Stoumpos, Joseph T Hupp, Tom J Savenije, Mercouri G Kanatzidis, and Ferdinand C Grozema. Interconversion between free charges and bound excitons in 2d hybrid lead halide perovskites. *The Journal of Physical Chemistry C*, 121(47):26566–26574, 2017.

[25] Lukas Gerhard and Wulf Wulfhekel. Conductance and adhesion in an atomically precise au-au point contact. *Physical Review B*, 101(3):035429, 2020.

[26] A. M. Glazer. The classification of tilted octahedra in perovskites. *Acta Crystallographica Section B*, 28(11):3384–3392, Nov 1972.

[27] V M Goldschmidt. Die Gesetze der Krystallochemie. *Naturwissenschaften*, 14(21):477–485, 1926.

[28] Martin A. Green and Anita Ho-Baillie. Perovskite solar cells: The birth of a new era in photovoltaics. *ACS Energy Letters*, 2(4):822–830, 2017.

[29] Wolfgang Haiss, Changsheng Wang, Iain Grace, Andrei S Batsanov, David J Schiffrin, Simon J Higgins, Martin R Bryce, Colin J Lambert, and Richard J Nichols. Precision control of single-molecule electrical junctions. *Nature materials*, 5(12):995–1002, 2006.

[30] Ryoma Hayakawa, Mohammad Amin Karimi, Jannic Wolf, Thomas Huhn, Martin Sebastian zoellner, Carmen Herrmann, and Elke Scheer. Large magnetoresistance in single-radical molecular junctions. *Nano letters*, 16(8):4960–4967, 2016.

[31] Michael H Huang and Po-Heng Lin. Shape-controlled synthesis of polyhedral nanocrystals and their facet-dependent properties. *Advanced Functional Materials*, 22(1):14–24, 2012.

[32] Yuan Huang, Yu-Hao Pan, Rong Yang, Li-Hong Bao, Lei Meng, Hai-Lan Luo, Yong-Qing Cai, Guo-Dong Liu, Wen-Juan Zhao, Zhang Zhou, et al. Universal mechanical exfoliation of large-area 2d crystals. *Nature communications*, 11(1):2453, 2020.

[33] Muhammad Imran, Vincenzo Caligiuri, Mengjiao Wang, Luca Goldoni, Mirko Prato, Roman Krahne, Luca De Trizio, and Liberato Manna. Benzoyl halides as alternative precursors for the colloidal synthesis of lead-based halide perovskite nanocrystals. *Journal of the American Chemical Society*, 140(7):2656–2664, 2018.

[34] Masahiko Inouye, Yutaka Hyodo, and Hiroyuki Nakazumi. Nucleobase recognition by artificial receptors possessing a ferrocene skeleton as a novel modular unit for hydrogen bonding and stacking interactions. *The Journal of Organic Chemistry*, 64(8):2704–2710, 1999.

[35] T J KEALY and P L PAUSON. A New Type of Organo-Iron Compound. *Nature*, 168(4285):1039–1040, 1951.

[36] Gregor Kieslich, Shijing Sun, and Anthony K. Cheetham. Solid-state principles applied to organic–inorganic perovskites: new tricks for an old dog. *Chem. Sci.*, 5:4712–4715, 2014.

[37] J. M. Krans, C. J. Muller, I. K. Yanson, Th. C. M. Govaert, R. Hesper, and J. M. van Ruitenbeek. One-atom point contacts. *Phys. Rev. B*, 48:14721–14724, Nov 1993.

[38] Chun-Hong Kuo, Yi-Ting Chu, Yen-Fang Song, and Michael H Huang. Cu_2o nanocrystal-templated growth of cu_2s nanocages with encapsulated au nanoparticles and in-situ transmission x-ray microscopy study. *Advanced Functional Materials*, 21(4):792–797, 2011.

[39] Jung-Hoon Lee, Nicholas C. Bristowe, June Ho Lee, Sung-Hoon Lee, Paul D. Bristowe, Anthony K. Cheetham, and Hyun Myung Jang. Resolving the physical origin of octahedral tilting in halide perovskites. *Chemistry of Materials*, 28(12):4259–4266, 2016.

[40] Kai Leng, Lin Wang, Yan Shao, Ibrahim Abdelwahab, Gustavo Grinblat, Ivan Verzhbitskiy, Runlai Li, Yongqing Cai, Xiao Chi, Wei Fu, et al. Electron tunneling at the molecularly thin 2d perovskite and graphene van der waals interface. *Nature Communications*, 11(1):5483, 2020.

[41] Wei Li, Zheming Wang, Felix Deschler, Song Gao, Richard H Friend, and Anthony K Cheetham. Chemically diverse and multifunctional hybrid organic–inorganic perovskites. *Nature Reviews Materials*, 2(3):16099, 2017.

[42] Dong Liang, Yuelin Peng, Yongping Fu, Melinda J Shearer, Jingjing Zhang, Jianyuan Zhai, Yi Zhang, Robert J Hamers, Trisha L Andrew, and Song Jin. Color-pure violet-light-emitting diodes based on layered lead halide perovskite nanoplates. *ACS nano*, 10(7):6897–6904, 2016.

[43] Kebin Lin, Jun Xing, Li Na Quan, F Pelayo García de Arquer, Xiwen Gong, Jianxun Lu, Liqiang Xie, Weijie Zhao, Di Zhang, Chuanzhong Yan, et al. Perovskite light-emitting diodes with external quantum efficiency exceeding 20 per cent. *Nature*, 562(7726):245–248, 2018.

[44] Jiakai Liu, Kepeng Song, Yongwoo Shin, Xin Liu, Jie Chen, Ke Xin Yao, Jun Pan, Chen Yang, Jun Yin, Liang-Jin Xu, et al. Light-induced self-assembly of cubic cspbbr3 perovskite nanocrystals into nanowires. *Chemistry of Materials*, 31(17):6642–6649, 2019.

[45] Mingzhen Liu, Michael B Johnston, and Henry J Snaith. Efficient planar heterojunction perovskite solar cells by vapour deposition. *Nature*, 501(7467):395–398, 2013.

[46] Dewei Ma, Yongping Fu, Lianna Dang, Jianyuan Zhai, Ilia A Guzei, and Song Jin. Single-crystal microplates of two-dimensional organic–inorganic lead halide layered perovskites for optoelectronics. *Nano Research*, 10:2117–2129, 2017.

[47] Shuang Ma, Molang Cai, Tai Cheng, Xihong Ding, Xiaoqiang Shi, Ahmed Alsaedi, Tasawar Hayat, Yong Ding, Zhan'ao Tan, and Songyuan Dai. Two-dimensional

organic-inorganic hybrid perovskite: from material properties to device applications. *Sci China Mater*, 61(10):1257, 2018.

[48] Joseph S Manser, Makhsud I Saidaminov, Jeffrey A Christians, Osman M Bakr, and Prashant V Kamat. Making and breaking of lead halide perovskites. *Accounts of chemical research*, 49(2):330–338, 2016.

[49] Lingling Mao, Weijun Ke, Laurent Pedesseau, Yilei Wu, Claudine Katan, Jacky Even, Michael R Wasielewski, Constantinos C Stoumpos, and Mercouri G Kanatzidis. Hybrid dion–jacobson 2d lead iodide perovskites. *Journal of the American Chemical Society*, 140(10):3775–3783, 2018.

[50] Christian A Martin, Dapeng Ding, Herre SJ Van Der Zant, and Jan M Van Ruitenbeek. Lithographic mechanical break junctions for single-molecule measurements in vacuum: possibilities and limitations. *New Journal of Physics*, 10(6):065008, 2008.

[51] Anyi Mei, Xiong Li, Linfeng Liu, Zhiliang Ku, Tongfa Liu, Yaoguang Rong, Mi Xu, Min Hu, Jiangzhao Chen, Ying Yang, et al. A hole-conductor–free, fully printable mesoscopic perovskite solar cell with high stability. *science*, 345(6194):295–298, 2014.

[52] Samuel A Miller, John A Tebboth, and John F Tremaine. 114. di cyclo pentadienyliron. *Journal of the Chemical Society (Resumed)*, pages 632–635, 1952.

[53] Debayan Mondal and Priya Mahadevan. Shape control of emissive properties of mn-doped cspbbr3 nanocrystals. *The Journal of Physical Chemistry C*, 125(21):11462–11467, 2021.

[54] Edoardo Mosconi, Anna Amat, Md. K. Nazeeruddin, Michael Grätzel, and Filippo De Angelis. First-principles modeling of mixed halide organometal perovskites for photovoltaic applications. *The Journal of Physical Chemistry C*, 117(27):13902–13913, 2013.

[55] Shigeto Nakashima, Yuuta Takahashi, and Manabu Kiguchi. Effect of the environment on the electrical conductance of the single benzene-1, 4-diamine molecule junction. *Beilstein journal of nanotechnology*, 2(1):755–759, 2011.

[56] Olga Nazarenko, Martin R Kotyrba, Sergii Yakunin, Marcel Aebli, Gabriele Rainò, Bogdan M Benin, Michael W:orle, and Maksym V Kovalenko. Guanidinium-formamidinium lead iodide: a layered perovskite-related compound with red luminescence at room temperature. *Journal of the American Chemical Society*, 140(11):3850–3853, 2018.

[57] Lin Niu, Qingsheng Zeng, Jia Shi, Chunxiao Cong, Chunyang Wu, Fucai Liu, Jiadong Zhou, Wei Fu, Qundong Fu, Chuanhong Jin, et al. Controlled growth and reliable thickness-dependent properties of organic–inorganic perovskite platelet crystal. *Advanced Functional Materials*, 26(29):5263–5270, 2016.

[58] Kouji Ogasahara, Michio Sorai, and Hiroshi Suga. Thermodynamic properties of ferrocene crystal. *Molecular Crystals and Liquid Crystals*, 71(3-4):189–211, 1981.

[59] Biswajit Pabi, Debayan Mondal, Priya Mahadevan, and Atindra Nath Pal. Probing metal-molecule contact at the atomic scale via conductance jumps. *Physical Review B*, 104(12):L121407, 2021.

[60] Biswajit Pabi, Jakub Sebesta, Richard Korytár, Oren Tal, and Atindra Nath Pal. Structural regulation of mechanical gating in molecular junctions. *Nano Letters*, 23(9):3775–3780, 2023.

[61] Atindra Nath Pal, Dongzhe Li, Soumyajit Sarkar, Sudipto Chakrabarti, Ayelet Vilan, Leeor Kronik, Alexander Smogunov, and Oren Tal. Nonmagnetic single-molecule spin-filter based on quantum interference. *Nature communications*, 10(1):5565, 2019.

[62] Atindra Nath Pal, Dongzhe Li, Soumyajit Sarkar, Sudipto Chakrabarti, Ayelet Vilan, Leeor Kronik, Alexander Smogunov, and Oren Tal. Nonmagnetic single-molecule spin-filter based on quantum interference. *Nature communications*, 10(1):1–8, 2019.

[63] Jun Pan, Yuequn Shang, Jun Yin, Michele De Bastiani, Wei Peng, Ibrahim Dursun, Lutfan Sinatra, Ahmed M El-Zohry, Mohamed N Hedhili, Abdul-Hamid Emwas,

et al. Bidentate ligand-passivated cspbi3 perovskite nanocrystals for stable near-unity photoluminescence quantum yield and efficient red light-emitting diodes. *Journal of the American Chemical Society*, 140(2):562–565, 2017.

[64] Lucheng Peng, Sumit Kumar Dutta, Debayan Mondal, Biswajit Hudait, Sanjib Shyamal, Renguo Xie, Priya Mahadevan, and Narayan Pradhan. Arm growth and facet modulation in perovskite nanocrystals. *Journal of the American Chemical Society*, 141(40):16160–16168, 2019. PMID: 31510737.

[65] Xiaogang Peng, Liberato Manna, Weidong Yang, Juanita Wickham, Erik Scher, Andreas Kadavanich, and A Paul Alivisatos. Shape control of cdse nanocrystals. *Nature*, 404(6773):59–61, 2000.

[66] Yonatan Plotnik, Mikael C Rechtsman, Daohong Song, Matthias Heinrich, Julia M Zeuner, Stefan Nolte, Yaakov Lumer, Natalia Malkova, Jingjun Xu, Alexander Szameit, et al. Observation of unconventional edge states in 'photonic graphene'. *Nature materials*, 13(1):57–62, 2014.

[67] Loredana Protesescu, Sergii Yakunin, Maryna I Bodnarchuk, Franziska Krieg, Riccarda Caputo, Christopher H Hendon, Ruo Xi Yang, Aron Walsh, and Maksym V Kovalenko. Nanocrystals of cesium lead halide perovskites (cspbx3, x= cl, br, and i): novel optoelectronic materials showing bright emission with wide color gamut. *Nano letters*, 15(6):3692–3696, 2015.

[68] Xiang Qi, Yupeng Zhang, Qingdong Ou, Son Tung Ha, Cheng-Wei Qiu, Han Zhang, Yi-Bing Cheng, Qihua Xiong, and Qiaoliang Bao. Photonics and optoelectronics of 2d metal-halide perovskites. *Small*, 14(31):1800682, 2018.

[69] Vikash Kumar Ravi, Pralay K Santra, Niharika Joshi, Jeetender Chugh, Sachin Kumar Singh, Håkan Rensmo, Prasenjit Ghosh, and Angshuman Nag. Origin of the substitution mechanism for the binding of organic ligands on the surface of cspbbr3 perovskite nanocubes. *The Journal of Physical Chemistry Letters*, 8(20):4988–4994, 2017.

[70] Harsha Reddy, Kun Wang, Zhaxylyk Kudyshev, Linxiao Zhu, Shen Yan, Andrea Vezzoli, Simon J Higgins, Vikram Gavini, Alexandra Boltasseva, Pramod Reddy, et al. Determining plasmonic hot-carrier energy distributions via single-molecule transport measurements. *Science*, 369(6502):423–426, 2020.

[71] Antonio Gaetano Ricciardulli, Sheng Yang, Jurgen H Smet, and Michael Saliba. Emerging perovskite monolayers. *Nature Materials*, 20(10):1325–1336, 2021.

[72] Gustav Rose. Beschreibung einiger neuen mineralien des urals. *Annalen der Physik*, 124(12):551–573, 1839.

[73] Carlos Sabater, María José Caturla, Juan José Palacios, and Carlos Untiedt. Understanding the structure of the first atomic contact in gold. *Nanoscale research letters*, 8(1):257, 2013.

[74] Michael Saliba, Juan-Pablo Correa-Baena, Michael Grätzel, Anders Hagfeldt, and Antonio Abate. Perovskite solar cells: from the atomic level to film quality and device performance. *Angewandte Chemie International Edition*, 57(10):2554–2569, 2018.

[75] Sagar Sarkar and Priya Mahadevan. Role of the a-site cation in determining the properties of the hybrid perovskite $CH_3NH_3PbBr_3$. *Phys. Rev. B*, 95:214118, Jun 2017.

[76] Stefan Schmaus, Alexei Bagrets, Yasmine Nahas, Toyo K Yamada, Annika Bork, Martin Bowen, Eric Beaurepaire, Ferdinand Evers, and Wulf Wulfhekel. Giant magnetoresistance through a single molecule. *Nature nanotechnology*, 6(3):185–189, 2011.

[77] Javad Shamsi, Alexander S Urban, Muhammad Imran, Luca De Trizio, and Liberato Manna. Metal halide perovskite nanocrystals: synthesis, post-synthesis modifications, and their optical properties. *Chemical reviews*, 119(5):3296–3348, 2019.

[78] Robert D Shannon. Revised effective ionic radii and systematic studies of interatomic distances in halides and chalcogenides. *Acta crystallographica section A: crystal physics, diffraction, theoretical and general crystallography*, 32(5):751–767, 1976.

[79] Enzheng Shi, Yao Gao, Blake P Finkenauer, Aidan H Coffey, Letian Dou, et al. Two-dimensional halide perovskite nanomaterials and heterostructures. *Chemical Society Reviews*, 47(16):6046–6072, 2018.

[80] Ian C Smith, Eric T Hoke, Diego Solis-Ibarra, Michael D McGehee, and Hemamala I Karunadasa. A layered hybrid perovskite solar-cell absorber with enhanced moisture stability. *Angewandte Chemie International Edition*, 53(42):11232–11235, 2014.

[81] Rune Søndenå, Svein Stølen, P Ravindran, Tor Grande, and Neil L Allan. Corner-versus face-sharing octahedra in a mn o 3 perovskites (a= ca, sr, and ba). *Physical Review B*, 75(18):184105, 2007.

[82] Yugang Sun and Younan Xia. Shape-controlled synthesis of gold and silver nanoparticles. *science*, 298(5601):2176–2179, 2002.

[83] Abhishek Swarnkar, Wasim J Mir, and Angshuman Nag. Can b-site doping or alloying improve thermal-and phase-stability of all-inorganic cspbx3 (x= cl, br, i) perovskites? *ACS Energy Letters*, 3(2):286–289, 2018.

[84] AF Takács, F Witt, S Schmaus, T Balashov, M Bowen, E Beaurepaire, and W Wulfhekel. Electron transport through single phthalocyanine molecules studied using scanning tunneling microscopy. *Physical Review B*, 78(23):233404, 2008.

[85] Na Tian, Zhi-You Zhou, Shi-Gang Sun, Yong Ding, and Zhong Lin Wang. Synthesis of tetrahexahedral platinum nanocrystals with high-index facets and high electro-oxidation activity. *science*, 316(5825):732–735, 2007.

[86] Hsinhan Tsai, Reza Asadpour, Jean-Christophe Blancon, Constantinos C Stoumpos, Jacky Even, Pulickel M Ajayan, Mercouri G Kanatzidis, Muhammad Ashraful Alam, Aditya D Mohite, and Wanyi Nie. Design principles for electronic charge transport in solution-processed vertically stacked 2d perovskite quantum wells. *Nature communications*, 9(1):2130, 2018.

[87] Hsinhan Tsai, Wanyi Nie, Jean-Christophe Blancon, Constantinos C Stoumpos, Reza Asadpour, Boris Harutyunyan, Amanda J Neukirch, Rafael Verduzco, Jared J Crochet, Sergei Tretiak, et al. High-efficiency two-dimensional ruddlesden–popper perovskite solar cells. *Nature*, 536(7616):312–316, 2016.

[88] Carlos Untiedt, Maria J Caturla, M Reyes Calvo, JJ Palacios, RC Segers, and JM Van Ruitenbeek. Formation of a metallic contact: jump to contact revisited. *Physical review letters*, 98(20):206801, 2007.

[89] Carlos Untiedt, Maria J Caturla, M Reyes Calvo, JJ Palacios, RC Segers, and JM Van Ruitenbeek. Formation of a metallic contact: jump to contact revisited. *Physical review letters*, 98(20):206801, 2007.

[90] Feng Wang and Vladislav Vasilyev. Molecular dynamics study of ferrocene topology under various temperatures. *International Journal of Quantum Chemistry*, 120(23):e26398, 2020.

[91] Kai Wang, Tao Wu, Congcong Wu, Rammohan Sriramdas, Xu Huang, Ke Wang, Yuanyuan Jiang, Hairui Liu, Yongke Yan, Dong Yang, et al. Nature of terrace edge states (tes) in lower-dimensional halide perovskite. *Journal of materials chemistry A*, 8(16):7659–7670, 2020.

[92] Nana Wang, Lu Cheng, Rui Ge, Shuting Zhang, Yanfeng Miao, Wei Zou, Chang Yi, Yan Sun, Yu Cao, Rong Yang, et al. Perovskite light-emitting diodes based on solution-processed self-organized multiple quantum wells. *Nature Photonics*, 10(11):699–704, 2016.

[93] Tariq Sheikh, Vaibhav Nawale, Nithin Pathoor, Chinmay Phadnis, Arindam Chowdhury, and Angshuman Nag. Molecular intercalation and electronic two dimensionality in layered hybrid perovskites. *Angewandte Chemie*, 132(28):11750–11756, 2020.

[94] H. L. Wells. Über die cäsium- und kalium-bleihalogenide. *Zeitschrift für anorganische Chemie*, 3(1):195–210, 1893.

[95] Zhengguo Xiao, Ross A Kerner, Lianfeng Zhao, Nhu L Tran, Kyung Min Lee, Tae-Wook Koh, Gregory D Scholes, and Barry P Rand. Efficient perovskite light-emitting diodes featuring nanometre-sized crystallites. *Nature Photonics*, 11(2):108–115, 2017.

[96] Hua Gui Yang, Cheng Hua Sun, Shi Zhang Qiao, Jin Zou, Gang Liu, Sean Campbell Smith, Hui Ming Cheng, and Gao Qing Lu. Anatase tio2 single crystals with a large percentage of reactive facets. *Nature*, 453(7195):638–641, 2008.

[97] IK Yanson, OI Shklyarevskii, Sz Csonka, H Van Kempen, S Speller, AI Yanson, and JM Van Ruitenbeek. Atomic-size oscillations in conductance histograms for gold nanowires and the influence of work hardening. *Physical review letters*, 95(25):256806, 2005.

[98] Jason J Yoo, Gabkyung Seo, Matthew R Chua, Tae Gwan Park, Yongli Lu, Fabian Rotermund, Young-Ki Kim, Chan Su Moon, Nam Joong Jeon, Juan-Pablo Correa-Baena, et al. Efficient perovskite solar cells via improved carrier management. *Nature*, 590(7847):587–593, 2021.

[99] Mingjian Yuan, Li Na Quan, Riccardo Comin, Grant Walters, Randy Sabatini, Oleksandr Voznyy, Sjoerd Hoogland, Yongbiao Zhao, Eric M Beauregard, Pongsakorn Kanjanaboos, et al. Perovskite energy funnels for efficient light-emitting diodes. *Nature nanotechnology*, 11(10):872–877, 2016.

[100] Yaping Zang, E-Dean Fung, Tianren Fu, Suman Ray, Marc H Garner, Anders Borges, Michael L Steigerwald, Satish Patil, Gemma Solomon, and Latha Venkataraman. Voltage-induced single-molecule junction planarization. *Nano Letters*, 21(1):673–679, 2020.

[101] Holly F. Zarick, Naiya Soetan, William R. Erwin, and Rizia Bardhan. Mixed halide hybrid perovskites: a paradigm shift in photovoltaics. *J. Mater. Chem. A*, 6:5507–5537, 2018.

[102] Yaxin Zhai, Sangita Baniya, Chuang Zhang, Junwen Li, Paul Haney, Chuan-Xiang Sheng, Eitan Ehrenfreund, and Zeev Valy Vardeny. Giant rashba splitting in 2d organic-inorganic halide perovskites measured by transient spectroscopies. *Science advances*, 3(7):e1700704, 2017.

[103] Baowei Zhang, Luca Goldoni, Juliette Zito, Zhiya Dang, Guilherme Almeida, Francesco Zaccaria, Jur De Wit, Ivan Infante, Luca De Trizio, and Liberato Manna. Alkyl phosphonic acids deliver cspbbr3 nanocrystals with high photoluminescence quantum yield and truncated octahedron shape. *Chemistry of Materials*, 31(21):9140–9147, 2019.

[104] Chunyi Zhao, Wenming Tian, Jing Leng, Yang Zhao, and Shengye Jin. Controlling the property of edges in layered 2d perovskite single crystals. *The Journal of Physical Chemistry Letters*, 10(14):3950–3954, 2019.

[105] J Zhao, NL Ross, and RJ Angel. Tilting and distortion of casno 3 perovskite to 7 gpa determined from single-crystal x-ray diffraction. *Physics and chemistry of minerals*, 31:299–305, 2004.

[106] Kaibo Zheng and Tonu Pullerits. Two dimensions are better for perovskites, 2019.

[107] Kaibo Zheng, Karel Zidek, Mohamed Abdellah, Maria E Messing, Mohammed J Al-Marri, and Tõnu Pullerits. Trap states and their dynamics in organometal halide perovskite nanoparticles and bulk crystals. *The Journal of Physical Chemistry C*, 120(5):3077–3084, 2016.

[108] Alexander S Zyazin, Johan WG van den Berg, Edgar A Osorio, Herre SJ van der Zant, Nikolaos P Konstantinidis, Martin Leijnse, Maarten R Wegewijs, Falk May, Walter Hofstetter, Chiara Danieli, et al. Electric field controlled magnetic anisotropy in a single molecule. *Nano letters*, 10(9):3307–3311, 2010.

[109] Vincenzo R Calderone, Andrea Testino, Maria Teresa Buscaglia, Marta Bassoli, Carlo Bottino, Massimo Viviani, Vincenzo Buscaglia, and Paolo Nanni. Size and

shape control of srtio3 particles grown by epitaxial self-assembly. *Chemistry of materials*, 18(6):1627–1633, 2006.

[110] Wei Chen, Qin Kuang, and Zhaoxiong Xie. Morphology evolution of natao 3 submicrometer single-crystals: from cubes to quasi-spheres. *Science China Materials*, 58:281–288, 2015.

[111] Samrat Das Adhikari, Amit K Guria, and Narayan Pradhan. Insights of doping and the photoluminescence properties of mn-doped perovskite nanocrystals. *The Journal of Physical Chemistry Letters*, 10(9):2250–2257, 2019.

[112] Nikolay S Pokryshkin, Vladimir N Mantsevich, and Victor Y Timoshenko. Anti-stokes photoluminescence in halide perovskite nanocrystals: From understanding the mechanism towards application in fully solid-state optical cooling. *Nanomaterials*, 13(12):1833, 2023.

[113] Vikash Kumar Ravi, Ganesh B. Markad, and Angshuman Nag. Band edge energies and excitonic transition probabilities of colloidal $cspbx_3$ (x = cl, br, i) perovskite nanocrystals. *ACS Energy Letters*, 1(4):665–671, 2016.

[114] Guangbao Wu, Rui Liang, Zhipeng Zhang, Mingzheng Ge, Guichuan Xing, and Guoxing Sun. 2d hybrid halide perovskites: structure, properties, and applications in solar cells. *Small*, 17(43):2103514, 2021.

[115] Mingshui Yao, Qiaohong Li, Guolin Hou, Chen Lu, Benli Cheng, Kechen Wu, Gang Xu, Fangli Yuan, Fei Ding, and Yunfa Chen. Dopant-controlled morphology evolution of wo3 polyhedra synthesized by rf thermal plasma and their sensing properties. *ACS applied materials & interfaces*, 7(4):2856–2866, 2015.

[116] Kongjun Zhu, Yang Cao, Xiaohui Wang, Lin Bai, Jinhao Qiu, and Hongli Ji. Hydrothermal synthesis of sodium niobate with controllable shape and structure. *CrystEngComm*, 14(2):411–416, 2012.

Chapter 2

Theoretical Concepts

1 Introduction

The emergence of quantum mechanics in the early twentieth century represented a significant scientific breakthrough for comprehending and forecasting material characteristics. In this framework, the system's state is articulated through a state function or wave function, denoted as ψ, and the determination of all measurable attributes is achievable through the resolution of the Schrödinger equation. Illustratively, when examining the Hydrogen atom, the intricate dynamics of the electron, along with its energy states (and consequently, the electronic structure of the Hydrogen atom), are delineated with remarkable precision, aligning closely with empirical observations[1]. A comprehensive grasp of the electronic structure of any given material system is pivotal for the comprehension and anticipation of its properties. Materials fundamentally consist of assemblies of atoms, constituting a system characterized by nuclei and electrons. The fundamental interaction governing this system is primarily electrostatic in nature. Nuclei are ~ 1800 times heavier than the electrons and with some approximations can be treated as classical particles fixed at particular lattice sites. Nevertheless, a quantum mechanical treatment is imperative for electrons. The presence of multiple electrons, coupled with the repulsive interactions among them, transforms the scenario into a many-body problem. Consequently, solving

the many-particle Schrödinger equation proves to be a formidable task. Many powerful methods for an improved though approximate solution of the many particle Schrödinger equation have been developed. These can handle around 100 electrons but are computationally demanding. So, the exact many-body wave function $\psi(\mathbf{r_1}, \mathbf{r_2}, \cdots, \mathbf{r_N})(N = \text{number of electrons in the system})$ remains inaccessible for most real systems. Hence we need some approximations to solve the many particle Schrödinger equation. This is generally done by reducing the many particle Schrödinger equation to some effective single particle equations and solving them. Density functional theory(DFT), as formulated by Kohn, Hohenberg, and Sham in the 1960′s, is a smart way to solve the many particle Schrödinger equation that reduces the many body problem to an effective single particle problem. This was done by considering the electron density $n(\mathbf{r})$ as a variable and expressing the energy of the system as a functional of the electron density, $E[n(\mathbf{r})]$. Determination of the ground state electron density $n_0(\mathbf{r})$ gives the ground state energy E_0, as well as the ground state wave function ψ_0 and hence the ground state electronic structure of any system. This is important because it is kind of solving the many particle Schrödinger equation by finding a function of just 3 variables, the electron density, rather than a complex function of $3N$ variables, the wave function.

We use DFT as implemented within the Vienna ab-initio simulation package (VASP) [2, 3] to calculate the electronic structure and structural properties of the systems considered as a part of this thesis. DFT has become a standard tool for exploring material properties and understanding them at the atomic level. It has enhanced our scientific understanding of various physical problems from different areas of science. It also comes out to be very useful in predicting material properties which are challenging to probe experimentally.

In this chapter, we give a brief introduction of the density functional theory and its formulation as a density functional based approach. We also discuss some technical details to use DFT in computational physics. The electronic structure calculation of a periodic solid allows the description in terms of Bloch states[5]. These are delocalized/extended electronic states which are assigned a quantum number $\mathbf{k}$ for the crystal momentum, together

with a band index n. **An usual expansion of the basis states involve plane wave.** This is widely used in electronic structure calculations but alternative representations are also available.

2 Formulation of Density functional theory

2.1 Many body Schrödinger equation and Born-Oppenheimer Approximation

In quantum mechanics the state of a system is described by a state function or wave function ψ, and all the measurable properties can be obtained by solving the Schrödinger equation. The time independent, non-relativistic Schrödinger equation $H\psi = E\psi$, is useful to calculate the electronic structure of atoms, molecules and solids. H is the Hamiltonian operator and ψ is a set of solutions, or eigenstates, of the Hamiltonian. Each solution, ψ_n , has an associated real eigenvalue, E_n, satisfying the eigenvalue equation. The detailed structure of the Hamiltonian depends on the physical system under consideration. For simple systems the Schrödinger equation can be solved exactly. For example, in case of Hydrogen atom, a system of a single electron moving under the potential of a single proton $v(\mathbf{r})$, the time independent Schrödinger equation becomes:

$$\left[-\frac{\hbar^2}{2m}\nabla^2 + v(\mathbf{r})\right]\psi(\mathbf{r}) = \varepsilon\psi(\mathbf{r}) \tag{2.1}$$

where m is the mass of the electron and the wave function $\psi(\mathbf{r})$, is a function of a single electron coordinate $\mathbf{r}$. Solving this equation gives the electronic structure of the Hydrogen atom and the dynamics of the electron is defined by the time dependent Schrödinger equation $H\psi = i\hbar\frac{\partial\psi}{\partial t}$, which is not needed further for electronic structure calculations. For a solid material of our interest the situation becomes complicated, where multiple electrons are interacting with multiple nuclei and among themselves. Such a many particle system is described by the many particle Schrödinger equation:

$$H\Psi(\mathbf{r}_i;\mathbf{R}_I) = E\Psi(\mathbf{r}_i;\mathbf{R}_I) \tag{2.2}$$

where the wave function Ψ is now a function of N electronic coordinates $\mathbf{r_i}$(i=1 to N) and M nuclear coordinates $\mathbf{R_I}$(I=1 to M). The Hamiltonian of the system is a sum of five terms which in atomic unit reads as:

$$H = -\frac{\hbar^2}{2m}\sum_i \bigtriangledown_i^2 + \frac{1}{2}\sum_{i\neq j}\frac{e^2}{|\mathbf{r}_i-\mathbf{r}_j|} - \frac{\hbar^2}{2M_I}\sum_I \bigtriangledown_I^2 + \frac{1}{2}\sum_{I\neq J}\frac{Z_I Z_J e^2}{|\mathbf{R}_I-\mathbf{R}_J|} - \sum_{i,I}\frac{Z_I e^2}{|\mathbf{R}_I-\mathbf{r}_i|} \tag{2.3}$$

where i , j refer to electrons and I , J refer to nuclei. Parameter e and m are the electronic charge and mass respectively. Z_I and M_I denote the nuclear charge and mass of the I^{th} nucleus respectively. This Hamiltonian can be written in a more compact form as:

$$H = T_e(\mathbf{r}) + V_{ee}(\mathbf{r}) + T_N(\mathbf{R}) + V_{NN}(\mathbf{R}) + V_{eN}(\mathbf{r},\mathbf{R}) \tag{2.4}$$

where $\mathbf{R}$ is now indicating a set of nuclear coordinates, and $\mathbf{r}$ is the set of electronic coordinates. First two terms, $T_e(\mathbf{r})$ and $V_{ee}(\mathbf{r})$ represent the kinetic energy of the electrons and the electron-electron coulomb repulsion respectively. The third and fourth terms, $T_N(\mathbf{R})$ and $V_{NN}(\mathbf{R})$ represent the kinetic energy of the nuclei and repulsive interaction between them respectively. The last term $V_{eN}(\mathbf{r},\mathbf{R})$ represents the interaction between electrons and nuclei and couples the electronic and nuclear degrees of freedom. This term prevents us from separating the total Hamiltonian into nuclear and electronic parts, which would make the problem a bit simpler and allow us to write the total wave function of the system as a product of nuclear and electronic terms, $\Psi(\mathbf{r};\mathbf{R}) = \Psi(\mathbf{r})\eta(\mathbf{R})$. The term $V_{eN}(\mathbf{r},\mathbf{R})$ is large and cannot be neglected. However, if we can assume that the nuclei are fixed and do not move then we can make the R dependence parametric and can split the problem into two separate parts. The separation of the nuclei and electrons into two separate mathematical problems is achieved using Born-Oppenheimer approximation(BOA)[13] or the Adiabatic approximation. The BOA rests on the fact that atomic nuclei are much heavier than electrons, each proton or neutron in a nucleus is $\sim$ 1800 times more massive than

an electron. This means that electrons respond much more rapidly to changes in their surroundings than nuclei can. This allows us to say that the nuclei are nearly fixed with respect to electron motion and at any instant of time for a particular nuclear configuration the electrons are at their possible ground state.

Initially, $T_N(\mathbf{R})$ can be neglected since T_N is much smaller than T_e due to larger nuclear mass, and then for a fixed nuclear configuration $\{\mathbf{R}_a\}$ we have:

$$H_{BOA}^{ele} = T_e(\mathbf{r}) + V_{ee}(\mathbf{r}) + V_{NN}(\mathbf{R}) + V_{eN}(\mathbf{r}, \mathbf{R}_a) \tag{2.5}$$

as the electronic Hamiltonian after BOA such that,

$$H_{BOA}^{ele}\Psi(\mathbf{r}; \mathbf{R}_a) = E^{ele}\Psi(\mathbf{r}; \mathbf{R}_a) \tag{2.6}$$

gives the electronic wave function $\Psi(\mathbf{r}; \mathbf{R}_a)$ and energy $E^{ele}(\mathbf{R}_a)$, which now depends on $\mathbf{R}$ parametrically. Generally $V_{NN}(\mathbf{R})$ is neglected in Equation (2.5), since in this case $\mathbf{R}$ is just a parameter so that $V_{NN}(\mathbf{R})$ is just a constant and shifts the eigenvalues only by some constant amount. In that case we can write H_{BOA}^{ele} as,

$$H_{BOA}^{ele} = T_e(\mathbf{r}) + V_{ee}(\mathbf{r}) + V_{eN}(\mathbf{r}, \mathbf{R}_a) \tag{2.7}$$

So, for any solid system the first step would be to solve Equation (2.7), that describes the electrons for fixed positions of the atomic nuclei. For a given set of electrons moving in the field of a set of nuclei, we get the lowest energy state or the ground state of the electrons. If we have M nuclei at positions ($\mathbf{R}_1$,$\mathbf{R}_2$,$\cdots$,$\mathbf{R}_M$) then we can express the ground-state electronic energy, E_0^{ele}, as a function of the positions of these nuclei, E_0^{ele}($\mathbf{R}_1$,$\mathbf{R}_2$,$\cdots$,$\mathbf{R}_M$). This function is known as the adiabatic potential energy surface of the atoms. Once we are able to calculate this potential energy surface we can know how does the energy of the material change as we move the atoms around[14].

But even after BOA the simplest possible electronic Hamiltonian[Equation (2.7)] for a fixed nuclear configuration $\{\mathbf{R}_a\}$, is not easy to solve. The term in the Hamiltonian defining the electron-electron interactions $V_{ee}(\mathbf{r})$, is the most critical one from the point of view of directly solving the equation. If this term was not there, that means for a non-interacting many electron system the equation reduces to a set of N independent single particle equations of the form,

$$h_i\varphi(\mathbf{r}_i) = \varepsilon\varphi(\mathbf{r}_i)[i = 1, 2, \cdots, N] \tag{2.8}$$

where N is the number of electrons in the system and h_i describes the kinetic and potential energies of the i^{th} electron. Solution of each such single particle equation gives the same set of single electron wave functions $\varphi_n(\mathbf{r})$ with energies ε_n. Then the ground state of the N electron system is simply expressed in terms of some simple or complex product of the N lowest energy wave functions $\varphi_1(\mathbf{r}_1)$, $\varphi_2(\mathbf{r}_2)$, ... ,$\varphi_N(\mathbf{r}_N)$ associated with the 1^{st}, 2^{nd}, ... ,N^{th} electron respectively. In band theory for periodic solid systems, the same approach is followed and the single electron states are called Bloch states[5]. But due to the presence of the electron-electron interaction term, individual electron wave function, $\varphi_i(\mathbf{r}_i)$, associated with the i^{th} electron, could not be found without simultaneously knowing the wave functions associated with all the other electrons in the system. This means, the Schrödinger equation is a many-body problem and we have to make some additional approximations to reduce it to an effective single particle problem. Various approaches were taken in this regard. Hartree-Fock (HF) and Density Functional theory (DFT) are two successful theories in which the two body interaction term is replaced by an effective single body potential. Next we are going to discuss the basic assumptions taken within these two approach to solve the electronic Hamiltonian after BOA[Equation (2.7)].

2.2 Hartree-Fock(HF) Theory : A wave function based approach

Hartree-Fock approach is an approximate way to solve the simplest form of the electronic Hamiltonian for an N electron system after BOA[Equation (2.7)]. We can write Equation

(2.7) as a sum of two terms gives as:

$$H_{BOA}^{ele} = -\frac{\hbar^2}{2m}\sum_i \bigtriangledown_i^2 + \frac{1}{2}\sum_{i\neq j}\frac{e^2}{|\mathbf{r}_i - \mathbf{r}_j|} - \sum_{i,I}\frac{Z_I e^2}{|\mathbf{R}_I - \mathbf{r}_i|} \tag{2.9}$$

$$= \sum_i \left(-\frac{\hbar^2}{2m}\bigtriangledown_i^2 - \sum_I \frac{Z_I e^2}{|\mathbf{R}_I - \mathbf{r}_i|}\right) + \frac{1}{2}\sum_{i\neq j}\frac{e^2}{|\mathbf{r}_i - \mathbf{r}_j|} \tag{2.10}$$

$$= \sum_i (T_i + V_{ion}(\mathbf{r}_i)) + \frac{1}{2}\sum_{i\neq j}\frac{e^2}{|\mathbf{r}_i - \mathbf{r}_j|} \tag{2.11}$$

$$= \sum_i h_i + V_{ee}(\mathbf{r}) \tag{2.12}$$

Here the main objective is to calculate the full electron wave function corresponding to the ground state of the above Hamiltonian. Now, as the electrons are fermions, the N electron wave function must satisfy the Pauli exclusion principle that prohibits two electrons with the same spin at the same spatial position. Mathematically, the many electron wave function must be anti-symmetric with respect to position/spin exchange between two electrons.

Now if we consider a system of N non-interacting electrons, we can exclude the electron-electron interaction term $V_{ee}(\mathbf{r})$ and the problem reduces to solving N single particle equations of the form:

$$h\chi(\mathbf{x}) = \varepsilon\chi(\mathbf{x}) \tag{2.13}$$

Where, $h = T + V_{ion}(\mathbf{r})$, is the Hamiltonian for a single electron under the potential of ion cores $V_{ion}(\mathbf{r})$. The eigenfunctions χ, defined by this equation are called spin orbitals and $\mathbf{x}$ is the space-spin coordinate. $\mathbf{x} = \{\mathbf{r},\sigma\}$ defines the position as well as spin state(up or down) of any single electron. Solution of each such single particle equation gives the same set of single electron wave functions $\chi_n(\mathbf{x})(n = 1, 2, \cdots, N)$. The spin orbitals are ordered in a way so that the orbital with n = 1 has the lowest energy, the orbital with n = 2 has the next lowest possible energy, and so on. Then the ground state of the N electron system may be expressed as a simple product of the N lowest energy wave

functions $\chi_1(\mathbf{x}_1)$, $\chi_2(\mathbf{x}_2)$, ... ,$\chi_N(\mathbf{x}_N)$ associated with the 1^{st}, 2^{nd}, ... ,N^{th} electron respectively. This approximation is called a Hartree product[15] and the energy of the ground state is the sum of the considered N spin orbital energies, $E_0 = \varepsilon_1 + \varepsilon_2 + \cdots + \varepsilon_N$. Along with its simplicity, the Hartree product has a serious drawback. It does not satisfy the antisymmetry principle. Fock in 1930 introduced a better approximation to the wave function by using a Slater determinant[16]. This is called Hartree-Fock approximation[17]. In the Hartree-Fock approximation, the N-electron wave function is formed by expressing the overall wave function as the determinant of a matrix of single-electron wave functions so that it satisfies the antisymmetry principle.

$$\Psi_{HF}(\mathbf{x}_1, \mathbf{x}_2, \cdots \mathbf{x}_N) = \frac{1}{\sqrt{N!}} \begin{vmatrix} \chi_1(\mathbf{x}_1) & \chi_1(\mathbf{x}_2) & \cdots & \chi_1(\mathbf{x}_N) \\ \chi_2(\mathbf{x}_1) & \chi_2(\mathbf{x}_2) & \cdots & \chi_2(\mathbf{x}_N) \\ \vdots & \vdots & \ddots & \vdots \\ \chi_N(\mathbf{x}_1) & \chi_N(\mathbf{x}_2) & \cdots & \chi_N(\mathbf{x}_N) \end{vmatrix} \tag{2.14}$$

This has a lot of advantages over the simple Hartree product. It vanishes if two electrons have the same coordinates or if two of the one-electron wave functions are the same. It changes sign on coordinate exchange. This means that the Slater determinant satisfies Pauli exclusion principle. Also, it does not distinguish between electrons and we cannot say which electron is in which single particle state. This is consistent with the strange results of quantum mechanics for identical particles.

Now let us see how the electron-electron interaction term $V_{ee}(\mathbf{r})$ is approximated using Slater determinant states to reduce the many body problem to an effective single particle problem. We start with the fact that Hartree-Fock wave functions will have the form of a Slater determinant which are normalized, and the electronic energy will be given by:

$$\begin{aligned} E_{HF}^{ele} = \langle \Psi_{HF} | H_{BOA}^{ele} | \Psi_{HF} \rangle &= \langle \Psi_{HF} | (\sum_i h_i) | \Psi_{HF} \rangle + \langle \Psi_{HF} | V_{ee}(\mathbf{r}) | \Psi_{HF} \rangle \\ &= \sum_i \varepsilon_i + \left\{ \sum_{ij} C_{ij} - \sum_{ij} J_{ij} \right\} \end{aligned} \tag{2.15}$$

After some rigorous mathematical steps which are not presented here, we can get the expressions for each of the terms in the above equation. ε_i is given by:

$$\varepsilon_i = \langle \chi_i | h | \chi_i \rangle = \int \chi_i^*(\mathbf{x}) \left[-\frac{\hbar^2}{2m} \bigtriangledown^2 + V_{ion}(\mathbf{r}) \right] \chi_i(\mathbf{x}) d\mathbf{x} \tag{2.16}$$

representing the energy of a noninteracting electron with spin orbital χ_i. C_{ij} and J_{ij} are called Coulomb integral and exchange integral respectively and are given by:

$$C_{ij} = \frac{e^2}{2} \int \int \chi_i^*(\mathbf{x}) \chi_j^*(\mathbf{x}') \frac{1}{|\mathbf{r} - \mathbf{r}'|} \chi_i(\mathbf{x}) \chi_j(\mathbf{x}') d\mathbf{x} d\mathbf{x}' \tag{2.17}$$

$$J_{ij} = \frac{e^2}{2} \int \int \chi_i^*(\mathbf{x}) \chi_j^*(\mathbf{x}') \frac{1}{|\mathbf{r} - \mathbf{r}'|} \chi_j(\mathbf{x}) \chi_i(\mathbf{x}') d\mathbf{x} d\mathbf{x}' \tag{2.18}$$

The exchange term given by Equation (2.18) is non zero only for like spins i.e. for $\sigma = \sigma'$.

Now for symmetric energy expressions, we can apply the variational theorem, which states that for any arbitrary Slater determinant state Ψ, the energy is always an upper bound to the true ground state energy of the system. Hence, we can obtain better approximate wave functions Ψ, by varying their parameters(spin orbitals χ) with the condition that the energy gets minimized. The electronic energy E_{HF}^{ele}, is now a functional of the spin orbitals $E_{HF}^{ele}[\{\chi_i\}]$ and we can vary the spin orbitals for the lowest energy within a given functional space. The corresponding Slater determinant would be the closest to the true ground state wave function of the system. Hence, Hartree-Fock method determines the set of spin orbitals giving the lowest energy and gives us the best possible ground state Slater determinant state. We want to minimize the Hartree-Fock energy $E_{HF}^{ele}[\{\chi_i\}]$, with respect to changes in the spin orbitals $\chi_i \rightarrow \chi_i + \delta\chi_i$, such that the procedure leaves them orthonormal. This can be done by Lagrange′s method of undetermined multipliers[18], where we introduce a functional $\mathcal{L}$ given as:

$$\mathcal{L}[\{\chi_i\}] = E_{HF}^{ele}[\{\chi_i\}] - \sum_j \varepsilon_j \int |\chi_j(\mathbf{x})|^2 d\mathbf{x} \tag{2.19}$$

where ε_j, are the undetermined Lagrange multipliers. Setting the first variation $\delta\mathcal{L} = 0$, and after some mathematical simplification, we obtain the Hartree-Fock equations defining the orbitals:

$$\begin{aligned}\left[-\frac{\hbar^2}{2m}\bigtriangledown^2 + V_{ion}(\mathbf{r})\right]\chi_i(\mathbf{x}) + \sum_{i\neq j}\left[\int|\chi_j(\mathbf{x}')|^2\frac{e^2}{|\mathbf{r}-\mathbf{r}'|}d\mathbf{x}'\right]\chi_i(\mathbf{x}) \\ -\sum_{i\neq j}\left[\int|\chi_j^*(\mathbf{x}')\frac{e^2}{|\mathbf{r}-\mathbf{r}'|}\chi_i(\mathbf{x}')d\mathbf{x}'\right]\chi_j(\mathbf{x}) = \varepsilon_i\chi_i(\mathbf{x})\end{aligned} \tag{2.20}$$

where ε_i is the energy eigenvalue associated with spin orbital χ_i. The second term in the Equation (2.20) gives the Coulomb interaction between an electron with spin orbital χ_i, and the average charge distribution of the other electrons. This is called the Coulomb term. We can define a corresponding Coulomb operator $\widehat{C_j}$ as:

$$\widehat{C_j}(\mathbf{x}) = \int|\chi_j(\mathbf{x}')|^2\frac{e^2}{|\mathbf{r}-\mathbf{r}'|}d\mathbf{x}' \tag{2.21}$$

giving the average local potential at point $\mathbf{r}$ due to the charge distribution of the electron in spin orbital χ_j. The third term in Equation (2.20) comes from the antisymmetry requirement of the wave function and does not have a simple classical analogue. This is called the exchange term and we can define a corresponding exchange operator $\widehat{J_j}$ in terms of its action on an arbitrary spin orbital χ_i as:

$$\widehat{J_j}(\mathbf{x})\chi_i(\mathbf{x}) = \left[\int\chi_j^*(\mathbf{x}')\frac{e^2}{|\mathbf{r}-\mathbf{r}'|}\chi_i(\mathbf{x}')d\mathbf{x}'\right]\chi_j(\mathbf{x}) \tag{2.22}$$

And in terms of these Coulomb and exchange operators, we have the Hartree-Fock single particle equations as:

$$\left[-\frac{\hbar^2}{2m}\bigtriangledown^2 + V_{ion}(\mathbf{r}) + \sum_{j\neq i}\widehat{C_j}(\mathbf{x}) - \sum_{j\neq i}\widehat{J_j}(\mathbf{x})\right]\chi_i(\mathbf{x}) = \varepsilon_i\chi_i(\mathbf{x}) \tag{2.23}$$

We define,

$$V_H(\mathbf{x}) = \sum_{j \neq i} \widehat{C_j}(\mathbf{x}) - \sum_{j \neq i} \widehat{J_j}(\mathbf{x}) \tag{2.24}$$

as the Hartree potential, which is the average effective potential experienced by an electron due to the presence of remaining $(N-1)$ electrons making Hartree-Fock approximation a mean field approach.

Now we have to solve these single particle Hartree-Fock equations and obtain the N spin orbitals with lowest energies and then construct the ground state wave function as a Stater determinant of those N spin orbitals. And the total energy corresponding to the ground state would be the sum of the considered spin-orbital energies. To solve the single electron equations in a practical calculation, we need to expand the spin orbitals in a basis set. If the set of K number of functions $\phi_1(\mathbf{x}), \phi_2(\mathbf{x}), \cdots, \phi_K(\mathbf{x})$ defines the basis set, then we can approximate the spin orbitals as:

$$\chi_i(\mathbf{x}) = \sum_{j=1}^{K} \alpha_{ij} \phi_j(\mathbf{x}) \tag{2.25}$$

Hence we only need to find the expansion coefficients, α_{ij} , for $i = 1, \cdots, N$ and $j = 1, \cdots, K$ to fully define all the spin orbitals that are used in the HF method. Choosing a large basis set and functions that are initially similar to the real spin orbitals, improves the accuracy but with an increased computational cost. Now, to find the spin orbitals one needs to solve the single electron equations[Equation (2.23)] for which we need to know the Hartree potential V_H. But to define the Hartree potential(V_H), we must know in turn, the individual spin orbitals associated with all the electrons. To break this loop, a Hartree-Fock calculation becomes an iterative procedure with the main steps as described below[14]:

Step1 : Make an initial estimate of the spin orbitals [Equation (2.25)] by specifying the expansion coefficients, α_{ij}.

Step2 : From the current estimate of the spin orbitals, define the Hartree potential V_H.

Step3 : Using this Hartree potential V_H from step 2, solve the single electron Hartree-Fock equations for the spin orbitals.

Step4 : If the spin orbitals found in step 3 are consistent with the orbitals used in step 2 satisfying some convergence criteria, then these are the final solutions to the Hartree-Fock problem. If not, then a new estimate or update for the spin orbitals must be made and we then return to step 2.

We are not going to discuss here the details of how to make an initial guess for spin orbitals, what shall be the convergence criteria and procedure to update the spin orbitals. But some basic problems associated with such wave function based approach needs to be discussed. One of the main problem is associated with the dimension of the wave function. Excluding the spin degrees of freedom, for a system of N electrons the total wave function is $3N$ dimensional. For example, the wave function for a nanocluster of 100 Pt atoms shall require more than 23,000 dimensions[14]. Accuracy of the calculation is another issue which depends on two main factors. (1) How accurately the electron-electron interaction is treated and (2) how accurately we represent the many electron Schrödinger wave function. Hartee-Fock method with Slater determinants includes exchange interaction, but this is not the only kind of electron correlation that we need to consider for good accuracy. Electrons repel each other according to Coulomb's law. Hartree-Fock replaces this instantaneous electron-electron repulsion with an average term where each electron feels the effect of an average electron charge cloud. This introduces an error in the wave function and the energy. Similarly, to accurately represent the true many electron Schrödinger wave function, we need infinitely large number of Slater determinants as basis set. But in Hartree-Fock theory we use a single Slater determinant state to represent the ground state, which is not a good approximation. The hypothetical energy of N electrons from a HF calculations using an infinitely large basis set, is known as the Hartree-Fock limit. This energy is not the same as the true ground state energy of the system and their difference is defined as the electron correlation energy. Hartree-Fock theory fails for systems where electron correlation is important. For example, Van der Waals systems where dispersion forces

results from instantaneous electron-electron interactions. Improvements can be made by considering Slater determinants that represents excited state along with the HF ground state. For example, configuration interaction (CI), coupled cluster (CC), Møller-Plesset perturbation theory (MP), quadratic configuration interaction (QCI) approach are among them.

2.3 Density Functional Theory : From wave function to electron density

The N electron wave function $\Psi(\mathbf{r}_1, \cdots\cdot, \mathbf{r}_N)$, is an abstract quantity that cannot be directly observed. The quantity that can be physically measured is the probability density $\Psi^*\Psi$. An equivalent quantity that can be physically measured in X-ray diffraction experiments is the electron density $n(\mathbf{r})$. The spin independent density of an N electron system is defined as,

$$n(\mathbf{r}_i) = N \int \Psi^*(\mathbf{r}_1, \cdots, \mathbf{r}_i, \cdots, \mathbf{r}_N)\Psi(\mathbf{r}_1, \cdots, \mathbf{r}_i, \cdots, \mathbf{r}_N) d\mathbf{r}_1 d\mathbf{r}_2 \cdot\cdot d\mathbf{r}_{(i-1)} d\mathbf{r}_{(i+1)} \cdot\cdot d\mathbf{r}_N \quad (2.26)$$

The electron density is a function of just 3 spatial variables and contains a large amount of information that is actually physically observable from the full wave function solution to the Schrödinger equation, which is a function of $3N$ coordinates. Like $\Psi(\mathbf{r}_1, \cdots\cdot, \mathbf{r}_N)$, $n(\mathbf{r})$ also vanishes at infinity and integrates out to the total number of particles, N in the system. If we are able to express the total energy E, of the electron system as a functional of the electron density $n(\mathbf{r})$, $E[n(\mathbf{r})]$, and apply variational method to determine the ground state electron density $n_0(\mathbf{r})$, corresponding to a minimum in $E[n(\mathbf{r})]$, then we can in-turn get all necessary information of the system including the ground state wave function Ψ_0. This is important because we can get the ground state solution for the electronic Hamiltonian[Equation (2.9)] by varying a function of 3 spatial variables for any electron system. A theory for electronic structure calculation based on the electron density $n(\mathbf{r})$, that was there since 1920 was the Thomas-Fermi(TF) theory[19, 20]. Thomas-Fermi theory gives a rough approximation to the exact solution of the many-electron Schrödinger equation. This was quite useful for describing some qualitative trends like total energies of

atoms, but in case of chemistry and materials science, which involve valence electrons, it was of almost no use. For example it did not lead to any chemical binding[21]. As stated by Walter Kohn in his Noble Lecture[21], it was the suggestion of the hypothesis, that a knowledge of the ground-state density of $n(\mathbf{r})$, for any electronic system (with or without interactions) uniquely determines the system, became the starting point of modern density functional theory(DFT) as formulated by Kohn, Hohenberg, and Sham.

The entire field of density functional theory rests on two fundamental mathematical theorems proved by Hohenberg and Kohn[22] and the derivation of a set of equations by Kohn and Sham[23] in the mid 1960's.

Hohenberg Kohn Theorem 1 : The basic statement of the theorem is that, The ground state density $n_0(\mathbf{r})$ of a bound system of interacting electrons in some external potential $V_{ext}(\mathbf{r})$ determines this potential uniquely[21, 22].

Proof: Let $n(\mathbf{r})$, be the ground state density of N electrons in the external potential $V_{ext}(\mathbf{r})$, corresponding to the ground state wave function Ψ, and the energy E, of the Hamiltonian, $H = T_e + V_{ee} + V_{ext}$. T_e and V_{ee} are the kinetic and electron-electron interaction energy operators respectively[see Equations (2.3) and (2.4) for detail expression of T_e and V_{ee}]. Let us consider V'_{ext}, a different external potential, which also corresponds to the same ground state density $n(\mathbf{r})$. This will result in a different Hamiltonian H' and corresponding ground state wavefunctions Ψ' . Now,

$$E = \langle\Psi|H|\Psi\rangle \tag{2.27}$$

$$= \langle\Psi|T_e + V_{ee}|\Psi\rangle + \int n(\mathbf{r})V_{ext}(\mathbf{r})d^3r \tag{2.28}$$

and

$$E' = \langle\Psi'|H'|\Psi'\rangle \tag{2.29}$$

$$= \langle\Psi'|T_e + V_{ee}|\Psi'\rangle + \int n(\mathbf{r})V'_{ext}(\mathbf{r})d^3r \tag{2.30}$$

Since Ψ' is not the corresponding ground state of H,

$$E = \langle\Psi|H|\Psi\rangle \tag{2.31}$$

$$< \langle\Psi'|H|\Psi'\rangle = \langle\Psi'|H'|\Psi'\rangle + \langle\Psi'|[H - H']|\Psi'\rangle \tag{2.32}$$

$$< E' + \int n(\mathbf{r})[V_{ext}(\mathbf{r}) - V'_{ext}(\mathbf{r})]d^3r \tag{2.33}$$

Similarly,

$$E' < E + \int n(\mathbf{r})[V'_{ext}(\mathbf{r}) - V_{ext}(\mathbf{r})]d^3r \tag{2.34}$$

Adding both the above Equations (2.33) and (2.34) we get,

$$(E + E') < (E' + E) \tag{2.35}$$

This contradictory result proves the first theorem. Now as $V_{ext}(\mathbf{r})$ determines H, so another way to restate this result is that the ground state energy $E_0[n(\mathbf{r})]$ and wave function $\Psi_0[n(\mathbf{r})]$ from Schrödinger's equation are unique functional of the electron density $n(\mathbf{r})$. And the ground state electron density $n_0(\mathbf{r})$ in an external potential uniquely determines all properties, including the energy and wave function, of the ground state.

Hohenberg Kohn Theorem 2 : The second theorem states that, the ground state energy can be obtained variationally: The exact ground state energy corresponding to the full solution of the Schrödinger equation is the global minimum value of the functional $E[n(\mathbf{r})]$. And the electron density that minimizes the energy of the overall functional is the true ground state electron density. So, if $n_0(\mathbf{r})$ is the ground state electron density, then this implies that, for any density $n'(\mathbf{r})$, other than ground state density,

$$E[n'(\mathbf{r})] \geq E[n_0(\mathbf{r})] \tag{2.36}$$

Kohn-Sham Formulation :

For the Hamiltonian, $H = T_e + V_{ee} + V_{ext}$ of N interacting electrons in the external potential V_{ext}, the total energy functional can be written as,

$$E[n(\mathbf{r})] = F[n(\mathbf{r})] + \int n(\mathbf{r}) V_{ext}(\mathbf{r}) d^3r \tag{2.37}$$

where $F[n(\mathbf{r})] = T[n(\mathbf{r})] + E_{ee}[n(\mathbf{r})]$, is an unknown, but otherwise universal functional of the electron density $n(\mathbf{r})$ only. $F[n(\mathbf{r})]$ in the above equation represents the sum of kinetic energy and the electron-electron interaction energy and is called the Hohenberg-Kohn functional. The ground state energy can be obtained by minimizing this energy functional, subject to the constraint that the number of electrons N is conserved($\int n(\mathbf{r}) d\mathbf{r} = N$), which leads to :

$$\frac{\delta}{\delta n(\mathbf{r})} \left[F[n(\mathbf{r})] + \int n(\mathbf{r}) V_{ext}(\mathbf{r}) d^3r - \mu_L \left(\int n(\mathbf{r}) d^3r - N \right) \right] = 0 \tag{2.38}$$

with the Euler equation :

$$\mu_L = \frac{\delta F[n(\mathbf{r})]}{\delta n(\mathbf{r})} + V_{ext}(\mathbf{r}) \tag{2.39}$$

where, μ_L is the Lagrange multiplier associated with the constraint of constant N. The main problem is that, Hohenberg-Kohn theorems does not provide any actual form of the energy functional. Practically, this is being done with approximate forms. An approach to solve this problem was proposed by Kohn and Sham[23] and the idea was to replace the interacting N-electrons system by a hypothetical system of N non-interacting electrons whose ground state density coincides with that of the interacting system. The approach was to write the energy functional described in the Hohenberg-Kohn theorems in terms of the single electron wave functions, $\phi_i(\mathbf{r})$. Then the electron density $n(\mathbf{r})$ of N electron system can be written as,

$$n(\mathbf{r}) = 2 \sum_{i=1}^{N} \phi_i^\star(\mathbf{r}) \phi_i(\mathbf{r}) \tag{2.40}$$

The factor of 2 comes because we are treating the problem without spin degrees of freedom and each orbital ϕ_i, can be occupied by two electrons with opposite spins. The total wave function Ψ_{KS}, for this type of system is exactly given by a Slater determinant of single particle orbitals $\phi_i(\mathbf{r}_i)$. Then the functional $F[n(\mathbf{r})]$ can be expressed as a sum of three terms as:

$$F[n(\mathbf{r})] = T_0[n(\mathbf{r})] + E_H[n(\mathbf{r})] + E_{XC}[n(\mathbf{r})] \tag{2.41}$$

where,

$$T_0[n(\mathbf{r})] = \sum_i \langle\phi_i| - \frac{\hbar^2}{2m}\nabla^2|\phi_i\rangle \tag{2.42}$$

$$E_H[n(\mathbf{r})] = \frac{e^2}{2}\int\int n(\mathbf{r})\frac{1}{|\mathbf{r}-\mathbf{r}'|}n(\mathbf{r}')d^3r d^3r' \tag{2.43}$$

$$= \frac{e^2}{2}\sum_{i,j}\langle\phi_i\phi_j|\frac{1}{|\mathbf{r}-\mathbf{r}'|}|\phi_i\phi_j\rangle \tag{2.44}$$

$T_0[n(\mathbf{r})]$ is the kinetic energy of a non-interacting electron gas of density $n(\mathbf{r})$ and $E_H[n(\mathbf{r})]$ is the classical electron-electron interaction energy(Hartree energy) of the electrons. $E_{XC}[n(\mathbf{r})]$ is the exchange-correlation energy, which contains the difference between the exact and non-interacting kinetic energies and also the non-classical contributions of the electron-electron interactions such as exchange energy. This is expressed as:

$$E_{XC}[n(\mathbf{r})] = T[n(\mathbf{r})] - T_0[n(\mathbf{r})] + E_{ee}[n(\mathbf{r})] - E_H[n(\mathbf{r})] \tag{2.45}$$

Minimization of the total energy functional from the Kohn-Sham formulation, by applying variational principle[Equation (2.38)] leads to the self consistent Kohn-Sham equations given as:

$$[-\frac{\hbar^2}{2m}\nabla^2 + V_{ext}(\mathbf{r}) + V_H(\mathbf{r}) + V_{XC}(\mathbf{r})]\phi_i(\mathbf{r}) = \epsilon_i\phi_i(\mathbf{r}) \tag{2.46}$$

For the electrons under the potential of nuclei, $V_{ext}(\mathbf{r})$ corresponds to the $V_{ion}(\mathbf{r})$ like in the Hartree-Fock single particle equations [Equation (2.23)]. $V_H(\mathbf{r})$ is the classical part of the Hartree potential given as,

$$V_H(\mathbf{r}) = \frac{\delta E_H[n(\mathbf{r})]}{\delta n(\mathbf{r})} \tag{2.47}$$

$$= e^2 \int \frac{n(\mathbf{r}')}{|\mathbf{r} - \mathbf{r}'|} d^3r' \tag{2.48}$$

This potential describes the Coulomb repulsion between the electron in any one of the Kohn-Sham orbital and the total electron density defined by all electrons in the system. So, a part of V_H involves a coulomb interaction between the electron and itself. The self-interaction is not physical, and the correction for this is also considered in the unknown exchange-correlation potential V_{XC} given as,

$$V_{XC}(\mathbf{r}) = \frac{\delta E_{XC}[n(\mathbf{r})]}{\delta n(\mathbf{r})} \tag{2.49}$$

One crucial point to remember is that, the ground state density obtained by solving the Kohn-Sham equations for an alternative non-interacting Kohn-Sham system, is the same as the exact ground state density. But the single particle wave functions ϕ_i are solely mathematical functions with no physical meaning associated to them. To get the single particle wave functions ϕ_i, we need to solve the Kohn-Sham equations[Equation (2.46)]. Now to solve the Kohn-Sham equations(forgetting for now that the function V_{XC} is unknown) we need to know the Hartree potential. And to define the Hartree potential we need to know the electron density which in-turn requires all the single electron wave functions ϕ_i. So, again to break this loop, and calculate the ground state density the problem is usually treated in an iterative way with the following steps[14] :

Step 1 : Define an initial, trial electron density, $n(r)$.

Step 2 : Solve the Kohn-Sham equations defined using the trial electron density to find the single-particle wave functions, ϕ_i.

Step 3 : Calculate the electron density defined by the Kohn-Sham single-particle wave functions from Step 2, $n_{KS}(\mathbf{r}) = 2\sum_i \phi_i^\star(\mathbf{r})\phi_i(\mathbf{r})$.

Step 4 : Compare the calculated electron density, $n_{KS}(\mathbf{r})$, with the electron density used in solving the Kohn-Sham equations, $n(\mathbf{r})$. If the two densities are consistent and satisfy some convergence criteria, then this is the ground state electron density and we get the ground state energy. If the two densities are different, $n(\mathbf{r})$ must be updated in some way. Once this is done, the process begins again from step 2.

In the above discussion of solving the Kohn-Sham equations, we ignored one important fact that the form of the function V_{XC} was not known. To define the mathematical problem(Kohn-Sham equations) properly, we need to know the form of the exchange-correlation potential $V_{XC}(\mathbf{r})$. For this, approximate forms of $V_{XC}(\mathbf{r})$ are used. In the next section we give a brief overview of some of the form of $E_{XC}[n(\mathbf{r})]$ most widely used in DFT calculations that leads to $V_{XC}(\mathbf{r})$.

2.4 Approximations for the exchange-correlation Energy $\mathbf{E_{XC}[n(r)]}$

Here we try to give a brief and general picture of how these approximations are done. For details we refer to the main articles that has been mentioned in the text. If Ψ is the ground state wave function of the electronic Hamiltonian[Equation (2.9)] for the N electron system, then the expectation value for the electron-electron interaction V_{ee} is given as,

$$\langle\Psi|V_{ee}|\Psi\rangle = \frac{e^2}{2}\int\int \frac{P(\mathbf{r},\mathbf{r}')}{|\mathbf{r}-\mathbf{r}'|}d^3r d^3r' \tag{2.50}$$

Where, $P(\mathbf{r},\mathbf{r}')$ is the pair-density giving the probability of simultaneously finding an electron at the point $\mathbf{r}$ within volume element d^3r, and another electron at $\mathbf{r}'$ in volume element d^3r'. For non-interacting electrons there is no correlation and the probability of finding a pair of electrons at the points $\mathbf{r}$ and $\mathbf{r}'$ is simply the product of the densities at the respective points as,

$$P^{claccical}(\mathbf{r},\mathbf{r}') = n(\mathbf{r})n(\mathbf{r}') \tag{2.51}$$

leading to the classical Hartree energy E_H[Equation (2.43)]. But quantum mechanical effect of exchange and correlation interactions reduce the classical value of the electron density at $\mathbf{r}$ due to the presence of the second electron at $\mathbf{r}'$. Therefore each electron creates a depletion, or hole, of electron density around itself as a direct consequence of exchange-correlation effects. Taking account of the hole, the pair-density can be written as,

$$P^{QM}(\mathbf{r},\mathbf{r}') = n(\mathbf{r})n(\mathbf{r}') + n(\mathbf{r})n_{_{XC}}(\mathbf{r},\mathbf{r}') \tag{2.52}$$

$n_{_{XC}}(\mathbf{r},\mathbf{r}')$ is called the exchange-correlation hole density, taking into account the quantum mechanical effects. The exchange-correlation energy functional, $E_{XC}[n(\mathbf{r})]$, can be defined as[24],

$$E_{XC}[n(\mathbf{r})] = \int n(\mathbf{r})\varepsilon_{_{XC}}(\mathbf{r})d^3r \tag{2.53}$$

where,

$$\varepsilon_{_{XC}}(\mathbf{r}) = \frac{e^2}{2}\int \frac{n_{_{XC}}(\mathbf{r},\mathbf{r}')}{|\mathbf{r}-\mathbf{r}'|}d^3r' \tag{2.54}$$

is the exchange-correlation energy per particle. The exchange-correlation potential(V_H), then follows from Equation (2.49). The functionals can be characterized by the way in which the density surrounding each electron is sampled in order to construct $\varepsilon_{_{XC}}(\mathbf{r})$.

Local Density Approximation(LDA) :

Local density approximation(LDA) can be called the mother of all approximations proposed by Hohenberg and Kohn in their original DFT paper[22]. The LDA approximates

the true exchange-correlation energy of a system at each point in space, by the exchange-correlation energy of a homogeneous electron gas(HEG) of the same density observed at that point. The homogeneous electron gas is the only system for which the form of the exchange-correlation energy is known precisely. LDA only uses the local density, and the exchange-correlation energy functional is written as,

$$E_{XC}^{LDA}[n(\mathbf{r})] = \int n(\mathbf{r})\varepsilon_{XC}^{HEG}(\mathbf{r})d^3r \tag{2.55}$$

where $\varepsilon_{XC}^{HEG}(\mathbf{r})$, is the exchange-correlation energy density corresponding to a homogeneous electron gas of density $n(\mathbf{r})$. $\varepsilon_{XC}^{HEG}(\mathbf{r})$ can be separated into exchange and correlation parts as,

$$\varepsilon_{XC}^{HEG}(\mathbf{r}) = \varepsilon_{X}^{HEG}(\mathbf{r}) + \varepsilon_{C}^{HEG}(\mathbf{r}). \tag{2.56}$$

This exchange part $\varepsilon_{X}^{HEG}(\mathbf{r})$ was derived analytically by Dirac and is known for a homogeneous electron gas [25]. However, the analytic expressions for ε_{C}^{HEG} in case of the homogeneous electron gas is only known in two limits of high[26, 27] and low[28] electron densities.

Generalized Gradient Approximation (GGA) :

LDA is the simplest approximation that is not appropriate for real systems where the electron density is not uniform due to formation of spatially directed bonds. So, the next approximation is the Generalized Gradient Approximation (GGA). To consider the spatial variation in the electron density, the exchange-correlation energy density is expressed in terms of both the local electron density as well as the gradient of the electron density. To represent this fact, we can express the exchange-correlation functional under GGA approximation as,

$$E_{XC}^{GGA}[n(\mathbf{r})] = \int n(\mathbf{r})\varepsilon_{XC}^{HEG}[n(\mathbf{r}), |\nabla n(\mathbf{r})|]d^3r \tag{2.57}$$

Most important work in developing GGA functional was initiated by Perdew and co-workers[29]. Now the information of the gradient of the electron density can be included in various ways leading to large number distinct GGA functionals. Some of the most popular forms are Perdew and Wang (PW91)[30], Becke-Lee-Yang-Par (B-LYP)[31] and Perdew, Burke and Enzerhof (PBE)[32] functionals.

Meta-Generalized Gradient Approximation(MGGA) :

The next type of approximations that follows after GGA is the Meta-Generalized Gradient Approximation(MGGA). MGGA functionals include information from $n(\mathbf{r})$, $\nabla n(\mathbf{r})$ and $\nabla^2 n(\mathbf{r})$. The kinetic energy density corresponding to the Kohn-Sham orbitals,

$$\tau(\mathbf{r}) = \frac{1}{2}\sum_{i=1}^{N} |\nabla \phi_i(\mathbf{r})|^2 \tag{2.58}$$

is equivalent to the Laplacian of the electron density, and thus may be used in meta-GGA functionals instead of $\nabla^2 n(\mathbf{r})$. The Tao-Perdew-Staroverov-Scuseria (TPSS) functional[33] is an example of meta-GGA functional.

Hybrid Functionals :

Hybrid functionals include contributions from the exact exchange(Hartree-Fock) energy with a GGA functional having a general form,

$$E_{XC}^{Hybrid} = \alpha(E_X^{HF} - E_X^{GGA}) + E_{XC}^{GGA} \tag{2.59}$$

where E_X^{HF} is the Hartree-Fock exchange energy expression as given in Equation 2.18 with Kohn-Sham orbitals used in place of spin orbitals. One of the feature of this quantity is that it is non-local. To evaluate it at a particular point of the configuration space the value of ϕ_i must be known at all points. The coefficient, α, determines the amount of exact-exchange mixing which is fitted semi-empirically. HSE functionals [34] named after J. Heyd, G. E. Scuseria, and M. Ernzerhof is one such example. These functionals are expected to be more accurate while studying the strongly correlated electron systems due

to their large self-interaction correction but are computationally expensive due to the non-local nature.

3 Numerical Approximations for DFT Calculations

Using DFT we are trying to calculate the electronic structure of a collection of atoms. DFT basically defines a mathematical problem for any such physical system with an approximate form of the exchange-correlation functional. The mathematical problem is to solve a set of mathematical equations(Kohn-Sham equations) in an iterative manner to get the ground state electron density. The problem cannot be solved analytically but numerically with a series of numerical approximations. For example integrations are done considering a finite number of grid points, infinite sums are truncated to finite ones. Due to such approximations errors may enter. In this regard, a well converged solution is the one which is very close to the exact solution of the mathematical problem defined by DFT. Here we make a brief discussion on such numerical approximations.

3.1 Plane Wave Basis and Energy cutoff :

To numerically solve the Kohn-Sham equations we first need a proper basis set to expand the single particle orbitals and represent them with the expansion coefficients. Here we are interested in the electronic structure of crystalline materials with periodic arrangements of atoms. The entire crystal can be generated from a periodic repetition of a basic unit called the unit cell defined by three unit vectors, $\mathbf{a}_1$, $\mathbf{a}_2$, $\mathbf{a}_3$. The single particle electronic states for the non-interacting electrons in periodic system are called Bloch states[5] with the form :

$$\phi_{\mathbf{k}}(\mathbf{r}) = e^{i\mathbf{k}\cdot\mathbf{r}} u_{\mathbf{k}}(\mathbf{r}) \tag{2.60}$$

where, $u_{\mathbf{k}}(\mathbf{r})$ is periodic in space with periodicity of the crystal, i.e. $u_{\mathbf{k}}(\mathbf{r} + n_1\mathbf{a}_1 + n_2\mathbf{a}_2 + n_3\mathbf{a}_3) = u_{\mathbf{k}}(\mathbf{r})$ for any integer values of n_1, n_2, n_3. So, Bloch states are basically plane waves modified by a periodic function $u_{\mathbf{k}}(\mathbf{r})$. Periodicity of $u_{\mathbf{k}}(\mathbf{r})$ allows it to expand in terms of plane waves as,

$$u_{\mathbf{k}}(\mathbf{r}) = \sum_{\mathbf{G}} C_{\mathbf{G}} e^{i\mathbf{G}\cdot\mathbf{r}} \tag{2.61}$$

where, $\mathbf{G} = m_1\mathbf{b}_1 + m_2\mathbf{b}_2 + m_3\mathbf{b}_3$, is a reciprocal lattice vector defined in terms of reciprocal space unit vectors $\mathbf{b}_1$, $\mathbf{b}_2$, $\mathbf{b}_3$(defined in terms of real space unit vectors $\mathbf{a}_1$, $\mathbf{a}_2$, $\mathbf{a}_3$ using the standard definition) for any integer values of m_1, m_2, m_3. So, now the Bloch states are given as,

$$\phi_{\mathbf{k}}(\mathbf{r}) = \sum_{\mathbf{G}} C_{\mathbf{G}+\mathbf{k}} e^{i(\mathbf{G}+\mathbf{k})\cdot\mathbf{r}} \tag{2.62}$$

This is an infinite sum of plane waves with kinetic energies $E = \frac{\hbar^2}{2m}|\mathbf{k} + \mathbf{G}|^2$. For a periodic system, such states are reasonable to choose as the single electron orbitals ϕ_i, in the Kohn-Sham equations and we can use plane waves as the basis set to expand the Kohn-Sham orbitals. This is why such DFT calculations are sometimes referred to as plane wave calculations. The problem is that Equation (2.62) involves a summation over an infinite number of possible values of $\mathbf{G}$. For practical calculations we need to truncate this infinite sum to a finite one. For this we consider a cutoff energy defined as,

$$E_{cut} = \frac{\hbar^2}{2m} G_{cut}^2 \tag{2.63}$$

so that, the plane waves with kinetic energy lower than the cutoff energy are included in the basis. The error introduced in this approximation can be minimized by increasing E_{cut} till the total energy of the system converges showing no significant variation with any further change in E_{cut}.

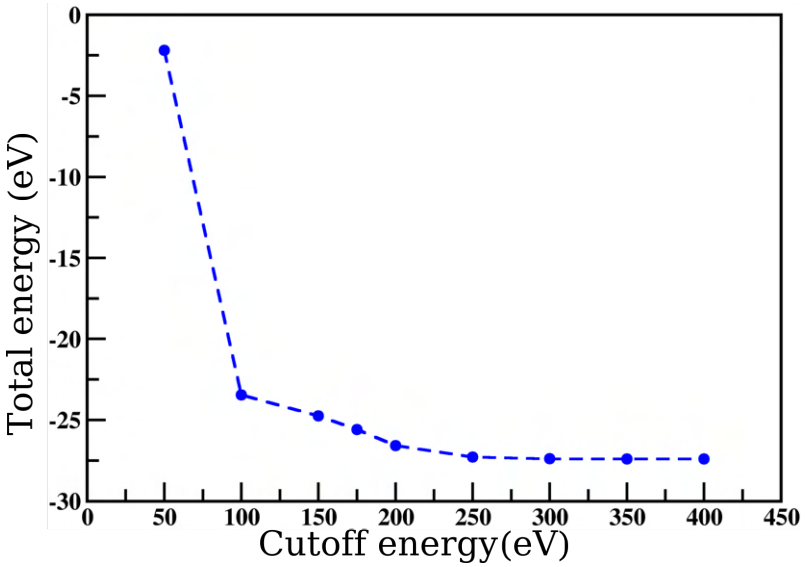

FIGURE 2.1: Total energy of Zns-ZB structure using a 8×8×8 k points grid as a function of the cutoff energy E_{cut}

Figure 2.1 shows the convergence of the total energy(using DFT as implemented in VASP) of Zns-ZB structure as a function of E_{cut}. GGA was considered for the exchange-correlation functional.

A 10×10×10 Monkhorst-Pack k-mesh was used for performing the k-space integrations(This is discussed in details in the next section). We can see from Figure 2.1 that, changing value of E_{cut} from 250 to 400 eV, the total energy change per atom is less than 1 meV. Hence we can use $E_{cut} = 300eV$ for the above calculation for a well converged result.

3.2 Performing K-Space Integrations :

In any practical DFT calculation, a large amount of time is spent in evaluating k-space integrals in the Brillouin zone with the form[14],

$$g = \frac{V_{cell}}{(2\pi)^3} \int_{BZ} g(\mathbf{k}) d\mathbf{k} \tag{2.64}$$

Where V_{cell}, is the volume of the unit cell of the crystal. Numerically integrals are evaluated by evaluating the value of the function $g(\mathbf{k})$, at some finite set of k-points within the

Brillouin zone and summing them with proper weight. Such method give more and more accurate results as we increase the number of k-points and the numerical method may converge to the exact result of the integral. The question is how to choose the k-points to evaluate such integrals efficiently. The most widely used method of considering equally spaced points in the Brillouin zone was developed by Monkhorst and Pack[35]. For example, for a cubic or almost cubic unit cell the reciprocal unit cell is also cubic and we can consider same number of k-points along each k-space unit vector $\mathbf{b}_i$. If N number of k-points are considered along each direction then the calculation is leveled as $N \times N \times N$ k points calculation. To test the convergence, the way is to increase the value of N till there is no significant variation in the total energy with any further change in N. Figure 2.2 shows the convergence of the total energy(using DFT as implemented in VASP) of ZnS zinc-blend structure as a function of N. GGA was considered for exchange-correlation functional with a converged E_{cut} value of 300 eV.

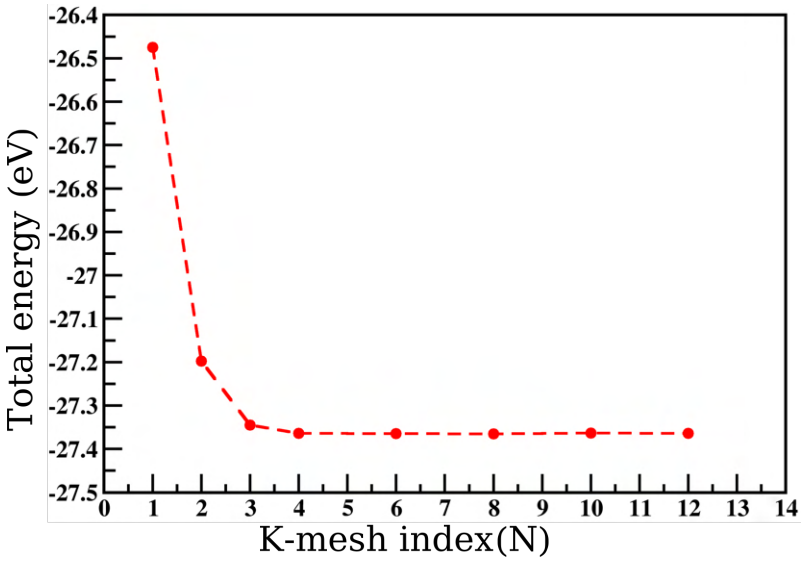

FIGURE 2.2: Total energy of Zns-ZB structure as a function of N implying a $N \times N \times N$ k points calculation

Changing the value of N from 7 to 8, the total energy change per atom is less than 1 meV. Hence we can use $7 \times 7 \times 7$ or $8 \times 8 \times 8$ k-points grid in the above calculation for a well converged result.

3.3 Frozen core approximation and Pseudopotential :

In any real material the electrons of the atoms that are chemically important are the valence electrons because they take part in bonding. The core electrons that are tightly attached to the nucleus remain more or less inert. Also the kinetic energy of the core electrons are much higher than the valence electrons and their wave function are highly oscillating on short length scale. As a result we need large energy cutoff value for a plane wave basis set to represent them. So, if we are able to approximate the properties of the core electrons then we can reduce the computation cost by reducing the number of plane waves in the basis set.

The popular approach to treat the core electrons is to use pseudopotentials. A pseudopotential replaces the electron density from the core electrons with a smoothed density chosen to match various important physical and mathematical properties of the true ion core. This is the frozen core approximation. In this approximation, if $|\psi^c\rangle$ and $|\psi^v\rangle$ represent the quantum states for core electrons and the valence electrons respectively then one can construct smooth valence states $|\phi^v\rangle$ orthogonal to $|\psi^c\rangle$ as[36],

$$|\phi^v\rangle = |\psi^v\rangle + \sum_c \alpha_c \psi^c(\mathbf{r}) \tag{2.65}$$

where α_c can be determined from the orthogonality condition $\alpha_c = \langle\psi^c|\phi^v\rangle$. The pseudo wave functions satisfies the modified Schrödinger equation:

$$\left[H + \sum_c (\epsilon^v - \epsilon^c)|\psi^c\rangle\langle\psi^c|\right]|\phi^v\rangle = \epsilon^v|\phi^v\rangle \tag{2.66}$$

So, we can construct a Pseudo-Hamiltonian,

$$H^{PH} = \left[H + \sum_c (\epsilon^v - \epsilon^c)|\psi^c\rangle\langle\psi^c|\right] \tag{2.67}$$

with the same eigenvalues as the original Hamiltonian H, but with a smoother wave function. The corresponding potential,

$$V^{PP} = V + \sum_{c} (\epsilon^{v} - \epsilon^{c}) |\psi^{c}\rangle\langle\psi^{c}| \tag{2.68}$$

is called pseudo-potential, where V is the nuclear potential in H. The second term is a correction term and repulsive in nature as $\epsilon^{v} > \epsilon^{c}$, indicating that the valence electrons experience a net repulsive force due to the core electrons. Figure 2.3 schematically illustrates the pseudo-potential approach. Beyond the core region i.e. above a cutoff radius, r_c pseudo-wavefunctions and pseudo-potentials are identical to the all electron wave functions and potential respectively, while in the core region (within r_c), a weaker potential will be experienced by this new set of valence states.

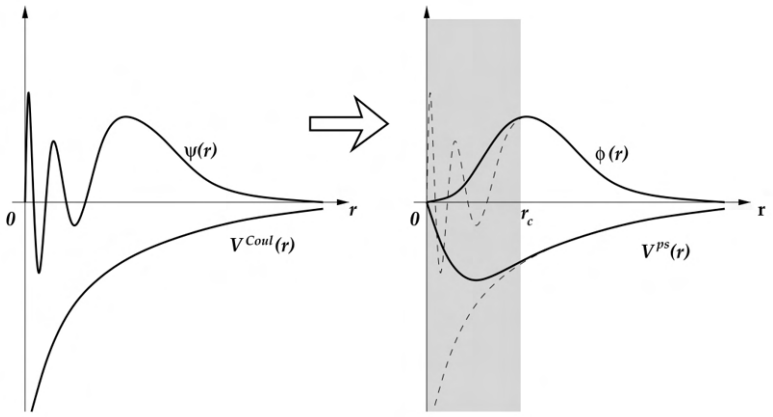

FIGURE 2.3: Schematic diagram of the Pseudopotential $V^{PS}(r)$ and pseudo-wavefunction $\phi(r)$. The left figure shows valence wave function $\psi(r)$ and Coulomb potential $V^{Coul}(r)$. In the right figure, r_c represents the cutoff radius beyond which the wave function and the potential are not affected.(Taken from, Atomic and Electronic Structure of Solids, E Kaxiras, Cambridge University Press[37])

In DFT calculations any pseudopotential for an atom define a minimum cutoff energy that should be used. Pseudopotentials requiring high cutoff energies are said to be hard, while pseudopotentials with low cutoff energies are called soft, which are computationally efficient. There are also ultrasoft pseudopotential(USPP)[38] that require very low cutoff energy.

3.4 Projector Augmented Wave(PAW) method :

One disadvantage of using USPPs is that the construction of the pseudopotential for each atom requires a number of empirical parameters to be specified. Current DFT codes typically only include USPPs that have been carefully developed and tested, but they do in some cases include multiple USPPs with varying degrees of softness for some elements[14]. Another frozen core approach that avoids some of the disadvantages of USPPs is the projector augmented-wave(PAW) method originally introduced by Blöchl[39] and later adapted for plane-wave calculations by Kresse and Joubert[40]. In such approximation, an all electron wave function is constructed, with which all integrals are calculated as a combination of smooth functions extending throughout space and contribution from the localized muffin tin orbitals[41, 42]. Hence the total wave function in this case is a combination of valence state wave functions $\tilde{\psi}_i^v(\mathbf{r})$ and a linear transformation function relating the all-electron valence functions $\psi_j^v(\mathbf{r})$ to $\tilde{\psi}_i^v(\mathbf{r})$ which is given as,

$$\psi_j^v(\mathbf{r}) = \tilde{\psi}_j^v(\mathbf{r}) + \sum_i (|\phi_i\rangle - |\tilde{\phi}_i\rangle)\langle\tilde{p}_i|\tilde{\phi}_i\rangle \tag{2.69}$$

In the above equation, index i is for the atomic site $\mathbf{R}$, $|\tilde{p}_i\rangle$ are the projector functions for localized pseudo partial wave which satisfy the orthogonality condition, $\langle\tilde{p}_i|\tilde{\phi}_j\rangle = \delta_{i,j}$. Within this formalism, the all electron charge density can be derived from Equation (2.69) as,

$$n(\mathbf{r}) = \tilde{n}(\mathbf{r}) + n^1(\mathbf{r}) - \tilde{n}^1(\mathbf{r}), \tag{2.70}$$

where,

$$\tilde{n}(\mathbf{r}) = \sum_i f_i |\tilde{\psi}_i(\mathbf{r})|^2 \tag{2.71}$$

$$n^1(\mathbf{r}) = \sum_i f_i \sum_{j,k} \langle\tilde{\psi}_i|\tilde{p}_j\rangle \phi_j(\mathbf{r})\phi_k(\mathbf{r})\langle\tilde{p}_k|\tilde{\psi}_i\rangle \tag{2.72}$$

$$\tilde{n}^1(\mathbf{r}) = \sum_i f_i \sum_{j,k} \langle\tilde{\psi}_i|\tilde{p}_j\rangle \tilde{\phi}_j(\mathbf{r})\tilde{\phi}_k(\mathbf{r})\langle\tilde{p}_k|\tilde{\psi}_i\rangle \tag{2.73}$$

In the above expressions, f_i's represent the occupancies of the eigenstates $\tilde{\psi}_i$, $\tilde{n}(\mathbf{r})$ is the pseudo-charge density and is evaluated from the pseudo-wavefunctions with plane wave basis. $n^1(\mathbf{r})$ and $\tilde{n}^1(\mathbf{r})$ are the on-site charge densities localized within the augmented sphere around each atom. Total energy of the system when calculated from these charge densities can also be divided into three parts.

4 Crystal Orbital Hamilton Populations(COHP)

The synergy between theoretical chemistry and physics is thriving when it comes to investigating the properties of solid-state materials. In the 21st century, ab initio calculations not only ensure a comprehensive grasp of existing phenomena but also play a pivotal role in predicting novel materials with great potential. However, a central goal of chemical theory has always been the pursuit of straightforward yet potent models that can be readily visualized, and such models are especially valuable when dealing with complex, three-dimensional structures such as crystals. In this context, expressing quantum-mechanical information in reciprocal space often presents a significant challenge for both chemical intuition and imaginative thinking.

To address these challenges within the framework of density-functional theory (DFT), the crystal orbital Hamilton population (COHP) analysis was introduced in 1993, serving as a DFT successor to the well-known crystal orbital overlap population (COOP) concept based on extended Hückel theory. The COHP method partitions the band-structure energy into orbital-pair contributions and relies on a localized basis, commonly used in both chemistry and parts of physics. By quantifying the interaction between two orbitals centered on neighboring atoms through the Hamiltonian matrix element $H_{\mu v} = \left\langle \phi_\mu | \hat{H} | \phi_\nu \right\rangle$, it uses the product of this element with the corresponding densities-of-states matrix as a precise measure of bonding strength. Energy-resolved COHP(E) plots have proven to be a valuable tool for differentiating bonding, nonbonding (representing no energetic effect), and antibonding contributions, much like their COOP(E) plot counterparts. This COHP

analysis has effectively addressed various inquiries and even enabled the generation of practical forecasts within the realm of chemistry, using the language of local, atom-centered orbitals and the underlying density-functional theory. In contrast, the field of physics has charted alternative avenues in its exploration of periodic systems. Bloch's theorem has guided these distinct approaches, advocating a unique treatment of periodic systems. In this framework, crystal wave functions are readily constructed using plane waves, which offer an orthonormal basis and, in principle, a comprehensive depiction of the Hilbert space. Plane waves, although a natural choice for describing crystalline systems from a mathematical standpoint, remain fundamentally nonchemical. The cost of employing plane waves becomes evident when considering that the atomic characteristics of the material are obscured within the plane-wave expansion, and even the atom's nodal structure is entirely eliminated using numerically tractable pseudopotential methods. Currently, there is an abundance of electronic-structure codes designed around plane-wave methodologies, solidifying their position as the preferred approach for conducting swift yet reliable theoretical research in materials science. Despite the dominance of plane-wave calculations in materials science, efforts have been made to incorporate chemical insights into these nonchemical computational approaches. One notable attempt in this direction dates back to 1995 when Sánchez-Portal and colleagues introduced a projection technique. This method allowed for the study of various solids and bore some resemblance to the approach presented in this study. Interestingly, while techniques for reconstructing local quantities such as Mulliken charges from plane-wave results have been explored, no public efforts have been made thus far to formulate a COHP-like quantity within the context of plane-wave calculations. The existence of such a method would offer valuable chemical models, ensuring that insightful chemical interpretations remain accessible even when utilizing state-of-the-art plane-wave codes.

4.1 Projected Crystal Orbital Hamilton Populations

Let us assume we have achieved a successful self-consistent electronic structure calculation employing a fine-meshed k-point set in reciprocal space, as required by Bloch's theorem. Consequently, we obtain the band functions denoted as $\psi_j(\mathbf{k}, \mathbf{r})$, where j represents the band number. Each specific band function can be expressed as follows:

$$\psi_j(\mathbf{k}, \mathbf{r}) = \sum_{\mathbf{G}} C_{j\mathbf{G}}(\mathbf{k}) \exp\{\mathbf{i}(\mathbf{k} + \mathbf{G}) \cdot \mathbf{r}\} \tag{2.74}$$

At first glance, these band functions may appear as mathematical constructs – essentially a linear combination of plane waves utilizing reciprocal lattice vectors G and expansion coefficients $C_{j\mathbf{G}}(\mathbf{k})$. However, it's important to note that such an expansion effectively describes the electronic structure of the system with a level of accuracy similar to what could have been achieved using a linear combination of atomic orbitals (LCAO). In essence, the LCAO wave functions and the band functions $\psi_j(\mathbf{k}, \mathbf{r})$ bear a close resemblance to each other, despite their fundamentally different origins. We can express a k-dependent LCAO function $\Phi_j(\mathbf{k}, \mathbf{r})$ for the jth band by combining atom-centered and orthonormal one-electron functions (orbitals) $\phi_\mu(\mathbf{r})$ with coefficients $c_{j\mu}(\mathbf{k})$:

$$\Phi_j(\mathbf{k}, \mathbf{r}) = c_{j\mu}(\mathbf{k})\phi_\mu(\mathbf{r}) + c_{j\nu}(\mathbf{k})\phi_\nu(\mathbf{r}) + \ldots \approx \psi_j(\mathbf{k}, \mathbf{r}) \tag{2.75}$$

In Figure 2.4, we observe that the band function $|\psi_j\rangle$, which was obtained through a periodic plane-wave calculation for carbon monoxide (CO), resembles the 3σ molecular orbital and is primarily composed of a carbon 2s atomic orbital. Consequently, there is a significant overlap between the band function and a local, genuine s orbital $|\phi_1\rangle$ due to symmetry, while the overlap with a p orbital $|\phi_2\rangle$ is exactly zero because they are perpendicular to each other. It's important to emphasize that the choice of localized orbitals $|\phi_\mu\rangle$ is essentially arbitrary, or more positively, a matter of chemical preference. This flexibility allows us to use any basis set that suits our specific chemical inquiry. For instance, one could opt for orbitals of the well-known Slater type. Nevertheless, we still

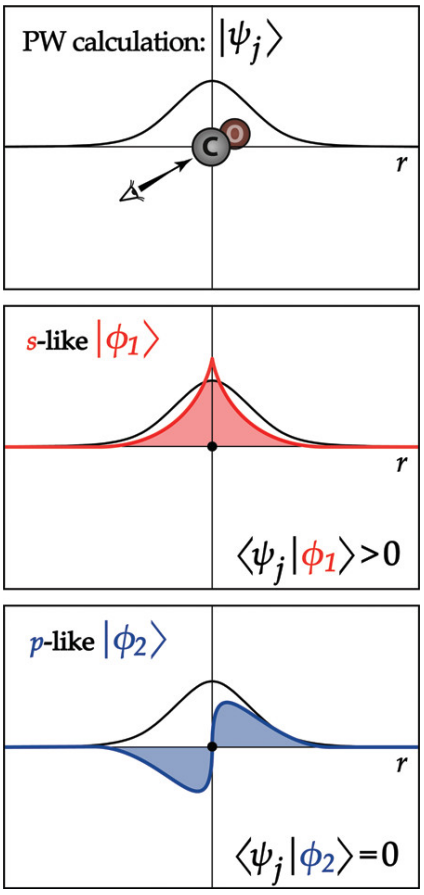

FIGURE 2.4: Schematic illustration of the projection technique from band function $|\psi_j\rangle$, taken from a periodic VASP calculation of the CO molecule, to local orbital $|\phi_\mu\rangle$. The band function (drawn in black, top) resembles a carbon 2s orbital and overlaps with the s-like local function $|\phi_1\rangle$ (middle). Its overlap with the p-like function $|\phi_2\rangle$, however, is zero due to orthogonality (bottom).

need a way to quantify how effectively any basis set can replicate the plane-wave band functions $|\psi_j\rangle$(k). To achieve this, we calculate the overlap matrix between the band functions and the local orbitals $||\phi_\mu\rangle\rangle$. For reasons that will become clear later on, we refer to this matrix as the "transfer matrix" $\mathbf{T}(\mathbf{k})$, and its elements are defined as:

$$T_{j\mu}(\mathbf{k}) = \langle\psi_j(\mathbf{k}) \mid \phi_\mu\rangle \tag{2.76}$$

In the LCAO framework, we obtain chemical insights directly from the atomic orbital coefficients c. By multiplying two coefficients, c_μ and c_ν, we can determine the density-matrix element $P_{\mu\nu}$. Likewise, in the context of plane waves, equivalent information is

encoded within the transfer matrix. Consequently, we have the ability to calculate a projected density matrix, denoted as P$^(proj)$, for each band j and each k-point. The elements of this projected density matrix are given by the equation:

$$P_{\mu vj}^{(\mathrm{proj})}(\mathbf{k}) = T_{j\mu}^{*}(\mathbf{k}) T_{jv}(\mathbf{k}) \tag{2.77}$$

To establish a COHP-like method, we must obtain the Hamiltonian matrix elements $H_{\mu\nu}(\mathbf{k})$ within the basis of the local functions. We accomplish this using the approach described in reference 9. The plane-wave Hamiltonian $\hat{H}^{(\mathrm{PW})}$, expanded within the context of a complete basis, can be expressed as follows:

$$\begin{aligned} H_{\mu\nu}^{(\mathrm{proj})}(\mathbf{k}) &= \left\langle \phi_\mu \left| \hat{H}^{(\mathrm{PW})} \right| \phi_v \right\rangle \\ &= \sum_j \langle \phi_\mu \mid \psi_j(\mathbf{k}) \rangle \, \varepsilon_j(\mathbf{k}) \, \langle \psi_j(\mathbf{k}) \mid \phi_v \rangle \end{aligned} \tag{2.78}$$

which is simply

$$H_{\mu\nu}^{(\mathrm{proj})}(\mathbf{k}) = \sum \varepsilon_j(\mathbf{k}) T_{j\mu}^{*}(\mathbf{k}) T_{j\nu}(\mathbf{k}) \tag{2.79}$$

With both matrices now transformed from a plane-wave to an orbital representation, we are able to construct an analogue to the conventional COHP, which we will refer to as the "projected crystal orbital Hamilton population" (pCOHP) going forward:

$$\begin{aligned} \mathrm{pCOHP}_{\mu v}(E, \mathbf{k}) = &\sum_j R \left[P_{\mu vj}^{(\mathrm{proj})}(\mathbf{k}) H_{v\mu}^{(\mathrm{proj})}(\mathbf{k}) \right] \\ &\times \delta \left(\varepsilon_j(\mathbf{k}) - E \right) \end{aligned} \tag{2.80}$$

The expression above is energy-dependent due to the presence of a delta function, ensuring that the density matrix has non-zero entries only at specific band energies $\varepsilon_j(\mathbf{k})$. In other words, the density matrix has been transformed into a density-of-states matrix. To obtain the real-space pCOHP(E), a summation over all orbitals μ (centered at the first

atom involved in the bond) and ν (at the second atom) is carried out, followed by a subsequent integration over k-space. This integration is most efficiently performed using the tetrahedron method, which was initially proposed by Andersen and later improved by Blochl.

5 Ab initio Molecular Dynamics (AIMD)

Ab initio molecular dynamics (AIMD) is a computational technique that combines the principles of quantum mechanics and classical molecular dynamics to simulate the time evolution of atoms and molecules within a material or chemical system. Unlike classical molecular dynamics, which relies on empirical force fields, AIMD starts from first principles, using quantum mechanical methods to calculate the forces acting on the nuclei of atoms. This approach provides a more accurate description of electronic structure and allows researchers to explore a wide range of phenomena at the atomic and molecular scale.

References

[1] D. J. Griffiths, Introduction to Quantum Mechanics, 2nd Ed. Prentice Hall, 2005.

[2] G. Kresse and J. Hafner, Phys. Rev. B **47**, 558 (1993) ; G. Kresse and J. Hafner, Phys. Rev. B **49**, 14251 (1994); G. Kresse and J. Furthmüller, Phys. Rev. B **54**, 11169 (1996).

[3] G. Kresse and J. Furthmüller, Comput. Mater. Sci., **6**, 15 (1996).

[4] K. Umemoto, R. M. Wentzcovitch, and P. B. Allen, Science **311**, 983 (2006).

[5] F. Blöch, Z. Physik **52**, 555 (1928).

[6] G. H. Wannier, Physical Review **52**, 191 (1937).

[7] W. Kohn, Physical Review **115**, 809 (1959).

[8] J. des Cloizeaux, Physical Review **129**, 554 (1963).

[9] N. Marzari, A. A. Mostofi, J. R. Yates, I. Souza, and D. Vanderbilt, Rev. Mod. Phys. **84**, 1419 (2012).

[10] A. A. Mostofi, J. R. Yates, Y.-S. Lee, I. Souza, D. Vanderbilt, and N. Marzari, Comput. Phys. Comm. **178**, 685 (2008).

[11] N. Marzari and D. Vanderbilt, Phys. Rev. B **56**, 12847 (1997).

[12] I. Souza, N. Marzari and D. Vanderbilt, Phys. Rev. B **65**, 035109 (2001).

[13] M. Born and J. R. Oppenheimer, Zur Quantentheorie der Molekeln, Ann. Physik 84, 457(1927).

[14] D. S. Sholl and J. A. Steckel, Density Functional Theory: A Practical Introduction(Wiley-Interscience) (2009).

[15] D. R. Hartree, The wave mechanics of an atom with non-Coulombic central field: Parts I, II, III. Proc. Cambridge Phil. Soc. 24, 89, 111, 426(1928).

[16] J. C. Slater, Phys. Rev. **34**, 1293 (1929).

[17] V. Fock, Naherungsmethode zur Losung des quanten-mechanischen Mehrkorperprobleme, Z. Phys. 61, 126(1930).

[18] G. Arfken, Mathematical Methods for Physicists. 3rd Edition, Academic Press, NY (1985).

[19] L. H. Thomas, Proc. Cambridge Philos. Soc. **23**, 542 (1927).

[20] E. Fermi, Atti Accad. Naz. Lincei, Cl. Sci. Fis. Mat. Nat. Rend. **6**, 602 (1927).

[21] W. Kohn, Rev. Mod. Phys. **71**, 1253 (1999).

[22] P. Hohenberg and W. Kohn, Phys. Rev. **136**, B864 (1964).

[23] W. Kohn and L. J. Sham, Phys. Rev. **140**, A1133 (1965).

[24] J. P. Perdew, K. Burke, and Y. Wang, Phys. Rev. B **54**, 16533 (1996).

[25] P. A. M. Dirac, Proc. Cambridge Phil. Roy. Soc. **26**, 376 (1930).

[26] M. Gell-Mann and K. A. Brueckner, Phys. Rev. **106**, 364 (1957).

[27] W. J. Carr and A. A. Maradudin, Phys. Rev. **133**, A371 (1964).

[28] E. Wigner, Phys. Rev. **46**, 1002 (1934).

[29] J. P. Perdew, Phys. Rev. Lett. **55**, 2370 (1985).

[30] J. P. Perdew and Y. Wang, Phys. Rev. B **45**, 13244 (1992).

[31] A. D. Becke, Phys. Rev. A **38**, 3098 (1988); C. Lee, W. Yang, R. G. Parr, Phys Rev. B **37**, 785 (1988); A. D. Becke, J. Chem. Phys. **96** 2155 (1992).

[32] J. P. Perdew, K. Burke, and M. Ernzerhof, Phys. Rev. Lett. **77**, 3865 (1996).

[33] J. Tao, J. P. Perdew, V. N. Staroverov, and G. E. Scuseria, Phys. Rev. Lett. **91**, 146401 (2003).

[34] J. Heyd, G. E. Scuseria, and M. Ernzerhof, J. Chem. Phys. **118**, 8207 (2003).

[35] Hendrik J. Monkhorst and James D. Pack, Phys. Rev. B **13**, 5188 (1976).

[36] James C. Phillips and Leonard Kleinman, Phys. Rev. **116**, 287 (1959).

[37] E. Kaxiras, Atomic and Electronic Structure of Solids, Cambridge University Press, UK,(2003).

[38] D. Vanderbilt, Phys. Rev. B. **41**, 8412 (1990).

[39] P.E. Blöchl, Phys. Rev. B **50**, 17953 (1994).

[40] G. Kresse, and J. Joubert, Phys. Rev. B textbf59, 1758 (1999).

[41] O. K. Andersen and R. V. Kasowski, Phys. Rev. B **4**, 1064 (1971).

[42] O. K. Andersen, 1971, Computational Methods in Band Theory, p. 178, edited by P. M. Marcus, J. F. Janak and A. R. Williams (Plenum Press).

Chapter 3

Structural Distortions in Hybrid Perovskites Revisited

1 Introduction

The structure plays an important role in determining the ensuing properties of a compound. Therefore an understanding of the microscopic considerations that favour a particular structure is essential to control its properties[4, 38, 60]. The perovskite structure is found in a wide range of crystalline materials with the chemical formula ABX_3, where A and B are usually two different cations and X is an anion[34, 47, 58]. This leads to the corner-sharing (BX_6) octahedral units while the A cations are positioned in the cuboctahedral (12-fold) sites between the octahedra[17]. Certain empirical considerations have emerged to determine if a system would occur in the perovskite structure. One such empirical parameter has been the tolerance factor[15]. This is a quantity which depends on the ionic radii of the atoms involved and one usually finds cubic perovskites to be favoured for tolerance factors close to 1, while smaller values upto 0.80 arising from a smaller A cation or larger B cation, predominantly, lead to distorted perovskites with octahedral tilting[14, 21, 43]. Outside this range, one finds that the three dimensional perovskite structure is no longer stable.

Recently, in contrast to traditional perovskites, which are based on inorganic atoms, there has been a lot of focus on hybrid perovskites as a consequence of their successful use in solar cells as well as their remarkable optoelectronic properties[20, 33, 54, 62]. These systems have an organic molecule at the A-site of the perovskite, and one has to move beyond the understanding that existed for the inorganic perovskites to understand the structural distortions found here[29, 37]. This was not merely associated with the definition of an ionic radii for a non-spherical object like a molecule, but new concepts needed to be considered to understand the nature of the distortions. Jang et al. [30] showed that the hydrogens associated with the molecule formed hydrogen bonds with the anions of the inorganic cage. This interaction, they concluded, led to the observed structural distortions. Sagar and Mahadevan [51] extended these ideas and showed that an asymmetric molecule at the A-site led to an increased hopping interaction of the hydrogens attached to one end of the molecule with the inorganic cage, usually the anions. This led to the molecule moving towards one end of the inorganic cage, thereby also contributing to the dipole moment associated with the structure. This increased interaction also led to the anions moving towards the hydrogens, thereby resulting in the octahedral tilts.

In this work we extend these ideas further by considering all possible molecules at the A site which lead to three dimensional perovskite structures. Certain generic features emerge. We first considered a molecule that has the same functional group on either end, and asked the question whether a symmetric molecule would lead to the absence of octahedral tilts, and hence a cubic perovskite structure. This would then imply that the symmetry of the molecule would become an additional parameter determining the presence or absence of structural distortions. Indeed the Pb-Cl-Pb bond angles in $FAPbCl_3$ are found to be near 180° in the plane parallel to the C_2 symmetry axis of the molecule. However, other factors come into play while determining the structural distortions for other three-dimensional hybrid perovskites, which is the orientation of the molecule in the cage. This is determined by the number of bonds that the hydrogens can form with the anions, and so two symmetric molecules may favour very different orientations.

Further in contrast to the inorganic perovskites where one finds structural changes across a series (when only the A site was varied) could be well described by the tolerance factor, here, such a monotonic evolution of structural properties with tolerance factor would no longer be valid.

In order to examine this aspect, we have considered two limiting cases, a symmetric molecule (formamidinium) and two asymmetric molecules (methylammonium and ethylammonium) in which we examine the structural distortions that take place. One finds that the shape of the molecule determines the extent of hydrogen bonding with the anions, and thereby determines the octahedral tilts. In case of an asymmetric molecule, methylammonium (MA), the presence of two different groups at its two ends leads to dissimilar bonding with the inorganic cage. Not only does this lead to an off-centering of the molecule, the anions which are a part of the inorganic network also move towards the hydrogen, with the Pb-X-Pb angles deviating significantly from 180°. For ethylammonium (EA) which is a larger molecule than MA and is more asymmetric, having a larger alkyl group, Pb-X-Pb bond angles in the bc plane (plane parallel to Molecular C-N bond) remain almost unchanged but the bond angles in the ac plane (plane parpendicular to molecular C-N bond) are found to have increased when one goes from MA to EA, keeping the anion fixed. The results were contrasted with a symmetric molecule formamidinium (FA), which has the same functional group on both sides of a central carbon atom, in addition to having its size in between MA and EA. Here, for the Cl based compound, one finds that the centre of the molecule lies at the centre of the ac plane. The Pb-X-Pb angles parallel to the plane of symmetry of the molecule are not distorted significantly but the Pb-X-Pb angles in the plane perpendicular to the plane of symmetry of the molecule show significant distortions. However, for the Br based compound, one finds that while the molecule is not displaced towards any anion in the plane of the molecule, the Pb-Br-Pb angles deviate significantly from near ideal values because steric repulsion between electrons on the Br atom and the hydrogens leads to deviations of the Pb-Br-Pb angles. These results suggest that for hybrid perovskites, apart from the size, the shape of the A-site cation plays an important role in the structural distortions.

The off-centering of the methyl-ammonium molecule happens at the cost of a reduction in the number of hydrogen bonds formed with the anions. In the absence of the off-centering, one would have six bonds between the hydrogens and the anions. The more localized Cl atoms, prevent the hydrogens from coming too close due to steric effects. This leads to two short bonds formed between H and the Cl atoms present in the ac plane and a slightly longer bond with the Cl atom towards which the molecule moves (ab plane). However, in the case where we have the more delocalized Br atoms as the anion, we find that a shorter hydrogen bond is formed with the bromine towards which the molecule moves (bc plane), while the Br atoms in the ac plane form longer hydrogen bonds. Hence these results give insights into the bond strength of the hydrogen-anion network, which could be key in trying to understand the dynamics of the molecule.

2 Methodology

Using first-principles density functional theory (DFT) calculations we investigate the electronic structure of the compounds $APbX_3$ (where A= MA, EA, FA, DMA and HAZ and X = Br and Cl). Here MA, EA, FA, DMA and HAZ denotes Methylammonium, Ethylammonium, Formamidinium, Dimethylammonium and Hydrazinium respectively. The orthorhombic unit cell was used for all the structures. $FAPbCl_3$[16] has a space group symmetry CmCm . In the case of $FAPbBr_3$ we have considered two sets of experimentally reported crystal structures of $FAPbBr_3$ at low temperature [16], trigonal (space group R-3) and orthorhombic (space group CmCm). These have been optimized within our calculations and the lower energy orthorhombic structure is discussed in the rest of the manuscript. The crystal structure of $MAPbX_3$[5], $EAPbX_3$[39], $DMAPbX_3$[50] and $HAZPbX_3$[50] (X = Br and Cl) of space group symmetry Pnma have been considered.

The optimized lattice parameter of the structures ($\sim$ 1% smaller on average than the experimental values) are tabulated below (Table **??**).

TABLE 3.1: The optimized lattice parameters and Effective ionic radii of molecular cations[50] of $APbX_3$ (where A= MA,EA,FA, DMA and HAZ and X = Br,Cl).

Compound	a(Å)	b(Å)	c(Å)	Effective ionic radii of the molecule(Å)
$MAPbCl_3$	7.526	11.397	8.355	2.17
$EAPbCl_3$	7.911	11.447	8.473	2.74
$FAPbCl_3$	8.793	7.369	11.429	2.53
$DMAPbCl_3$	5.848	5.787	11.574	2.72
$HAZPbCl_3$	5.731	11.080	5.620	2.17
$MAPbBr_3$	7.975	11.840	8.564	2.17
$EAPbBr_3$	8.045	11.936	8.633	2.74
$FAPbBr_3$	9.173	7.691	11.919	2.53
$DMAPbBr_3$	6.088	6.028	12.164	2.72
$HAZPbBr_3$	5.995	11.632	5.893	2.17

The DFT calculations were performed using the generalized gradient approximation (GGA) [44] for the exchange correlation functional and projector augmented wave (PAW) [6, 26] potentials for the ionic part, as implemented in the Vienna ab initio Simulation Package (VASP) [22–25]. During relaxation, corrections for the nonlocal, weak van der Waals dispersion interaction [13, 30, 57] (optB86b-vdW) [19, 20] were included. A gamma-centered Monkhorst-Pack k mesh [35] of $8 \times 6 \times 8$ was used to perform the k-space integrations. In addition to this, an energy cut-off of 400 eV was used for the kinetic energy of the plane waves included in the basis and the internal positions were optimized until the forces on the atoms were less than $10^{-3} eV/\text{Å}$ to find the minimum energy structure. Bader charges of all the compounds mentioned above have been calculated using Bader Charge Analysis Code[19, 49, 55, 61]. In order to perform the Crystal Orbital Hamilton Population (COHP) analyses, we used the wave function obtained from the DFT calculations. With the crystal orbital expansion coefficients, the COHP analysis decomposes the DOS into bonding and antibonding interactions for a specific pair of atoms within the LOBSTER code [7, 8, 35, 36, 45]. ICOHP is calculated by integrating the projected COHP up to the highest occupied orbital. This provides a measure of covalent bond strength of a particular bond. However one should mention that ICOHP is not equal to the bond energy. It provides a resonable estimate in this regards.

All schematic representations of the crystal structures were generated using the VESTA program[34].

3 Results and discussion

Considering the most extensively studied member of these series, Methylammonium lead halide ($CH_3NH_3PbX_3$), it was shown that it undergoes a series of temperature dependent structural phase transitions with an increased degree of octahedral tilting as the temperature decreases[1, 32, 57] . At low temperature, by symmetry lowering, the system enters an orthorhombic phase due to octahedral rotations about all the pseudo cubic directions with all Pb-X-Pb bond angles deviating from 180°[59]. The octahedral rotations were attributed to the hydrogen bonding of the molecule with the anions of the cage[30]. This interaction led to the hydrogen atoms moving towards the anions and vice-versa[51]. This has been the explanation for the octahedral tilts that one finds in these systems. Subsequently, it was shown that an asymmetric molecule like methylammonium has stronger covalent interactions for the ammonium end of the molecule with the anions, than the methyl end of the molecule. Although both ends of the molecule have three hydrogens attached, from a Bader charge analysis we found that the hydrogen associated with the nitrogen atom is more positive (0.48e) than the hydrogen attached to the carbon (0.11e). This leads to stronger Coulomb attraction between the positively charged hydrogen atoms on the amine side with the anions, resulting in shorter bonds compared to those formed by the hydrogens that are a part of the methyl group. As a result of these interactions, the molecule moves away from the centre of the inorganic cage that it is located in. These ideas can be clearly seen by examining the H-Cl bond lengths shown in Fig.3.1. With the molecule at the centre of the cage, one finds the bond lengths to be 2.43Å, 2.40Å and 2.79Å, while the off-centering measured with respect to the centre of the network formed by the Pb atoms is 0.242Å (in the ac plane). This leads to the hydrogen at the ammonium end of the molecule having bond lengths of 2.26Å, 2.26Å and 2.34Å with the anions. This

also leads to the Pb-X-Pb angle becoming 156.4°, 156.4° and 167.5° respectively. So all the Pb-X-Pb bond angles of the unit cell are found to deviate significantly from 180°.

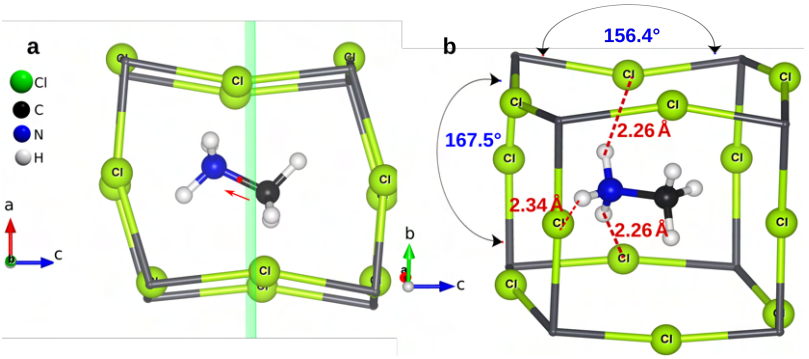

FIGURE 3.1: (a) Off-centering of the molecule (red arrow) from the geometric centre of the cage formed by Pb atoms. The solid green line passes through the centre of the Pb cage. (b) Shortest bonds (red dotted line) made by the anion (Cl) and hydrogen of the MA molecule and bond angles of MAPbCl_3.

We then considered the example of a symmetric molecule like formamidinium (-NH2- CH - NH2-) at the A-site of the perovskite. Formamidinium has two amine groups on either side of the central carbon atom. The question we asked was how the structural distortions would develop in this case. In order to examine these aspects, we place the molecule in the inorganic cage formed by Pb and X atoms. Carrying out a structural optimization of the internal positions, we find that the Pb-X-Pb angles are around 176.80° for the planes that are perpendicular to the ab plane which contains the molecule, while, on the other hand, in the plane parallel to the ab plane we see larger distortions of Pb-X-Pb angles (Fig 3.2). In contrast to the case of methylammonium at the A site, formamidinium is a symmetric molecule. The hydrogens attached to the amine groups at both ends have a bader charge of 0.49e, so both ends of the molecule are equally attracted to the chlorine atoms that form a part of the inorganic cage. Consequently, the molecule stays at the centre of the cage with the bond distances between the hydrogens and chlorine atoms found to be 2.38Å and 2.39Å. These are larger than what we have for $MAPbX_3$, indicating a weaker interaction here. This is consistent with the observation of rotational dynamics of the FA ion seen even in the orthorhombic phase for a related compound[53].

However, examining the plane parallel to the ab plane , we find that the molecule has no

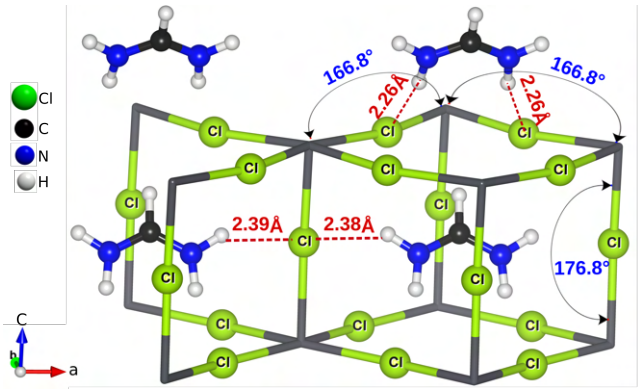

FIGURE 3.2: Shortest bonds (red dotted line) made by the anion (Cl) and hydrogen of the FA molecule and bond angles of FAPbCl_3.

inversion symmetry about that plane. This leads to a displacement of the molecule, with the hydrogens (H_N) forming a bond of length 2.26Å. The off-centering of the molecule is found to be 0.081Å(ab plane) which is measured with respect to the centre of the Pb cage. The displacements also lead to a distortion of the Pb-X-Pb angle which is now found to be 166.80° (Fig 3.2). On the other hand for $FAPbBr_3$ in its ground state trigonal structure, the molecule is rotated inside the inorganic cage but the structural distortions do not follow any trends discussed previously.

Now examining the other molecules that form three dimensional structures, one finds that they have different orientations inside the inorganic cage. This led to the next question, which was to determine the factors that led to the favored orientation. If steric repulsions were the dominant interactions between the cage and the molecule, one would have the molecule to be oriented diagonally inside the inorganic cage. However, considering the case of $FAPbCl_3$ the most stable structure is 257 meV lower when the molecule is in 110 plane than when it is in 111 plane i.e placed diagonally inside the cage. On the other hand for $DMAPbCl_3$ (where, DMA = Dimethylammonium $[(CH_3)_2NH_2]$) the ground state structure is 461 meV lower when the molecule is placed diagonally in the 111 plane than in the 110 plane. While in both cases one has the hydrogens attached to the molecule interacting with the anions, a decomposition of the charge around each atom into Bader charges suggests that the H_N and H_C are different. This arises from the significant electronegativity difference of the atoms that they are attached to. Hydrogen attached to

the nitrogen is more positive (+0.48e), than the hydrogen attached to the carbon (+0.10e). This allows them to come closer to the anion, forming shorter bonds, which are primarily electrostatic in nature. The horizontal orientation of the molecule in $FAPbX_3$, $MAPbX_3$ and $EAPbX_3$ systems allows more bonds to be formed, compared to any other orientation. However, $DMAPbX_3$ which has H_C atoms at two ends interacting with the anions, cannot come too close to them, and therefore sits diagonally inside the cage (Fig 3.3), minimizing its H_N bondlengths.

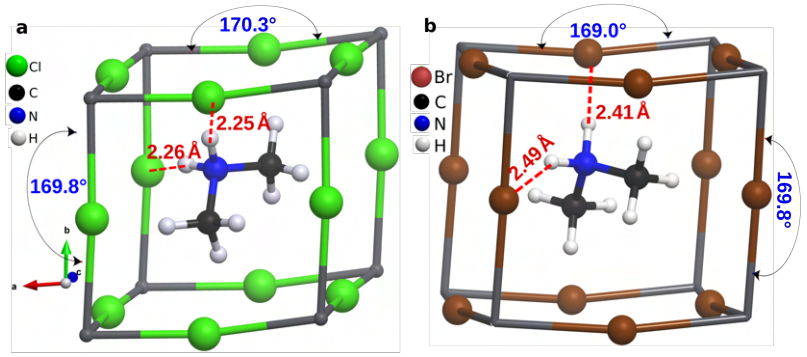

FIGURE 3.3: Shortest bonds (red dotted line) made by the anion (Br/Cl) and hydrogen of the (a) $DMAPbCl_3$ and (b) $DMAPbBr_3$ Compound and bond angles of the respective structures.

On the other hand for the molecule Hydrazinium $[H_3N - NH_2]$ which contains an NH_3 and an NH_2 group at its two ends, one finds that the three hydrogens attached to the NH_3 group form shorter bonds. The resulting orientation leads to a significant deviation of the Pb-X-Pb bondangles (159.2° and 162.9° for the chlorine compound and 158.9° and 162.8° for its bromine counterpart)(Fig 3.4)

The next aspect we examined was the definition of tolerance factor for these materials. In the case of inorganic compounds, this was a useful concept that helped one determine if the perovskite of the form ABO_3 would have a rotation of its BO_6 motifs, so that B-O-B angles would deviate from their values of 180° found at the ideal perovskite limit. This operation also reduces the symmetry from cubic. One usually finds cubic perovskites for tolerance factors in the range 0.9 - 1.0, whereas values of 0.80 - 0.89 arising from a smaller A cation or larger B cation predominantly lead to distorted perovskites with octahedral tilting. Considering the effective ionic radii [52] of Sr^{2+}, Ti^{4+} and O^{2-} to be 1.44Å, 0.60Å

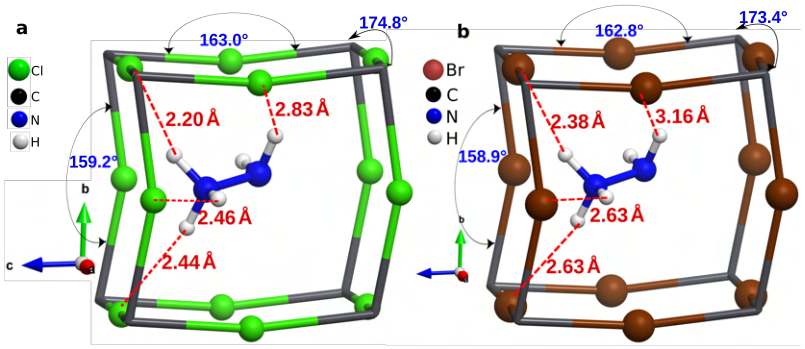

FIGURE 3.4: Shortest bonds (red dotted line) made by the anion (Br/Cl) and hydrogen of the (a) $HAZPbCl_3$ and (b) $HAZPbBr_3$ Compound and bond angles of the respective structures.

and 1.42 Å for $SrTiO_3$ gives a value of tolerance factor of 1.0, consistent with its ideal cubic structure. But in $CaTiO_3$, Ca^{2+} having an effective ionic radii of 1.12 Å results in a tolerance factor of 0.88 and this leads to octahedral tilting with the symmetry of the unit cell now reducing to orthorhombic.

These ideas have been borrowed to discuss the distortions in hybrid perovskites also, despite some ambiguities in defining an ionic radius for the molecule[2, 40]. The non-spherical shape associated with the molecule have led to various definitions of the ionic radii. G. Kieslich et al. have proposed one way [21] which involves calculating the effective ionic radii of organic cations from the existing crystallographic data of hybrid perovskites[14]. Depending on the level of anisotropy, the organic ions were considered either as a sphere or a cylinder. Using this approach the effective radii for a set of organic molecules were calculated, that can be used to estimate the tolerance factors for the corresponding perovskite systems. The effective radii for MA, FA and EA were reported to be 2.17Å , 2.53Å and 2.74 Å respectively[21].

Considering the hybrid perovskites of the form $APbCl_3$, changing the molecule from MA to FA to EA, one finds that the tolerance factor changes from 0.938 to 1.02 to 1.08, a monotonic increase. One would expect a monotonic approach of the Pb-Cl-Pb angles to 180°. However, this is not found to be the case[13, 48]. The effective radius of FA lies between MA and EA but the distortion pattern does not follow the same trend. Armed with the understanding of structural distortions in $MAPbX_3$, if MA(CH_3NH_3) is replaced

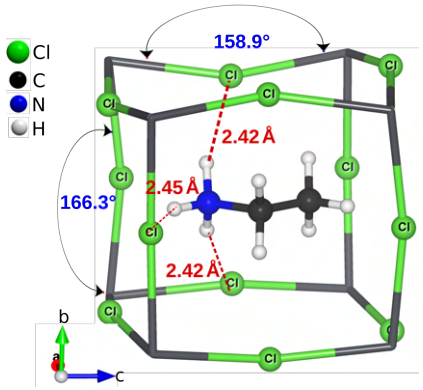

FIGURE 3.5: Shortest bonds (red dotted line) made by the chlorine atom and hydrogen of the EA molecule and bond angles of EAPbCl_3.

by EA ($CH_3CH_2NH_3$) within the octahedral cavity, the distortion pattern for MA and EA based Cl perovskites are found to be very similar because of the asymmetric shape. The Pb-Cl-Pb bond angles in the bc plane remain almost unchanged i.e 167.5° for $MAPbCl_3$ and 166.3° for $EAPbCl_3$ but the bond angles in the ac plane increase from 156.4° to 158.9° as result of the larger size of the EA molecule which leads to a larger unit cell volume (Fig 3.5). The change in Pb-Br-Pb angles in $MAPbBr_3$ and $EAPbBr_3$ also follow the same trend when we move from the chloride to the bromide compounds(Fig 3.6). In contrast with the materials mentioned above, $FAPbX_3$ shows very different distortions, arising from the symmetry of the molecule as we had discussed earlier. This contradicts the previous understanding that emerged from inorganic perovskites, where only the tolerance factor was sufficient to discuss structural trends.

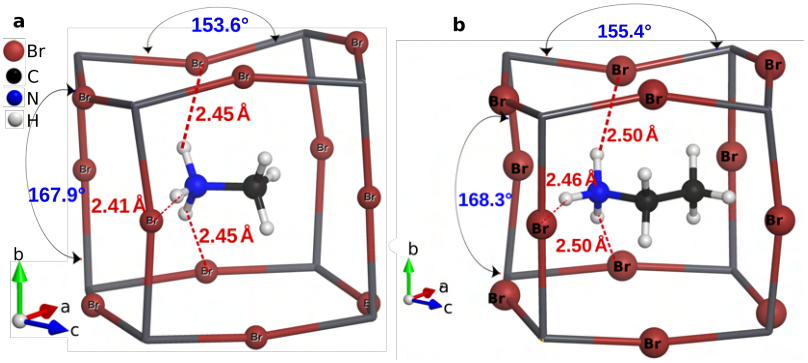

FIGURE 3.6: Shortest bonds (red dotted line) made by the anion (Br) and hydrogen of the (a) MA and (b) EA molecule and bond angles of the respective structures.

As we have already discussed, the MA Molecule in $MAPbX_3$ (X= Cl/Br) moves towards

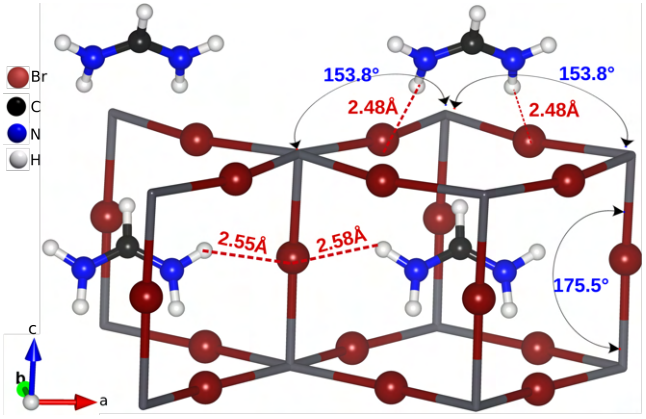

FIGURE 3.7: Shortest bonds (red dotted line) made by the anion (Br) and hydrogen of the FA molecule and bond angles of FAPbBr_3.

one side of the inorganic cage. It is expected that the hydrogen of the ammonium end would make the shortest bond with the halogen atoms, which are in the same plane. But on the contrary, we find that more localized nature of electrons present on chlorine prevent the hydrogens of the ammonium group from coming too close. Hence the H-Cl bond length in $MAPbCl_3$ is 2.36Å for the chlorine atom in the same plane, while it is 2.26Å with the out of plane chlorine atoms(Fig 3.1b). The same bond length trend is seen in $EAPbCl_3$. Two shorter bonds of length 2.42Å are found with the out of plane chlorine atoms, while the in plane chlorine atoms make a longer bond of length 2.45Å(Fig 3.5). However in case of $MAPbBr_3$ one finds the trend to be reversed, the shortest bond of length 2.41Å is found in the same plane as the molecule, while the longer bonds of length 2.45Å are found with the bromine atoms which are out of plane (Fig 3.6a). $EAPbBr_3$ also follow the same trend(Fig 3.6b). A Bader charge analysis of $MAPbCl_3$ and $MAPbBr_3$ helps us understand the reason for this trend. The charge on the chlorine atoms in $MAPbCl_3$ is found to be -0.66e while it is less localized in bromine atoms in $MAPbBr_3$ (-0.60e). Therefore, steric effects due to the bromine atom in $MAPbBr_3$ are less compared to the chlorine atoms of $MAPbCl_3$. This explain the variations in the anion-hydrogen bond lengths with a change in the anion.

Now in the case of $FAPbBr_3$ due to the larger anion (Bromine) one can find more significant distortions of Pb-Br-Pb angles (Fig 3.7) than its Chlorine counterpart. Here one can

find the off-centering of the molecule is very negligible (0.002Å) in ab plane with respect to the Pb cage. The Pb-Br-Pb angle parallel to the plane of symmetry of the molecule is 175.5° and the angle perpendicular to the plane of the symmetry of the molecule is 153.8° . Here one can relate this trend with the former tolerance factor concept where the tolerance factor will decrease when one increase the size of X anion for a fixed A side cation and B side anion, resulting the more octahedral tilting.

Finally to compare the orbital interaction energies between the hydrogen bonding of the ammonium group of $MAPbX_3$ and $FAPbX_3$ (where X = Cl/Br), ICOHP is calculated, this ICOHP study measures the covalent bond strength of a particular bond. From the tabulated values of ICOHP and the corresponding bond length of the hydrogen bonds formed by the hydrogen of amine group of the molecule and the halide atom in table 3.2, one could easily conclude that the ICOHP value or the covalency of a bond is directly related to the bond length and the nature of the anion .

Crystal System	Hydrogen Bond	Bond Length	ICOHP
$MAPbCl_3$	$H_N - Cl$ (ab plane)	2.34Å	0.3067
	$H_N - Cl$ (bc plane)	2.26Å	0.3454
$MAPbBr_3$	$H_N - Br$ (ab plane)	2.41Å	0.3464
	$H_N - Br$ (bc plane)	2.45Å	0.3006
$FAPbCl_3$	$H_N - Cl$ (ac plane)	2.39Å	0.1824
	$H_N - Cl$ (ab plane)	2.26Å	0.2337
$FAPbBr_3$	$H_N - Br$ (ac plane)	2.48Å	0.1586
	$H_N - Br$ (ab plane)	2.55Å	0.2750

TABLE 3.2: Bond length and corresponding ICOHP of hydrogen bonds formed by the hydrogen associated with the ammonium end of the molecule (H_N) and the Halide atom.

4 Conclusion

In conclusion we have re-examined the validity of the concept of a tolerance factor while discussing the trends in structural distortion in hybrid halide perovskites. We find that the symmetry of the molecule must be considered in any discussion of structural trends. While it has been understood, for some time that hydrogen bonding with the anions controls the

B-X-B bond angles in perovskites of the form ABX_3, steric repulsions between the electrons in anion and hydrogens play an important role in determining the H-X bond lengths.

References

[1] Tom Baikie, Yanan Fang, Jeannette M Kadro, Martin Schreyer, Fengxia Wei, Subodh G Mhaisalkar, Michael Graetzel, and Tim J White. Synthesis and crystal chemistry of the hybrid perovskite (CH3NH3)PbI3 for solid-state sensitised solar cell applications. *J. Mater. Chem. A*, 1(18):5628–5641, 2013.

[2] Christopher J. Bartel, Christopher Sutton, Bryan R. Goldsmith, Runhai Ouyang, Charles B. Musgrave, Luca M. Ghiringhelli, and Matthias Scheffler. New tolerance factor to predict the stability of perovskite oxides and halides. *Science Advances*, 5(2), 2019.

[3] P E Blöchl. Projector augmented-wave method. *Physical Review B*, 50(24):17953–17979, dec 1994.

[4] G. Catalan. Progress in perovskite nickelate research. *Phase Transitions*, 81(7-8):729–749, 2008.

[5] Kun Chen, Xiaohui Deng, Richard Goddard, and Harun Tüysüz. Pseudomorphic Transformation of Organometal Halide Perovskite Using the Gaseous Hydrogen Halide Reaction. *Chemistry of Materials*, 28(15):5530–5537, aug 2016.

[6] Tianran Chen, Wei-Liang Chen, Benjamin J Foley, Jooseop Lee, Jacob P C Ruff, J Y Peter Ko, Craig M Brown, Leland W Harriger, Depei Zhang, Changwon Park, Mina Yoon, Yu-Ming Chang, Joshua J Choi, and Seung-Hun Lee. Origin of long lifetime of band-edge charge carriers in organic–inorganic lead iodide perovskites. *Proceedings of the National Academy of Sciences*, 114(29):7519–7524, 2017.

[7] Volker L. Deringer, Andrei L. Tchougréeff, and Richard Dronskowski. Crystal orbital hamilton population (cohp) analysis as projected from plane-wave basis sets. *The Journal of Physical Chemistry A*, 115(21):5461–5466, 2011. PMID: 21548594.

[8] Richard Dronskowski and Peter E. Bloechl. Crystal orbital hamilton populations (cohp): energy-resolved visualization of chemical bonding in solids based on density-functional calculations. *The Journal of Physical Chemistry*, 97(33):8617–8624, 1993.

[9] David A Egger and Leeor Kronik. Role of Dispersive Interactions in Determining Structural Properties of Organic–Inorganic Halide Perovskites: Insights from First-Principles Calculations. *The Journal of Physical Chemistry Letters*, 5(15):2728–2733, aug 2014.

[10] Douglas H Fabini, Tom Hogan, Hayden A Evans, Constantinos C Stoumpos, Mercouri G Kanatzidis, and Ram Seshadri. Dielectric and Thermodynamic Signatures of Low-Temperature Glassy Dynamics in the Hybrid Perovskites CH3NH3PbI3 and HC(NH2)2PbI3. *The Journal of Physical Chemistry Letters*, 7(3):376–381, 2016.

[11] Douglas H. Fabini, Ting Ann Siaw, Constantinos C. Stoumpos, Geneva Laurita, Daniel Olds, Katharine Page, Jerry G. Hu, Mercouri G. Kanatzidis, Songi Han, and Ram Seshadri. Universal dynamics of molecular reorientation in hybrid lead iodide perovskites. *Journal of the American Chemical Society*, 139(46):16875–16884, 2017. PMID: 29094934.

[12] Douglas H Fabini, Constantinos C Stoumpos, Geneva Laurita, Andreas Kaltzoglou, Athanassios G Kontos, Polycarpos Falaras, Mercouri G Kanatzidis, and Ram Seshadri. Reentrant Structural and Optical Properties and Large Positive Thermal Expansion in Perovskite Formamidinium Lead Iodide. *Angewandte Chemie International Edition*, 55(49):15392–15396, 2016.

[13] Somayeh Gholipour, et al. Globularity-selected large molecules for a new generation of multication perovskites. *Advanced Materials*, 29(38):1702005, 2017.

[14] A. M. Glazer. The classification of tilted octahedra in perovskites. *Acta Crystallographica Section B*, 28(11):3384–3392, Nov 1972.

[15] V M Goldschmidt. Die Gesetze der Krystallochemie. *Naturwissenschaften*, 14(21):477–485, 1926.

[16] Sharada Govinda, Bhushan P Kore, Diptikanta Swain, Akmal Hossain, Chandan De, Tayur N Guru Row, and D D Sarma. Critical Comparison of FAPbX3 and MAPbX3 (X = Br and Cl): How Do They Differ? *The Journal of Physical Chemistry C*, 122(25):13758–13766, jun 2018.

[17] Martin A. Green and Anita Ho-Baillie. Perovskite solar cells: The birth of a new era in photovoltaics. *ACS Energy Letters*, 2(4):822–830, 2017.

[18] Stefan Grimme. Semiempirical GGA-type density functional constructed with a long-range dispersion correction. *Journal of Computational Chemistry*, 27(15):1787–1799, nov 2006.

[19] Graeme Henkelman, Andri Arnaldsson, and Hannes Jónsson. A fast and robust algorithm for bader decomposition of charge density. *Computational Materials Science*, 36(3):354–360, 2006.

[20] Jinsong Huang, Yongbo Yuan, Yuchuan Shao, and Yanfa Yan. Understanding the physical properties of hybrid perovskites for photovoltaic applications. *Nature Reviews Materials*, 2(7):17042, 2017.

[21] Gregor Kieslich, Shijing Sun, and Anthony K. Cheetham. Solid-state principles applied to organic–inorganic perovskites: new tricks for an old dog. *Chem. Sci.*, 5:4712–4715, 2014.

[22] Ji ří Klimeš, David R. Bowler, and Angelos Michaelides. Van der waals density functionals applied to solids. *Phys. Rev. B*, 83:195131, May 2011.

[23] Jiří Klimeš, David R Bowler, and Angelos Michaelides. Chemical accuracy for the van der waals density functional. *Journal of Physics: Condensed Matter*, 22(2):022201, dec 2009.

[24] G Kresse and J Furthmüller. Efficiency of ab-initio total energy calculations for metals and semiconductors using a plane-wave basis set. *Computational Materials Science*, 6(1):15–50, 1996.

[25] G Kresse and J Furthmüller. Efficient iterative schemes for ab initio total-energy calculations using a plane-wave basis set. *Physical Review B*, 54(16):11169–11186, oct 1996.

[26] G. Kresse and J. Hafner. Ab initio molecular dynamics for liquid metals. *Physical Review B*, 47(1):558–561, 1993.

[27] G Kresse and J Hafner. Ab initio molecular-dynamics simulation of the liquid-metal–amorphous-semiconductor transition in germanium. *Physical Review B*, 49(20):14251–14269, may 1994.

[28] G Kresse and D Joubert. From ultrasoft pseudopotentials to the projector augmented-wave method. *Physical Review B*, 59(3):1758–1775, jan 1999.

[29] Jin-Wook Lee, Shaun Tan, Sang Il Seok, Yang Yang, and Nam-Gyu Park. Rethinking the a cation in halide perovskites. *Science*, 375(6583):eabj1186, 2022.

[30] Jung-Hoon Lee, Nicholas C. Bristowe, June Ho Lee, Sung-Hoon Lee, Paul D. Bristowe, Anthony K. Cheetham, and Hyun Myung Jang. Resolving the physical origin of octahedral tilting in halide perovskites. *Chemistry of Materials*, 28(12):4259–4266, 2016.

[31] Kyuho Lee, Éamonn D Murray, Lingzhu Kong, Bengt I Lundqvist, and David C Langreth. Higher-accuracy van der Waals density functional. *Physical Review B*, 82(8):81101, aug 2010.

[32] Aurelien M A Leguy, et al. The dynamics of methylammonium ions in hybrid organic–inorganic perovskite solar cells. *Nature Communications*, 6(1):7124, 2015.

[33] Wei Li, Zheming Wang, Felix Deschler, Song Gao, Richard H Friend, and Anthony K Cheetham. Chemically diverse and multifunctional hybrid organic–inorganic perovskites. *Nature Reviews Materials*, 2(3):16099, 2017.

[34] Mingzhen Liu, Michael B Johnston, and Henry J Snaith. Efficient planar heterojunction perovskite solar cells by vapour deposition. *Nature*, 501(7467):395–398, 2013.

[35] Stefan Maintz, Volker L. Deringer, Andrei L. Tchougréeff, and Richard Dronskowski. Analytic projection from plane-wave and paw wavefunctions and application to chemical-bonding analysis in solids. *Journal of Computational Chemistry*, 34(29):2557–2567, 2013.

[36] Stefan Maintz, Volker L. Deringer, Andrei L. Tchougréeff, and Richard Dronskowski. Lobster: A tool to extract chemical bonding from plane-wave based dft. *Journal of Computational Chemistry*, 37(11):1030–1035, 2016.

[37] Giovanni Mannino, Ioannis Deretzis, Emanuele Smecca, Antonino La Magna, Alessandra Alberti, Davide Ceratti, and David Cahen. Temperature-dependent optical band gap in cspbbr3, mapbbr3, and fapbbr3 single crystals. *The Journal of Physical Chemistry Letters*, 11(7):2490–2496, 2020. PMID: 32148047.

[38] Srimanta Middey, Priya Mahadevan, and D. D. Sarma. Dependence of magnetism on gdfeo$_3$ distortion in the t_{2g} system $a$ruo$_3$ (a = sr, ca). *Phys. Rev. B*, 83:014416, Jan 2011.

[39] Mona Mittal, Atanu Jana, Sagar Sarkar, Priya Mahadevan, and Sameer Sapra. Size of the organic cation tunes the band gap of colloidal organolead bromide perovskite nanocrystals. *The Journal of Physical Chemistry Letters*, 7(16):3270–3277, 2016. PMID: 27494515.

[40] David B. Mitzi. Templating and structural engineering in organic–inorganic perovskites. *J. Chem. Soc., Dalton Trans.*, pages 1–12, 2001.

[41] Koichi Momma and Fujio Izumi. *VESTA*: a three-dimensional visualization system for electronic and structural analysis. *Journal of Applied Crystallography*, 41(3):653–658, jun 2008.

[42] Hendrik J Monkhorst and James D Pack. Special points for Brillouin-zone integrations. *Physical Review B*, 13(12):5188–5192, jun 1976.

[43] Edoardo Mosconi, Anna Amat, Md. K. Nazeeruddin, Michael Grätzel, and Filippo De Angelis. First-principles modeling of mixed halide organometal perovskites for photovoltaic applications. *The Journal of Physical Chemistry C*, 117(27):13902–13913, 2013.

[44] Eve M Mozur, Annalise E Maughan, Yongqiang Cheng, Ashfia Huq, Niina Jalarvo, Luke L Daemen, and James R Neilson. Orientational Glass Formation in Substituted Hybrid Perovskites. *Chemistry of Materials*, 29(23):10168–10177, 2017.

[45] Ryky Nelson, Christina Ertural, Janine George, Volker L. Deringer, Geoffroy Hautier, and Richard Dronskowski. Lobster: Local orbital projections, atomic charges, and chemical-bonding analysis from projector-augmented-wave-based density-functional theory. *Journal of Computational Chemistry*, 41(21):1931–1940, 2020.

[46] John P Perdew, Kieron Burke, and Matthias Ernzerhof. Generalized Gradient Approximation Made Simple. *Physical Review Letters*, 77(18):3865–3868, oct 1996.

[47] Gustav Rose. Beschreibung einiger neuen mineralien des urals. *Annalen der Physik*, 124(12):551–573, 1839.

[48] Majid Safdari, Andreas Fischer, Bo Xu, Lars Kloo, and James M. Gardner. Structure and function relationships in alkylammonium lead(ii) iodide solar cells. *J. Mater. Chem. A*, 3:9201–9207, 2015.

[49] Edward Sanville, Steven D. Kenny, Roger Smith, and Graeme Henkelman. Improved grid-based algorithm for bader charge allocation. *Journal of Computational Chemistry*, 28(5):899–908, 2007.

[50] Bayrammurad Saparov and David B. Mitzi. Organic–inorganic perovskites: Structural versatility for functional materials design. *Chemical Reviews*, 116(7):4558–4596, 2016. PMID: 27040120.

[51] Sagar Sarkar and Priya Mahadevan. Role of the a-site cation in determining the properties of the hybrid perovskite $CH_3NH_3PbBr_3$. *Phys. Rev. B*, 95:214118, Jun 2017.

[52] R. D. Shannon. Revised effective ionic radii and systematic studies of interatomic distances in halides and chalcogenides. *Acta Crystallographica Section A*, 32(5):751–767, Sep 1976.

[53] V. K. Sharma, R. Mukhopadhyay, A. Mohanty, V. García Sakai, M. Tyagi, and D. D. Sarma. Contrasting effects of fa substitution on ma/fa rotational dynamics in faxma1–xpbi3. *The Journal of Physical Chemistry C*, 125(24):13666–13676, 2021.

[54] Samuel D Stranks and Henry J Snaith. Metal-halide perovskites for photovoltaic and light-emitting devices. *Nature Nanotechnology*, 10(5):391–402, 2015.

[55] W Tang, E Sanville, and G Henkelman. A grid-based bader analysis algorithm without lattice bias. *Journal of Physics: Condensed Matter*, 21(8):084204, jan 2009.

[56] Yun Wang, Tim Gould, John F Dobson, Haimin Zhang, Huagui Yang, Xiangdong Yao, and Huijun Zhao. Density functional theory analysis of structural and electronic properties of orthorhombic perovskite CH3NH3PbI3. *Physical Chemistry Chemical Physics*, 16(4):1424–1429, 2014.

[57] Mark T Weller, Oliver J Weber, Paul F Henry, Antonietta M Di Pumpo, and Thomas C Hansen. Complete structure and cation orientation in the perovskite photovoltaic methylammonium lead iodide between 100 and 352 K. *Chem. Commun.*, 51(20):4180–4183, 2015.

[58] H. L. Wells. Über die cäsium- und kalium-bleihalogenide. *Zeitschrift für anorganische Chemie*, 3(1):195–210, 1893.

[59] P S Whitfield, N Herron, W E Guise, K Page, Y Q Cheng, I Milas, and M K Crawford. Structures, Phase Transitions and Tricritical Behavior of the Hybrid Perovskite Methyl Ammonium Lead Iodide. *Scientific Reports*, 6(1):35685, 2016.

[60] Joshua Young and James M. Rondinelli. Octahedral rotation preferences in perovskite iodides and bromides. *The Journal of Physical Chemistry Letters*, 7(5):918–922, 2016. PMID: 26899936.

[61] Min Yu and Dallas R. Trinkle. Accurate and efficient algorithm for bader charge integration. *The Journal of Chemical Physics*, 134(6):064111, 2011.

[62] Holly F. Zarick, Naiya Soetan, William R. Erwin, and Rizia Bardhan. Mixed halide hybrid perovskites: a paradigm shift in photovoltaics. *J. Mater. Chem. A*, 6:5507–5537, 2018.

Chapter 4

Facet Modulation in $CsPbBr_3$ Nanocrystals

1 Introduction

To introduce lead halide perovskite nanocrystals, we can contextualize them within the realm of research involving colloidal semiconductor nanocrystals. This area of study has a rich history that spans several decades and remains vibrant today. Traditional colloidal semiconductor nanocrystals primarily consist of binary compounds, characterized by relatively straightforward crystal structures. These structures include tetrahedrally bonded compounds such as zinc-blende (comprising chalcogenides like ZnS, ZnSe, CdS, CdSe, HgTe, and pnictides like InP, InAs) or wurtzite (including ZnS, ZnSe, CdS, CdSe). Additionally, face-centred rock-salt-type compounds like PbS and PbSe fall within this category[2]. Semiconductor nanocrystals that are spherical or cubic and smaller than 20 nm, exhibiting quantum confinement in all three dimensions, are often referred to as quantum dots (QDs). In these traditional semiconductor nanocrystals, the anions and cations within the crystal structures occupy identical crystallographic positions or sublattices. In contrast, a new generation of perovskite nanocrystals, based on $CsPbX_3$ (with X representing Cl, Br, or I), has recently emerged as highly efficient optical materials

for various optoelectronic applications. Extensive research efforts have been dedicated to comprehending the underlying principles governing their formation and achieving stable nanocrystals with remarkable optical properties[6, 28, 37].

Nanoscale materials exhibit physical and chemical properties that are profoundly influenced by their dimensions and morphology. This phenomenon has spurred significant endeavors directed towards the advancement of controlled nanomaterial synthesis[11, 25, 30, 32, 35]. The ultimate objective is to deliberately craft nanostructured materials featuring customizable architectures and foreseeable characteristics through strategic design. This, in turn, enables the creation of desired functionalities. In general, the growth of colloidal crystals with controlled shapes is considered a process governed by kinetics. In this process, low-energy facets persist, while high-energy facets disappear, resulting in a specific final shape enclosed by these low-energy surfaces [33]. While initially, controlling the geometric shape of nanocrystals might seem like a scientific curiosity, its significance extends far beyond aesthetic considerations. The shape not only influences the physicochemical properties of nanocrystals but also determines their suitability and value in various applications, ranging from catalysis to electronics, photonics, information storage, and energy conversion/storage.

For instance, consider Cu_2O nanocrystals, which exhibit highly facet-dependent photocatalytic activity and electrical conductivity[19]. Octahedral nanocrystals exposing (111) facets are both photocatalytically active and electrically conductive, whereas nanocubes with (100) facets are inactive and non-conductive. Consequently, researchers are actively exploring different methods to engineer the shapes of these nanocrystals. Sun et al.[30] discovered that polyvinylpyrrolidone (PVP) can selectively stabilize the 100 facets of silver nanocrystals, thereby promoting the formation of silver nanocubes. Huang et al. [11] reported the use of facet-specific peptide sequences as regulating agents for the predictable synthesis of platinum nanocrystals with selectively exposed crystal surfaces.

An entire study on halide perovskite materials largely adopted the synthetic protocol developed by Kovalenko and his co-workers[27]. For all high-temperature reactions, these

nanocrystals typically lead to six stable facets and form a cube or platelet-shaped nanostructures. Though these isotropic nanocrystals formed for all three halides, which showed the most intense emissions attained predominantly in a cube shape[1, 27, 29], this indeed remained a challenge for creating new stable facets, designing different other-shaped nanocrystals, and observing their new properties. Significant efforts have been put forward in developing these nanocrystals with varying ligands and precursors[7, 13, 23], tuning the reaction temperature[7], finding an alternate solution for avoiding fast cooling[8], and adding several reaction-controlling additives for improving the phase and optical stability[20, 23, 29, 31]. However, beyond the six facets of the cube shape, stabilization of other facets or directional growth of these facets of perovskite nanocrystals is also an open question. Although size has been tuned in some cases[7, 9], the cube remained the predominant shape for the nanocrystals obtained at high-temperature reaction modules. In contrast to previous findings, Peng et al. presented a novel observation of shape modulation in isotropic perovskite nanocrystals, achieved through controlled arm growth. Their investigations indicated that these armed structures originated from intermediate 26-faceted rhombic cuboctahedron nanocrystals with $CsPbBr_3$ structures, which formed under conditions characterized by a shortage of halides (as referenced). Following treatment with OLA-H-Br, these multifaceted intermediate structures with polyhedral shapes transformed into six-faceted armed nanostructures. In this chapter, our exploration focused on assessing the formation energy of various facets. By subjecting the nanocrystals to halide-deficient conditions, we reported that contrary to expectations for cubic nanocrystals, additional facets could be stabilized. This resulted in the formation of a 26-faceted polyhedron transforming into six-faceted armed nanostructures under halide-rich conditions, a finding that aligns with the experimental observations[24].

2 Methodology

Surface energy calculations for $CsPbBr_3$ were conducted using the projected augmented wave (PAW) technique [6, 26], implemented within the framework of density functional

theory (DFT) as part of the Vienna ab initio simulation package (VASP)[22–25]. The exchange-correlation functional employed in this study was the generalized gradient approximation (GGA)[44]. To account for the influence of dispersive interactions within the system, the DFT-D2 method developed by Grimme [13] was incorporated. In order to perform k-space integrations, a gamma-centered Monkhorst-Pack[35] k mesh with dimensions of $4 \times 4 \times 1$ was utilized. Furthermore, a kinetic energy cut-off of 400 eV was selected for the plane waves included in the basis set. $CsPbBr_3$ at room temperature adopts an orthorhombic structure with space group symmetry Pbnm. The lattice parameters utilized in these calculations were derived from experimental measurements[1], specifically, a = 8.21 Å, b = 8.28 Å, and c = 11.80 Å. These optimized unit cell parameters served as the foundation for constructing the surfaces corresponding to the low-energy facets observed in experimental investigations.

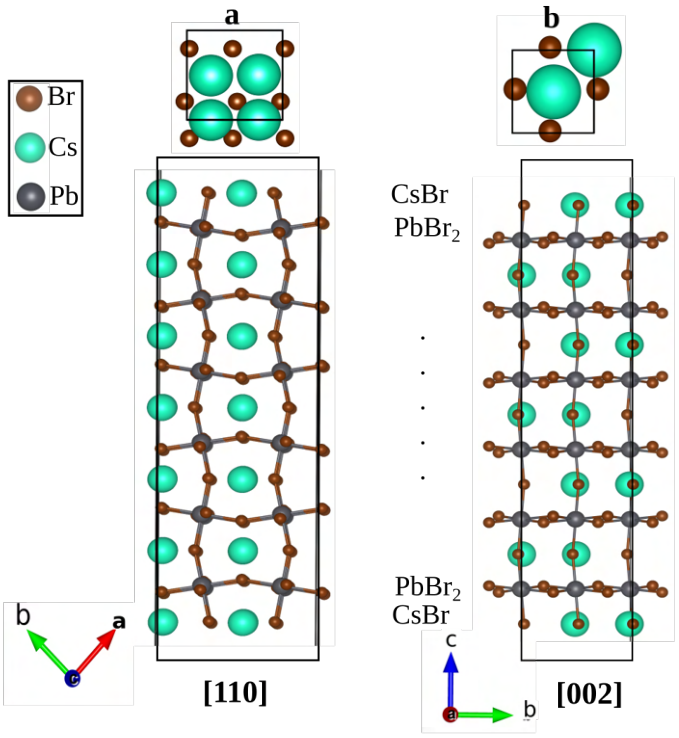

FIGURE 4.1: Top as well as side view of the (a) [110] and (b) [002] facets for orthorhombic CsPbBr3 shown with the termination considered in the calculations

At first, symmetric slabs comprising 17 layers were constructed, oriented along the [110] and [002] directions. In the $CsPbBr_3$ crystal along these directions, there is a repeating

pattern of neutral CsBr and $PbBr_2$ planes, giving rise to two potential surface terminations for the slab: the CsBr or the PbBr2 surface termination. Prior research[40] has demonstrated that the CsBr-terminated surface is energetically more favorable. This preference arises because achieving a $PbBr_2$ termination would necessitate the disruption of $PbBr_6$ octahedra, which is energetically expensive.

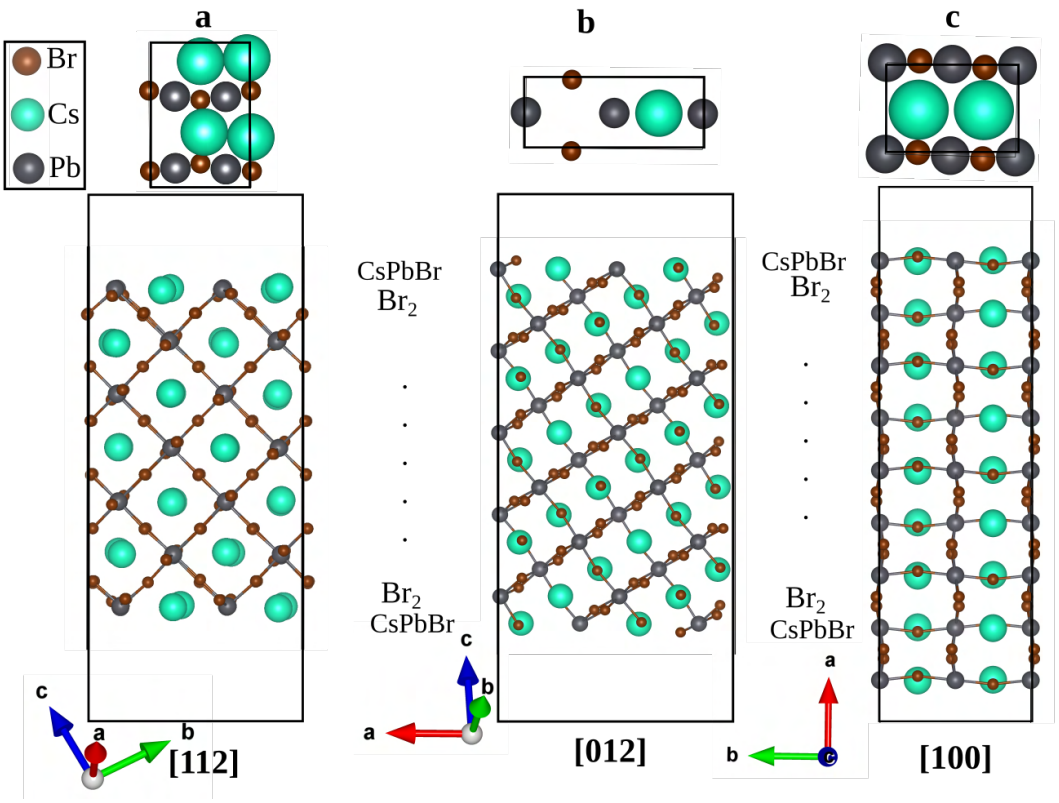

FIGURE 4.2: Top as well as side view of the (a) [112], (b) [012], and the (c) [100] facets for orthorhombic $CsPbBr_3$ shown with the termination considered in the calculations

A similar methodology was employed to construct slabs corresponding to the noncubic [112], [012], and [100] facets. These slabs, like the previous ones, consist of a total of 17 layers, terminated with a CsPbBr layer, and maintain mirror symmetry relative to the central layer. In these slabs, there exist dangling bond states associated with the Pb atoms of the surface layer. To address this, they have been passivated using pseudohydrogens, each carrying a charge of $\frac{5}{3}$ electron units. The density functional theory utilized in this study necessitates the periodicity of the lattice. Therefore, consecutive slabs were employed, separated by a 20 Å vacuum, to ensure that the periodically repeated units in

the growth direction remain effectively decoupled. To ensure the convergence of results concerning slab size, calculations were conducted using both 9-layer and 17-layer slabs. The results presented in this thesis are based on the larger 17-layer slabs, although the findings from the smaller slabs exhibited similar qualitative trends.

3 Results and discussion

To investigate the impact of diverse experimental conditions on growth, symmetric slabs were meticulously constructed for each of the surfaces under examination. The terminating layer for each facet considered has been specified in Table 4.1. For each of the surfaces considered, the lattice constants were held constant at their experimental values, while the internal positions were permitted to adjust in order to minimize the total energy. The optimized structures in each case were used to calculate the surface energy. The surface energy[1, 12] is given by Equation 4.1 below where μ_{Cs}, μ_{Pb}, and μ_{Br} are the chemical potentials for Cs, Pb and Br respectively.

$$\Omega = \frac{1}{2}\left[E^{Slab}_{CsPbBr_3} - N_{Cs}\mu_{Cs} - N_{Pb}\mu_{Pb} - N_{Br}\mu_{Br}\right] \tag{4.1}$$

In the given context $E^{Slab}_{CsPbBr_3}$ represents the total energy of the slab. N_{Cs}, N_{Pb}, and N_{Br} are the counts of Cs atoms, Pb atoms, and Br atoms within the slab, respectively. The factor of 1/2 accounts for the presence of two identical surfaces within the slab.μ_α denotes the absolute value of the chemical potential of atom α. Furthermore, the chemical potential μ_{CsPbBr_3} of a stoichiometric $CsPbBr_3$ phase is determined by the sum of three terms, each representing the chemical potentials of the individual atomic constituents within the crystal. This can be expressed as follows.

$$\mu_{CsPbBr_3} = \mu_{Cs} + \mu_{Pb} + 3\mu_{Br} \tag{4.2}$$

As the surface is in equilibrium with the bulk $CsPbBr_3$ so we can say $E^{Bulk}_{CsPbBr_3} = \mu_{CsPbBr_3}$ using this we can rewrite the equation (1) as

$$\Omega = \frac{1}{2}\left[E^{Slab}_{CsPbBr_3} - N_{Cs}E^{Bulk}_{CsPbBr_3} - (N_{Pb} - N_{Cs})\mu_{Pb} - (N_{Br} - 3N_{Cs})\mu_{Br}\right] \tag{4.3}$$

In our calculations, it is essential that the constrained values for the chemical potentials of Pb and Br satisfy two conditions: (1) They must adhere to the thermodynamic equilibrium growth condition for bulk $CsPbBr_3$. (2) They must prevent the formation of CsBr as secondary phases. These conditions impose constraints on the chemical potentials, as described below.

$$\Delta\mu_{Cs} + \Delta\mu_{Pb} + 3\Delta\mu_{Br} = \Delta H_{CsPbBr_3} \tag{4.4}$$

$$\Delta\mu_{Cs} + \Delta\mu_{Br} \leq \Delta H_{CsBr} \tag{4.5}$$

Here $\Delta\mu$ represents the variation of chemical potentials from the chemical potential of that element which is taken as the energy of the ground state configuration of that particular element. We have taken the most stable crystal structure for Pb[3] and Cs[34]. For Br we consider Br_2 dimer in a large cubic unit cell of dimension 10Å. A similar calculation was performed for H_2 as well as CH_3NH_3 ion. ΔH_{AB} is the formation energy of the compound AB. The formation energy of $CsPbBr_3$(ΔH_{CsPbBr_3}) and CsBr (ΔH_{CsBr}) were calculated to be -9.838 eV and -2.377 eV respectively.

Facet (surface termination)	Surface Energy
(100)(CsPbBr)	$-5.229 + 2\Delta\mu_{Br} - 4\Delta\mu_H$
(012)(CsPbBr)	$-2.659 + 2\Delta\mu_{Br} - 4\Delta\mu_H$
(002)(CsBr)	$-5.204 + \Delta\mu_{Pb} + 2\Delta\mu_{Br}$
(110)(CsBr)	$-5.159 + 2\Delta\mu_{Pb} + 4\Delta\mu_{Br}$
(112)(CsPbBr)	$-8.431 + 4\Delta\mu_{Br} - 8\Delta\mu_H$

TABLE 4.1: Calculated surface energies for different facets

In the experiments, octylamine (OLA) ions, initially employed to prevent nanocrystal agglomeration, were substituted with short-chain methylammonium (MA) ions to facilitate

the calculations. It was established that these MA ions did not significantly influence the formation of hexapods. However, their presence was considered when determining the acceptable range of chemical potentials for Cs. Nevertheless, prior research[28] had demonstrated that MA ions can replace Cs atoms on the surface. Therefore, additional calculations were conducted to determine the formation energy associated with MA ions replacing Cs atoms at the surface, as well as the energy associated with MA ions binding to surface Br atoms (see Table4.2).

Facet (surface termination)	**Formation energy for surface Cs atom replaced by MA ion**	**Formation energy of MA ion adsorbed on a surface Br atom**
(110)(CsBr)	$+1.982 - \Delta\mu_{CH3NH3} + \Delta\mu_{Cs}$	$-1.880 - \Delta\mu_{CH3NH3}$
(112)(CsPbBr)	$+1.980 - \Delta\mu_{CH3NH3} + \Delta\mu_{Cs}$	$-1.710 - \Delta\mu_{CH3NH3}$
(100)(CsPbBr)	$+1.334 - \Delta\mu_{CH3NH3} + \Delta\mu_{Cs}$	$-1.547 - \Delta\mu_{CH3NH3}$
(012)(CsPbBr)	$+1.703 - \Delta\mu_{CH3NH3} + \Delta\mu_{CS}$	$-1.632 - \Delta\mu_{CH3NH3}$
(002)(CsBr)	$+0.906 - \Delta\mu_{CH3NH3} + \Delta\mu_{Cs}$	$-0.883 - \Delta\mu_{CH3NH3}$

TABLE 4.2: Calculated Formation energies for different facets for MA ion binding replacing a Cs atom and MA ion adsorbed to surface Br atom. The composition of the surface layer of each facet has been indicated.

The choice of chemical potential was made under Br-rich conditions, where the formation energies favored MA ions attaching to the surface Br atoms, as indicated in Table 4.3. Furthermore, the pseudohydrogens employed served as a means to passivate the surface dangling bonds associated with the Pb atoms. These interactions can introduce complexities in experimental setups, which in turn impose limits on $\Delta\mu_H$. In this context, a conservative value of $\Delta\mu_H$ = -1.0 eV was utilized under Br-rich conditions to account for allowable variations in the chemical potential.

Facet (surface termination)	Cs is Replaced by the molecule	Molecule is adsorbed
(110)(CsBr)	+0.482 eV	-3.380 eV
(112)(CsPbBr)	+0.480 eV	-3.21 eV
(100)(CsPbBr)	-0.166 eV	-3.047 eV
(012)(CsPbBr)	+0.203 eV	-3.132 eV
(002)(CsBr)	-0.594 eV	-2.38 eV

TABLE 4.3: Formation energies calculated with the MA ion adsorbed on top of a surface Br atom and Cs is replaced by the molecule under the condition $\Delta\mu_{Cs}$= -1.5 eV, $\Delta\mu_{Pb}$=-8.338 eV, $\Delta\mu_{Br}$=0.0 eV.and $\Delta\mu_H$=-1.0 eV

The surface energy values provided in Table 4.1 were calculated for various facets under conditions of Br scarcity, where the chemical potentials are as follows: $\Delta\mu_{Cs} = -1.51$ eV,

$\Delta\mu_{Pb} = -2.728$ eV, $\Delta\mu_{Br} = -2.730$ eV, and $\Delta\mu_H = 0.0$ eV. It's important to note that these conditions satisfy the requirements outlined in Equation (4.4) and Equation (4.5). Under these specified conditions, the presence of $PbBr_2$ as an impurity is expected. Notably, the calculated surface energy for all facets (as shown in Figures 4.1 and 4.2) yielded negative values. This implies that all facets could potentially form under these conditions, aligning with the experimental observation of polyhedron formation characterized by 26 facets (Table4.4).

Facet (Surface termination)	**Bromine poor condition** $\Delta\mu_{Cs} = -1.50$ $\Delta\mu_{Pb} = -2.72$ $\Delta\mu_{Br} = -2.37$ $\Delta\mu_H = 0.00$	**Bromine rich condition** $\Delta\mu_{Cs} = -1.51$ $\Delta\mu_{Pb} = -8.33$ $\Delta\mu_{Br} = 0.00$ $\Delta\mu_H = -1.00$
(100) (CsPbBr)	-9.969 eV	-1.229 eV
(012) (CsPbBr)	-7.933 eV	+1.341 eV
(002) (CsBr)	-15.865 eV	-13.542 eV
(110) (CsBr)	-17.729 eV	-17.835 eV
(112) (CsPbBr)	-17.911 eV	-0.431 eV

TABLE 4.4: Surface energy for facets of CsPbBr3 calculated for 17 layer slab under Bromine rich and Bromine poor conditions.

Under Br-rich conditions, where the chemical potentials are as follows: $\Delta\mu_{Cs} = -1.51$ eV, $\Delta\mu_{Pb} = -8.338$ eV, $\Delta\mu_{Br} = 0.0$ eV, and $\Delta\mu_H = -1.0$ eV, it was observed that only the (110) and (002) facets were stabilized. In contrast, all other facets exhibited considerably higher energies, making them thermodynamically unstable (Table 4.4). These findings strongly support the formation of hexapod structures in the case of $CsPbBr_3$ nanostructures, as consistent with experimental observations. The stability of the (110) and (002) facets under Br-rich conditions suggests their prominence in the formation of hexapods.

4 Conclusion

In conclusion, our comprehensive computational study has shed light on the thermodynamic stability of various facets in $CsPbBr_3$ nanostructures under both Br-poor and

Br-rich conditions. Under Br-poor conditions, where $\Delta\mu_{Cs} = -1.51$ eV, $\Delta\mu_{Pb} = -2.728$ eV, $\Delta\mu_{Br} = -2.730$ eV, and $\Delta\mu_H = 0.0$ eV, all facets exhibited negative surface energies, indicating their potential to form. This observation aligns with the experimental findings of polyhedron structures with 26 facets. Conversely, under Br-rich conditions, where $\Delta\mu_{Cs} = -1.51$ eV, $\Delta\mu_{Pb} = -8.338$ eV, $\Delta\mu_{Br} = 0.0$ eV, and $\Delta\mu_H = -1.0$ eV, only the (110) and (002) facets were found to be stable, while all other facets exhibited significantly higher energies, rendering them unstable. These results provide strong support for the experimental observation of hexapod formations in $CsPbBr_3$ nanostructures. Overall, our computational insights into the thermodynamic stability of facets offer valuable guidance for understanding and controlling the growth and formation of specific crystal morphologies in perovskite nanocrystals, with implications for their diverse applications in the field of materials science and optoelectronics.

References

[1] Quinten A Akkerman, Valerio D'Innocenzo, Sara Accornero, Alice Scarpellini, Annamaria Petrozza, Mirko Prato, and Liberato Manna. Tuning the optical properties of cesium lead halide perovskite nanocrystals by anion exchange reactions. *Journal of the American Chemical Society*, 137(32):10276–10281, 2015.

[2] Quinten A Akkerman, Gabriele Rainò, Maksym V Kovalenko, and Liberato Manna. Genesis, challenges and opportunities for colloidal lead halide perovskite nanocrystals. *Nature materials*, 17(5):394–405, 2018.

[3] Federica Bertolotti, Loredana Protesescu, Maksym V Kovalenko, Sergii Yakunin, Antonio Cervellino, Simon JL Billinge, Maxwell W Terban, Jan Skov Pedersen, Norberto Masciocchi, and Antonietta Guagliardi. Coherent nanotwins and dynamic disorder in cesium lead halide perovskite nanocrystals. *ACS nano*, 11(4):3819–3831, 2017.

[4] P E Blöchl. Projector augmented-wave method. *Physical Review B*, 50(24):17953–17979, dec 1994.

[5] N Bouad, L Chapon, R-M Marin-Ayral, F Bouree-Vigneron, and J-C Tedenac. Neutron powder diffraction study of strain and crystallite size in mechanically alloyed pbte. *Journal of Solid State Chemistry*, 173(1):189–195, 2003.

[6] Yunhua Chen, Sara R Smock, Anne H Flintgruber, Frédéric A Perras, Richard L Brutchey, and Aaron J Rossini. Surface termination of cspbbr3 perovskite quantum dots determined by solid-state nmr spectroscopy. *Journal of the American Chemical Society*, 142(13):6117–6127, 2020.

[7] Yitong Dong, Tian Qiao, Doyun Kim, David Parobek, Daniel Rossi, and Dong Hee Son. Precise control of quantum confinement in cesium lead halide perovskite quantum dots via thermodynamic equilibrium. *Nano letters*, 18(6):3716–3722, 2018.

[8] Anirban Dutta, Rakesh Kumar Behera, Sumit Kumar Dutta, Samrat Das Adhikari, and Narayan Pradhan. Annealing cspbx3 (x= cl and br) perovskite nanocrystals at high reaction temperatures: phase change and its prevention. *The journal of physical chemistry letters*, 9(22):6599–6604, 2018.

[9] Anirban Dutta, Sumit Kumar Dutta, Samrat Das Adhikari, and Narayan Pradhan. Tuning the size of cspbbr3 nanocrystals: all at one constant temperature. *ACS Energy Letters*, 3(2):329–334, 2018.

[10] Stefan Grimme. Semiempirical GGA-type density functional constructed with a long-range dispersion correction. *Journal of Computational Chemistry*, 27(15):1787–1799, nov 2006.

[11] Michael H Huang and Po-Heng Lin. Shape-controlled synthesis of polyhedral nanocrystals and their facet-dependent properties. *Advanced Functional Materials*, 22(1):14–24, 2012.

[12] Xin Huang, Tula R Paudel, Peter A Dowben, Shuai Dong, and Evgeny Y Tsymbal. Electronic structure and stability of the c h 3 n h 3 pbb r 3 (001) surface. *Physical Review B*, 94(19):195309, 2016.

[13] Muhammad Imran, Vincenzo Caligiuri, Mengjiao Wang, Luca Goldoni, Mirko Prato, Roman Krahne, Luca De Trizio, and Liberato Manna. Benzoyl halides as alternative precursors for the colloidal synthesis of lead-based halide perovskite nanocrystals. *Journal of the American Chemical Society*, 140(7):2656–2664, 2018.

[14] G Kresse and J Furthmüller. Efficiency of ab-initio total energy calculations for metals and semiconductors using a plane-wave basis set. *Computational Materials Science*, 6(1):15–50, 1996.

[15] G Kresse and J Furthmüller. Efficient iterative schemes for ab initio total-energy calculations using a plane-wave basis set. *Physical Review B*, 54(16):11169–11186, oct 1996.

[16] G. Kresse and J. Hafner. Ab initio molecular dynamics for liquid metals. *Physical Review B*, 47(1):558–561, 1993.

[17] G Kresse and J Hafner. Ab initio molecular-dynamics simulation of the liquid-metal–amorphous-semiconductor transition in germanium. *Physical Review B*, 49(20):14251–14269, may 1994.

[18] G Kresse and D Joubert. From ultrasoft pseudopotentials to the projector augmented-wave method. *Physical Review B*, 59(3):1758–1775, jan 1999.

[19] Chun-Hong Kuo, Yi-Ting Chu, Yen-Fang Song, and Michael H Huang. Cu_2o nanocrystal-templated growth of cu_2s nanocages with encapsulated au nanoparticles and in-situ transmission x-ray microscopy study. *Advanced Functional Materials*, 21(4):792–797, 2011.

[20] Joseph S Manser, Makhsud I Saidaminov, Jeffrey A Christians, Osman M Bakr, and Prashant V Kamat. Making and breaking of lead halide perovskites. *Accounts of chemical research*, 49(2):330–338, 2016.

[21] Koichi Momma and Fujio Izumi. *VESTA*: a three-dimensional visualization system for electronic and structural analysis. *Journal of Applied Crystallography*, 41(3):653–658, jun 2008.

[22] Hendrik J Monkhorst and James D Pack. Special points for Brillouin-zone integrations. *Physical Review B*, 13(12):5188–5192, jun 1976.

[23] Jun Pan, Yuequn Shang, Jun Yin, Michele De Bastiani, Wei Peng, Ibrahim Dursun, Lutfan Sinatra, Ahmed M El-Zohry, Mohamed N Hedhili, Abdul-Hamid Emwas, et al. Bidentate ligand-passivated cspbi3 perovskite nanocrystals for stable near-unity photoluminescence quantum yield and efficient red light-emitting diodes. *Journal of the American Chemical Society*, 140(2):562–565, 2017.

[24] Lucheng Peng, Sumit Kumar Dutta, Debayan Mondal, Biswajit Hudait, Sanjib Shyamal, Renguo Xie, Priya Mahadevan, and Narayan Pradhan. Arm growth and facet modulation in perovskite nanocrystals. *Journal of the American Chemical Society*, 141(40):16160–16168, 2019. PMID: 31510737.

[25] Xiaogang Peng, Liberato Manna, Weidong Yang, Juanita Wickham, Erik Scher, Andreas Kadavanich, and A Paul Alivisatos. Shape control of cdse nanocrystals. *Nature*, 404(6773):59–61, 2000.

[26] John P Perdew, Kieron Burke, and Matthias Ernzerhof. Generalized Gradient Approximation Made Simple. *Physical Review Letters*, 77(18):3865–3868, oct 1996.

[27] Loredana Protesescu, Sergii Yakunin, Maryna I Bodnarchuk, Franziska Krieg, Riccarda Caputo, Christopher H Hendon, Ruo Xi Yang, Aron Walsh, and Maksym V Kovalenko. Nanocrystals of cesium lead halide perovskites (cspbx3, x= cl, br, and i): novel optoelectronic materials showing bright emission with wide color gamut. *Nano letters*, 15(6):3692–3696, 2015.

[28] Vikash Kumar Ravi, Pralay K Santra, Niharika Joshi, Jeetender Chugh, Sachin Kumar Singh, Håkan Rensmo, Prasenjit Ghosh, and Angshuman Nag. Origin of the substitution mechanism for the binding of organic ligands on the surface of cspbbr3

perovskite nanocubes. *The Journal of Physical Chemistry Letters*, 8(20):4988–4994, 2017.

[29] Javad Shamsi, Alexander S Urban, Muhammad Imran, Luca De Trizio, and Liberato Manna. Metal halide perovskite nanocrystals: synthesis, post-synthesis modifications, and their optical properties. *Chemical reviews*, 119(5):3296–3348, 2019.

[30] Yugang Sun and Younan Xia. Shape-controlled synthesis of gold and silver nanoparticles. *science*, 298(5601):2176–2179, 2002.

[31] Abhishek Swarnkar, Wasim J Mir, and Angshuman Nag. Can b-site doping or alloying improve thermal-and phase-stability of all-inorganic cspbx3 (x= cl, br, i) perovskites? *ACS Energy Letters*, 3(2):286–289, 2018.

[32] Na Tian, Zhi-You Zhou, Shi-Gang Sun, Yong Ding, and Zhong Lin Wang. Synthesis of tetrahexahedral platinum nanocrystals with high-index facets and high electro-oxidation activity. *science*, 316(5825):732–735, 2007.

[33] B Viswanath, Paromita Kundu, Aditi Halder, and N Ravishankar. Mechanistic aspects of shape selection and symmetry breaking during nanostructure growth by wet chemical methods. *The Journal of Physical Chemistry C*, 113(39):16866–16883, 2009.

[34] CE Weir, GJ Piermarini, and S Block. On the crystal structures of cs ii and ga ii. *The Journal of Chemical Physics*, 54(6):2768–2770, 1971.

[35] Hua Gui Yang, Cheng Hua Sun, Shi Zhang Qiao, Jin Zou, Gang Liu, Sean Campbell Smith, Hui Ming Cheng, and Gao Qing Lu. Anatase tio2 single crystals with a large percentage of reactive facets. *Nature*, 453(7195):638–641, 2008.

[36] Yi Yang, Fei Gao, Shiwu Gao, and Su-Huai Wei. Origin of the stability of two-dimensional perovskites: a first-principles study. *Journal of Materials Chemistry A*, 6(30):14949–14955, 2018.

[37] Baowei Zhang, Luca Goldoni, Juliette Zito, Zhiya Dang, Guilherme Almeida, Francesco Zaccaria, Jur De Wit, Ivan Infante, Luca De Trizio, and Liberato Manna.

Alkyl phosphonic acids deliver cspbbr3 nanocrystals with high photoluminescence quantum yield and truncated octahedron shape. *Chemistry of Materials*, 31(21):9140–9147, 2019.

Chapter 5

Shape Controlled Emissive Properties of Mn-doped $CsPbBr_3$ Nanocrystals

1 Introduction

In most instances, the augmentation of functionalities in nanocrystals has traditionally involved a process known as doping. In certain scenarios, this doping procedure has also led to alterations in the optical properties of these nanocrystals[11, 13, 14, 22, 24, 32, 36, 41]. Moreover, in other cases, doping has played a crucial role in stabilizing the crystal structure, resulting in a configuration entirely distinct from the original, undoped form[10, 16]. On occasion, the dopant levels are positioned within the bandgap of the host material, potentially facilitating the transformation of wide bandgap semiconductors into intermediate bandgap semiconductors[3]. Although these aspects of dopant functionality have been extensively investigated and are reasonably well comprehended, the perplexing aspect arises when the same dopant atom, within the same material, exhibits varying behavior due to different structural arrangements.

This chapter delves into one such instance where nanocrystals assume different shapes and explores the reasons behind why Mn doping may emit light in one case while remaining non-emissive in another[7, 30].

The study of Pb-based halide perovskites has garnered considerable attention due to their high solar cell efficiency and improved optoelectronic properties[4–6, 9, 26, 28, 35, 39]. Numerous approaches, including the introduction of dopant atoms and various synthesis techniques, have been employed to investigate these materials. When examining nanocrystals of inorganic Pb-based halide perovskites using transmission electron microscopy (TEM), they frequently exhibit cubic facets[25]. Recent work, however, research has demonstrated that altering the growth conditions can lead to variations in the nanocrystals' shapes. Under halide-deficient conditions, it was observed that more facets, beyond those expected for a typical cubic nanocrystal, were stabilized. This resulted in the formation of a polyhedron with 26 facets. Further adjustments to the growth conditions allowed for additional modifications of the nanocrystal's shape. The introduction of more halide salts caused the non-cubic facets to disappear, leaving behind a structure with only cubic facets. However, unlike the regular cubic-shaped nanocrystal initially formed, this modified structure featured protruding arms, resulting in a larger surface area[33]. Since the nanocrystal structures realized under different experimental conditions possessed well-defined facets, they provided an ideal system for investigating why Mn doping was emissive in some cases but not in others. In this chapter, we have conducted an investigation into inorganic halide perovskite CsPbBr3 nanocrystals. Our theoretical approach involved varying the halide content to influence the nanocrystal shape. To elucidate the mechanisms governing shape modulation, we considered the thermodynamical stabilization of distinct facets under different experimental conditions and computed their relative energies. Halide-deficient conditions favored the stabilization of facets associated with a polyhedral structure with 26 faces, while halide-rich conditions minimized the energy associated with the cubic facets. Subsequently, we explored the effects of Mn doping on these facets and observed that Mn doping in the cubic facets resulted in emissive behavior, whereas non-cubic facets remained non-emissive. Recent experimental investigations into Mn doping in $CsPbCl_3$ nanocrystals

with shape variations have shown that doping was feasible in structures with arm-like extensions formed under halide-rich conditions, but not within the polyhedron formed under halide-poor conditions[7].

Although the initial assessment of dopant concentration relied on Mn emissivity, we present evidence that Mn doping can occur without resulting in emission. This discovery may account for the variations in emissivity observed in different shapes and underscores the potential of nanocrystal shape manipulation for tailoring materials with optimized optoelectronic properties.

2 Methodology

First-principle calculations were carried out employing a plane wave basis set within the framework of the Vienna Ab initio Simulation Package (VASP)[22–25], as documented in the reference. These calculations utilized projected augmented-wave potentials[6, 26]. The choice of the exchange-correlation functional was based on the generalized gradient approximation (GGA)[44], specifically the Perdew–Burke–Ernzerhof functional. To accurately model structural properties, it was imperative to account for nonlocal and weak van der Waals (vdW) interactions[13]. To address this requirement, a GGA+vdW density functional theory approach was employed, known to offer a dependable estimation of lattice parameters[10, 30, 57].

To ensure reliable results, a plane-wave energy cutoff of 550 eV was utilized, and Brillouin zone sampling was carried out using a $4 \times 4 \times 1$ Monkhorst–Pack grid[35] , which was deemed adequate for achieving both energy and force convergence.

For structural relaxations, the ions were allowed to adjust their positions until the atomic forces reached a magnitude of less than 0.01 eV/Å. The calculations were based on the experimentally determined crystal structure of bulk $CsPbBr_3$, which falls under the Pbnm space group, as reported in reference[1]. During these calculations, the lattice parameters were held constant at their experimental values: a = 8.21Å, b = 8.29Å, and c = 11.80Å,

while the internal atomic positions were permitted to relax. Subsequently, the optimized unit cell was employed to generate the surfaces corresponding to the low-energy facets observed in experimental observations.

Initially, we constructed symmetric slabs consisting of 17 layers oriented along the [110] and [002] crystallographic directions of the CsPbBr3 crystal. Along these directions, the crystal exhibits an arrangement of alternating neutral CsBr and PbBr2 planes, resulting in two potential surface terminations for the slab: either the CsBr or the PbBr2 surface termination. Prior research[40] established that the energetically preferred surface termination is CsBr. Achieving a $PbBr_2$ termination would necessitate the breaking of $PbBr_6$ octahedra, incurring a substantial energy penalty.

We extended a similar approach to construct slabs corresponding to the noncubic [112], [012], and [100] facets. These slabs, also comprising 17 layers, were terminated with a CsPbBr layer while maintaining mirror symmetry relative to the central layer, as in our previous constructions. To address the dangling bond states associated with the Pb atoms on the surface layer, pseudohydrogens with a charge equivalent to 5/3 of an electron unit were used to passivate these sites.

To ensure accurate calculations and prevent interactions between consecutive slabs, a vacuum separation of 20Å was introduced. Various slab sizes were considered to guarantee convergence of results concerning slab size, with the larger slab size results being presented here. It's important to note, however, that the results obtained with a smaller slab exhibited qualitative similarities. Schematic representations of the crystal structures were generated using VESTA software[34].

3 Results and discussion

At lower temperatures, $CsPbBr_3$ adopts an orthorhombic crystal structure as its preferred configuration. However, as the temperature increases, it undergoes a phase transition into a tetragonal structure, occurring at approximately 361 K[15, 38].

In our investigation of nanocrystals derived from these perovskites, we initially observed the stabilization of only cubic facets. However, recent experiments have successfully synthesized a nanocrystal featuring 26 facets. This distinctive nanocrystal not only exhibits the anticipated cubic facets of [110] and [002] but also includes facets from the [100], [112], and [012] set, which have been effectively stabilized. These facets are depicted in Figure5.1, with the chosen termination for subsequent analysis being specified in our calculations.

Concerning the cubic facets, there is an option to terminate them with either a $PbBr_2$ surface layer or a CsBr layer. However, opting for a $PbBr_2$ termination disrupts the octahedral coordination of the surface Pb atoms. This disruption bears computational implications, as the active states in hybrid perovskites contributing to the valence and conduction bands involve the Pb s, p, and Br p states. The perturbation of octahedral coordination around Pb leads to the breakage of specific bonds and, consequently, incurs computational expenses.

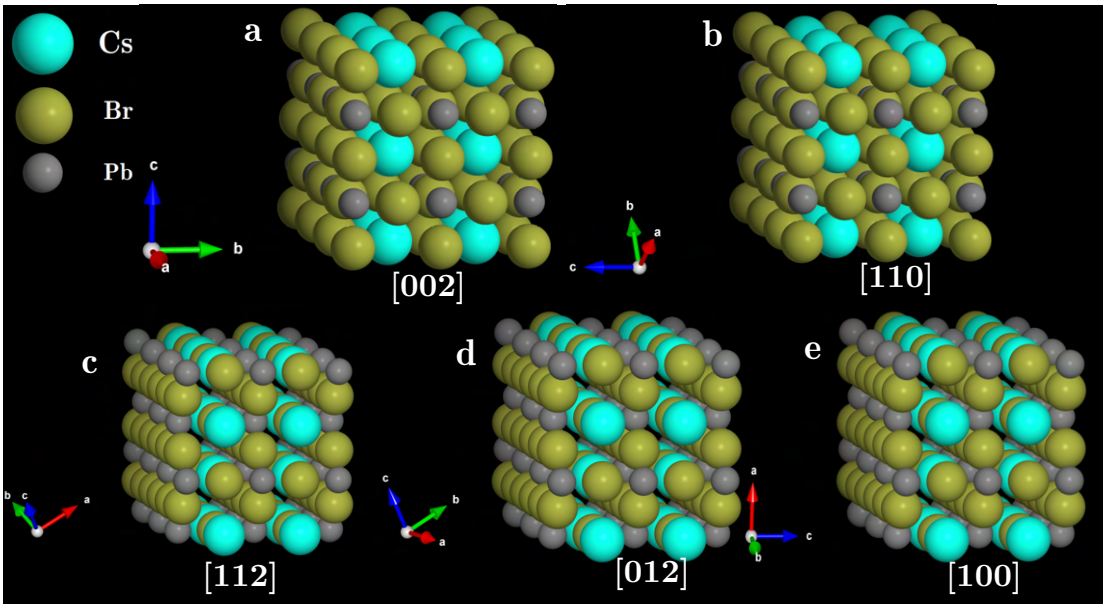

FIGURE 5.1: Slab model of cubic (a) [002] and (b) [110] facets and non-cubic (c) [112], (d) [012] , (e) [100] facets for orthorhombic $CsPbBr_3$ shown with the termination considered in the calculations

For each of the facets under discussion, we employed a 17-layered symmetric slab and carried out atomic position optimizations. When examining the cubic facets [110] and [002], we observed that the Pb–Br–Pb angles in the surface layer approached approximately

157.5°, a value closely resembling the Pb–Br–Pb bond angle of approximately 158° found in the central layer of the slab. Likewise, our investigation of the [112] and [012] facets revealed a Pb–Br–Pb bond angle of 159.2° in the surface layer.

To explore Mn doping within the various shapes arising under halide-rich and halide-poor conditions, we examined each facet to identify the preferred location for the doped Mn atom. In all instances, we exclusively considered substitutional Mn doping at the Pb site.

For the [110] surface, our approach involved the replacement of one of the Pb atoms in the uppermost $PbBr_2$ layer with Mn. This particular Pb atom is coordinated by six Br atoms, with bond lengths ranging from 2.9 to 3.12Å. The substitution with Mn resulted in a structural configuration featuring four Mn–Br bond lengths in the range of 2.5–2.6Å, while the remaining two Mn–Br bond lengths measured 3.11 and 3.45 Å. This variation was due to the substantial energy cost associated with straining the crystal to attain uniform bond lengths for all six bonds. We also explored an alternative configuration where Mn replaced a Pb atom in the central $PbBr_2$ layer, but this configuration was determined to be energetically less favorable by 88 meV. Consequently, our findings suggested that Mn doping on these facets predominantly occurred in the surface layer.

In the case of the [112] facet, our investigations indicated that substituting Pb with Mn in the topmost layer remained energetically favored. However, the replacement of Pb with Mn in the subsurface layer or the central layer incurred significant energy costs, amounting to 930 and 198 meV, respectively. This pattern once again underscores the preference for surface doping.

It is important to highlight that the surface Mn atom is surrounded by some of the pseudohydrogen passivants. This results in a highly non-monotonic variation in the energy cost associated with Mn doping. Unlike the cubic facets, where there might be a possibility of some doped Mn atoms diffusing into deeper lattice sites, the substantial cost associated with doping at the subsurface site makes such diffusion challenging.

With the most stable Mn doping locations identified for each of the facets, we can proceed to assess the formation energy using the equation[21] described in equation 5.1:

$$E_f(\alpha) = E(\alpha) - E(0) + \sum n(\alpha)\mu(\alpha) \tag{5.1}$$

Here, E(α) and E(0) represent the total energies of the supercell with and without defect α. n(α) denotes the number of each atom added or removed, where the convention n(α) = -1 is used if an atom is added, while n(α) = +1 is employed if an atom is removed. $\mu(\alpha)$ represents the chemical potential of atom α. These values are provided for each of the facets in Table 5.1, and they have been computed under both Mn-rich and Pb-rich conditions. Notably, all of the formation energies are quite similar and are found to be negative, suggesting that all facets appear to be suitable for the introduction of Mn.

Facet (termination)	Formation energy
[112](CsPbBr)	−1.0014eV
[100](CsPbBr)	−0.4542eV
[012](CsPbBr)	−0.2571eV
[110](CsPb)	−0.1395eV
[002](CsPb)	−0.3295eV

TABLE 5.1: Formation Energy of Mn doping each Noncubic Facet [112], [100], and [012] and Cubic Facets [110], [002] for Mn-Rich and Pb-Rich Conditions(The termination has been indicated in each case).

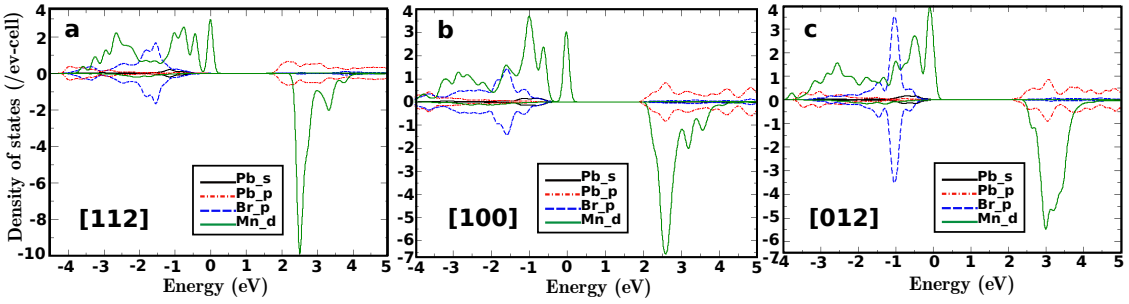

FIGURE 5.2: Up (upper panel) and the down (lower panel) spin projected Pb s,p, Br p, and the Mn d partial density of states for (a) [112], (b) [100], and the (c) [012] facet

To investigate the effects of Mn doping, we proceeded to analyze the partial density of states, as depicted in Figure5.2 for the [112], [100], and [012] facets. In addition to the

up and down spin-projected (upper and lower panels, respectively) Mn d partial density of states, we also plotted the contributions from Pb s, Pb p, and Br p orbitals originating from a single Pb and Br atom belonging to the surface layer. This allowed us to pinpoint the band edges associated with the host material. In all cases, the system was observed to exhibit insulating behavior.

When examining the results presented in Figure 5.2a, it becomes evident that the Mn up-spin states are occupied, while the Mn down-spin states remain unoccupied. This observation implies that Mn isovalently substitutes for the Pb atom and carries a valency of +2. Alongside the Mn d states, the valence band incorporates contributions from Pb s states that are hybridized with Br p states, as previously discussed in the context of understanding the electronic structure of $CsPbBr_3$. The predominantly Pb s states resulting from these interactions are situated deeper within the valence band and do not significantly contribute within the depicted energy window. In contrast, the conduction band primarily consists of Pb p states. It's worth noting that while the up-spin Mn d states are located within the band gap, the Mn d down-spin states reside within the conduction band. A similar scenario is observed for Mn doping into the [100] and [012] surfaces, although the depth of the Mn d down-spin states within the conduction band varies in Figure 5.2b and Figure 5.2c.

A comparable analysis was conducted for the cubic facets [110] and [002], as illustrated in Figure 5.3a and 5.3b, respectively. In both instances, the system was confirmed to exhibit insulating behavior, and the predominant character of the states contributing to the valence and conduction bands resembled what was observed in Figure 2.

However, in this particular scenario, it is evident that both the up and down states associated with Mn are positioned within the band gap of the host material for both the [110] and [002] facets. This placement of Mn states within the band gap stands out as a notable distinction when compared to the [112], [100], and [012] facets, where the up-spin Mn d states were found within the band gap while the down-spin states resided within the conduction band.

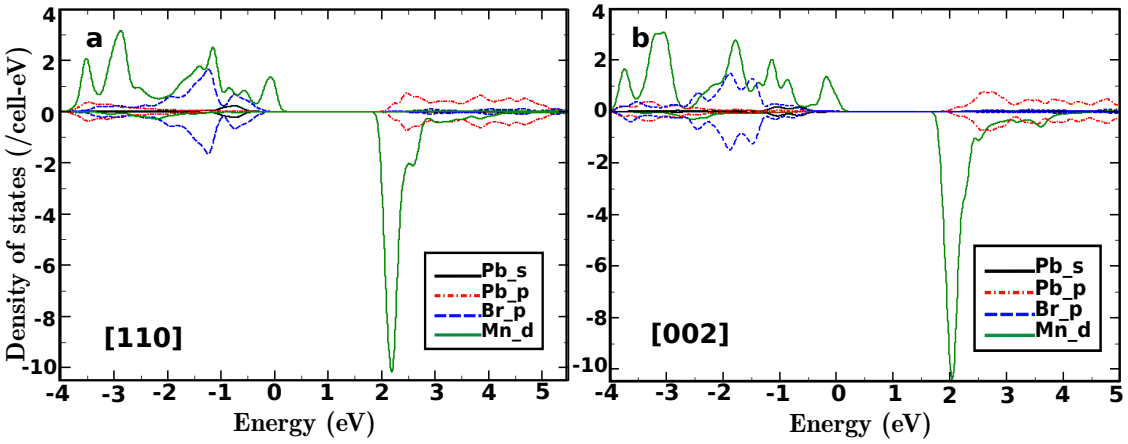

FIGURE 5.3: Up (upper section of the panel) and the down (lower section of the panel) spin projected Pb s,p, Br p, and the Mn d partial density of states for (a) [110] and the (b) [002] facet.

The density of states shown in Figures 5.2 and 5.3 clearly demonstrates that the placement of Mn d states can lead to distinct behaviors. Upon examining the density of states in Figure 5.2a, for example, it becomes evident that the host states exhibit a band gap of 2.25 eV, which closely resembles the value of 2.34 eV observed for the host states in Figure 5.3a.

Assuming uniform onsite energies for all the d levels on Mn, the exchange splitting (dE) that is observed can be related to the energy difference between configurations at a Mn site and can be expressed as follows 5.2:

$$dE = E\left(\mathrm{d}^4_{\mathrm{up}}\ \mathrm{d}^1_{\mathrm{dn}}\right) - E\left(\mathrm{d}^5_{\mathrm{up}}\right) \tag{5.2}$$

This equation reflects the energy difference between the configurations at a Mn site, with d orbitals accommodating different numbers of up-spin and down-spin electrons.

Assuming an intra-atomic exchange interaction strength (J) between parallel spins on Mn, we can relate the exchange splitting to J, where a fully polarized configuration is considered at the Mn site. In this scenario, Mn dE can be expressed as:, Mn, $dE = 4J$, However, it's important to note that this assumption doesn't hold exactly because the up-spin Mn d electron occupancy is 4.85 while the down-spin occupancy is 0.488 in both of these cases.

Since J is an intrinsic atomic property, this would imply that the exchange splitting in the two cases should be similar. However, we observe that the exchange splitting for Figure 2a is calculated to be 2.11 eV, while it is smaller, measured at 1.83 eV, for the Mn d partial density of states shown in Figure 3a. This discrepancy arises due to the initial assumption of the same orbital energies for both sets of Mn atoms. The ligand field created by the first shell of neighbors results in a different splitting of the Mn d levels in the two cases.

In Figure 5.2a, the Mn atom is surrounded by a first shell of neighbors consisting of three Mn–Br bond lengths in the range of 2.52–2.55å, along with two shorter bonds between Mn and pseudohydrogens. In contrast, in the case illustrated in Figure 3a, there are four short Mn–Br bond lengths in the range of 2.50–2.60Å, while the remaining two Mn–Br bond lengths are longer, measuring 3.11 and 3.45Å. This difference results in a significant crystal-field splitting between the Mn d levels, which is responsible for the smaller exchange splitting observed in this case.

To provide additional support for this observation, we have represented the orbital-projected density of states in Figure 5.5. The presence of long Mn–Br bonds, as seen in Figure 5.4a for Mn doping in the [110] facet, leads to the stabilization of the dxy orbital relative to the dxz orbital by approximately 0.3 eV. This stabilization shifts the minority spin Mn states into the band gap, contributing to the electronic structure of the material.

We can now consider the implications of the different positions of the Mn d levels. The situation depicted in Figure 5.2 is schematically represented in Figure 5.6a. In this case, the photoexcited electron decays from the host conduction band to the Mn d up-spin levels where the hole is located. Consequently, the transition probability from these levels is expected to be low.

Conversely, the scenario illustrated in Figure 5.3 corresponds to what is shown in Figure 5.6b. In this case, the photoexcited electron decays via a transition between the Mn d levels. As a result, the transition probability for this process is expected to be high.

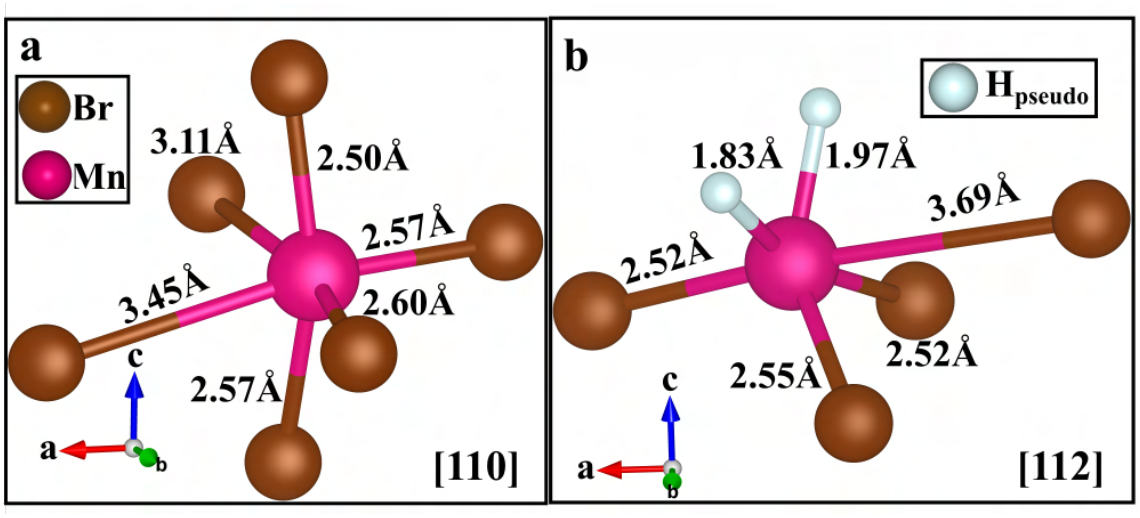

FIGURE 5.4: Mn–Br bond lengths for the surface doped Mn in the (a) [110] and the (b) [112] facet

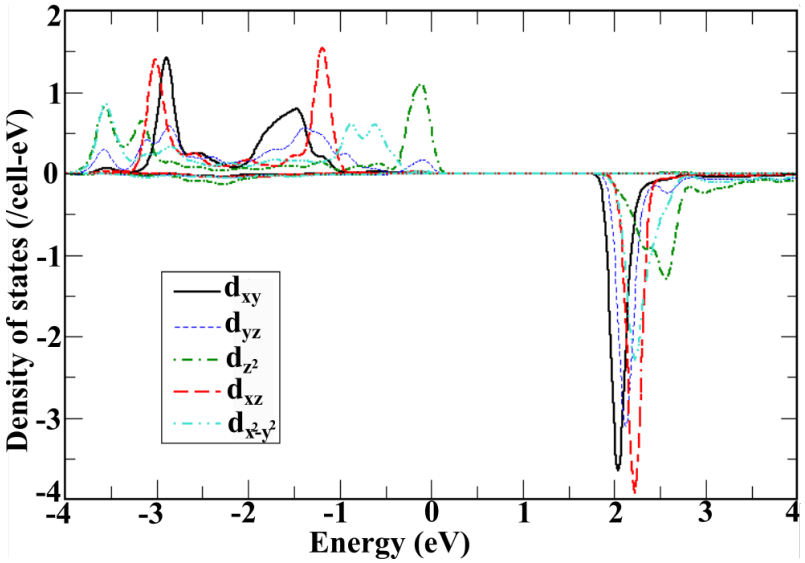

FIGURE 5.5: Orbital projected density of states of Mn d levels in [110] facets for the majority (upper section) and minority (lower section) spin.

In conclusion, our analysis reveals that the presence of other facets in the 26-faceted polyhedron introduces a substantial proportion of nonemissive sites. This is the primary reason why Mn doping does not lead to emission in this case. In contrast, the cubic facets are found to be emissive, and as a consequence, efficiency may be enhanced by designing a structure with exclusively cubic facets and a larger surface area, as demonstrated by the structure with arms. This insight suggests that manipulating the shape of the nanocrystal could be a promising strategy for designing materials with optimized optoelectronic

properties.

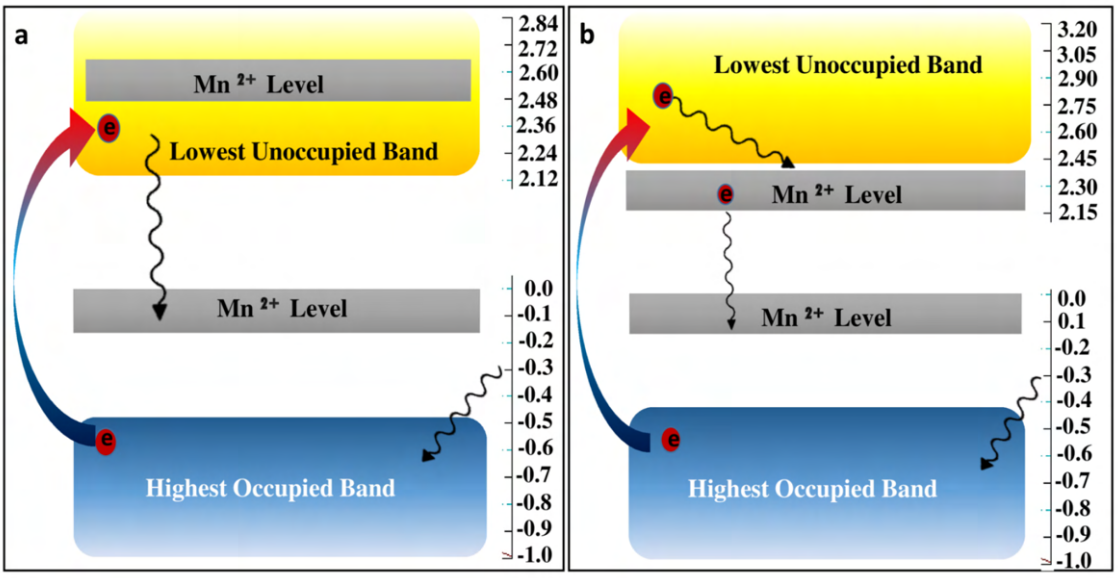

FIGURE 5.6: A schematic diagram showing the transitions taking place in the (a) noncubic facets and (b) the cubic facets.

4 Conclusion

The investigation of Mn doping in both cubic and noncubic facets of $CsPbBr_3$ has been undertaken. In both scenarios, Mn doping was observed to substitute a surface or near-surface Pb atom. However, there were distinctive electronic behaviors:

(1) Cubic Facets: Mn doping in cubic facets results in the emergence of Mn states within the band gap of the host material. This leads to emissive behavior, accounting for the emissive nature of Mn doping in cubic facets.

(2) Noncubic Facets: Conversely, Mn doping in noncubic facets induces emission from the conduction band of the host material to the Mn states. This elucidates the nonemissive character of Mn doping in noncubic facets.

This study underscores the potential for enhancing optical properties by controlling the facets that can be stabilized experimentally. Tuning the facet structure offers a promising avenue for improving the optical properties of materials.

References

[1] Federica Bertolotti, Loredana Protesescu, Maksym V Kovalenko, Sergii Yakunin, Antonio Cervellino, Simon JL Billinge, Maxwell W Terban, Jan Skov Pedersen, Norberto Masciocchi, and Antonietta Guagliardi. Coherent nanotwins and dynamic disorder in cesium lead halide perovskite nanocrystals. *ACS nano*, 11(4):3819–3831, 2017.

[2] P E Blöchl. Projector augmented-wave method. *Physical Review B*, 50(24):17953–17979, dec 1994.

[3] Shyamashis Das, Somnath Ghara, Priya Mahadevan, A Sundaresan, J Gopalakrishnan, and DD Sarma. Designing a lower band gap bulk ferroelectric material with a sizable polarization at room temperature. *ACS Energy Letters*, 3(5):1176–1182, 2018.

[4] Samrat Das Adhikari, Amit K Guria, and Narayan Pradhan. Insights of doping and the photoluminescence properties of mn-doped perovskite nanocrystals. *The Journal of Physical Chemistry Letters*, 10(9):2250–2257, 2019.

[5] Anirban Dutta, Rakesh Kumar Behera, and Narayan Pradhan. Solvent polarity: How does this influence the precursor activation, reaction rate, crystal growth, and doping in perovskite nanocrystals? *ACS Energy Letters*, 4(4):926–932, 2019.

[6] SK Dutta, A Dutta, AK Guria, N Pradhan, et al. Chemically tailoring the dopant emission in manganese-doped cspbcl 3 perovskite nanocrystals. *Angewandte Chemie (International ed. in English)*, 56(30):8746–8750, 2017.

[7] Sumit Kumar Dutta and Narayan Pradhan. Coupled halide-deficient and halide-rich reaction system for doping in perovskite armed nanostructures. *The Journal of Physical Chemistry Letters*, 10(21):6788–6793, 2019.

[8] David A Egger and Leeor Kronik. Role of Dispersive Interactions in Determining Structural Properties of Organic–Inorganic Halide Perovskites: Insights from First-Principles Calculations. *The Journal of Physical Chemistry Letters*, 5(15):2728–2733, aug 2014.

[9] Di Gao, Bo Qiao, Zheng Xu, Dandan Song, Pengjie Song, Zhiqin Liang, Zhaohui Shen, Jingyue Cao, Junjie Zhang, and Suling Zhao. Postsynthetic, reversible cation exchange between pb2+ and mn2+ in cesium lead chloride perovskite nanocrystals. *The Journal of Physical Chemistry C*, 121(37):20387–20395, 2017.

[10] Celine Gerard, Ruma Das, Priya Mahadevan, and DD Sarma. Effective mass-driven structural transition in a mn-doped zns nanoplatelet. *The Journal of Physical Chemistry Letters*, 4(6):1023–1027, 2013.

[11] M Goryca, T Kazimierczuk, M Nawrocki, A Golnik, JA Gaj, P Kossacki, P Wojnar, and G Karczewski. Optical manipulation of a single mn spin in a cdte-based quantum dot. *Physical review letters*, 103(8):087401, 2009.

[12] Stefan Grimme. Semiempirical GGA-type density functional constructed with a long-range dispersion correction. *Journal of Computational Chemistry*, 27(15):1787–1799, nov 2006.

[13] H-E Gumlich. Electro-and photoluminescence properties of mn2+ in zns and zncds. *Journal of Luminescence*, 23(1-2):73–99, 1981.

[14] Abhijit Hazarika, Arunasish Layek, Suman De, Angshuman Nag, Saikat Debnath, Priya Mahadevan, Arindam Chowdhury, and Dipankar Das Sarma. Ultranarrow and widely tunable mn 2+-induced photoluminescence from single mn-doped nanocrystals of zns-cds alloys. *physical review letters*, 110(26):267401, 2013.

[15] Shunsuke Hirotsu, Jimpei Harada, Masashi Iizumi, and Kazuo Gesi. Structural phase transitions in cspbbr3. *Journal of the Physical Society of Japan*, 37(5):1393–1398, 1974.

[16] Niladri S Karan, Suresh Sarkar, DD Sarma, Paromita Kundu, N Ravishankar, and Narayan Pradhan. Thermally controlled cyclic insertion/ejection of dopant ions and reversible zinc blende/wurtzite phase changes in zns nanostructures. *Journal of the American Chemical Society*, 133(6):1666–1669, 2011.

[17] G Kresse and J Furthmüller. Efficiency of ab-initio total energy calculations for metals and semiconductors using a plane-wave basis set. *Computational Materials Science*, 6(1):15–50, 1996.

[18] G Kresse and J Furthmüller. Efficient iterative schemes for ab initio total-energy calculations using a plane-wave basis set. *Physical Review B*, 54(16):11169–11186, oct 1996.

[19] G. Kresse and J. Hafner. Ab initio molecular dynamics for liquid metals. *Physical Review B*, 47(1):558–561, 1993.

[20] G Kresse and J Hafner. Ab initio molecular-dynamics simulation of the liquid-metal–amorphous-semiconductor transition in germanium. *Physical Review B*, 49(20):14251–14269, may 1994.

[21] G Kresse and D Joubert. From ultrasoft pseudopotentials to the projector augmented-wave method. *Physical Review B*, 59(3):1758–1775, jan 1999.

[22] Dietrich Langer and Sumiaki Ibuki. Zero-phonon lines and phonon coupling in zns: Mn. *Physical Review*, 138(3A):A809, 1965.

[23] Kyuho Lee, Éamonn D Murray, Lingzhu Kong, Bengt I Lundqvist, and David C Langreth. Higher-accuracy van der Waals density functional. *Physical Review B*, 82(8):81101, aug 2010.

[24] Y Léger, L Besombes, L Maingault, D Ferrand, and H Mariette. Geometrical effects on the optical properties of quantum dots doped with a single magnetic atom. *Physical review letters*, 95(4):047403, 2005.

[25] Ming Liu, Guohua Zhong, Yongming Yin, Jingsheng Miao, Ke Li, Chengqun Wang, Xiuru Xu, Clifton Shen, and Hong Meng. Aluminum-doped cesium lead bromide perovskite nanocrystals with stable blue photoluminescence used for display backlight. *Advanced Science*, 4(11):1700335, 2017.

[26] Wenyong Liu, Qianglu Lin, Hongbo Li, Kaifeng Wu, István Robel, Jeffrey M Pietryga, and Victor I Klimov. Mn^{2+}-doped lead halide perovskite nanocrystals with dual-color emission controlled by halide content. *Journal of the American Chemical Society*, 138(45):14954–14961, 2016.

[27] Priya Mahadevan and Alex Zunger. Room-temperature ferromagnetism in mn-doped semiconducting cdgep 2. *Physical review letters*, 88(4):047205, 2002.

[28] Wasim J Mir, Metikoti Jagadeeswararao, Shyamashis Das, and Angshuman Nag. Colloidal mn-doped cesium lead halide perovskite nanoplatelets. *ACS Energy Letters*, 2(3):537–543, 2017.

[29] Koichi Momma and Fujio Izumi. *VESTA*: a three-dimensional visualization system for electronic and structural analysis. *Journal of Applied Crystallography*, 41(3):653–658, jun 2008.

[30] Debayan Mondal and Priya Mahadevan. Shape control of emissive properties of mn-doped cspbbr3 nanocrystals. *The Journal of Physical Chemistry C*, 125(21):11462–11467, 2021.

[31] Hendrik J Monkhorst and James D Pack. Special points for Brillouin-zone integrations. *Physical Review B*, 13(12):5188–5192, jun 1976.

[32] R Parrot and C Blanchard. Effect of uniaxial stresses on the e 4 level of a 3 d 5 ion in tetrahedral symmetry: Study of mn++ in zns. *Physical Review B*, 6(10):3992, 1972.

[33] Lucheng Peng, Sumit Kumar Dutta, Debayan Mondal, Biswajit Hudait, Sanjib Shyamal, Renguo Xie, Priya Mahadevan, and Narayan Pradhan. Arm growth and facet modulation in perovskite nanocrystals. *Journal of the American Chemical Society*, 141(40):16160–16168, 2019.

[34] John P Perdew, Kieron Burke, and Matthias Ernzerhof. Generalized Gradient Approximation Made Simple. *Physical Review Letters*, 77(18):3865–3868, oct 1996.

[35] Daniel Rossi, David Parobek, Yitong Dong, and Dong Hee Son. Dynamics of exciton–mn energy transfer in mn-doped cspbcl3 perovskite nanocrystals. *The Journal of Physical Chemistry C*, 121(32):17143–17149, 2017.

[36] Dang Dinh Thong and O Goede. Optical study of highly mn-doped zns crystals. *physica status solidi (b)*, 120(2):K145–K150, 1983.

[37] Yun Wang, Tim Gould, John F Dobson, Haimin Zhang, Huagui Yang, Xiangdong Yao, and Huijun Zhao. Density functional theory analysis of structural and electronic properties of orthorhombic perovskite CH3NH3PbI3. *Physical Chemistry Chemical Physics*, 16(4):1424–1429, 2014.

[38] TJ Whitcher, LC Gomes, D Zhao, M Bosman, X Chi, Y Wang, A Carvalho, HK Hui, Q Chang, MBH Breese, et al. Dual phases of crystalline and electronic structures in the nanocrystalline perovskite cspbbr3. *NPG Asia Materials*, 11(1):70, 2019.

[39] Kunyuan Xu, Chun Che Lin, Xiaobin Xie, and Andries Meijerink. Efficient and stable luminescence from mn_{2+} in core and core–isocrystalline shell cspbcl3 perovskite nanocrystals. *Chemistry of Materials*, 29(10):4265–4272, 2017.

[40] Yi Yang, Fei Gao, Shiwu Gao, and Su-Huai Wei. Origin of the stability of two-dimensional perovskites: a first-principles study. *Journal of Materials Chemistry A*, 6(30):14949–14955, 2018.

[41] Jung Ho Yu, Xinyu Liu, Kyoung Eun Kweon, Jin Joo, Jiwon Park, Kyung-Tae Ko, Dong Won Lee, Shaoping Shen, Kritsanu Tivakornsasithorn, Jae Sung Son, et al. Giant zeeman splitting in nucleation-controlled doped cdse: Mn2+ quantum nanoribbons. *Nature materials*, 9(1):47–53, 2010.

Chapter 6

Origin of Dual Band Gap in 2D Perovskites

1 Introduction

In the quest to enhance the performance of optoelectronic devices such as solar cells, light-emitting diodes (LEDs), and photodetectors, the design and engineering of semiconductor materials play a pivotal role[6, 7, 19, 20, 22, 32, 35, 36]. The discovery of perovskite materials with remarkable photovoltaic efficiency has revitalized the field of solar energy conversion. Traditional bulk perovskites, however, exhibit limitations in terms of stability and toxicity. This has motivated researchers to explore novel perovskite-based materials, leading to the focus on two-dimensional perovskites as a possible option. Two-dimensional perovskites are layered structures composed of alternating organic and inorganic layers. There could be two types of stackings, one in which the cation of one inorganic layer lies directly above that of the next inorganic layer[5] is what we will be focusing on in this chapter. Unlike their three-dimensional counterparts, these materials offer improved stability while retaining the desirable optoelectronic properties of perovskite

semiconductors[4, 26, 27, 30, 38]. These materials, with their layered architecture and tunable band structures, hold the promise of revolutionizing various technological domains, including photovoltaics, light-emitting diodes (LEDs), and sensors[31, 34].

It has been seen that the photophysics of these 2D RP perovskites is controlled by low-energy edge states, which improve the optoelectronic properties of these materials [2, 33, 37]. The photogenerated excitons dissociate into long-lived free carriers at the crystal edge when they diffuse from the bulk to the edge region [2, 37]. Further, with increasing the number of the inorganic layers in each unit from n=1 to n=5, the binding energies have been seen to vary from 450 meV to 100 meV[1, 8–10], indicating that excitons are more dominant than free carriers. One viewpoint that exists is that the formation of edge states above a critical thickness has been associated with the strain relaxations of the surface concerning the bulk. These structural relaxations lead to states which are located in the band gap, as has been seen in various semiconductors. However, some of the experimental results do not support this picture. There are instances of n = 1 perovskites showing anomalous conductivity at the edges, which is attributed to edge states[33].

In the case of perfect crystals, their crystal structures exhibit a continuous, uniform pattern with no discernible boundaries. In practice, though, the crystal structure typically includes inherent boundaries. These boundaries give rise to differences in the chemical compositions of the atoms located at the crystal's edges compared to those found in the interior. Consequently, the material's edge region displays distinct properties when contrasted with its bulk. For example, the different edge configurations have been confirmed to significantly impact the optoelectronic properties of the typical 2D material of graphene[25, 34]. As for 2D RP perovskites, their edge regions have been reported to exhibit many unique properties different from the bulk region. The most characteristic property of the edge states is the low energy PL emission. The edge state was first observed in $(BA)_2(MA)_{n-1}Pb_nI_{3n+1}$ with n > 2 [2]. Through photoluminescence (PL) mapping using various spectral bands, the study exclusively detected lower energy emissions (at 1.68 eV) at the crystal's edge in an exfoliated crystal of $(BA)_2(MA)_{n-1}Pb_nI_{3n+1}$(where n =

3). This was in addition to the conventional emission band at 2.01 eV, which emanated from all regions of the crystal[2, 37]. Zhao et al.[37]discovered that the emission from the edge states in $(BA)_2(MA)_{n-1}Pb_nI_{3n+1}$ can be manipulated through a cation exchange process involving MA^+ and BA^+ ions. They observed that emission could be eliminated by rinsing the material with a BAI solution and generated by rinsing with an MAI solution. Importantly, this cation exchange process was found to be repeatable. Shortly thereafter, Zhang et al.[39] conducted a theoretical exploration into the origin of edge states and proposed that these states arose due to distinct chemical properties exhibited by iodine (I) and lead (Pb) atoms. The principal factor driving charge separation in the edge states was identified as the presence of unsaturated iodine bonds at the periphery. In two-dimensional perovskites, the valence band maxima (VBM) was predominantly constituted by I atomic orbitals, while the conduction band minima (CBM) was formed by Pb atom orbitals. Although the unsaturated iodine and lead bonds at the edge region didn't introduce trap states within the original bandgap, they did influence orbital localization. Metallic Pb atoms were capable of rectifying unsaturated chemical bonds and repairing defects through changes in their oxidation states, thereby promoting electron delocalization. On the other hand, the unsaturated covalent bonds of iodide exerted a strong force that localized holes. This disparity in confinement between electrons and holes resulted in charge separation, giving rise to the edge states. Furthermore, the prolonged existence of carriers in these edge states could be explained by the limited overlap of wave functions between electrons and holes and the brief quantum coherence between excited and ground electronic states.

In this chapter through Density Functional Theory (DFT) simulations, we intend to elucidate the roles of organic-inorganic interactions, lattice distortions, and quantum confinement effects in shaping the electronic band structure of these materials. We hypothesize that the interplay between organic cations and inorganic frameworks plays a pivotal role in generating the edge state as well as the dual-band gap phenomenon. The interaction is found to be weaker at the surface, compared to what is found in the bulk. This allows for the easy removal of the molecular units from the surface and the edges compared to

the bulk. The consequent reconstructions that take place to accommodate the removal of a molecular unit lead to the modified electronic structure of regions of the surface/edges compared to the bulk. This leads to the dual emission and also provides us with a route to quench it. The primary defect being formed is neutral, involving a molecule in addition to an apical anion. It is therefore surprising to see that the energy to form the second similar defect, especially at the edges is lower than what is required for the first. This suggests that depending on the synthesis conditions, one can have large regions with these defects forming. We have also found that the formation energy of some defects is negative and can be changed with experimental conditions as mentioned above, Zhao et al.[37] also found by their TEM-SAED that the edge state dual emission of 2D RP perovskites can be generated or eliminated by MA+ or BA+ solution treatment, respectively. The presence of edge states in 2D RP perovskites was attributed to the distortion of their structure induced by stress. Furthermore, this stress at the periphery renders 2D RP perovskites unstable, prompting them to alleviate the stress through structural rearrangements, such as the creation of BA-vacancies or substitutions. The desorption energy of various vacancy sites was also computed using the BA_2PbI_4 nanoribbon containing seven inorganic octahedrons. Among these sites, the BA-vacancy, situated at the nanoribbon's edge, exhibited the lowest desorption energy at 5.01 eV, compared to the desorption energies of other vacancy sites ranging from 5.16 to 5.18 eV. This suggests that BA-vacancies are more likely to form at the edges of 2D RP perovskites[17].

2 Methodology

To delve into the underlying causes of the dual-band gap phenomenon observed in two-dimensional layered perovskite semiconductors, we conducted rigorous first-principles calculations. These calculations were performed employing a plane wave basis set and implemented within the framework of density functional theory (DFT) using the Vienna Ab initio Simulation Package (VASP)[22–25], complemented by projected augmented-wave potentials. Our approach involved approximating the exchange-correlation functional within

the generalized gradient approximation (GGA) as outlined in the Perdew-Burke-Ernzerhof functional[48]. In our computational framework, the incorporation of nonlocal, weak van der Waals (vdW) interaction was deemed essential for accurately predicting the structural properties of these materials. Specifically, we employed a GGA+vdW [14, 17] density functional theory calculation, which proved to be highly effective in estimating the lattice parameters. A plane-wave energy cutoff of 550 eV, coupled with Brillouin zone sampling using $4 \times 4 \times 1$ Monkhorst-Pack grids[39], was found to ensure the convergence of energies and forces during our calculations. For structural relaxations, we allowed the ions within the system to adjust their positions until the atomic forces reached a tolerance level of less than 0.001 eV/Å, ensuring the attainment of energetically favourable configurations. In our investigation, we selected a representative layered 2D perovskite structure characterized by the chemical formula $(BA)_2PbI_4$. We adopted the experimental crystal structure of bulk $(BA)_2PbI_4$[28], which belongs to the Pbnm space group, as our starting point. While we held the lattice parameters fixed at their experimentally determined values of a = 8.21Å, b = 8.29Å, and c = 11.80Å, we allowed the internal atomic positions to relax to their most stable positions. The optimized unit cell was then employed to construct surfaces corresponding to the low-energy facets observed in experimental observations. Initially, we generated symmetric slabs stacked along the [001] direction, consisting of 17 layers. Notably, the $(BA)_2PbI_4$ crystal comprises alternating neutral BAI and PbI_2 planes along these directions, giving rise to two potential surface terminations for the slab, either the BAI or the PbI_2 surface termination. Prior research has indicated that the BAI-terminated surface is energetically favored due to the significant energy cost associated with breaking the PbI_6 octahedra required for a PbI_2 termination. Moreover, these 2D layer perovskites are typically terminated with hydrophobic BA molecules on the surface. This also helps to improve the stability in the presence of moisture. To prevent unwanted interactions between consecutive slabs, we introduced a vacuum region of 15Å between them. This configuration ensured that the periodically repeated units in the growth direction remained well-decoupled. All schematic representations of the crystal structures were generated using the VESTA software.

3 Result and Discussion

In this chapter, we have investigated the factors governing the formation and stability of low-emission edge states in $(BA)_2PbI_4$ perovskites. Our analysis has involved determining the formation energy, a key parameter in understanding these aspects. For that, we have defined the formation energy as[21],

$$\Delta H_f = E(A) - E(0) + \sum_{\alpha} n_\alpha \mu_\alpha \tag{6.1}$$

Where E(A) and E(0) are the total energies of the supercell with and without the defect A. n is the number of each atom that makes up the defect, where the convention n= -1 if an atom is added from the reservoir, while n = +1 if an atom is removed to the reservoir, has been used. Here μ_α is the chemical potential of the atom. Since the formation energies are conventionally defined with respect to the elemental solid(s), we express μ_α as the sum of a component due to the element in its most commonly occurring structure μ_s, and an excess chemical potential $\Delta\mu_\alpha$, i.e. $\mu_\alpha = \mu_s + \Delta\mu_\alpha$. Here μ_s for Pb[3] and Iodine[29] correspond to the total energies evaluated for the fully optimized elemental solids in their observed crystal structures. The chemical potential for BA molecule was evaluated by considering a single BA molecule enclosed within a cube of dimensions 10Å.

In our initial investigation, we assessed the stability of the slab by removing a BA molecule from the surface layer, as depicted in Figure 1a. However, upon removing one BA molecule from the surface, we observed a significant distortion in the nearest PbI_6 octahedra. Specifically, the bond length of an out-of-plane iodine atom increased from 3.23Å to 4.47Å, i.e an increase of 1.24Å, as shown in Figure 6.1b. This suggests that the interaction of the apical iodine with the Pb-I network is very weak, and so the removal of the molecule is accompanied by the dislodging of an apical I atom.

Given these observations, we sought to determine whether it is energetically favorable to remove a single BA molecule or an entire BA-I unit from the surface. To address this, we computed the

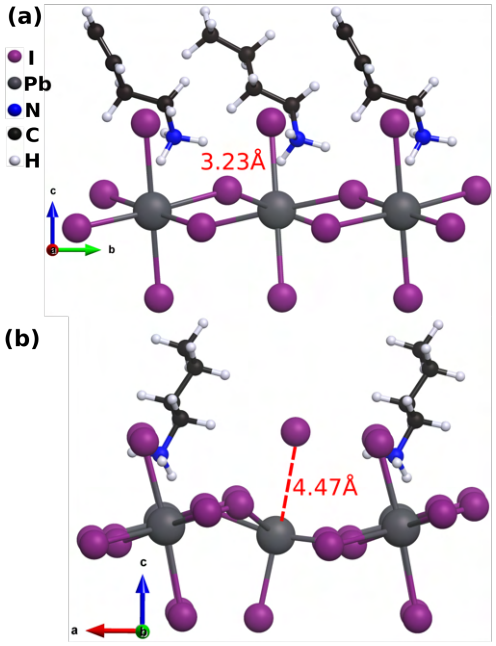

FIGURE 6.1: The bondlength change of the epical iodine of surface layer (a) before and (b) after removing the molecule

formation energy associated with removing them. Utilizing Equation 6.1 where, E(A) is the energy without the BA molecule in one case or without the BA-I unit in the other, the computed formation energies given in Table 6.1.

	Formation Energy (eV)
Only one BA molecule was removed from the surface layer	$5.35 + \Delta\mu_{BA}$
One (BA+I) unit removed from the surface layer	$4.13 + \Delta\mu_{BA} + \Delta\mu_{I}$

TABLE 6.1: Formation energies in terms of chemical potential from Equation 6.1, when only one BA+ molecule removed and when one (BA-I) unit removed

To evaluate the formation energies under different conditions, the limits on the chemical potentials were evaluated. To determine these ranges, we apply the condition of thermodynamic stability of bulk $(BA)_2PbI_4$, as defined by equations 6.2a or 6.2b.

$$2\Delta\mu_{BAI} + \Delta\mu_{PbI_2} = H_f\left(BA_2PbI_4\right) \tag{6.2a}$$

$$2\Delta\mu_{BA} + \Delta\mu_{Pb} + 4\Delta\mu_{I} = H_f\left(BA_2PbI_4\right) \tag{6.2b}$$

Furthermore, in selecting the chemical potentials, we took into account the constraint that prevents the precipitation of BAI and PbI_2 in the reaction. This condition imposes

limitations on the chemical potentials, as specified in Equation 6.3. As Formation energy from 6.2b is more negative than 6.2a. So It will not give the proper constraint and conditions for further analysis. That is why here We will use only equation 2a for further analysis.

$$\Delta\mu_{BA} + \Delta\mu_I < \Delta H_f(BAI) \tag{6.3a}$$

$$\Delta\mu_{Pb} + 2\Delta\mu_I < \Delta H_f(PbI_2) \tag{6.3b}$$

Here, H_f(AB) corresponds to the formation energy of the compound AB. As in the expression of the formation energy in Table 6.1, the only variable term is the chemical potential of iodine so we have chosen the two extreme conditions for iodine i.e iodine-rich ($\Delta\mu_I$ = 0.00 eV) and iodine-poor (($\Delta\mu_I$ = -3.37 eV)

	I poor condition: $\Delta\mu_{BA} = 0.00$eV $\Delta\mu_I = -3.37$eV	**I rich condition:** $\Delta\mu_{BA} = -5.73$eV $\Delta\mu_I = 0.00$eV
Only one BA molecule was removed from the surface layer	5.35eV	−0.37eV
One (BA+I) unit removed from the surface layer	0.76eV	−1.59eV

TABLE 6.2: Formation energies under different reaction conditions(halide rich and halide poor).

From the analysis presented in Table 6.2 we see that it is more favorable to remove an entire BA-I unit from the surface than to remove just one BA molecule, with the formation energies becoming negative under iodine rich conditions. These results suggest that one can tune the experimental conditions making it difficult for either BA or BA-I to form. We also compared the energy required to remove one BA-I unit from the bulk layer (Figure 6.2). The defect formation energies for removing a BA-I unit from the surface and from the bulk are given in Table 6.3 in terms of the chemical potentials of BA molecule ($\Delta\mu_{BA}$) and Iodine ($\Delta\mu_I$).

	Formation Energy (eV)
(BA+I) unit removed from Surface Layer	$4.13 + \Delta\mu_{BA} + \Delta\mu_I$
(BA+I) unit removed from Bulk	$6.16 + \Delta\mu_{BA} + \Delta\mu_I$

TABLE 6.3: Formation energies in terms of chemical potential from Equation 6.1, when (BA+I) unit is removed from surface and bulk.

Again here one needs to impose the conditions for the chemical potentials. under BA-rich, I-poor conditions one has $\Delta\mu_{BA}$ = 0.00 eV, $\Delta\mu_{Pb}$ = -1.42 eV and $\Delta\mu_{I}$ = -3.37 eV, and the formation energies are found to be +0.76 eV and +2.79 eV for one (BA+I) unit removed from surface layer and bulk respectively (Table 3). On the other hand under BA-poor, I-rich conditions one has $\Delta\mu_{BA}$ = -5.73 eV, $\Delta\mu_{Pb}$ = -3.46 eV and $\Delta\mu_{I}$ = 0.00 eV, with the formation energies found to be -1.59 eV and +0.43 eV for one (BA+I) unit removed from surface layer and bulk respectively (Table 6.3). These results suggest that it is easier to remove one BA-I unit from the surface of the slab than the bulk of the slab, and by choosing appropriate reaction conditions, the formation energy may be made positive.

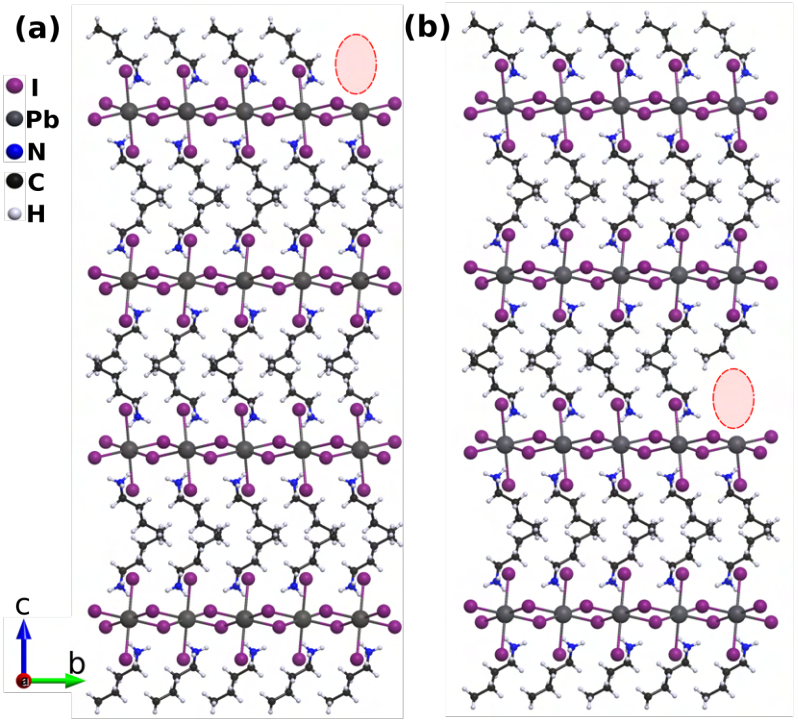

FIGURE 6.2: Schematic representation of the slab model used for the calculations for BA-I defect in different site

	BA rich I poor condition: $\Delta\mu_{BA} = 0.00$eV $\Delta\mu_{Pb} = -1.42$eV $\Delta\mu_{I} = -3.37$eV	Moderate BA Moderate I condition: $\Delta\mu_{BA} = -2.86$eV $\Delta\mu_{Pb} = -2.44$eV $\Delta\mu_{I} = -1.68$eV	BA poor I rich condition: $\Delta\mu_{BA} = -5.73$eV $\Delta\mu_{Pb} = -3.46$eV $\Delta\mu_{I} = 0.00$eV
(BA+I) unit removed from Surface Layer	+0.76eV	−0.40eV	−1.59eV
(BA+I) unit removed from Bulk	+2.79eV	+1.62eV	+0.43eV

TABLE 6.4: Defect formation energies under different reaction conditions (different moleculer concentrations)

To understand why it is easier to form such defects at the surface, we carried out an analysis of the Bader charges as well as examined the structure. Firstly, the Coulomb attraction between the H_N of the surface layer molecule and the apical I atom belonging to the inorganic network (Bader charge of H_N = +0.50e and I = -0.61e and bond length 2.55Å) is weaker than that in the bulk layer(Bader charge of H_N = +0.53e and I= -0.60e and bond length 2.50Å). Furthermore, there is a notable redistribution of charges within the adjacent Pb-I octahedra of the surface layer. As a result of this redistribution, it costs less to remove a BA-I unit from the surface layer in comparison to the bulk.

Subsequently, we extended our analysis to a slab model that incorporates edges. In this model, we introduced a vacuum along the crystal's z and y axes. Removing a BA-I unit from the edge of the xy plane and determining the formation energy under different conditions, we find that it costs less to remove the BA-I unit from the edge compared to the bulk (Table 6.6).

	Formation Energy (eV)
(BA+I) unit removed from the Edge of the slab	$1.46 + \Delta\mu_{BA} + \Delta\mu_I$
(BA+I) unit removed from Bulk	$6.27 + \Delta\mu_{BA} + \Delta\mu_I$

TABLE 6.5: Formation energies in terms of chemical potential from the equation: 6.1, when (BA-I) unit is removed from the edge of the slab and from the bulk.

Under BA-rich and I-poor conditions, $\Delta\mu_{BA}$ = 0.00 eV, $\Delta\mu_{Pb}$ = -1.42 eV and $\Delta\mu_I$ = -3.37 eV, the formation energies are found to be positive (Table 6.6), while under BA-poor and I-rich conditions, with $\Delta\mu_{BA}$ = -5.73 eV, $\Delta\mu_{Pb}$ = -3.46 eV and $\Delta\mu_I$ = 0.00 eV, the formation energies were negative and lower than those for the surface This suggests that the defects form more easily along the edges. This is consistent with experiments that have seen the formation of these defects along steps.

We now examine the energy cost involved in removing the second BA-I unit, once the first BA-I unit has been removed. We find that it is easier to remove the second unit after the first one has been removed (Table 6.8) due to the charge reconstruction and defect tolerance in the surface.

	BA rich I poor condition: $\Delta\mu_{BA} = 0.00$eV $\Delta\mu_{Pb} = -1.42$eV $\Delta\mu_{I} = -3.37$eV	Moderate BA Moderate I condition: $\Delta\mu_{BA} = -2.86$eV $\Delta\mu_{Pb} = -2.44$eV $\Delta\mu_{I} = -1.68$eV	BA poor I rich condition: $\Delta\mu_{BA} = -5.73$eV $\Delta\mu_{Pb} = -3.46$eV $\Delta\mu_{I} = 0.00$eV
(BA+I) unit removed from the Edge of the slab	-1.90eV	-3.07eV	-4.27eV
(BA+I) unit removed from Bulk	$+2.89$eV	$+1.74$eV	$+0.54$eV

TABLE 6.6: Defect formation energies under different reaction conditions(different moleculer concentrations)

	Formation Energy (eV)
2^{nd} $(BA + I)$ removed from surface	$+2.575 + \Delta\mu_{BA} + \Delta\mu_{I}$
2^{nd} $(BA + I)$ removed from bulk	$+3.407 + \Delta\mu_{BA} + \Delta\mu_{I}$
2^{nd} $(BA + I)$ removed from edge	$-0.715 + \Delta\mu_{BA} + \Delta\mu_{I}$
2^{nd} $(BA + I)$ removed from bulk	$+1.861 + \Delta\mu_{B} + \Delta\mu_{I}$

TABLE 6.7: Formation energies in terms of chemical potential from Equation 6.1, when 2^{nd} (BA-I) unit is removed after the 1^{st} one from different site

We now turn our attention to exploring whether the observed trend persists in the context of 3D hybrid perovskite systems. To investigate this, we examined the most extensively studied member of this series, Methylammonium lead iodide ($MAPbI_3$). We performed a similar analysis on a 17-layer orthorhombic structure of $MAPbI_3$, terminated by a MAI surface, where we removed one MA molecule and a MAI unit from both the surface layer and the bulk layer. Our objective was to determine which scenario has lower energy. To do so, we calculated the formation energies for all four of these cases in terms of the chemical potential of MA and I.

In order to assess the formation energies under varying conditions, we established limits on the chemical potentials. To determine these limits, we employed the criterion of thermodynamic stability for bulk $MAPbI_3$, as specified by Equations 6.4.

$$\Delta\mu_{MAI} + \Delta\mu_{PbI_2} = H_f\,(MAPbI_3) \tag{6.4}$$

Moreover, in the selection of chemical potentials, we considered the constraint that prevents the precipitation of MAI and PbI_2 in the reaction. This constraint places restrictions

	BA rich I poor condition: $\Delta\mu_{BA} = 0.00$eV $\Delta\mu_{Pb} = -1.42$eV $\Delta\mu_I = -3.37$eV	Moderate BA Moderate I condition: $\Delta\mu_{BA} = -2.86$eV $\Delta\mu_{Pb} = -2.44$eV $\Delta\mu_I = -1.68$eV	BA poor I rich condition: $\Delta\mu_{BA} = -5.73$eV $\Delta\mu_{Pb} = -3.46$eV $\Delta\mu_I = 0.00$eV
2^{nd} $(BA + I)$ removed from Surface	-0.795	-1.965	-3.155
2^{nd} (BA + I) removed from bulk (Surface structure)	+0.037	-1.133	-2.323
2^{nd} $(BA + I)$ removed from Edge	-4.085	-5.255	-6.445
2^{nd} (BA + I) removed from bulk (Edged structure)	-1.509	-2.679	-3.869

TABLE 6.8: Defect formation energies under different reaction conditions(different moleculer concentrations)

	Formation Energy (eV)
MA molecule removed from surface	$+4.658 + \Delta\mu_{BMA} + \Delta\mu_I$
MA molecule removed from bulk	$+4.957 + \Delta\mu_{MA} + \Delta\mu_I$
MA+I unit removed from surface	$+6.117 + \Delta\mu_{MA} + \Delta\mu_I$
MA+I unit removed from bulk	$+6.142 + \Delta\mu_{MA} + \Delta\mu_I$

TABLE 6.9: when only one MA+ molecule removed and when one (MA+I) unit removed from different sites

on the chemical potentials, as outlined in equations 6.5a and 6.5b.

$$\Delta\mu_{MA} + \Delta\mu_I < \Delta H_f(MAI) \tag{6.5a}$$

$$\Delta\mu_{Pb} + 2\Delta\mu_I < \Delta H_f(PbI_2) \tag{6.5b}$$

As indicated in the formation energy expression presented in Table 6.9, similar to previous analyses, it is necessary to consider the conditions for the chemical potentials. Under MA-rich and I-poor conditions, i.e $\Delta\ \mu_{MA} = 0.00$ eV, $\Delta\mu_{Pb} = -4.15$ eV and $\Delta\mu_I = -1.64$ eV we find that the formation energies are found to be positive for removing both MA as well as MA-I units from both the surface and the bulk (Table 6.10). Conversely, under MA-poor and I-rich conditions, i.e $\Delta\mu_{BA} = -4.85$ eV, $\Delta\mu_{Pb} = -4.21$ eV and $\Delta\mu_I = 0.00$ eV, we find that these defects may form though the formation energies are more positive

than what was found for the 2d perovskites (Table 6.10). Additionally the cost is similar to remove either MA or an MA-I unit.

	BA rich I poor condition: $\Delta\mu_{MA} = 0.00$eV $\Delta\mu_{Pb} = -4.15$eV $\Delta\mu_{I} = -1.64$eV	Moderate BA Moderate I condition: $\Delta\mu_{MA} = -2.42$eV $\Delta\mu_{Pb} = -4.19$eV $\Delta\mu_{I} = -0.82$eV	BA poor I rich condition: $\Delta\mu_{MA} = -4.48$eV $\Delta\mu_{Pb} = -4.21$eV $\Delta\mu_{I} = 0.00$eV
MA molecule removed from surface	+4.65	+2.23	-0.20
MA molecule removed from bulk	+4.95	+2.53	+0.10
MA+I unit removed from surface	+4.47	+2.87	-0.20
MA+I unit removed from bulk	+4.50	+2.89	+0.10

TABLE 6.10: Defect formation energies under different reaction conditions(different moleculer concentrations)

The reason for this observation is possibly the fact that in the case of the 3D perovskite, both ends of the molecule form bonds with the inorganic Pb-I network. In contrast, for the 2D perovskite, only one end of the molecule interacts with a single iodine atom belonging to the network, rendering the molecule more easily removable from the surface.

4 Conclusion

In this study, we probed the low-emission edge states in BA_2PbI_4 perovskites, focusing on formation energy as a key parameter. Removing a BA molecule from the surface revealed significant distortions, emphasizing weak iodine interaction. Calculations of formation energies under different conditions highlighted the preference for removing entire BA-I units than only one BA molecule, especially under iodine-rich environments. Edge analysis suggested defects form more easily along edges than in the bulk, consistent with experimental observations. Extending findings for 2D perovskites to 3D perovskites($MAPbI_3$) showcased some different trends due to the stronger interaction between the molecule and the inorganic cage. This systematic exploration provides crucial insights for controlling defect formation in perovskite materials.

References

[1] J-C Blancon, Andreas V Stier, Hsinhan Tsai, Wanyi Nie, Costas C Stoumpos, Boubacar Traore, L Pedesseau, Mikael Kepenekian, Fumiya Katsutani, GT Noe, et al. Scaling law for excitons in 2d perovskite quantum wells. *Nature communications*, 9(1):2254, 2018.

[2] J-C Blancon, Hsinhan Tsai, Wanyi Nie, Costas C Stoumpos, Laurent Pedesseau, Claudine Katan, Mikaël Kepenekian, Chan Myae Myae Soe, Kannatassen Appavoo, Matthew Y Sfeir, et al. Extremely efficient internal exciton dissociation through edge states in layered 2d perovskites. *Science*, 355(6331):1288–1292, 2017.

[3] N Bouad, L Chapon, R-M Marin-Ayral, F Bouree-Vigneron, and J-C Tedenac. Neutron powder diffraction study of strain and crystallite size in mechanically alloyed pbte. *Journal of Solid State Chemistry*, 173(1):189–195, 2003.

[4] Thomas M Brenner, David A Egger, Leeor Kronik, Gary Hodes, and David Cahen. Hybrid organic—inorganic perovskites: low-cost semiconductors with intriguing charge-transport properties. *Nature Reviews Materials*, 1(1):1–16, 2016.

[5] J Calabrese, NL Jones, RL Harlow, N Herron, DL Thorn, and Y Wang. Preparation and characterization of layered lead halide compounds. *Journal of the American Chemical Society*, 113(6):2328–2330, 1991.

[6] Stefaan De Wolf, Jakub Holovsky, Soo-Jin Moon, Philipp Loper, Bjoern Niesen, Martin Ledinsky, Franz-Josef Haug, Jun-Ho Yum, and Christophe Ballif. Organometallic halide perovskites: sharp optical absorption edge and its relation to photovoltaic performance. *The journal of physical chemistry letters*, 5(6):1035–1039, 2014.

[7] Letian Dou, Yang Yang, Jingbi You, Ziruo Hong, Wei-Hsuan Chang, Gang Li, and Yang Yang. Solution-processed hybrid perovskite photodetectors with high detectivity. *Nature communications*, 5(1):5404, 2014.

[8] Mateusz Dyksik, Herman Duim, Duncan K Maude, Michal Baranowski, Maria Antonietta Loi, and Paulina Plochocka. Brightening of dark excitons in 2d perovskites. *Science advances*, 7(46):eabk0904, 2021.

[9] Mateusz Dyksik, Shuli Wang, Watcharaphol Paritmongkol, Duncan K Maude, William A Tisdale, Michal Baranowski, and Paulina Plochocka. Tuning the excitonic properties of the 2d (pea) 2 (ma) n- 1pb n i3 n+ 1 perovskite family via quantum confinement. *The Journal of Physical Chemistry Letters*, 12(6):1638–1643, 2021.

[10] María C Gélvez-Rueda, Eline M Hutter, Duyen H Cao, Nicolas Renaud, Constantinos C Stoumpos, Joseph T Hupp, Tom J Savenije, Mercouri G Kanatzidis, and Ferdinand C Grozema. Interconversion between free charges and bound excitons in 2d hybrid lead halide perovskites. *The Journal of Physical Chemistry C*, 121(47):26566–26574, 2017.

[11] Stefan Grimme. Accurate description of van der waals complexes by density functional theory including empirical corrections. *Journal of computational chemistry*, 25(12):1463–1473, 2004.

[12] Stefan Grimme. Semiempirical gga-type density functional constructed with a long-range dispersion correction. *Journal of computational chemistry*, 27(15):1787–1799, 2006.

[13] G Kresse and J Furthmüller. Efficiency of ab-initio total energy calculations for metals and semiconductors using a plane-wave basis set. *Computational Materials Science*, 6(1):15–50, 1996.

[14] G Kresse and J Furthmüller. Efficient iterative schemes for ab initio total-energy calculations using a plane-wave basis set. *Physical Review B*, 54(16):11169–11186, oct 1996.

[15] G. Kresse and J. Hafner. Ab initio molecular dynamics for liquid metals. *Physical Review B*, 47(1):558–561, 1993.

[16] G Kresse and J Hafner. Ab initio molecular-dynamics simulation of the liquid-metal–amorphous-semiconductor transition in germanium. *Physical Review B*, 49(20):14251–14269, may 1994.

[17] Devesh R Kripalani, Yongqing Cai, Jun Lou, and Kun Zhou. Strong edge stress in molecularly thin organic–inorganic hybrid ruddlesden–popper perovskites and modulations of their edge electronic properties. *ACS nano*, 16(1):261–270, 2022.

[18] Kyuho Lee, Éamonn D Murray, Lingzhu Kong, Bengt I Lundqvist, and David C Langreth. Higher-accuracy van der waals density functional. *Physical Review B*, 82(8):081101, 2010.

[19] Dong Liang, Yuelin Peng, Yongping Fu, Melinda J Shearer, Jingjing Zhang, Jianyuan Zhai, Yi Zhang, Robert J Hamers, Trisha L Andrew, and Song Jin. Color-pure violet-light-emitting diodes based on layered lead halide perovskite nanoplates. *ACS nano*, 10(7):6897–6904, 2016.

[20] Kebin Lin, Jun Xing, Li Na Quan, F Pelayo García de Arquer, Xiwen Gong, Jianxun Lu, Liqiang Xie, Weijie Zhao, Di Zhang, Chuanzhong Yan, et al. Perovskite light-emitting diodes with external quantum efficiency exceeding 20 per cent. *Nature*, 562(7726):245–248, 2018.

[21] Priya Mahadevan and Alex Zunger. Room-temperature ferromagnetism in mn-doped semiconducting cdgep 2. *Physical review letters*, 88(4):047205, 2002.

[22] Anyi Mei, Xiong Li, Linfeng Liu, Zhiliang Ku, Tongfa Liu, Yaoguang Rong, Mi Xu, Min Hu, Jiangzhao Chen, Ying Yang, et al. A hole-conductor–free, fully printable mesoscopic perovskite solar cell with high stability. *science*, 345(6194):295–298, 2014.

[23] Hendrik J Monkhorst and James D Pack. Special points for brillouin-zone integrations. *Physical review B*, 13(12):5188, 1976.

[24] John P. Perdew, Kieron Burke, and Matthias Ernzerhof. Generalized gradient approximation made simple. *Phys. Rev. Lett.*, 77:3865–3868, Oct 1996.

[25] Yonatan Plotnik, Mikael C Rechtsman, Daohong Song, Matthias Heinrich, Julia M Zeuner, Stefan Nolte, Yaakov Lumer, Natalia Malkova, Jingjun Xu, Alexander Szameit, et al. Observation of unconventional edge states in 'photonic graphene'. *Nature materials*, 13(1):57–62, 2014.

[26] Xiang Qi, Yupeng Zhang, Qingdong Ou, Son Tung Ha, Cheng-Wei Qiu, Han Zhang, Yi-Bing Cheng, Qihua Xiong, and Qiaoliang Bao. Photonics and optoelectronics of 2d metal-halide perovskites. *Small*, 14(31):1800682, 2018.

[27] Michael Saliba, Juan-Pablo Correa-Baena, Michael Grätzel, Anders Hagfeldt, and Antonio Abate. Perovskite solar cells: from the atomic level to film quality and device performance. *Angewandte Chemie International Edition*, 57(10):2554–2569, 2018.

[28] Tariq Sheikh, Aparna Shinde, Shailaja Mahamuni, and Angshuman Nag. Possible dual bandgap in (c4h9nh3) 2pbi4 2d layered perovskite: single-crystal and exfoliated few-layer. *ACS Energy Letters*, 3(12):2940–2946, 2018.

[29] C Shimomura, K Takemura, Y Fujii, S Minomura, M Mori, Y Noda, and Y Yamada. Structure analysis of high-pressure metallic state of iodine. *Physical Review B*, 18(2):715, 1978.

[30] Ian C Smith, Eric T Hoke, Diego Solis-Ibarra, Michael D McGehee, and Hemamala I Karunadasa. A layered hybrid perovskite solar-cell absorber with enhanced moisture stability. *Angewandte Chemie International Edition*, 53(42):11232–11235, 2014.

[31] Hsinhan Tsai, Reza Asadpour, Jean-Christophe Blancon, Constantinos C Stoumpos, Jacky Even, Pulickel M Ajayan, Mercouri G Kanatzidis, Muhammad Ashraful Alam, Aditya D Mohite, and Wanyi Nie. Design principles for electronic charge transport in solution-processed vertically stacked 2d perovskite quantum wells. *Nature communications*, 9(1):2130, 2018.

[32] Hsinhan Tsai, Wanyi Nie, Jean-Christophe Blancon, Constantinos C Stoumpos, Reza Asadpour, Boris Harutyunyan, Amanda J Neukirch, Rafael Verduzco, Jared J Crochet, Sergei Tretiak, et al. High-efficiency two-dimensional ruddlesden–popper perovskite solar cells. *Nature*, 536(7616):312–316, 2016.

[33] Kai Wang, Tao Wu, Congcong Wu, Rammohan Sriramdas, Xu Huang, Ke Wang, Yuanyuan Jiang, Hairui Liu, Yongke Yan, Dong Yang, et al. Nature of terrace edge states (tes) in lower-dimensional halide perovskite. *Journal of materials chemistry A*, 8(16):7659–7670, 2020.

[34] Nana Wang, Lu Cheng, Rui Ge, Shuting Zhang, Yanfeng Miao, Wei Zou, Chang Yi, Yan Sun, Yu Cao, Rong Yang, et al. Perovskite light-emitting diodes based on solution-processed self-organized multiple quantum wells. *Nature Photonics*, 10(11):699–704, 2016.

[35] Zhengguo Xiao, Ross A Kerner, Lianfeng Zhao, Nhu L Tran, Kyung Min Lee, Tae-Wook Koh, Gregory D Scholes, and Barry P Rand. Efficient perovskite light-emitting diodes featuring nanometre-sized crystallites. *Nature Photonics*, 11(2):108–115, 2017.

[36] Jason J Yoo, Gabkyung Seo, Matthew R Chua, Tae Gwan Park, Yongli Lu, Fabian Rotermund, Young-Ki Kim, Chan Su Moon, Nam Joong Jeon, Juan-Pablo Correa-Baena, et al. Efficient perovskite solar cells via improved carrier management. *Nature*, 590(7847):587–593, 2021.

[37] Chunyi Zhao, Wenming Tian, Jing Leng, Yang Zhao, and Shengye Jin. Controlling the property of edges in layered 2d perovskite single crystals. *The Journal of Physical Chemistry Letters*, 10(14):3950–3954, 2019.

[38] Kaibo Zheng and Tonu Pullerits. Two dimensions are better for perovskites, 2019.

[39] Kaibo Zheng, Karel Zidek, Mohamed Abdellah, Maria E Messing, Mohammed J Al-Marri, and Tõnu Pullerits. Trap states and their dynamics in organometal halide perovskite nanoparticles and bulk crystals. *The Journal of Physical Chemistry C*, 120(5):3077–3084, 2016.

Chapter 7

Why Do We Have a Jump in Conductance in Single Molecular Junctions?

1 Introduction

The pursuit of achieving the ultimate level of miniaturization in electronic components has propelled the exploration of materials with characteristic dimensions in the nanometer scale. These materials encompass molecules[4], which necessitate a comprehensive understanding of their behavior before their integration into electronic circuits. Despite remarkable advancements in this field[10, 12, 20, 45], the establishment of effective microscopic-level contacts has proven to be a challenging endeavor.

Molecular electronics hinges on the pivotal concept of the molecular junction[28], which can be categorized into two primary types: ensemble molecular junctions and single molecular junctions. Our primary focus resides in the latter category, which involves the encapsulation of a limited number, or even a single molecule, between two nanoelectrodes. Conversely, ensemble molecular junctions rely on a collective behavior involving multiple

molecules. When we contemplate metallic electrodes and scrutinize metal-metal contacts, we encounter a regime in which quantum tunneling takes precedence, eventually transitioning into the formation of tangible contacts. This transition from a tunneling transport regime to contact formation typically manifests as a sudden and discernible increase in electrical conductance, which is often referred to as a "jump to contact" [15, 61].

For example, metals such as Iridium(Ir) and Nickel (Ni) do show the Jump to contact with reduced probability compared to Gold (Au), Platinum (Pt), Copper (Cu), and Silver (Ag). However, Tungsten (W) do not show the jump to contact. and transition is completely continuous[62]. Research has indicated that this phenomenon can be effectively elucidated through the application of a generic potential energy model, in which the elastic constant of the metal emerges as the sole independent parameter[58]. The formation of a bond between a metal and a molecule is an intricate process that exhibits a high degree of sensitivity to various factors, including the binding groups involved and the geometrical configuration of the electrodes[11, 24, 26, 43, 46, 47, 63, 64]. Notably, the phenomenon known as the "jump to molecular contact" has been documented in the context of flat molecules through experiments reliant on scanning tunneling microscopy. This phenomenon is thought to originate from the presence of two closely matched adsorption geometries, one of which bridges the junction through a soft phonon emanating from the molecular side groups.

Recent experiments, involving the utilization of organometallic compounds conducted in a solution, have also highlighted instances of a jump in conductance . This particular observation has been ascribed to the emergence of one-dimensional coordination polymers within these junctions. However, despite these intriguing findings, the comprehensive understanding of the role of metal-molecule interactions in bond formation remains limited, and a unified conceptual framework is yet to be established.

In the context of this present chapter, we offer an exploration into the occurrence of the "jump to molecular contact" phenomenon in the realm of single molecular junctions. Our investigation centers on the study of charge transport through 4,4'-bipyridine (4,4'-BPY) and 2,2'-bipyridine (2,2'-BPY) molecules attached to gold electrodes[40]. Our aim is to

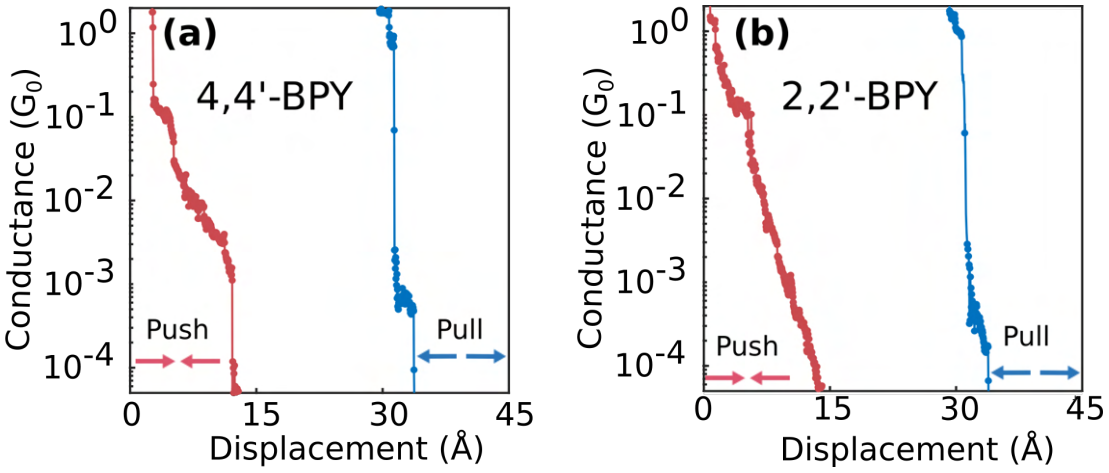

FIGURE 7.1: Conductance traces for (a) 4, 4'-BPY and (b) 2, 2'-BPY. Blue represents trace during pull and red represents trace during pull push[40]

elucidate the microscopic origins underlying the formation of metal-molecular contacts. Research reveals that molecular junctions are formed during the breaking traces for both 4,4'-BPY and 2,2'-BPY molecules[40]. An intriguing revelation is that 4,4'-BPY forms molecular junctions isotropically, displaying conductance jumps not only in the breaking (pull) traces but also in the making (push) traces, a characteristic absent in the case of 2,2'-BPY Figure (7.1).

Our investigations, involving density functional theory (DFT) and molecular dynamics (MD) simulations, unveil two pivotal mechanisms contributing to the "jump to molecular contact" phenomenon. Firstly, while 2,2'-BPY tends to lie flat on the gold surface, 4,4'-BPY exhibits two stable minima, one with the molecule positioned flat on the surface and another with the molecule standing vertically, despite both molecules featuring a similar anchoring group composed of nitrogen. This peculiarity in the behavior of 4,4'-BPY arises from the fact that the nitrogen in 4,4'-BPY forms a remarkably stronger bond, whereas the orientation of 2,2'-BPY on the gold surface does not allow for such a robust bond, owing to steric hindrances posed by the hydrogen atoms attached to the carbon atoms.

Moreover, we propose an alternative mechanism, wherein the observed "jump to molecular contact" phenomenon in the case of 4,4'-BPY may be attributed to the fact that the molecule breaks by pulling along a few gold atoms, owing to the presence of a robust

Au-N bond compared to the Au-Au bond. Consequently, during the formation of contacts in the push loops, the directionality of bonding need not be a significant concern.

2 Methodology

In order to model our experimental setup comprehensively, we utilized density functional theory (DFT) based ab initio electronic structure calculations. The choice of the generalized gradient approximation (GGA) with the Perdew-Burke-Ernzerhof exchange-correlation functional[48] was instrumental in ensuring a reliable description of the electronic interactions. We also incorporated dispersion corrections (DFT-D2)[14, 17] to account for van der Waals interactions, which play a crucial role in molecular junctions. These calculations were meticulously implemented using the Vienna ab initio simulation package (VASP)[22–25], a widely recognized tool for performing electronic structure calculations.

Our simulations involved the exploration of various aspects of the molecular junctions formed by 4,4'-bipyridine (4,4'-BPY) and 2,2'-bipyridine (2,2'-BPY) molecules in conjunction with gold electrodes. To capture the electronic behavior with high precision, we employed a Gamma point k-space sampling method[39] and set a plane-wave cutoff energy of 500 eV. The convergence criteria were established at forces less than 10^{-3} eV per atom and energy convergence to a remarkable tolerance of 10^{-5} eV, ensuring that our calculations accurately represented the system's electronic properties.

For our ab initio molecular dynamics (MD) simulations[2, 11, 27], which are essential to examine the dynamic behavior of the system, we maintained the temperature at a realistic 300 K to mimic room temperature conditions. The temperature control was achieved through an NVT canonical ensemble, and a Nosé-Hoover thermostat[15, 38, 48] was used to regulate the system's temperature fluctuations. This ensemble is ideal for maintaining constant temperature conditions while allowing the system to evolve dynamically. The atomic geometry of the molecular junctions was modeled based on the optimized structure

of a gold slab sandwiched between the two molecules. This involved constructing a gold slab with eight layers and maintaining a separation of 15 Å between the slabs, ensuring an appropriate representation of the junction's structure. During the simulations, we systematically pulled the gold electrodes apart in increments of 0.1 Å, a process known as a breaking trace. After each step, the entire system was relaxed, and this was accomplished by performing 200 MD steps, each with a time step of 0.5 femtoseconds. This iterative approach allowed us to capture the intricate dynamics and electronic interactions within the molecular junctions.

3 Results and discussion

As we delved into the literature of metallic contacts, we found that certain metals, such as Gold (Au), Platinum (Pt), Copper (Cu), and Silver (Ag), exhibit the intriguing "jump to contact" phenomenon. In contrast, metals like Iridium (Ir) and Nickel (Ni) "jump to contact" phenomenon is less probable and Tungsten (W) do not manifest any discernible signature of this phenomenon. Therefore, our primary objective was to capture this "jump to contact" phenomenon within our computational framework.

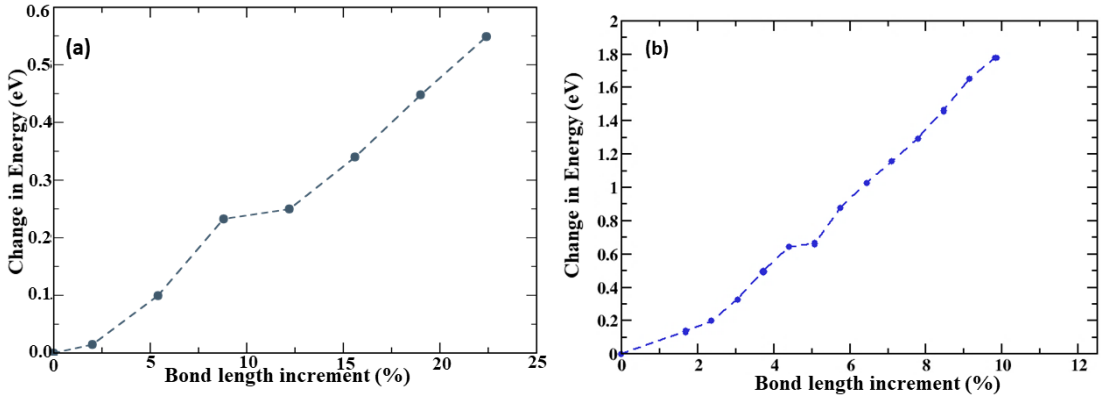

FIGURE 7.2: Change in total energy with respect to stretching of the bond of (a)Gold-Gold atom and (b)Silver-Silver atom

To accomplish this, we introduced a pyramidal gold electrode and systematically stretched it from the tip of the electrode. This controlled manipulation allowed us to probe the energy variations within the system as the applied strain. Figure 7.2 illustrates this process

for both Gold and Silver, while Figure 7.3 provides the corresponding data for Tungsten and Iridium.

One observation from our simulations is the inflection in the energy as a function of strain at approximately 8.8% in the case of Gold (Figure 7.2a). This abrupt jump in the energy possibly emerges from a change in the structure/charge density locally. It is essential to note that the hopping interaction strength between any two atoms is intrinsically linked to their separation and follows a power-law behavior. Hence, the observed jump in energy with strain can be translated into a jump in the bond length, and consequently the hopping interaction strength. This observed discontinuity in the hopping interaction strength between metal atoms directly correlates with a distinctive jump in the conductance. This crucial insight provides a foundation for understanding the "jump to contact" phenomenon, shedding light on the abrupt conductance changes that characterize certain metals, such as Gold and Silver. By conducting these simulations, we have paved the way for a deeper comprehension of the underlying mechanisms at play in the behavior of these materials at the molecular level.

The jump in the energy is seen for both gold (Au) as well as silver (Ag) electrodes (Figure 7.2), and its interpretation is consistent with experiment[16, 62].

However, as we have mentioned earlier, not all metals exhibit this jump in conductance. To address this aspect, we extended this analysis to Tungsten and Iridium metal electrodes(Figure 7.3). For Tungsten electrodes, our simulations reveal no discernible signature of a change in the energy slope, as seen in Figure 7.3a. In the case of the Iridium electrode, one finds a small inflection, which is also consistent with experimental reports[62].

Subsequently, we placed the molecule at the tip of a gold electrodes, and pulled the molecule. The energy variations as a function of the applied strain are shown in Figure 7.4. Surprisingly, our calculations revealed a continuous and smooth variation in the energy. These observations suggest that one expects a monotonic change in the conductance in this scenario.

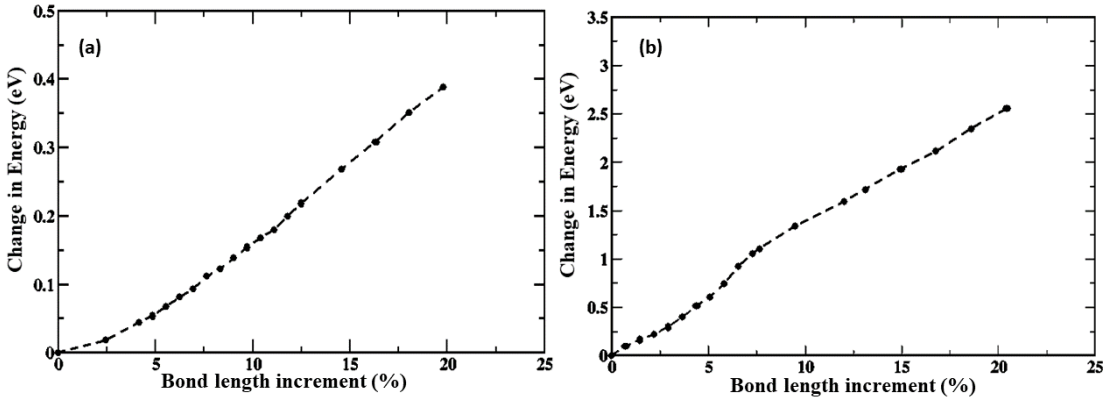

FIGURE 7.3: Change in total energy with respect to stretching of the bond of (a) Tungsten-Tungsten atom and (b)Iridium -Iridium atom

However these results contradict the experimental observations, where a prominent "jump to contact" phenomenon is consistently observed[40]. This difference between our computational predictions and experimental observations highlight the intricacies and nuances of molecular junction behavior that are not yet fully understood.

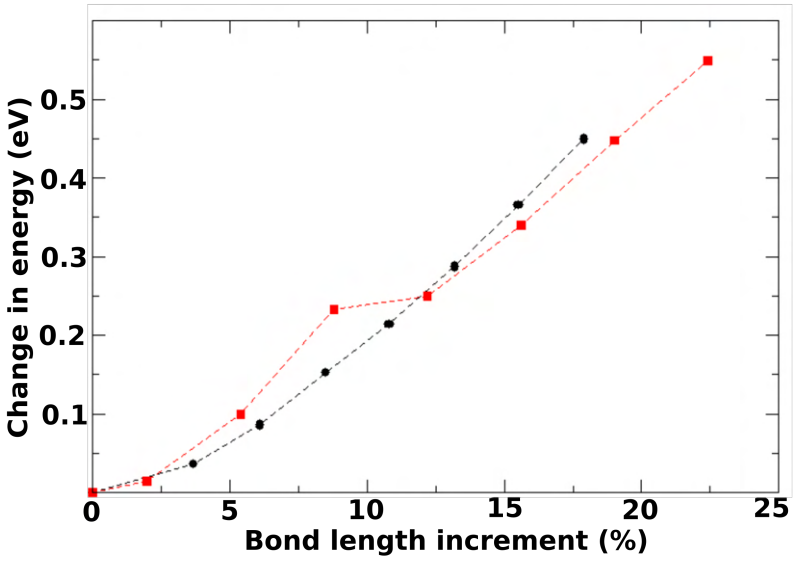

FIGURE 7.4: Change in total energy with respect to stretching of the bond of molecule-Au (black) and Au-Au atom (red)

We go on to explore the origin of the jump in conductance observed in experiments. We considered two pyramidal Gold (Au) electrodes and placed a 4,4'-bipyridine (4,4'-BPY) molecule symmetrically between them. The distance between the Au atom and nitrogen of the molecule was kept at 2.12 Å. This is the energetically favoured distance. Positioning

the molecule at this distance from the electrodes led to the establishment of an effective length, defined as the distance between the tips of the two electrodes, measuring 11.10 Å. The other Au-Au bondlengths were 2.65 Å.

Subsequently, we conducted molecular dynamics simulations at a temperature of 300 K to examine the dynamic behavior of the system. After 200 iterations we found that the positions of the Au atoms within the electrodes remained at similar positions with no substantial changes. However, during the course of the simulations, we observed that two atoms from the electrodes gradually approached the molecule, resulting in the formation of shorter Au-molecule bonds. The gradual approach of atoms of the electrode towards the molecule and the consequent formation of shorter bonds may hold the key to understanding the "jump to contact" phenomenon in molecular junctions.

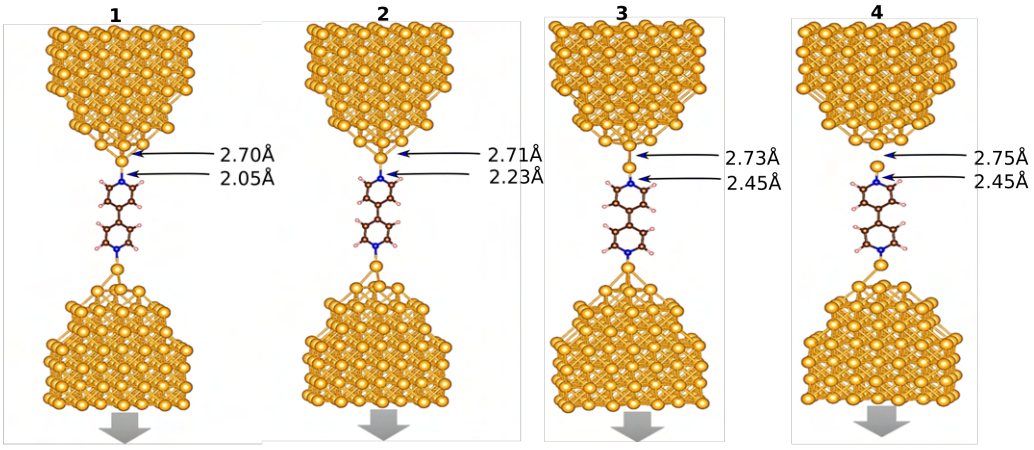

FIGURE 7.5: MD snapshot of the molecular junction with 4, 4'-BPY for an effective length of the electrode (1) 11.10 Å, (2) 11.60 Å, (3) 12.20 Å, and(4) 12.45 Å.

We systematically increased the effective length between the two pyramidal Gold (Au) electrodes to the values shown in Figure 7.5. This process revealed two significant observations.

Movement of an Au Atom: As the effective length was extended, we observed the migration of an Au atom from one of the electrodes towards the 4,4'-bipyridine (4,4'-BPY) molecule. This relocation suggests a dynamic interaction within the junction, potentially influencing its conductance properties.

Additionally, the 4,4'-BPY molecule was no longer symmetrically positioned with respect to the electrodes as the effective length increased. On one side, the distance between the molecule and one end of the electrode measured 2.45 Å, while on the other side, it extended to 2.55 Å. This asymmetry introduced a variation in the configuration of the molecular junction. The converged effective length was determined to be 12.20 Å (as depicted in Figure 7.5, 3). Even as we further increased the effective length to 13.00 Å (as shown in Figure 7.5, 4), the Au atom continued to move towards the molecule.

In contrast, a similar calculation conducted with 2,2'-bipyridine (2,2'-BPY) revealed a distinct behavior. Here, when we increased the separation between the molecule and the electrode, the Au atom did not detach from the electrode, in contrast to the observations made with 4,4'-BPY (Figure 7.6).

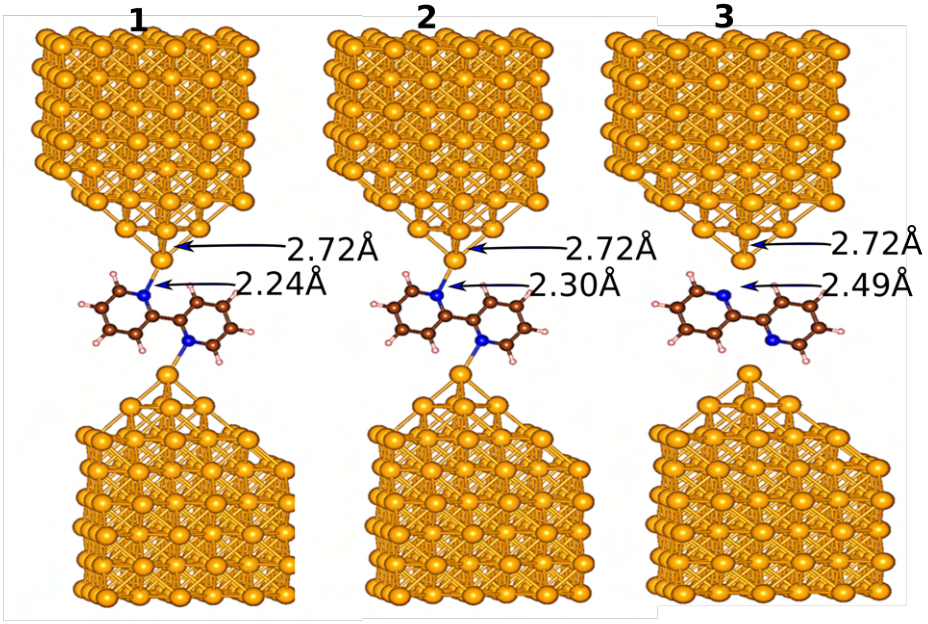

FIGURE 7.6: MD snapshot of the molecular junction with 2, 2-BPY for an effective length of the electrode (1) 6.65 Å, (2) 6.80 Å, and (3) 6.89 Å.

In order to provide a more comprehensive understanding of the observed behavior, we conducted static calculations by placing both 4,4'-bipyridine (4,4'-BPY) and 2,2'-bipyridine (2,2'-BPY) molecules on a gold (Au) surface at a fixed distance(Figure 7.7. These calculations provided some insights into the orientations and preferences of these molecules on

gold surface.

Our results indicate that for 4,4'-BPY on gold, there exist two distinct energy minima, whereas for 2,2'-BPY, only a single energy minimum is observed(Figure 7.8. When we allowed for complete structural optimization in each case, the preferred orientations of the molecules were revealed.

For 4,4'-BPY: Panel (a) of Figure 7.7 shows that the molecule predominantly favors an orientation that is nearly vertical to the surface. In this configuration, 4,4'-BPY interacts strongly with the gold surface through its nitrogen atoms. This interaction is further substantiated by the charge density distribution shown in the inset of Figure 7.7(a), where substantial electron density is found on several gold atoms beyond the nearest neighbor, underscoring the strong interaction between the nitrogen in 4,4'-BPY and the gold surface. For 2,2'-BPY: In the case of 2,2'-BPY, panels (c) and (d) of Figure 7.7 illustrate that the molecule tends to adopt a horizontal orientation with respect to the gold surface. This orientation allows the molecule to interact primarily through its carbon backbone with the gold surface. Consequently, this horizontal orientation represents a stable configuration for 2,2'-BPY molecules. The underlying rationale for these molecular orientations becomes evident. The choice of orientation is influenced by the mode of interaction with the gold surface. In the horizontal position, both molecules interact favorably through their carbon backbones, establishing stable orientations. Conversely, in the vertical orientation, 4,4'-BPY exhibits strong interaction with the gold surface through its nitrogen atoms, leading to the vertical orientation preference.

These observations provide a clear link between the molecular orientation and the nature of the interactions with the gold surface, shedding light on the stability and behavior of 4,4'-BPY and 2,2'-BPY molecules in molecular junctions. Understanding these preferences is pivotal in deciphering the conductance behaviour of molecular junctions involving different molecules and metals.

The critical difference in behavior between 4,4'-bipyridine (4,4'-BPY) and 2,2'-bipyridine (2,2'-BPY) on a gold (Au) surface arises from their Au-N bond lengths. Specifically, the

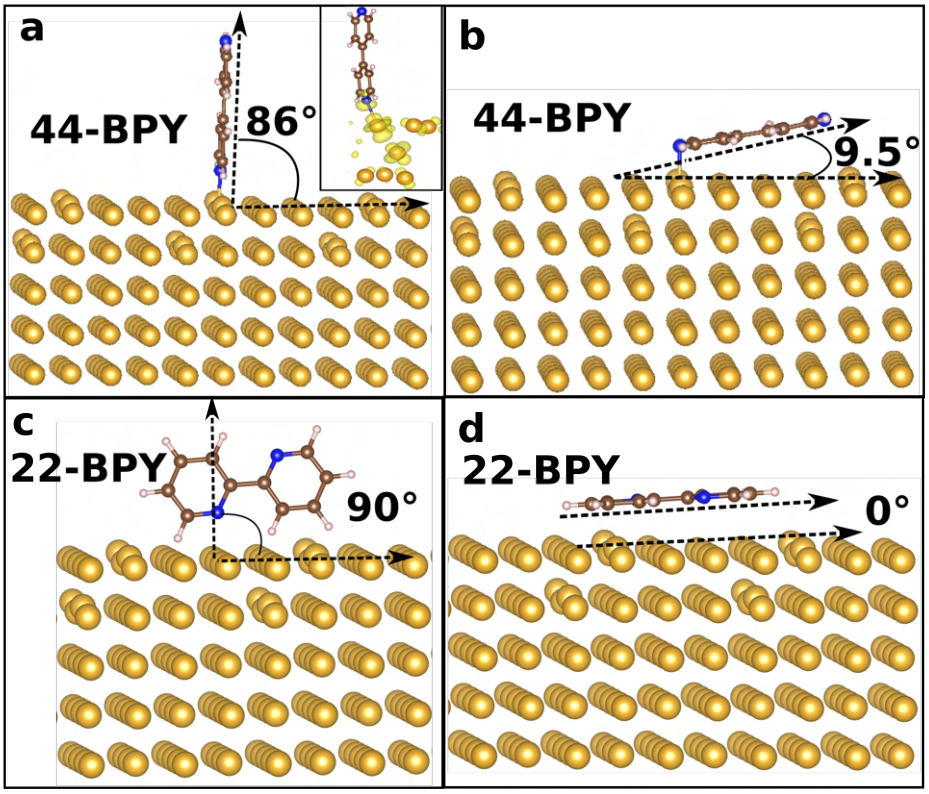

FIGURE 7.7: Complete optimized structure for vertically aligned and horizontally aligned orientations of the molecules shown in panels (a) and(b) for 4, 4 -BPY and in panel (c) for 2, 2-BPY. Charge density of a state formed as a result of interactions between Au and the molecule

Au-N bond length is significantly longer for 2,2'-BPY, measured at 2.24 Å. This elongated bond is due to steric effects involving the neighboring atoms. This prevents the 2,2'-BPY molecule from coming too close to the Au surface. As a result, 2,2'-BPY exhibits only one stable minimum orientation on the Au surface.

Conversely, in the case of 4,4'-BPY, the strong bonding interaction involving nitrogen atoms is highly directional and allows for the molecule to approach the Au surface closely, resulting in the formation of two stable minimum orientations.

The implication of this observation is that during the "push cycle," there may be reduced reproducibility when using 4,4'-BPY, as the strong bonding interactions are highly orientation-dependent. Only certain orientations would result in the formation of strong

bonds. This could potentially lead to variations in the conductance behavior during the push cycle.

However, our molecular dynamics (MD) simulations and an analysis of the charge density of the bonding state between 4,4'-BPY and the Au surface have provided insights into the robustness of the interaction between them. In certain cases, the interaction between 4,4'-BPY and the Au surface is sufficiently strong to pull one or more Au atoms out of their positions. Consequently, during the push cycle, these displaced Au atoms can reattach to other gold atoms, forming contacts. It's important to note that the bonding between Au atoms, known to involve s orbitals, is isotropic.

1. Molecule breaks with Au, so it the push involaves a Au-Au bond (isotropic).
2. The jump to contact is associated with the Au atoms (hence similar to earlier metal work).
3. Some which are lying horizontally which are also pulled up - jump in conductance

This characteristic of isotropic bonding between Au atoms offers the reproducibility required for the "jump to contact" phenomenon, even in cases where no molecular junction is formed during the pull cycle. Experimental observations have corroborated this, as a "jump to contact" is observed in numerous cases despite the absence of a molecular junction during the pull cycle.

In essence, the presence of two stable orientations of 4,4'-BPY on the Au surface opens up the possibility for a "jump" between these orientations via a soft phonon mode of the molecule during the push cycle. This dynamic process can contribute to the observed "jump to contact" phenomenon, providing a deeper understanding of the conductance behavior in molecular junctions involving 4,4'-bipyridine and gold electrodes.

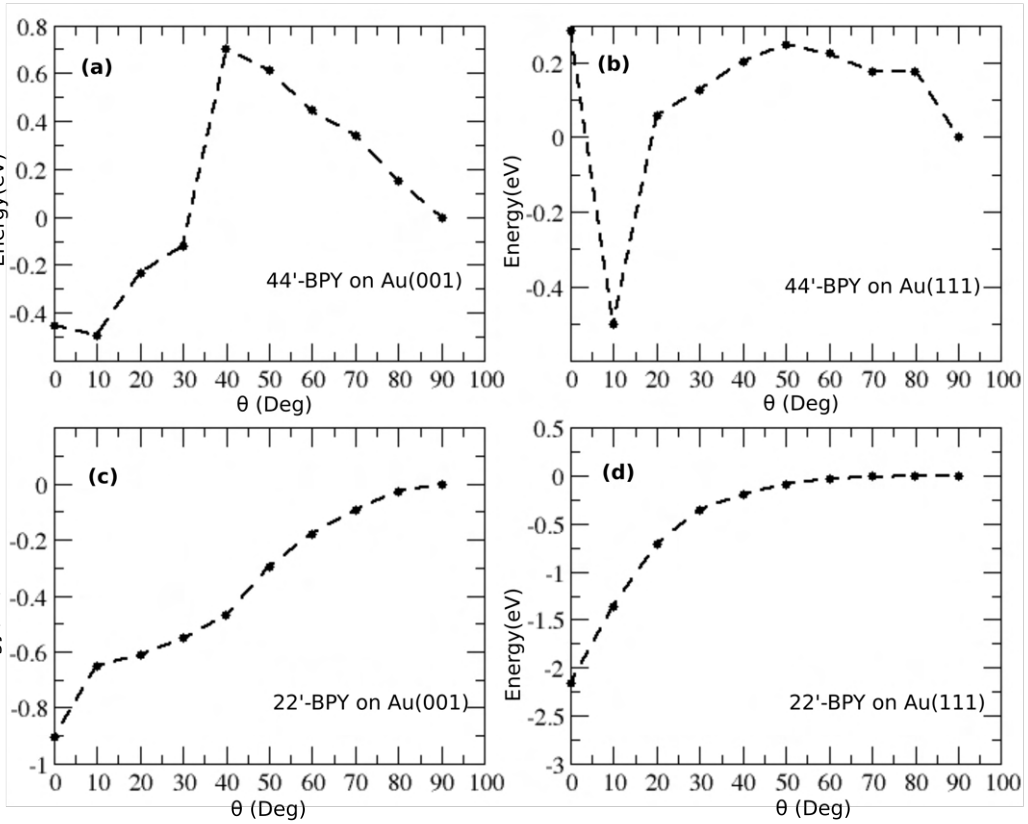

FIGURE 7.8: Energy vs. the orientation of the molecule on Au surface (a) 44'-BPY on Au (001) (b)44'-BPY on Au (111) (c) 22'-BPY on Au (001) (d) 22'-BPY on Au (111)

4 Conclusion

In conclusion, this chapter delves into the intricate world of single molecular junction conductance, shedding light on the fascinating "jump to contact" phenomenon. Through a comprehensive series of computational simulations and analyses, we have unraveled key insights into the behavior of molecules when interfaced with metal electrodes, particularly focusing on the cases of 4,4'-bipyridine (4,4'-BPY) and 2,2'-bipyridine (2,2'-BPY) with gold (Au) electrodes.

Our journey began with the exploration of the abrupt conductance changes observed in certain metals, notably Gold (Au) and Silver (Ag), known as the "jump to contact." By employing systematic computational methods, we successfully captured and elucidated the origins of this intriguing phenomenon. This involved manipulating the bond length

between metal atoms in a pyramidal electrode configuration, revealing how this transition leads to a sudden change in hopping interaction strength, ultimately manifesting as a jump in conductance.

However, not all metals exhibit this abrupt conductance behavior. Through similar investigations involving Tungsten (W) and Iridium (Ir) electrodes, we verified that the absence of the "jump to contact" in these cases aligned with experimental observations, underscoring the validity of our computational framework.

We then probed further into the behavior of 4,4'-BPY and 2,2'-BPY molecules when connected to Au electrodes. These investigations unearthed the complexities of molecular orientations on the metal surface. While 4,4'-BPY displayed two stable orientations due to strong bonding interactions between its nitrogen atoms and the Au surface, 2,2'-BPY preferred a horizontal orientation. This preference was attributed to its interaction through the carbon backbone, which was hindered in the vertical orientation due to steric effects.

The pronounced difference in the Au-N bond lengths for these molecules contributed to their distinct behavior. The highly directional and strong bonding interactions of nitrogen in 4,4'-BPY added a layer of complexity, as certain orientations formed strong bonds while others did not. However, our simulations and charge density analysis revealed that strong interactions between 4,4'-BPY and Au could displace Au atoms, leading to the formation of contacts between Au atoms during the push cycle. The isotropic nature of bonding between Au atoms supported the reproducibility of this "jump to contact" phenomenon, even in the absence of a molecular junction during the pull cycle.

Intriguingly, the presence of two stable orientations of 4,4'-BPY on the Au surface introduced the possibility of a "jump" between these orientations through a soft phonon mode during the push cycle, further contributing to the observed "jump to contact."

In essence, this chapter has provided a deeper understanding of the complex interplay between molecules and metal electrodes in molecular junctions, shedding light on the intricate mechanisms governing conductance changes and the "jump to contact" phenomenon.

These findings not only contribute to our fundamental understanding of nanoscale electronic components but also offer valuable insights for the design and control of molecular electronic devices.

References

[1] Michael P Allen and Dominic J Tildesley. *Computer simulation of liquids*. Oxford university press, 2017.

[2] Sriharsha V Aradhya, Michael Frei, András Halbritter, and Latha Venkataraman. Correlating structure, conductance, and mechanics of silver atomic-scale contacts. *ACS nano*, 7(4):3706–3712, 2013.

[3] Sriharsha V Aradhya, Michael Frei, Mark S Hybertsen, and L Venkataraman. Van der waals interactions at metal/organic interfaces at the single-molecule level. *Nature materials*, 11(10):872–876, 2012.

[4] Arieh Aviram and Mark A Ratner. Molecular rectifiers. *Chemical physics letters*, 29(2):277–283, 1974.

[5] Alexei Bagrets, Stefan Schmaus, Ali Jaafar, Detlef Kramczynski, Toyo Kazu Yamada, Mébarek Alouani, Wulf Wulfhekel, and Ferdinand Evers. Single molecule magnetoresistance with combined antiferromagnetic and ferromagnetic electrodes. *Nano Letters*, 12(10):5131–5136, 2012.

[6] Zoltán Balogh, Péter Makk, and András Halbritter. Alternative types of molecule-decorated atomic chains in au–co–au single-molecule junctions. *Beilstein journal of nanotechnology*, 6(1):1369–1376, 2015.

[7] Zoltán Balogh, Dávid Visontai, Péter Makk, Katalin Gillemot, László Oroszlány, László Pósa, Colin Lambert, and András Halbritter. Precursor configurations and

post-rupture evolution of ag–co–ag single-molecule junctions. *Nanoscale*, 6(24):14784–14791, 2014.

[8] Anders Borges, E-Dean Fung, Fay Ng, Latha Venkataraman, and Gemma C Solomon. Probing the conductance of the σ-system of bipyridine using destructive interference. *The journal of physical chemistry letters*, 7(23):4825–4829, 2016.

[9] M. R. Calvo, C. Sabater, W. Dednam, E. B. Lombardi, M. J. Caturla, and C. Untiedt. Influence of relativistic effects on the contact formation of transition metals. *Phys. Rev. Lett.*, 120:076802, Feb 2018.

[10] Brian Capozzi, Jianlong Xia, Olgun Adak, Emma J Dell, Zhen-Fei Liu, Jeffrey C Taylor, Jeffrey B Neaton, Luis M Campos, and Latha Venkataraman. Single-molecule diodes with high rectification ratios through environmental control. *Nature nanotechnology*, 10(6):522–527, 2015.

[11] Fang Chen, Xiulan Li, Joshua Hihath, Zhifeng Huang, and Nongjian Tao. Effect of anchoring groups on single-molecule conductance: comparative study of thiol-, amine-, and carboxylic-acid-terminated molecules. *Journal of the American Chemical Society*, 128(49):15874–15881, 2006.

[12] Longji Cui, Sunghoon Hur, Zico Alaia Akbar, Jan C Klöckner, Wonho Jeong, Fabian Pauly, Sung-Yeon Jang, Pramod Reddy, and Edgar Meyhofer. Thermal conductance of single-molecule junctions. *Nature*, 572(7771):628–633, 2019.

[13] M. A. Fernández, C. Sabater, W. Dednam, J. J. Palacios, M. R. Calvo, C. Untiedt, and M. J. Caturla. Dynamic bonding of metallic nanocontacts: Insights from experiments and atomistic simulations. *Phys. Rev. B*, 93:085437, Feb 2016.

[14] Daan Frenkel and Berend Smit. *Understanding molecular simulation: from algorithms to applications*, volume 1. Elsevier, 2001.

[15] Lukas Gerhard and Wulf Wulfhekel. Conductance and adhesion in an atomically precise au-au point contact. *Physical Review B*, 101(3):035429, 2020.

[16] Lukas Gerhard and Wulf Wulfhekel. Conductance and adhesion in an atomically precise au-au point contact. *Physical Review B*, 101(3):035429, 2020.

[17] Stefan Grimme. Accurate description of van der waals complexes by density functional theory including empirical corrections. *Journal of computational chemistry*, 25(12):1463–1473, 2004.

[18] Stefan Grimme. Semiempirical gga-type density functional constructed with a long-range dispersion correction. *Journal of computational chemistry*, 27(15):1787–1799, 2006.

[19] Wolfgang Haiss, Changsheng Wang, Iain Grace, Andrei S Batsanov, David J Schiffrin, Simon J Higgins, Martin R Bryce, Colin J Lambert, and Richard J Nichols. Precision control of single-molecule electrical junctions. *Nature materials*, 5(12):995–1002, 2006.

[20] Ryoma Hayakawa, Mohammad Amin Karimi, Jannic Wolf, Thomas Huhn, Martin Sebastian zoellner, Carmen Herrmann, and Elke Scheer. Large magnetoresistance in single-radical molecular junctions. *Nano letters*, 16(8):4960–4967, 2016.

[21] William G Hoover. Canonical dynamics: Equilibrium phase-space distributions. *Physical review A*, 31(3):1695, 1985.

[22] Shimin Hou, Jiaxing Zhang, Rui Li, Jing Ning, Rushan Han, Ziyong Shen, Xingyu Zhao, Zenquan Xue, and Quande Wu. First-principles calculation of the conductance of a single 4,4 bipyridine molecule. *Nanotechnology*, 16(2):239–244, jan 2005.

[23] Y Isshiki, S Fujii, T Nishino, and M Kiguchi. Impact of junction formation processes on single molecular conductance. *Physical Chemistry Chemical Physics*, 20(12):7947–7952, 2018.

[24] M Kamenetska, M Koentopp, AC Whalley, YS Park, ML Steigerwald, C Nuckolls, MS Hybertsen, and L Venkataraman. Formation and evolution of single-molecule junctions. *Physical review letters*, 102(12):126803, 2009.

[25] Maria Kamenetska. *Single molecule junction conductance and binding geometry.* Columbia University, 2012.

[26] Satoshi Kaneko, Ryoji Takahashi, Shintaro Fujii, Tomoaki Nishino, and Manabu Kiguchi. Controlling the formation process and atomic structures of single pyrazine molecular junction by tuning the strength of the metal–molecule interaction. *Physical Chemistry Chemical Physics*, 19(15):9843–9848, 2017.

[27] Tatsuya Konishi, Manabu Kiguchi, Mai Takase, Fumika Nagasawa, Hideki Nabika, Katsuyoshi Ikeda, Kohei Uosaki, Kosei Ueno, Hiroaki Misawa, and Kei Murakoshi. Single molecule dynamics at a mechanically controllable break junction in solution at room temperature. *Journal of the American Chemical Society*, 135(3):1009–1014, 2013.

[28] J. M. Krans, C. J. Muller, I. K. Yanson, Th. C. M. Govaert, R. Hesper, and J. M. van Ruitenbeek. One-atom point contacts. *Phys. Rev. B*, 48:14721–14724, Nov 1993.

[29] G Kresse and J Furthmüller. Efficiency of ab-initio total energy calculations for metals and semiconductors using a plane-wave basis set. *Computational Materials Science*, 6(1):15–50, 1996.

[30] G Kresse and J Furthmüller. Efficient iterative schemes for ab initio total-energy calculations using a plane-wave basis set. *Physical Review B*, 54(16):11169–11186, oct 1996.

[31] G. Kresse and J. Hafner. Ab initio molecular dynamics for liquid metals. *Physical Review B*, 47(1):558–561, 1993.

[32] G Kresse and J Hafner. Ab initio molecular-dynamics simulation of the liquid-metal–amorphous-semiconductor transition in germanium. *Physical Review B*, 49(20):14251–14269, may 1994.

[33] Georg Kresse and Jürgen Hafner. Ab initio molecular dynamics for liquid metals. *Physical review B*, 47(1):558, 1993.

[34] Kyuho Lee, Éamonn D Murray, Lingzhu Kong, Bengt I Lundqvist, and David C Langreth. Higher-accuracy van der waals density functional. *Physical Review B*, 82(8):081101, 2010.

[35] Zong-Liang Li, Bin Zou, Chuan-Kui Wang, and Yi Luo. Electronic transport properties of molecular bipyridine junctions: Effects of isomer and contact structures. *Physical Review B*, 73(7):075326, 2006.

[36] Junyang Liu, Xiaotao Zhao, Jueting Zheng, Xiaoyan Huang, Yongxiang Tang, Fei Wang, Ruihao Li, Jiuchan Pi, Cancan Huang, Lin Wang, et al. Transition from tunneling leakage current to molecular tunneling in single-molecule junctions. *Chem*, 5(2):390–401, 2019.

[37] A Magyarkuti, Kasper Primdal Lauritzen, Z Balogh, A Nyáry, G Mészáros, P Makk, Gemma C Solomon, and A Halbritter. Temporal correlations and structural memory effects in break junction measurements. *The Journal of Chemical Physics*, 146(9):092319, 2017.

[38] Péter Makk, Damian Tomaszewski, Jan Martinek, Zoltán Balogh, Szabolcs Csonka, Maciej Wawrzyniak, Michael Frei, Latha Venkataraman, and András Halbritter. Correlation analysis of atomic and single-molecule junction conductance. *ACS nano*, 6(4):3411–3423, 2012.

[39] Hendrik J Monkhorst and James D Pack. Special points for brillouin-zone integrations. *Physical review B*, 13(12):5188, 1976.

[40] CJ Muller, JM Van Ruitenbeek, and LJ De Jongh. Conductance and supercurrent discontinuities in atomic-scale metallic constrictions of variable width. *Physical review letters*, 69(1):140, 1992.

[41] Shuichi Nosé. A unified formulation of the constant temperature molecular dynamics methods. *The Journal of chemical physics*, 81(1):511–519, 1984.

[42] Biswajit Pabi, Debayan Mondal, Priya Mahadevan, and Atindra Nath Pal. Probing metal-molecule contact at the atomic scale via conductance jumps. *Physical Review B*, 104(12):L121407, 2021.

[43] Atindra Nath Pal, Tal Klein, Ayelet Vilan, and Oren Tal. Electronic conduction during the formation stages of a single-molecule junction. *Beilstein journal of nanotechnology*, 9(1):1471–1477, 2018.

[44] Atindra Nath Pal, Tal Klein, Ayelet Vilan, and Oren Tal. Electronic conduction during the formation stages of a single-molecule junction. *Beilstein journal of nanotechnology*, 9(1):1471–1477, 2018.

[45] Atindra Nath Pal, Dongzhe Li, Soumyajit Sarkar, Sudipto Chakrabarti, Ayelet Vilan, Leeor Kronik, Alexander Smogunov, and Oren Tal. Nonmagnetic single-molecule spin-filter based on quantum interference. *Nature communications*, 10(1):1–8, 2019.

[46] Young S Park, Adam C Whalley, Maria Kamenetska, Michael L Steigerwald, Mark S Hybertsen, Colin Nuckolls, and Latha Venkataraman. Contact chemistry and single-molecule conductance: a comparison of phosphines, methyl sulfides, and amines. *Journal of the American Chemical Society*, 129(51):15768–15769, 2007.

[47] Gorka Pera, Santiago Martín, Luz M Ballesteros, Adam J Hope, Paul J Low, Richard J Nichols, and Pilar Cea. Metal–molecule–metal junctions in langmuir–blodgett films using a new linker: Trimethylsilane. *Chemistry–A European Journal*, 16(45):13398–13405, 2010.

[48] John P. Perdew, Kieron Burke, and Matthias Ernzerhof. Generalized gradient approximation made simple. *Phys. Rev. Lett.*, 77:3865–3868, Oct 1996.

[49] Su Ying Quek, Maria Kamenetska, Michael L Steigerwald, Hyoung Joon Choi, Steven G Louie, Mark S Hybertsen, JB Neaton, and Latha Venkataraman. Mechanically controlled binary conductance switching of a single-molecule junction. *Nature nanotechnology*, 4(4):230–234, 2009.

[50] Carlos Sabater, María José Caturla, Juan José Palacios, and Carlos Untiedt. Understanding the structure of the first atomic contact in gold. *Nanoscale research letters*, 8(1):257, 2013.

[51] Carlos Sabater, María José Caturla, Juan José Palacios, and Carlos Untiedt. Understanding the structure of the first atomic contact in gold. *Nanoscale research letters*, 8(1):257, 2013.

[52] Elke Scheer and Juan Carlos Cuevas. *Molecular electronics: an introduction to theory and experiment*, volume 15. World Scientific, 2017.

[53] Stefan Schmaus, Alexei Bagrets, Yasmine Nahas, Toyo K Yamada, Annika Bork, Martin Bowen, Eric Beaurepaire, Ferdinand Evers, and Wulf Wulfhekel. Giant magnetoresistance through a single molecule. *Nature nanotechnology*, 6(3):185–189, 2011.

[54] Wolfgang Schneider, Alexander Sladek, Andreas Bauer, Klaus Angermaier, and Hubert Schmidbaur. Structural investigation of bis(isonitrile)gold(i) complexes. *Zeitschrift für Naturforschung B*, 52(1):53–56, 1997.

[55] Nadja Sändig and Francesco Zerbetto. Molecules on gold. *Chem. Commun.*, 46:667–676, 2010.

[56] Nosé Shuichi. Constant temperature molecular dynamics methods. *Progress of Theoretical Physics Supplement*, 103:1–46, 1991.

[57] AF Takács, F Witt, S Schmaus, T Balashov, M Bowen, E Beaurepaire, and W Wulfhekel. Electron transport through single phthalocyanine molecules studied using scanning tunneling microscopy. *Physical Review B*, 78(23):233404, 2008.

[58] ML Trouwborst, EH Huisman, FL Bakker, SJ Van der Molen, and BJ Van Wees. Single atom adhesion in optimized gold nanojunctions. *Physical review letters*, 100(17):175502, 2008.

[59] C. Untiedt, M. J. Caturla, M. R. Calvo, J. J. Palacios, R. C. Segers, and J. M. van Ruitenbeek. Formation of a metallic contact: Jump to contact revisited. *Phys. Rev. Lett.*, 98:206801, May 2007.

[60] C. Untiedt, A. I. Yanson, R. Grande, G. Rubio-Bollinger, N. Agraït, S. Vieira, and J.M. van Ruitenbeek. Calibration of the length of a chain of single gold atoms. *Phys. Rev. B*, 66:085418, Aug 2002.

[61] Carlos Untiedt, Maria J Caturla, M Reyes Calvo, JJ Palacios, RC Segers, and JM Van Ruitenbeek. Formation of a metallic contact: jump to contact revisited. *Physical review letters*, 98(20):206801, 2007.

[62] Carlos Untiedt, Maria J Caturla, M Reyes Calvo, JJ Palacios, RC Segers, and JM Van Ruitenbeek. Formation of a metallic contact: jump to contact revisited. *Physical review letters*, 98(20):206801, 2007.

[63] Ran Vardimon, Tamar Yelin, Marina Klionsky, Soumyajit Sarkar, Ariel Biller, Leeor Kronik, and Oren Tal. Probing the orbital origin of conductance oscillations in atomic chains. *Nano letters*, 14(6):2988–2993, 2014.

[64] Latha Venkataraman, Jennifer E Klare, Iris W Tam, Colin Nuckolls, Mark S Hybertsen, and Michael L Steigerwald. Single-molecule circuits with well-defined molecular conductance. *Nano letters*, 6(3):458–462, 2006.

[65] Latha Venkataraman, Jennifer E Klare, Iris W Tam, Colin Nuckolls, Mark S Hybertsen, and Michael L Steigerwald. Single-molecule circuits with well-defined molecular conductance. *Nano letters*, 6(3):458–462, 2006.

[66] Anton Vladyka, Mickael L Perrin, Jan Overbeck, Rubén R Ferradás, Víctor García-Suárez, Markus Gantenbein, Jan Brunner, Marcel Mayor, Jaime Ferrer, and Michel Calame. In-situ formation of one-dimensional coordination polymers in molecular junctions. *Nature communications*, 10(1):1–9, 2019.

[67] S. A. G. Vrouwe, E. van der Giessen, S. J. van der Molen, D. Dulic, M. L. Trouwborst, and B. J. van Wees. Mechanics of lithographically defined break junctions. *Phys. Rev. B*, 71:035313, Jan 2005.

[68] PJ Wheeler, JN Russom, K Evans, NS King, and D Natelson. Shot noise suppression at room temperature in atomic-scale au junctions. *Nano letters*, 10(4):1287–1292, 2010.

[69] Bingqian Xu and Nongjian J Tao. Measurement of single-molecule resistance by repeated formation of molecular junctions. *science*, 301(5637):1221–1223, 2003.

[70] Bingqian Xu, Xiaoyin Xiao, and Nongjian J. Tao. Measurements of single-molecule electromechanical properties. *Journal of the American Chemical Society*, 125(52):16164–16165, 2003. PMID: 14692738.

[71] A. I. Yanson, G. Rubio Bollinger, H. E. Van Den Brom, N. Agraït, and J. M. Van Ruitenbeek. Formation and manipulation of a metallic wire of single gold atoms. *Nature*, 395(6704):783–785, 1998.

Chapter 8

Temperature Dependent Ring Rotation and Single Molecular Junction Study of Ferrocene Molecule

1 Introduction

The pursuit of smaller and more efficient electronic devices is a major driving force in the field of molecular electronics. Researchers are actively investigating novel molecular materials, functional groups, and design principles, intending to tailor the properties of individual molecules to fulfil specific electronic functions[12, 18, 28, 36, 45, 52, 54, 58]. This endeavour encompasses the development of molecular wires, switches, and rectifiers, opening the door to groundbreaking innovations in the design and utilization of electronic components. Customizing molecular components for specific functionalities represents a promising avenue in this field. This process, combined with a careful examination of the intrinsic density of states of metal electrodes at the Fermi level[1, 21, 47], has the potential

to lead to the realization of electronic functions such as rectification[5] and molecular-scale switching[50, 51].

Recent years have witnessed a significant focus on exploring the electronic structure and transport properties of metal/molecule/metal junctions under the influence of external stimuli[4, 9, 37, 46, 59, 60]. These investigations have unveiled the intricate responses of these junctions to various factors, including light, temperature, mechanical force, electric fields, and environmental conditions. A comprehensive understanding of this response is pivotal for unravelling the behaviour of molecular junctions and exploring their potential applications. The conformation or geometry of the molecule within the junction is another critical parameter that cannot be overlooked. It exerts a profound influence on charge transfer to or from the molecule and shapes the evolution of the junction itself. The impact of conformation is evident in studies of the torsional angle-dependent conductance of biphenyl rings[32, 33, 53, 55] and the structure-assisted contact formation in bipyridine isomers[40] . In recent experiments, it has been found that a single-molecule junction with

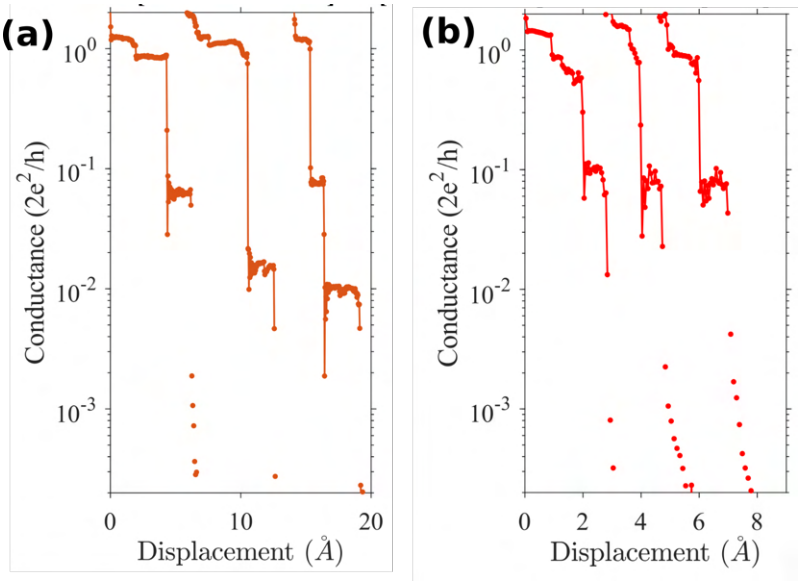

FIGURE 8.1: Conductance traces of ferrocene molecular junction attached to gold tips (a) 77 K (orange) and (b) 300 K (red). (Adapted from Ph.D. Thesis of Biswajit Pabi)

an organometallic molecule ferrocene shows temperature-dependent conductance changes. At low temperature (77K) there are two molecular conductance plateaus seen in the experiment, one at $10^{-1}G_0$ (high) and another at $10^{-2}G_0$ (low) whereas at room temperature

(300K) the low conductance Plateau is absent (Figure 8.1). Earlier studies[41] have shown that low conductance is associated with the parallel configuration, while high conductance is associated with the perpendicular configuration. In this chapter, our primary focus centres on examining conductance measurements of ferrocene distinguished by its barrel-shaped structure [29] that consists of an iron atom nestled between two cyclopentadienyl (Cp) rings[17, 31]. One of the most notable attributes of ferrocene pertains to its temperature-dependent rotational dynamics, particularly the motion of the two Cp rings. As the temperature decreases, the rotational motion slows down due to the presence of a finite activation energy barrier[3, 8, 16, 39, 56], as visually represented in Figure 8.2.

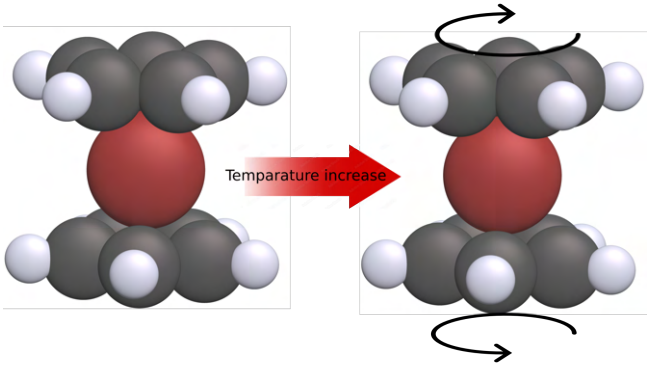

FIGURE 8.2: Schematic of ferrocene and graphical demonstration of temperature modified rotational dynamics of its cyclopentadienyl (Cp) rings where arrows describe the free rotation at room temperature.

Our investigation provides the theoretical understanding of the experimental observations (Figure 8.1), and explains the temperature-dependent conformational changes in ferrocene between two electrode tips. This behaviour arises from temperature-induced alterations in the rotational dynamics of the Cp rings, which, in turn, disrupts the coupling between the metal and the molecule. Significantly, this effect is most pronounced in configurations where the Cp rings are in direct contact with the metallic electrodes. As a result, the presence of a specific configuration becomes exquisitely sensitive to temperature variations. In summary, the role of temperature-assisted intra-molecular rotation introduces an entirely new dimension for understanding and controlling the formation of dynamic molecular junctions. This phenomenon sheds light on the intricate relationship between

temperature, molecular dynamics, and electronic behavior within these systems, unveiling a multitude of opportunities for innovative applications and deeper insights into the field of molecular electronics.

2 Methodology

We have conducted electronic structure calculations based on density functional theory (DFT) employing the Perdew-Burke-Ernzerhof (PBE) generalized gradient approximation [44] for the exchange-correlation functional. These calculations were carried out using the Vienna ab initio simulation package (VASP) [22–25], a well-established tool in the field. In certain cases, we complemented our DFT calculations with molecular dynamics (MD) simulations[2, 11, 27] to gain deeper insights into the origins of temperature-induced accessibility to various conformations in Au/ferrocene/Au single-molecule junctions and its subsequent impact on conductance.

Our ab-initio MD simulations encompassed both low temperature (77K) and room temperature (300K) scenarios for molecular junctions formed by ferrocene molecules oriented in parallel and perpendicular arrangements relative to the gold electrode axis(Figure 8.3). The initial junction geometry was established based on the optimized structure of a gold slab-molecule-gold slab configuration, employing six layers for each slab and separated by a vacuum region of 15Å.

To maintain the system at the desired temperature, we utilized a Nosé-Hoover thermostat[15, 38, 48] within an NVT canonical ensemble, ensuring precise temperature control during the simulations. Dispersion corrections were also incorporated using the DFT-D2 method developed by Grimme [13, 30, 57], as van der Waals interactions play a crucial role in accurately describing long-range interactions between atoms and molecules.

Our k-space sampling[35] was limited to Γ point only, and we employed a cutoff energy of 500 eV for the plane-wave basis set, ensuring accurate representation of the electronic

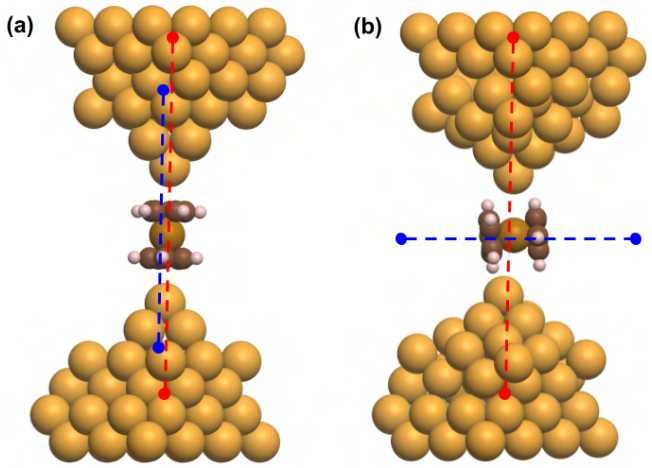

FIGURE 8.3: The two possible geometry considered in the calculations (a) the molecular orientation is parallel to the electrode axis (red line), and (b)the the molecular orientation is perpendicular to the electrode axis. blue line is the molecular axis

states. The energy convergence criteria were set at $10^{-}5$ eV, and structural relaxations were carried out until the forces on each atom were smaller than $10^{-}3$ eV.

3 Results and discussion

In order to understand the reasons behind the temperature-dependent conformations in Au/ferrocene/Au single-molecule junctions, we performed DFT calculations for both conformations. The geometry considered in the calculations involved two pyramidal gold electrodes between which the ferrocene molecule was placed. Two distinct arrangements of the molecule are possible, one in which the molecular orientation is parallel to the electrode axis, and the other in which it is perpendicular[42]. The relative stability of the parallel and perpendicular junction configurations is depicted in Figure 8.4. In general, we observed that the parallel configuration is energetically favoured when the inter-electrode separation is larger (d2 = 9.20 Å), while the perpendicular orientation becomes more stable at smaller separations (d1 = 7.90 Å). We selected these structures for our subsequent analysis.

To explore how the local geometry changes with temperature, we conducted molecular dynamics simulations at both 300 K and 77 K. At 300 K, when the molecule is positioned

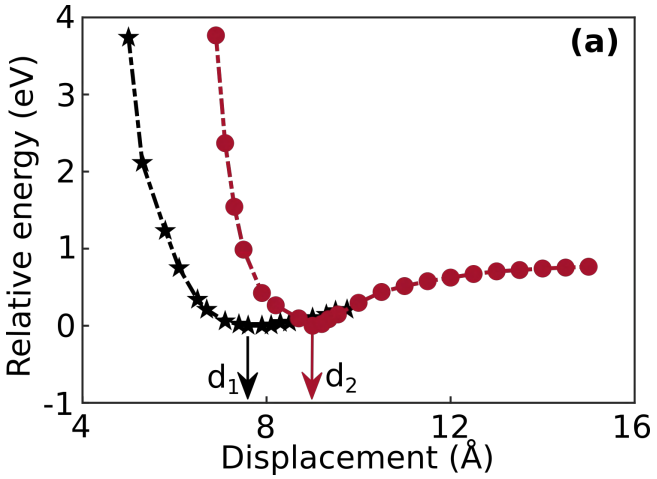

FIGURE 8.4: Total energy of Au/ferrocene/Au junctions as a function of electrode separation. The calculations are done for perpendicular (red) and parallel (black) configurations at different electrode separations,

in a perpendicular orientation, the iron (Fe) atom within the molecule establishes a stable bond with the gold (Au) electrodes. The displacement of the Fe atom from the electrode axis is minimal, measuring only 0.03 Å, 0.02 Å, and 0.02 Å, respectively, at different MD timescales (6 ps, 12 ps, and 18 ps), as depicted in Figure 8.5a. Conversely, the behavior of the molecule when positioned parallel to the electrode axis exhibits a notably different pattern. In this alignment,a significant off- centering of the Fe atom with the electrode axis can be found i.e., 0.57Å, 0.86Å and 1.07Å respectively at the previously mentioned MD timescale (Figure 8.5b). These results indicate that at room temperature, the molecule can establish a stable configuration over time when placed in a perpendicular orientation. However, when it is oriented parallel to the electrode axis, the configuration becomes unstable over time, leading to a rapid displacement of the molecule away from the electrode axis. This instability can be the fundamental reason for the experimental observation of only one conductance peak associated with the molecular junction at 300 K.

In contrast, at low temperatures (77 K), the off-centering of the molecule for both parallel and perpendicular configurations is negligible, as depicted in Figure 8.6. This suggests the establishment of a stable electrode-molecule bond for both configurations, corroborating the experimentally observed presence of two stable junction configurations at 77 K.

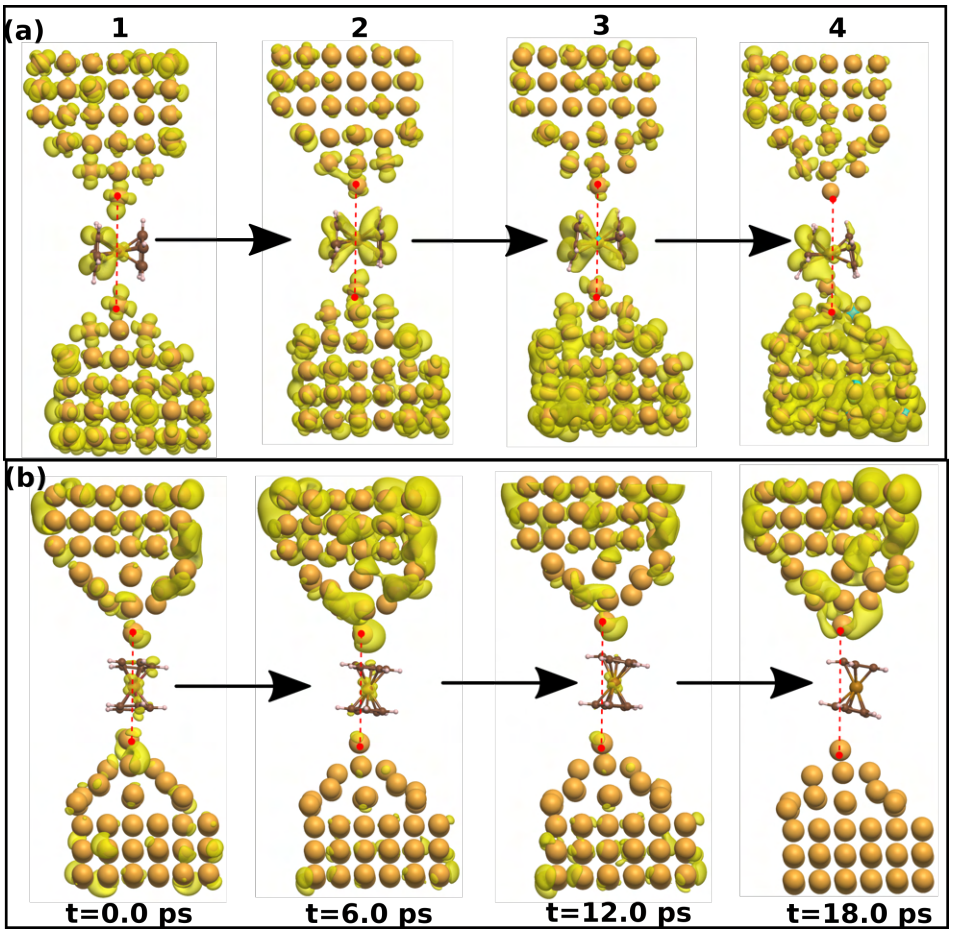

FIGURE 8.5: Room temperature MD snapshot of the gold molecular junction with ferrocene molecule at perpendicular (a) and parallel (b) to the electrode axis (red line) at time t= 0 ps, 6.0 ps, 12.0 ps and 18.0 ps.

To gain a deeper insight into the origins of the unstable junction formation at room temperature when the molecule is in a parallel orientation, we examine the bond formed between the molecule and the electrodes. An idea of the bonding can be obtained from the charge density plot around the Fermi energy, as shown in Figure 8.7. This suggests that there is an interaction between the frontier orbitals of the gold electrodes and the π-orbitals (py) of the molecule in the spin-up channel. The matrix element governing the hopping between the s orbital of the gold tip and the py orbital of the carbon atom in the molecule involves a term denoted as $E_{s,y} = mV_{pp\sigma}$, where m represents the direction cosine between the gold s orbital and the carbon py orbital, and $V_{pp\sigma}$ stands for the Slater-Koster parameter[7, 43, 49].

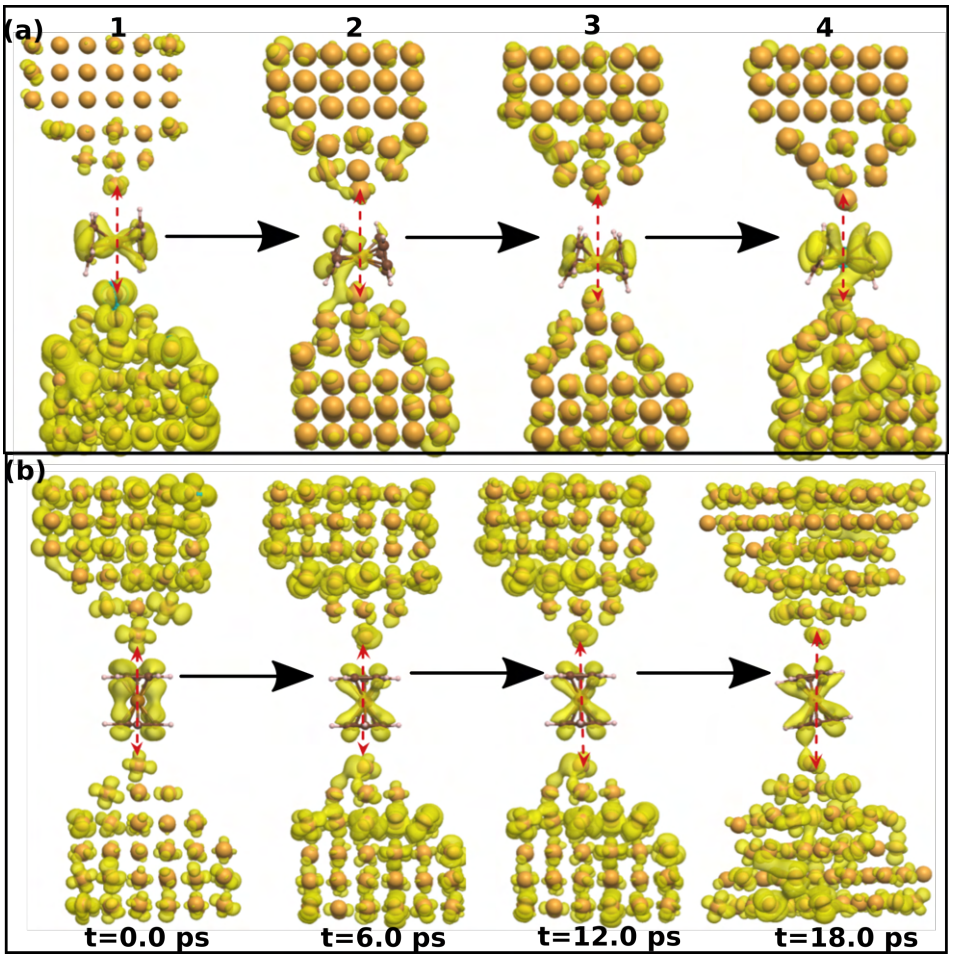

FIGURE 8.6: Low-temperature MD snapshot of the gold molecular junction with ferrocene molecule at perpendicular (a) and parallel (b) to the electrode axis (red line) at time t= t= 0 ps, 6.0 ps, 12.0 ps and 18.0 ps.

As the Cp rings rotate freely at a frequency of 17° per picosecond, we find that some of the matrix elements between the molecule and the electrode may reduce and vanish at some positions. As the steric interaction strength remains relatively constant, this rotational motion prompts the molecule to move off-center from the junction, thereby mitigating the effects of steric repulsion. It's worth noting that at low temperatures, this effect is less pronounced, as the rotation of the Cp ring is restricted.

On the other hand, in the perpendicular conformation, the coupling between the electrode and the molecule involves the Au-s and d orbitals of the immobile iron (Fe) atom. This stable coupling ensures that the coupling strength remains almost constant with time, allowing for the formation of a stable junction for both 77K and 300K.

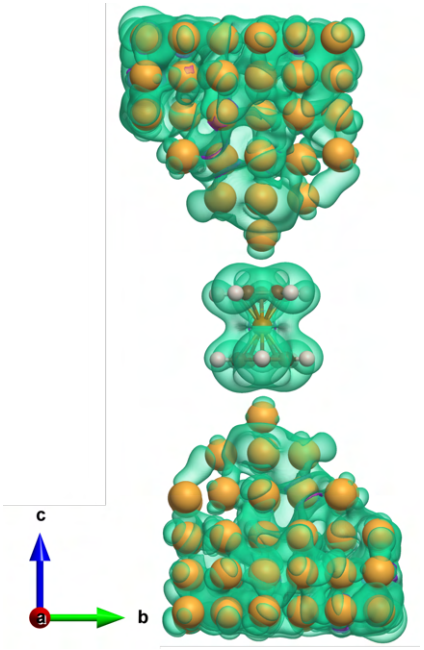

FIGURE 8.7: The spatially resolved charge density plot around the Fermi energy showing the contributions of the frontier orbitals of the gold electrodes and the π-orbitals (py) of the molecule

4 Conclusion

In conclusion, our exploration of the behaviour of ferrocene molecules in single-molecule junctions, with a particular focus on the influence of temperature, has unveiled a rich tapestry of dynamic interactions and electronic behaviour. The temperature-dependent rotational dynamics of the cyclopentadienyl (Cp) rings in ferrocene play a pivotal role in determining the stability and conductance of the molecular junctions. Our findings reveal that at room temperature, the molecule can assume a stable configuration when oriented perpendicularly to the electrode axis, forming a secure bond with minimal displacement. However, when placed in parallel, the configuration becomes progressively unstable, leading to significant off-centering of the molecule from the electrode axis and the observation of only one conductance peak.

In contrast, at lower temperatures, the dynamic nature of the Cp ring rotations is less pronounced, resulting in the existence of two stable configurations for the junction. This

temperature-dependent phenomenon sheds light on the intricate interplay between molecular dynamics, electronic behaviour, and temperature in single-molecule junctions.

Our study underscores the significance of temperature as a crucial factor in shaping the behaviour of dynamic molecular junctions and adds a new dimension to the field of molecular electronics. These insights hold potential for applications where control over the stability and conductance of molecular junctions is paramount, offering opportunities for developing advanced electronic components and devices. By delving into the realm of molecular dynamics within single-molecule junctions, we not only advance our fundamental understanding of these systems but also pave the way for future innovations in the realm of molecular electronics, where the temperature becomes a tool for tailoring the behaviour and functionality of electronic components.

References

[1] Olgun Adak, Richard Korytár, Andrew Y Joe, Ferdinand Evers, and Latha Venkataraman. Impact of electrode density of states on transport through pyridine-linked single molecule junctions. *Nano letters*, 15(6):3716–3722, 2015.

[2] Michael P Allen and Dominic J Tildesley. *Computer simulation of liquids*. Oxford university press, 2017.

[3] Markus Appel, Bernhard Frick, Tinka Luise Spehr, and Bernd Stühn. Molecular ring rotation in solid ferrocene revisited. *The Journal of Chemical Physics*, 142(11), 2015.

[4] Sriharsha V Aradhya and Latha Venkataraman. Single-molecule junctions beyond electronic transport. *Nature nanotechnology*, 8(6):399–410, 2013.

[5] Arunabh Batra, Pierre Darancet, Qishui Chen, Jeffrey S Meisner, Jonathan R Widawsky, Jeffrey B Neaton, Colin Nuckolls, and Latha Venkataraman. Tuning rectification in single-molecular diodes. *Nano letters*, 13(12):6233–6237, 2013.

[6] P E Blöchl. Projector augmented-wave method. *Physical Review B*, 50(24):17953–17979, dec 1994.

[7] Timothy B Boykin, Gerhard Klimeck, and Fabiano Oyafuso. Valence band effective-mass expressions in the sp 3 d 5 s* empirical tight-binding model applied to a si and ge parametrization. *Physical Review B*, 69(11):115201, 2004.

[8] Michael Bühl and Sonja Grigoleit. Molecular dynamics of neutral and protonated ferrocene. *Organometallics*, 24(7):1516–1527, 2005.

[9] Nadim Darwish, Albert C Aragones, Tamim Darwish, Simone Ciampi, and Ismael Diez-Perez. Multi-responsive photo-and chemo-electrical single-molecule switches. *Nano letters*, 14(12):7064–7070, 2014.

[10] David A Egger and Leeor Kronik. Role of Dispersive Interactions in Determining Structural Properties of Organic–Inorganic Halide Perovskites: Insights from First-Principles Calculations. *The Journal of Physical Chemistry Letters*, 5(15):2728–2733, aug 2014.

[11] Daan Frenkel and Berend Smit. *Understanding molecular simulation: from algorithms to applications*, volume 1. Elsevier, 2001.

[12] Marc H Garner, Haixing Li, Yan Chen, Timothy A Su, Zhichun Shangguan, Daniel W Paley, Taifeng Liu, Fay Ng, Hexing Li, Shengxiong Xiao, et al. Comprehensive suppression of single-molecule conductance using destructive σ-interference. *Nature*, 558(7710):415–419, 2018.

[13] Stefan Grimme. Semiempirical GGA-type density functional constructed with a long-range dispersion correction. *Journal of Computational Chemistry*, 27(15):1787–1799, nov 2006.

[14] Stefan Grimme. Semiempirical gga-type density functional constructed with a long-range dispersion correction. *Journal of computational chemistry*, 27(15):1787–1799, 2006.

[15] William G Hoover. Canonical dynamics: Equilibrium phase-space distributions. *Physical review A*, 31(3):1695, 1985.

[16] Masahiko Inouye, Yutaka Hyodo, and Hiroyuki Nakazumi. Nucleobase recognition by artificial receptors possessing a ferrocene skeleton as a novel modular unit for hydrogen bonding and stacking interactions. *The Journal of Organic Chemistry*, 64(8):2704–2710, 1999.

[17] T J KEALY and P L PAUSON. A New Type of Organo-Iron Compound. *Nature*, 168(4285):1039–1040, 1951.

[18] Manabu Kiguchi, Tatsuhiko Ohto, Shintaro Fujii, Kazunori Sugiyasu, Shigeto Nakajima, Masayuki Takeuchi, and Hisao Nakamura. Single molecular resistive switch obtained via sliding multiple anchoring points and varying effective wire length. *Journal of the American Chemical Society*, 136(20):7327–7332, 2014.

[19] Ji ří Klimeš, David R. Bowler, and Angelos Michaelides. Van der waals density functionals applied to solids. *Phys. Rev. B*, 83:195131, May 2011.

[20] Jiří Klimeš, David R Bowler, and Angelos Michaelides. Chemical accuracy for the van der waals density functional. *Journal of Physics: Condensed Matter*, 22(2):022201, dec 2009.

[21] Chih-Hung Ko, Min-Jie Huang, Ming-Dung Fu, and Chun-hsien Chen. Superior contact for single-molecule conductance: electronic coupling of thiolate and isothiocyanate on pt, pd, and au. *Journal of the American Chemical Society*, 132(2):756–764, 2010.

[22] G Kresse and J Furthmüller. Efficiency of ab-initio total energy calculations for metals and semiconductors using a plane-wave basis set. *Computational Materials Science*, 6(1):15–50, 1996.

[23] G Kresse and J Furthmüller. Efficient iterative schemes for ab initio total-energy calculations using a plane-wave basis set. *Physical Review B*, 54(16):11169–11186, oct 1996.

[24] G. Kresse and J. Hafner. Ab initio molecular dynamics for liquid metals. *Physical Review B*, 47(1):558–561, 1993.

[25] G Kresse and J Hafner. Ab initio molecular-dynamics simulation of the liquid-metal–amorphous-semiconductor transition in germanium. *Physical Review B*, 49(20):14251–14269, may 1994.

[26] G Kresse and D Joubert. From ultrasoft pseudopotentials to the projector augmented-wave method. *Physical Review B*, 59(3):1758–1775, jan 1999.

[27] Georg Kresse and Jürgen Hafner. Ab initio molecular dynamics for liquid metals. *Physical review B*, 47(1):558, 1993.

[28] Leif Lafferentz, Francisco Ample, Hao Yu, Stefan Hecht, Christian Joachim, and Leonhard Grill. Conductance of a single conjugated polymer as a continuous function of its length. *Science*, 323(5918):1193–1197, 2009.

[29] Brent Lawson, Percy Zahl, Mark S Hybertsen, and Maria Kamenetska. Formation and evolution of metallocene single-molecule circuits with direct gold-π links. *Journal of the American Chemical Society*, 144(14):6504–6515, 2022.

[30] Kyuho Lee, Éamonn D Murray, Lingzhu Kong, Bengt I Lundqvist, and David C Langreth. Higher-accuracy van der Waals density functional. *Physical Review B*, 82(8):81101, aug 2010.

[31] Samuel A Miller, John A Tebboth, and John F Tremaine. 114. di cyclo pentadienyl-iron. *Journal of the Chemical Society (Resumed)*, pages 632–635, 1952.

[32] Artem Mishchenko, David Vonlanthen, Velimir Meded, Marius Burkle, Chen Li, Ilya V Pobelov, Alexei Bagrets, Janne K Viljas, Fabian Pauly, Ferdinand Evers,

et al. Influence of conformation on conductance of biphenyl-dithiol single-molecule contacts. *Nano letters*, 10(1):156–163, 2010.

[33] Artem Mishchenko, Linda A Zotti, David Vonlanthen, Marius Burkle, Fabian Pauly, Juan Carlos Cuevas, Marcel Mayor, and Thomas Wandlowski. Single-molecule junctions based on nitrile-terminated biphenyls: a promising new anchoring group. *Journal of the American Chemical Society*, 133(2):184–187, 2011.

[34] Koichi Momma and Fujio Izumi. *VESTA*: a three-dimensional visualization system for electronic and structural analysis. *Journal of Applied Crystallography*, 41(3):653–658, jun 2008.

[35] Hendrik J Monkhorst and James D Pack. Special points for Brillouin-zone integrations. *Physical Review B*, 13(12):5188–5192, jun 1976.

[36] Pavel Moreno-García, Andrea La Rosa, Viliam Kolivoska, Daniel Bermejo, Wenjing Hong, Koji Yoshida, Masoud Baghernejad, Salvatore Filippone, Peter Broekmann, Thomas Wandlowski, et al. Charge transport in c60-based dumbbell-type molecules: mechanically induced switching between two distinct conductance states. *Journal of the American Chemical Society*, 137(6):2318–2327, 2015.

[37] Shigeto Nakashima, Yuuta Takahashi, and Manabu Kiguchi. Effect of the environment on the electrical conductance of the single benzene-1, 4-diamine molecule junction. *Beilstein journal of nanotechnology*, 2(1):755–759, 2011.

[38] Shuichi Nosé. A unified formulation of the constant temperature molecular dynamics methods. *The Journal of chemical physics*, 81(1):511–519, 1984.

[39] Kouji Ogasahara, Michio Sorai, and Hiroshi Suga. Thermodynamic properties of ferrocene crystal. *Molecular Crystals and Liquid Crystals*, 71(3-4):189–211, 1981.

[40] Biswajit Pabi, Debayan Mondal, Priya Mahadevan, and Atindra Nath Pal. Probing metal-molecule contact at the atomic scale via conductance jumps. *Physical Review B*, 104(12):L121407, 2021.

[41] Biswajit Pabi, Jakub Sebesta, Richard Korytár, Oren Tal, and Atindra Nath Pal. Structural regulation of mechanical gating in molecular junctions. *Nano Letters*, 23(9):3775–3780, 2023.

[42] Atindra Nath Pal, Dongzhe Li, Soumyajit Sarkar, Sudipto Chakrabarti, Ayelet Vilan, Leeor Kronik, Alexander Smogunov, and Oren Tal. Nonmagnetic single-molecule spin-filter based on quantum interference. *Nature communications*, 10(1):5565, 2019.

[43] DA Papaconstantopoulos and MJ Mehl. The slater–koster tight-binding method: a computationally efficient and accurate approach. *Journal of Physics: Condensed Matter*, 15(10):R413, 2003.

[44] John P Perdew, Kieron Burke, and Matthias Ernzerhof. Generalized Gradient Approximation Made Simple. *Physical Review Letters*, 77(18):3865–3868, oct 1996.

[45] Su Ying Quek, Maria Kamenetska, Michael L Steigerwald, Hyoung Joon Choi, Steven G Louie, Mark S Hybertsen, JB Neaton, and Latha Venkataraman. Mechanically controlled binary conductance switching of a single-molecule junction. *Nature nanotechnology*, 4(4):230–234, 2009.

[46] Harsha Reddy, Kun Wang, Zhaxylyk Kudyshev, Linxiao Zhu, Shen Yan, Andrea Vezzoli, Simon J Higgins, Vikram Gavini, Alexandra Boltasseva, Pramod Reddy, et al. Determining plasmonic hot-carrier energy distributions via single-molecule transport measurements. *Science*, 369(6502):423–426, 2020.

[47] Jorge M Seminario, Cecilia E De La Cruz, and Pedro A Derosa. A theoretical analysis of metal- molecule contacts. *Journal of the American Chemical Society*, 123(23):5616–5617, 2001.

[48] Nosé Shuichi. Constant temperature molecular dynamics methods. *Progress of Theoretical Physics Supplement*, 103:1–46, 1991.

[49] John C Slater and George F Koster. Simplified lcao method for the periodic potential problem. *Physical review*, 94(6):1498, 1954.

[50] Timothy A Su, Haixing Li, Michael L Steigerwald, Latha Venkataraman, and Colin Nuckolls. Stereoelectronic switching in single-molecule junctions. *Nature chemistry*, 7(3):215–220, 2015.

[51] Timothy A Su, Haixing Li, Vivian Zhang, Madhav Neupane, Arunabh Batra, Rebekka S Klausen, Bharat Kumar, Michael L Steigerwald, Latha Venkataraman, and Colin Nuckolls. Single-molecule conductance in atomically precise germanium wires. *Journal of the American Chemical Society*, 137(38):12400–12405, 2015.

[52] Timothy A Su, Madhav Neupane, Michael L Steigerwald, Latha Venkataraman, and Colin Nuckolls. Chemical principles of single-molecule electronics. *Nature Reviews Materials*, 1(3):1–15, 2016.

[53] Latha Venkataraman, Jennifer E Klare, Colin Nuckolls, Mark S Hybertsen, and Michael L Steigerwald. Dependence of single-molecule junction conductance on molecular conformation. *Nature*, 442(7105):904–907, 2006.

[54] Latha Venkataraman, Young S Park, Adam C Whalley, Colin Nuckolls, Mark S Hybertsen, and Michael L Steigerwald. Electronics and chemistry: varying single-molecule junction conductance using chemical substituents. *Nano letters*, 7(2):502–506, 2007.

[55] David Vonlanthen, Artem Mishchenko, Mark Elbing, Markus Neuburger, Thomas Wandlowski, and Marcel Mayor. Chemically controlled conductivity: torsion-angle dependence in a single-molecule biphenyldithiol junction. *Angew. Chem., Int. Ed*, 48(47):8886–8890, 2009.

[56] Feng Wang and Vladislav Vasilyev. Molecular dynamics study of ferrocene topology under various temperatures. *International Journal of Quantum Chemistry*, 120(23):e26398, 2020.

[57] Yun Wang, Tim Gould, John F Dobson, Haimin Zhang, Huagui Yang, Xiangdong Yao, and Huijun Zhao. Density functional theory analysis of structural and electronic

properties of orthorhombic perovskite CH3NH3PbI3. *Physical Chemistry Chemical Physics*, 16(4):1424–1429, 2014.

[58] Tamar Yelin, Richard Korytár, Nirit Sukenik, Ran Vardimon, Bhupesh Kumar, C Nuckolls, Ferdinand Evers, and Oren Tal. Conductance saturation in a series of highly transmitting molecular junctions. *Nature materials*, 15(4):444–449, 2016.

[59] Yaping Zang, E-Dean Fung, Tianren Fu, Suman Ray, Marc H Garner, Anders Borges, Michael L Steigerwald, Satish Patil, Gemma Solomon, and Latha Venkataraman. Voltage-induced single-molecule junction planarization. *Nano Letters*, 21(1):673–679, 2020.

[60] Alexander S Zyazin, Johan WG van den Berg, Edgar A Osorio, Herre SJ van der Zant, Nikolaos P Konstantinidis, Martin Leijnse, Maarten R Wegewijs, Falk May, Walter Hofstetter, Chiara Danieli, et al. Electric field controlled magnetic anisotropy in a single molecule. *Nano letters*, 10(9):3307–3311, 2010.

Chapter 9

Summary and Conclusions

In conclusion, this thesis marks a significant contribution to the field of perovskite materials, unraveling the intricate interplay between structure and properties. While exploring the traditional perovskite structure and its deviations in hybrid perovskites, a notable shift is observed with the introduction of organic molecules at the A-site. The focus on molecular symmetry reveals a different insight—specifically, that the shape of the molecule dictates the extent of hydrogen bonding with the inorganic cage, ultimately determining octahedral tilts in hybrid perovskite structures. The shape and symmetry of these organic molecules were identified as crucial parameters influencing structural distortions, challenging the conventional understanding based solely on ionic radii.

The exploration extended to perovskite nanocrystals, where this thesis addresses a long-standing puzzle: why do these nanocrystals overwhelmingly adopt a cubic shape under various synthesis conditions? The revelation of a 26-faceted polyhedron under halide-deficient conditions provides a key to understanding the formation energy of different facets and their consequential impact on optical properties, especially in the presence of dopants. This section underscores the potential for tailoring the properties of perovskite nanocrystals for applications in catalysis and optoelectronics.

Shifting focus to 2D perovskites, the choice of spacer cation emerged as a critical factor influencing interlayer interactions and edge state emissions. Cation exchange processes were identified as manipulators of edge states, offering controlled modifications. Theoretical insights from DFT simulations shed light on the interplay of organic-inorganic interactions, lattice distortions, and quantum confinement effects, emphasizing the distinct properties at the surface compared to the bulk.

The journey concluded with an exploration of different conductance features in Molecular electronics by addressing a fundamental question in the field—how to tune the resistance of a molecule covalently attached to two electrodes—the study employs mechanical break junctions to unravel unusual features in single molecular junctions. The exploration of the temperature-dependent conductance changes in ferrocene, known for its barrel-shaped structure, unveils a fascinating relationship between intra-molecular rotation, dynamic junction formation, and electronic behavior. Future research in this domain holds promises for dynamic control and responsive molecular electronic devices, contributing to the evolving field of nanoelectronics.

In summary, this thesis stands at the intersection of perovskite materials and molecular electronics, presenting a comprehensive exploration of their diverse structural and electronic properties. The emphasis on molecular symmetry, nanocrystal facets, and the behavior of individual molecules in electronic circuits, particularly ferrocene and BPY, contributes to the evolving landscape of materials science.

1 Outlook and future aspects

The findings presented in this thesis pave the way for several promising avenues of future research, offering an exciting outlook for both perovskite materials and molecular electronics.

1.1 Perovskite Materials:

1. Tailoring Nanocrystal Properties: Future investigations can delve deeper into the controlled synthesis of perovskite nanocrystals, aiming to unlock the full potential of varied shapes for catalysis and optoelectronic applications. Understanding the growth mechanisms and facets' stability under different conditions will be crucial.

2. Exploration of Dopant Effects: The study on the impact of dopants on the optical properties of perovskite nanocrystals, particularly the selective emissivity on specific facets, opens up avenues for tailoring functionalities. Future work can explore a wider range of dopants and their effects on nanocrystal properties.

3. 2D Perovskites and Edge States: Further exploration of 2D perovskites and their edge states is warranted. Investigating additional spacer cations and their influence on edge state emissions can provide a more comprehensive understanding. Moreover, experimental validations of theoretical predictions can contribute to the development of novel materials.

1.2 Molecular Electronics:

1. Molecular Junctions and Novel Molecules: The study on molecular junctions, especially with ferrocene and bipyridine (BPY), opens the door to a broader exploration of molecules for electronic applications. Future research can focus on identifying and understanding the behavior of new molecules in electronic circuits, pushing the boundaries of molecular electronics.

2. Temperature-Dependent Conductance: The intriguing relationship between temperature, molecular dynamics, and conductance in ferrocene suggests a rich area for further investigation. Exploring other molecules with distinct structural features and their responses to temperature variations can provide a deeper understanding of dynamic molecular junction behavior.

3. Applications in Molecular Electronics: As the field of molecular electronics continues to evolve, practical applications are on the horizon. Future research can explore the integration of these molecular components into functional electronic devices, contributing to the development of molecular-scale circuits and potentially revolutionizing electronic technology.

1.3 Cross-disciplinary Perspectives:

1. Integration of Perovskites and Molecular Electronics: Exploring the synergies between perovskite materials and molecular electronics represents a novel frontier. Investigating the incorporation of perovskite nanocrystals or 2D perovskites into molecular-scale circuits could lead to the development of hybrid materials with unprecedented functionalities.

2. Multifunctional Materials: The potential for developing multifunctional materials that exhibit unique structural and electronic properties, as demonstrated in this thesis, opens up new opportunities. Future research can explore materials that simultaneously exhibit perovskite-like structures and molecular electronic functionalities.

In conclusion, this thesis sets the stage for a diverse array of future investigations, ranging from refining the understanding of perovskite materials to unlocking the full potential of molecular electronics. The integration of these two dynamic fields holds promise for innovative materials and devices that can shape the landscape of materials science and electronics in the years to come. Researchers and practitioners are encouraged to build upon these foundational insights, pushing the boundaries of knowledge and driving advancements in these exciting and interconnected domains.